CRANFIELD UNIVERSITY

N THAPAR

LIQUID-LIQUID DISPERSIONS FROM IN-LINE ROTOR-STATOR MIXERS

SCHOOL OF MECHANICAL ENGINEERING

PhD THESIS

CRANFIELD UNIVERSITY

SCHOOL OF MECHANICAL ENGINEERING

PhD THESIS

Academic Year 1998-2001

N THAPAR

LIQUID-LIQUID DISPERSIONS FROM IN-LINE ROTOR-STATOR MIXERS

Supervisor: Prof. D. E. Brown

July 2004

This thesis is submitted in partial fulfilment of the requirements for the degree of Doctor of Philosophy.

Abstract

Experiments were performed on an industrial scale Silverson in-line rotor-stator mixer to investigate its liquid-liquid dispersion capabilities. A non-coalescing kerosene-water system was used in the tests and the effect of stator geometry, rotor-speeds, flowrates and dispersed phase concentrations on the droplet size distribution was investigated.

The rotor-speed and the dispersed phase concentration were found to have the most influence on droplet size. Drop sizes were also seen to increase with an increase in open area. No differences were observed in the droplet sizes or power draw of the stators with the smallest and similar open areas (Emulsor Screens and Square Hole High Shear screen). The power supplied to the fluid was proportional to N^3 indicating the mixer was operating under turbulent conditions. d_{32} was correlated against the rotor speed and dispersed phase and the relationship was found to be close to that described by Chen and Middleman (1967). This analysis suggested that inertial stresses in the viscous sub-range were mainly responsible for drop break-up.

$$d_{32} = 2x10^{9}(1+20\Phi)(We\,\mathrm{Re}^{4})^{-1/7}$$

An estimation of the average energy dissipation rate was made in order to determine the Kolomogov length scale. The droplet sizes ranged from below the Kolmogorov length scale to significantly higher, suggesting that droplet break-up is due to inertial and viscous sub-range eddies.

The Re could be defined in different regions within the mixer these values were used along with the nominal residence times in each region to determine where in the mixer the main drop break-up was occurring. The residence times for each region were in the following order: Shear Gap < Stator < Inlet < Rotor < Volute. The relatively long residence times and the magnitude of the stresses indicated that droplet break-up in a single pass through the in-line rotor-stator mixer is predominately determined by the viscous and inertial stresses in the rotor region.

Acknowledgements

I would like to thank the members of my support panel, in particular Professor Don Brown for his support, guidance and patience.

Many thanks are due to Peter Matthews, Harold Rothman and everyone at Silverson Machines Ltd for their unlimited support and for supplying the in-line rotor-stator mixer, constructing the test rigs and also giving me the use of their Malvern Mastersizer

I would also like to thank my friends and colleagues at BHR Group Ltd, especially Barry Johnson and the rest of the HILINE staff and members, for their assistance and guidance. Special thanks are due to John Brown and John Knopp for their aid with the instrumentation on the rig and to the guys in the workshops, who were ever willing to help.

I also owe a debt of gratitude to BHR Group Ltd and also the EPSRC for their financial support. In addition, I would like to thank the EPSRC Loan pool for making their Malvern Mastersizer available to me.

I would like to thank my friends, Tabs, Atul and Jin for continually pestering me to finish this thesis.

Finally, I would like to thank my Family; my mum and dad and my two brothers, this is for you.

LIST OF FIGURES V

LIST OF TABLES IX

LIST OF PLATES X

NOMENCLATURE XI

CHAPTER 1. INTRODUCTION 1

CHAPTER 2. LITERATURE REVIEW 3

2.1. ROTOR-STATOR MIXER BACKGROUND 3

2.1.1. Mixer Comparison 3

2.1.2. Rotor-Stator mixer designs 6

2.1.3. In-line rotor-stator mixers 9

2.1.4. In-line rotor-stator mixer designs available on the market 9

2.1.5. Operation of an in-line rotor-stator mixer 11

2.1.6. Industrial applications 12

2.1.7. Summary 14

2.2. LIQUID-LIQUID THEORY 15

2.2.1. Forces affecting drop stability 17

2.2.2. Drop break-up in turbulent flow 20

2.2.3. Mean drop size correlations 29

2.2.4. The effect of dispersed phase volume fraction, Φ, on turbulence 31

2.2.5. Summary 32

2.3. ROTOR-STATOR MIXERS 34

2.3.1. Flow patterns and Reynolds numbers in an in-line rotor-stator mixer 34

2.3.2. Drop Break-up in shear and elongated flow fields 42

2.3.3. Drop break-up in a rotor-stator mixer 55

2.3.4. Turbulent energy dissipation rates, ε 58

2.3.5. Energy dissipation and droplet size 60

2.3.6. Turbulent break-up in the shear gap 61

2.4. POWER CONSUMPTION IN A ROTOR-STATOR MIXER 62

2.4.1. Total power supplied to fluid 62

2.4.2. Shaft power - P_{SHAFT} 63

2.4.3. Pumping power - P_{PUMP} 65

2.4.4. Mechanical losses – P_{MECH} 67

2.4.5. Disc friction losses – P_{DISC} 67

2.4.6. Leakage (recirculation) losses – P_{LEAK} 67
2.4.7. Hydraulic losses – $P_{HYDRAULIC}$ 67
2.5. DROPLET SIZE MEASUREMENT TECHNIQUES 69
2.5.1. On-line drop size measurement techniques 69
2.5.2. Off-line drop size measurement techniques 70
2.5.3. Technique selection 71
2.6. CONCLUSIONS 71

CHAPTER 3. GOALS, AIMS AND OBJECTIVES 73

CHAPTER 4. EXPERIMENTAL EQUIPMENT, MATERIALS AND METHODS 74

4.1. EXPERIMENTAL RIG AND INSTRUMENTATION 74
4.1.1. Experimental Rig 75
4.1.2. Materials of Construction 78
4.1.3. Flowrate and Φ control 78
4.1.4. Rotor-stator mixer design 79
4.2. EXPERIMENTAL MATERIALS 82
4.2.1. Immiscible liquids 82
4.2.2. Kerosene-Water Stability 83
4.3. DROPLET SIZE MEASUREMENT 85
4.3.1. Malvern Mastersizer 85
4.3.2. Video Probe 89
4.3.3. Droplet size distributions 92
4.4. SAMPLING TECHNIQUE 94
4.4.1. Continuous Sampling 94
4.5. MEASUREMENT OF POWER SUPPLIED TO THE FLUID 97
4.5.1. Thermometric method of power measurement 98
4.5.2. Recycle loop and instrumentation 98
4.5.3. Experimental procedure 100
4.5.4. P_{SHAFT} 101
4.5.5. P_{PUMP} 102
4.5.6. P_{MECH} 102
4.5.7. P_{DISC} 102
4.5.8. P_{LEAK} and $P_{HYDRAULIC}$ 103
4.5.9. Losses through the control valve and pipe work 103

CHAPTER 5. RESULTS 104

5.1 MEASUREMENT TECHNIQUE VALIDATION 104

5.2. In-line rotor-stator performance tests 105
5.3. Power Measurement 105

CHAPTER 6. DISCUSSION 106

6.1. Measurement technique and Sampling validation 106
6.1.1. Kerosene-Water Stability 106
6.1.2. Comparison of measurement techniques 107
6.1.3. Sampling technique validation 109
6.2. Drop Size Distributions 112
6.2.1. Volume frequency curves 112
6.2.2. The relationship between d_{32} and d_{max} 113
6.2.3. The effect of rotational speed, N, on droplet size 115
6.2.4. The effect of dispersed phase concentration, Φ 118
6.2.5. The effect of flowrate, Q, on droplet size 120
6.2.6. The correlation of d_{32} with N 121
6.2.7. Correlation of d_{32} with We and Re 124
6.2.8. Summary 127
6.3. Power Measurement 129
6.3.1. Losses across the control valve and the pipework 129
6.3.2. P_{SHAFT} 130
6.3.3. P_{PUMP} 134
6.3.4. P_{MECH} and P_{DISC} 137
6.3.5. Power supplied to the fluid by the rotor, P_{FLUID} 139
6.3.6. Energy dissipation and the Kolmogorov length scale 142
6.3.7. Summary 144
6.4. An explanation of the trends in droplet size based on energy dissipation 145
6.5. Flow regimes in the rotor-stator mixer: Re analysis 149
6.5.1. Inlet pipe 149
6.5.2. Rotor region 152
6.5.3. Shear Gap 157
6.5.4. Stator 163
6.5.5. Volute 165
6.5.6. Summary 166

CHAPTER 7. CONCLUSIONS 168

CHAPTER 8. FUTURE WORK 171

8.1. Liquid-Liquid Dispersions 171

8.2. POWER MEASUREMENT 172

REFERENCES **174**

APPENDIX 1 EXPERIMENTAL RIG OPERATING PROCEDURES **181**

APPENDIX 2 NAMES AND ADDRESSES OF EQUIPMENT SUPPLIERS **188**

APPENDIX 3 THEORETICAL BACKGROUND TO DIFFRACTION MEASUREMENT **190**

8.2.1. Principles of Laser Diffraction *191*

APPENDIX 4 DROPLET SIZE DISTRIBUTIONS **195**

APPENDIX 5 ..... **208**

LIST OF FIGURES

Figure 2.1 A comparison of different mixers and droplet sizes they can produce (Cohen, 1998) 4

Figure 2.2 In-line mixer used in conjunction with an in-tank device (Courtesy of Silverson Machines Ltd) 7

Figure 2.3 Multi-stage In-line mixer (Courtesy of Silverson Machines Ltd) 8

Figure 2.4 A Silverson type mixer (Right) and a toothed mixer (Left) the stators are at the top and the rotors are below 10

Figure 2.5 A standard single-stage Greerco mixer 11

Figure 2.6 General shape of the energy spectrum (its Fourier Transform), Keey (1967) 21

Figure 2.7 A Silverson type rotor and stator configuration 37

Figure 2.8 Flow pattern through a stator (Sparks 1996) 39

Figure 2.9 Flow pattern in the volute (Sparks, 1996) 41

Figure 2.10 Basic types of globule deformation (Hinze 1955) 42

Figure 2.11 Flow patterns that can cause one of the basic types of globule deformation. 43

Figure 2.12 Break-up of droplets in Couette flow field (Karam & Bellinger, 1968) 45

Figure 2.13 Effect of viscosity ratio on E_B in simple shear flow field (Grace, 1982) 48

Figure 2.14 Effect of viscosity ratio on drop draw ratio necessary for break-up at E_B (Grace, 1982) 50
Figure 2.15 Effect of viscosity ratio on reduced burst time at E_B (Grace, 1982) 50
Figure 2.16 Effect of viscosity ratio on E_B in hyperbolic flow field (Grace, 1982) 52
Figure 2.17 Maximum stable drop deformation in extensional shear field versus viscosity ratio (Grace, 1982). 53
Figure 2.18 Drop deformation for burst at critical shear in extensional shear (Grace, 1982) 54
Figure 2.19 Effect of viscosity ratio on critical burst time for extensional shear (Grace, 1982) 55
Figure 2.20 Shaft power versus flow rate for a range of shaft speeds for a Silverson 64
Figure 2.21 Shaft power versus flow rate for a range of shear gap thickness for a Silverson mixer (Sparks, 1996) 66
Figure 2.22 Overall power balance for a Silverson Unit (Sparks, 1996). 68
Figure 4.1 A flow diagram of the test rig 75
Figure 4.2 Standard Silverson rotor and stators. Clockwise from top left; Rotor; Emulsor screen; General purpose disintegrating head; Slotted Head; Square hole high shear screen. 80
Figure 4.3 Stirred vessel used to create dispersions 84
Figure 4.4 A Schematic diagram of a Malvern Mastersizer 86
Figure 4.5 A schematic diagram of the flow cell and Hydro 2000G arrangement 87
Figure 4.6 Video Probe housing 90
Figure 4.7 Sampling arrangement. Clockwise from top left; (a) The inline rotor-stator with sample point and Video probe in place; (b) Watson Marlow pump used for supplying diluent; (c) Inlet to Mastersizer flow cell and pump and stirrer unit used for flushing the cell; (d) Sample point with sampling arrangement. 95
Figure 4.8 A schematic of the continuous sampling system. 96
Figure 4.9 Flow loop set-up for thermometric power measurement 99
Figure 6.1 Droplets collecting at the top of the sample under a microscope (5% dispersed phase concentration, undiluted) 106

Figure 6.2 Image at 3000 rpm and $\Phi = 5\%$ 110
Figure 6.3 A comparison of DSD measured using the Mastersizer and the Video Probe for a rotor speed of 3000 rpm and $\Phi = 5\%$ at 0.8l/s..... 111
Figure 6.4 Correlation between d_{32} and d_{max}. 114
Figure 6.5 d_{32} versus N (RPM) for the ES and SHHSS (69.85 mm rotor) for varying Φ 117
Figure 6.6 d_{32} versus N (RPM) for four different screens (50.8 mm rotor), 0.4 l/s and $\Phi = 10\%$..... 117
Figure 6.7 d_{32} versus N for 0.4 l/s and 0.8 l/s (at $\Phi = 10\%$ & 20%)..... 120
Figure 6.8 d_{32} versus rotor speed for the SHHSS and the ES at different Φ and Q.... 122
Figure 6.9 d_{32}/D versus $(WeRe^4)^{-1/7}$ for different Φ..... 125
Figure 6.10 Measured d_{32} versus calculated d_{32} 126
Figure 6.11 Power input across the control valve versus flowrate..... 130
Figure 6.12 Shaft power (W) versus rotational speed (RPM) for the Emulsor Screen. 131
Figure 6.13 Shaft power (W) versus rotational speed (RPM) for the Square Hole High Shear Screen..... 131
Figure 6.14 A comparison of values for P_{shaft} from the ES and the SHHSS at 0.4l/s and 0.8l/s..... 132
Figure 6.15 Measured P_{SHAFT} data versus correlation..... 134
Figure 6.16 Pumping Power versus Flowrate for a range of shaft speed, 69.85 mm rotor and Emulsor screen. 135
Figure 6.17 A comparison of pumping power values from both the ES and the SHHSS at different flowrates (for increasing N). 136
Figure 6.18 Mechanical and Disc frictional losses versus rotational speed. 138
Figure 6.19 P_{FLUID} versus N and the dependency of P_{FLUID} on N. 141
Figure 6.20 $P_{FLUID}/\rho D^5$ versus N^3. 141
Figure 6.21 The Kolmogorov length scale versus impeller speed 144
Figure 6.22 A comparison of d_{32} and λ_k versus N (at 0.4l/s for ES)..... 146
Figure 6.23 Volume DSD generated by the 67.85mm rotor with the Emulsor Screen at Q = 0.4 l/s and $\Phi = 10\%$, for varying N (rpm). 154

Figure 6.24 Comparison between E/Screen and SHHSS: 8000rpm & 0.4l/s (69.85mm rotor)..... 161
Figure 6.25 Schematic showing the "Lip" at the top of the Silverson rotor..... 162

Figure A. 1 Flow diagram of the rotor-stator liquid-liquid contactor rig 182
Figure A.2 A comparison of particle size distributions (Volume and Number) generated by the Mastersizer and the Video Probe for Latex beads 98 μm. 195
Figure A.3 Comparison of particle size distributions (Volume & Number) generated by the Mastersizer and the Video Probe for Latex beads 113 μm. 196
Figure A.4 Volume DSD generated by the 67.85mm rotor with the Emulsor Screen at Q = 0.4 l/s and Φ = 10%, for varying N (rpm). 197
Figure A.5 Volume DSD generated by the 69.85mm rotor with the Emulsor Screen at Q = 0.4 l/s and Φ = 20%, for varying N (rpm). 197
Figure A.6 Volume DSD generated by the 69.85mm rotor with the Emulsor screen at Q = 0.4 l/s and Φ = 30%, for varying N (rpm). 198
Figure A.7 Volume DSD generated by the 69.85mm rotor with the Emulsor Screen at Q = 0.4 l/s and Φ = 40%, for varying N (rpm). 198
Figure A.8 Volume DSD generated by the 69.85mm rotor with the Emulsor Screen at Q = 0.8 l/s and Φ = 5%, for varying N (rpm). 199
Figure A.9 Volume DSD generated by the 69.85mm rotor with the Emulsor Screen at Q = 0.8 l/s and Φ = 10%, for varying N (rpm). 199
Figure A.10 Volume DSD generated by the 69.85mm rotor with the Emulsor Screen at Q = 0.8 l/s and Φ = 20%, for varying N (rpm). 200
Figure A.11 Volume DSD generated by the 69.85mm rotor with the Emulsor Screen at Q = 0.8 l/s and Φ = 30%, for varying N (rpm). 200
Figure A.12 Volume DSD generated by the 69.85mm rotor with the SQHHS Screen at Q = 0.4 l/s and Φ = 10%, for varying N (rpm)..... 201
Figure A.13 Volume DSD generated by the 69.85mm rotor with the SQHHS

Screen at Q = 0.4 l/s and Φ = 20%, for varying N (rpm). 201
Figure A.14 Volume DSD generated by the 69.85mm rotor with the SQHHS
Screen at Q = 0.4 l/s and Φ = 30%, for varying N (rpm). 202
Figure A.15 Volume DSD generated by the 69.85mm rotor with the SQHHS
Screen at Q = 0.8 l/s and Φ = 05%, for varying N (rpm). 202
Figure A.16 Volume DSD generated by the 69.85mm rotor with the SQHHS
Screen at Q = 0.8 l/s and Φ = 10%, for varying N (rpm). 203
Figure A.17 Volume DSD generated by the 69.85mm rotor with the SQHHS
Screen at Q = 0.8 l/s and Φ = 20%, for varying N (rpm). 203
Figure A.18 Volume DSD generated by the 50.80mm rotor with the Emulsor
Screen at Q = 0.4 l/s and Φ = 10%, for varying N (rpm). 204
Figure A.19 Volume DSD generated by the 50.80mm rotor with the Emulsor
Screen at Q = 0.4 l/s and N = 7000 rpm for varying Φ (%). 204
Figure A.20 Volume DSD generated by the 50.80mm rotor with the Emulsor
Screen at Q = 1.4 l/s and Φ = 10%, for varying N (rpm). 205
Figure A.21 Volume DSD generated by the 50.80mm rotor with the Slotted
Head at Q = 0.4 l/s and Φ = 10%, for varying N (rpm). 205
Figure A.22 Volume DSD generated by the 50.80mm rotor with the SHHS
Screen at Q = 0.4 l/s and Φ = 10%, for varying N (rpm) 206
Figure A.23 Volume DSD generated by the 50.80mm rotor with the SHHS
Screen at Q = 0.4 l/s and N = 7000 rpm for varying Φ (%). 206
Figure A.24 Volume DSD generated by the 50.80mm rotor with the GDH at
Q = 0.4 l/s and Φ = 10%, for varying N (rpm)..... 207
Figure A.25 Volume DSD generated by the 50.80mm rotor with the GDH at
Q = 0.4 l/s and N = 7000 rpm for varying Φ (%)..... 207

LIST OF TABLES

Table 2.1 Typical Liquid-Liquid Applications that have benefited by using Rotor-Stator Mixers (Silverson Machines, 1999) 12

Table 2.2 A summary of theoretical correlations to predict droplet size 33

Table 2.3 Flow patterns that cause each deformation mode..... 44

Table 4.1 Dimensions of the rotors and stators investigated..... 81

Table 4.2 Physical properties of Alcosol D70 and water 82

Table 6.1 Latex beads tested using the Mastersizer and the video probe..... 107

Table 6.2 The best fit exponents on N for varying Φ 123

Table 6.3 Gradients of the lines in Figures 6.11 125

Table 6.4 The best fit exponents on ε for varying Φ 147

Table 6.5 d_{max} with corresponding Re and γ' and G_B values in the Rotor Region (69.85mm rotor, ES, 0.4l/s and ϕ=10%) with λ_k..... 155

Table 6.6 Re_δ for the ES and SHHSS (69.85 mm) 158

Table 6.7 Critical shear rates, G_B, and burst times, t_B, for drop diameters equivalent to d_{max} and d_{32} and the corresponding nominal shear rates (γ') from both the ES and SHHSS (at 0.4l/s and ϕ=10%)..... 159

Table 6.8 Re_{stator} in the stator holes and corresponding τ and γ' 163

Table 6.9 Re_{volute} and corresponding values for τ and γ' 165

Table A.1 A summary of estimated absorption values as recommended by Malvern Instruments Ltd. 194

Table A.2 Calculated G_B and t_B for measured d_{max} and d_{32} from ES and SHHSS 208

LIST OF PLATES

Plate 0.1 Photograph of test rig (Front View)..... 76

Plate 0.2 Photograph of test rig (side view)..... 77

Nomenclature

Symbol	Meaning	Units
α	Constant	-
β	Kolmogorov constant	-
δ	Shear gap	m
ε	Mass specific local energy dissipation rate	W/kg
ε_{max}	Maximum local energy dissipation	W/kg
ε_{avg}	Mean energy dissipation rate	W/kg
Φ	Dispersed phase volume concentration	-
γ'	Shear rate	s^{-1}
Λ	Shaft torque	(Nm)
λ	Wavelength light	m
λ_k	Kolmogorov length scale	μm
μ_c	Dynamic viscosity of the continuous phase	Ns/m^2
μ_d	Dynamic viscosity of the dispersed phase	Ns/m^2
ρ_c	The density of the continuous phase	kg/m^3
σ	Interfacial tension	N/m
τ_c	The disruptive stress due to turbulent pressure fluctuations	N/m^2
τ_k	Kolmogorov time scale	s
τ_s	Resistive force per unit area due to interfacial tension	N/m^2
τ_v	Resistive force per unit area due to viscosity	N/m^2
ν	Kinematic viscosity	m^2/s
A_1	Constant	-
a	Distance from scatterer to detector	m
a_s	Interfacial area	m^2
B_1	Energy concentration factor	-
B_2	Constant	-

C	Constant	-
C_p	Specific heat capacity	J/kgK
d	Droplet diameter	μm
d_{max}	Maximum stable drop diameter	μm
d_{32}	Sauter mean diameter	μm
d_{43}	Volume mean diameter	μm
D	Rotor diameter	m
D_{RADIAL}	Radial length of a region in the mixer	m
D	Drop deformation = $\frac{L-B}{L+B}$	
E_B	The reduced shear required for break-up	
E	Energy	J
E(k)	Energy spectrum function	m/s^3
E(k)	Energy spectrum function	m/s^3
$I(\Theta)$	Intensity of the scattered light (as a function of angle, Θ)	
I_0	Intensity of the incident light	
J_1	Bessel function	
.k	Wavenumber	m^{-1}
k_p	*I*maginary (absorption) part of the of the refractive index	
N	Rotational speed	RPM
N_p	*C*omplex refractive index of the particle	
n_p	Real part of the refractive index	
$\dot{m}$	Mass flowrate	kg/s
P	Power	W
P_{FLUID}	Power supplied to the fluid by the rotor	W
P_{LEAK}	Leakage losses	W
P_{MECH}	Mechanical losses	W
P_0	Power number	-
P_{SHAFT}	Power supplied by the motor shaft	W
P_{PUMP}	Pumping power	W

$P_{HYDRAULIC}$	Hydraulic losses	W
Δp	Differential pressure	N/m^2
Q	Flowrate	l/s
Re	Reynolds number $\left(\frac{\rho_c N D^2}{\mu_c}\right)$	-
ΔT	Differential temperature	K
ΔT_s	Temperature rise over a single pass	K
t	Time	s
t_b	Reduced burst time	s
u_k	Kolmogorov velocity scale	m/s
$\overline{U^2(d)}$	Mean square velocity difference across the surface of the drop with diameter d.	m^2/s^2
U'	Mean velocity	m/s
V	Volume	m^3
v_{tip}	Rotor tip speed	m/s
v_{RADIAL}	Nominal radial velocity	m/s
We	Weber Number $\left(\frac{\rho_c N^2 D^3}{\sigma}\right)$	-
We_{crit}	Critical Weber Number	-
x	Particle diameter	m

CHAPTER 1. INTRODUCTION

The generation of dispersions has traditionally been performed in stirred tanks. However, other devices are rapidly becoming more popular and are proving to be more efficient. One such alternative is the Rotor-Stator mixer, which consists of a high-speed rotor spinning close to a motionless stator. Any liquid (or solid-liquid) mixture passing through it is subjected to high shear forces, chopping and turbulence. The Rotor-Stator Mixer, due to its versatility, high-energy dissipation rates and cost efficiency is increasing in popularity and as a result there is a wide range of different designs available on the market.

The main aim of this work was to quantify the behaviour of an industrial sized in-line rotor-stator mixer with regards to its liquid-liquid performance. Radial flow devices, such as those manufactured by Silverson Machines Ltd, were the main emphasis of this research.

The generation of liquid-liquid dispersions and the various parameters affecting the droplet size distributions were investigated. A number of different stator designs were tested for a number of different operating conditions, (varying rotor speed, dispersed phase concentration and flowrate).

Particular emphasis was put on the droplet size distribution generated under different operating conditions. This then led to the application of various mechanistic correlations to determine the dominant break-up mechanisms in the mixer.

In order to achieve the main goals a liquid-liquid contactor rig was constructed incorporating hygienic fittings to maintain cleanliness. The droplet size distribution is an important parameter in characterising liquid-liquid dispersions. The small droplet sizes expected from the rotor-stator mixer led to the use of a laser diffraction unit (Malvern Mastersizer) to measure drop sizes.

The mechanistic correlations show a dependency on droplet size with energy dissipation rate and therefore the measurement of power supplied to the fluid was also performed.

Following on from this introduction an assessment of the current level of knowledge on rotor-stator mixers, with particular emphasis on liquid-liquid theories, is given (Chapter 2). The findings of the literature determine the main goals of this research and are presented in Chapter 3.

Chapter 4 then details the experimental approach adopted to achieve the main aims. A detailed description of the liquid-liquid contactor rig is given and the materials used in the experiments. A description of the experimental methodology is provided including the validation of the drop size measurement technique and the sampling strategy used. The technique used for power measurement is also described.

Chapter 5 then reviews the experiments performed and details the location of the corresponding results. A discussion of these results is given in Chapter 6, followed by conclusions and recommendations for future work

CHAPTER 2. LITERATURE REVIEW

The mixing of two immiscible liquids is an important unit operation in the chemical and process industry. The most common immiscible liquid dispersions contain an organic and an aqueous phase and are traditionally manufactured using stirred vessels.

However, increased competitiveness in the process industry has made mixer selection more rigorous and analytical and consequently alternative devices, such as Rotor–Stator mixers are rapidly growing in popularity. The rotor-stator's versatile nature, high shear and energy dissipation rates makes it ideal for processes requiring fast disintegration, homogenisation, dissolving, emulsification and dispersions.

Despite their popularity, there is very little literature openly available on their design. Operators are very much dependent on their own experience and that of the manufacturers, both of which may result in discrepancies in performance. The lack of detailed design information has led to the requirement of laboratory testing and pilot plant trials.

Laboratory testing is predominantly concerned with the measurement of the mean droplet size and the size distribution. Droplet size distribution is an important parameter in characterising liquid-liquid dispersions as rate dependent processes are greatly influenced by interfacial area. To be able to establish effective design guides, an understanding of the mechanisms involved in the process of drop break-up is required.

2.1. Rotor-stator mixer background

2.1.1. Mixer Comparison

Selecting the correct type and size of mixer has traditionally been based on the experience of operators and mixer manufacturers. Consequently, different mixer types are used based on their performance on specific applications.

Generally, mixer manufacturers tend to consider rotor-stators to be best suited for blending dissimilar viscosity liquids, dissolving low viscosity liquids and also high-contact reactions as well as liquid-liquid emulsions (Dietsche, 1998). The main performance and selection criterion of these mixers with regards to liquid-liquid dispersions is the droplet size distributions generated by them.

Cohen (1998) showed a comparison of different in-line mixers based on their droplet generating properties (Figure 2.1). Unfortunately the author does not define tank turnover and it is not known whether the comparisons are based on the similar size mixer, similar volumes and for what liquid systems. However, it is reasonable to assume that the mixture was re-circulated through each mixing device until an equilibrium droplet size had been achieved and that the mixers used were ones that the different manufacturers would recommend for the same duty.

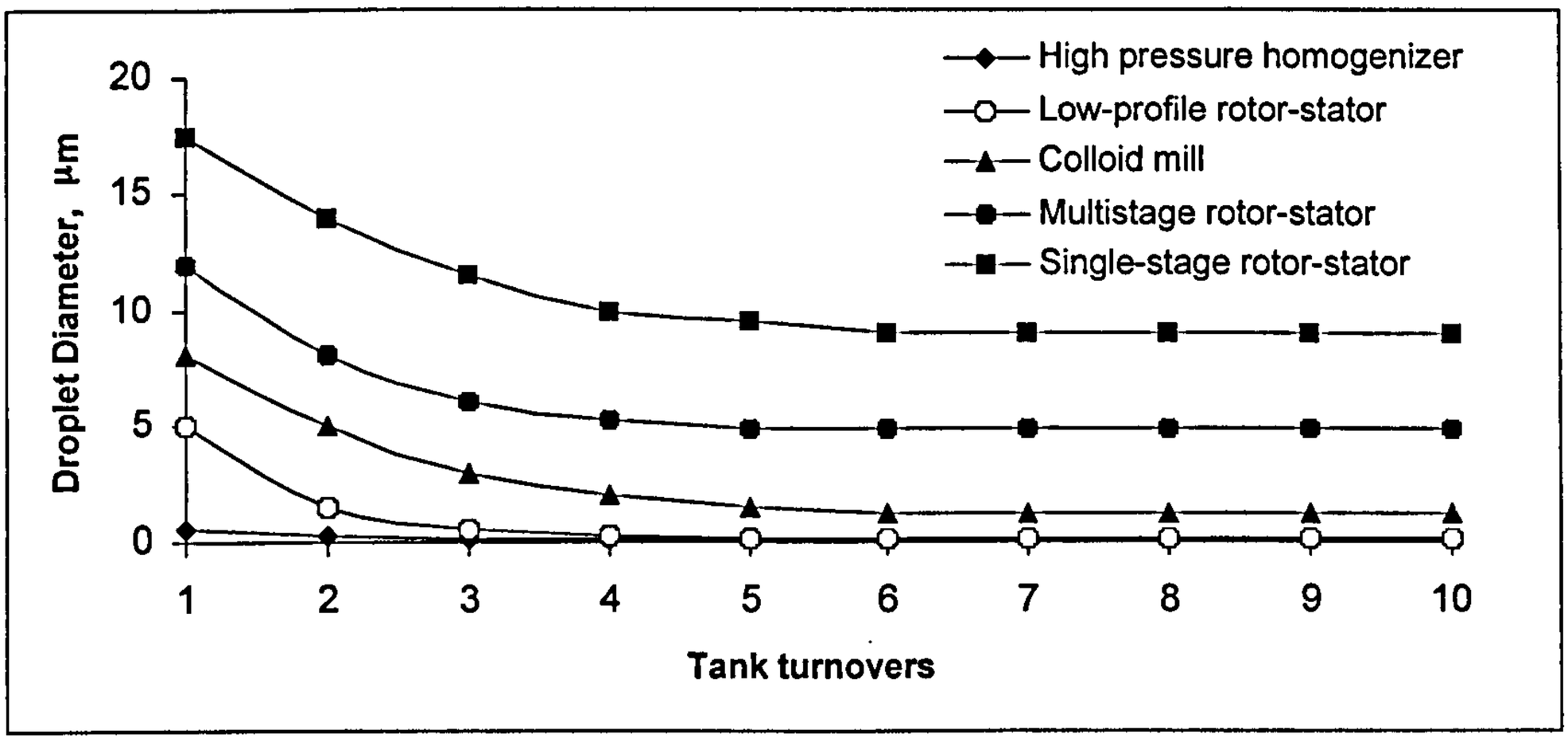

Figure 2.1 A comparison of different mixers and droplet sizes they can produce (Cohen, 1998)

It can be seen from Figure 2.1 that there are various mixers available for the production of liquid-liquid dispersions. However, for applications that require fine droplet size distributions the High-Pressure Homogeniser tends to be the preferred option. This mixer consists of a high-pressure pump that forces a fluid (two immiscible liquids) at very high velocities through a narrow orifice.

The Colloid mill, a rotor-stator device which consists of a conical rotor and stator, is also an effective device for producing small droplets. The surfaces of the rotor and the stator can be either smooth or toothed and can consist of one or more pairs of concentrically arranged discs of various designs. The fluid is retained in the mixing head for longer periods than a traditional rotor-stator mixer, hence more energy is dissipated to the fluid.

It is worth noting that Cohen (1998) claims that the low-profile rotor-stator also generates droplet sizes close to those from the High Pressure Homogeniser. This mixer is essentially a multi-stage rotor-stator device (a number of concentrically arranged fine toothed discs) which runs at high speeds. Although this claim is unsubstantiated, it gives a good idea of the capabilities of a rotor-stator mixer by making changes to the operating speeds and geometry.

The trends exhibited in Figure 2.1 agree with the findings of Schubert (1997) who investigated the relationship between power per unit volume of various mixers and their resultant droplet sizes and also the observations of Dietsche (1998). They both characterised the High-Pressure Homogeniser and Colloid Mill with high shear-rates and higher power per unit volume than other designs. It was claimed that this was the reason for their finer droplet size distributions.

This makes High-Pressure Homogenisers and Colloid Mills suited to applications that involve fine emulsions (the pressure homogeniser can generate sub-micron emulsions and is often used in the homogenisation of milk), fine particle break up and in the case of the Colloid Mills, viscous emulsions.

However, the High-Pressure Homogeniser is limited to use with low viscosity liquids, typically below 0.5 Pa.s (Dietsche, 1998). Also the energy consumption and equipment size limit these units to low flow capacities. The Colloid Mill almost always requires pump assistance and also has a low capacity range. Both these units are difficult to clean in place.

In-line rotor-stator mixers incorporate relatively high power per unit volume and do not suffer the same disadvantages of the High-Pressure Homogeniser and the colloid mills. Furthermore, Figure 2.1 and the investigations of Schubert (1997) reveal that the droplet size distributions generated by these mixers can be close to those of the High-Pressure Homogeniser and the Colloid Mill depending on the physical properties of the fluids being mixed. An added advantage of rotor-stator devices is that their performance can be improved greatly by changing the design of the rotor and the stator.

Further advantages of the in-line rotor-stator mixer are discussed in Section 2.13.

2.1.2. Rotor-Stator mixer designs

Rotor-stator mixers consist of a high-speed rotor that spins very close to a motionless stator and any fluid mixture passing through it is subjected to high shear forces, chopping and turbulence. The clearance between the rotor tip and the stator wall is typically below 1 mm and is commonly referred to as the shear gap. Rotor-stator mixers can be used in a number of different configurations, as batch (in-tank) or as continuous in-line devices. Cohen (1998) discussed the three most common configurations in detail.

(a) Batch single stage.
(b) Single-stage in-line systems.
(c) Multi-stage in-line systems.

The batch single stage units refer to in-tank devices. The single stage in-line systems can be incorporated into a pipeline, as a once through mixer or, as is often the case, in conjunction with an agitator in a vessel (Figure 2.2).

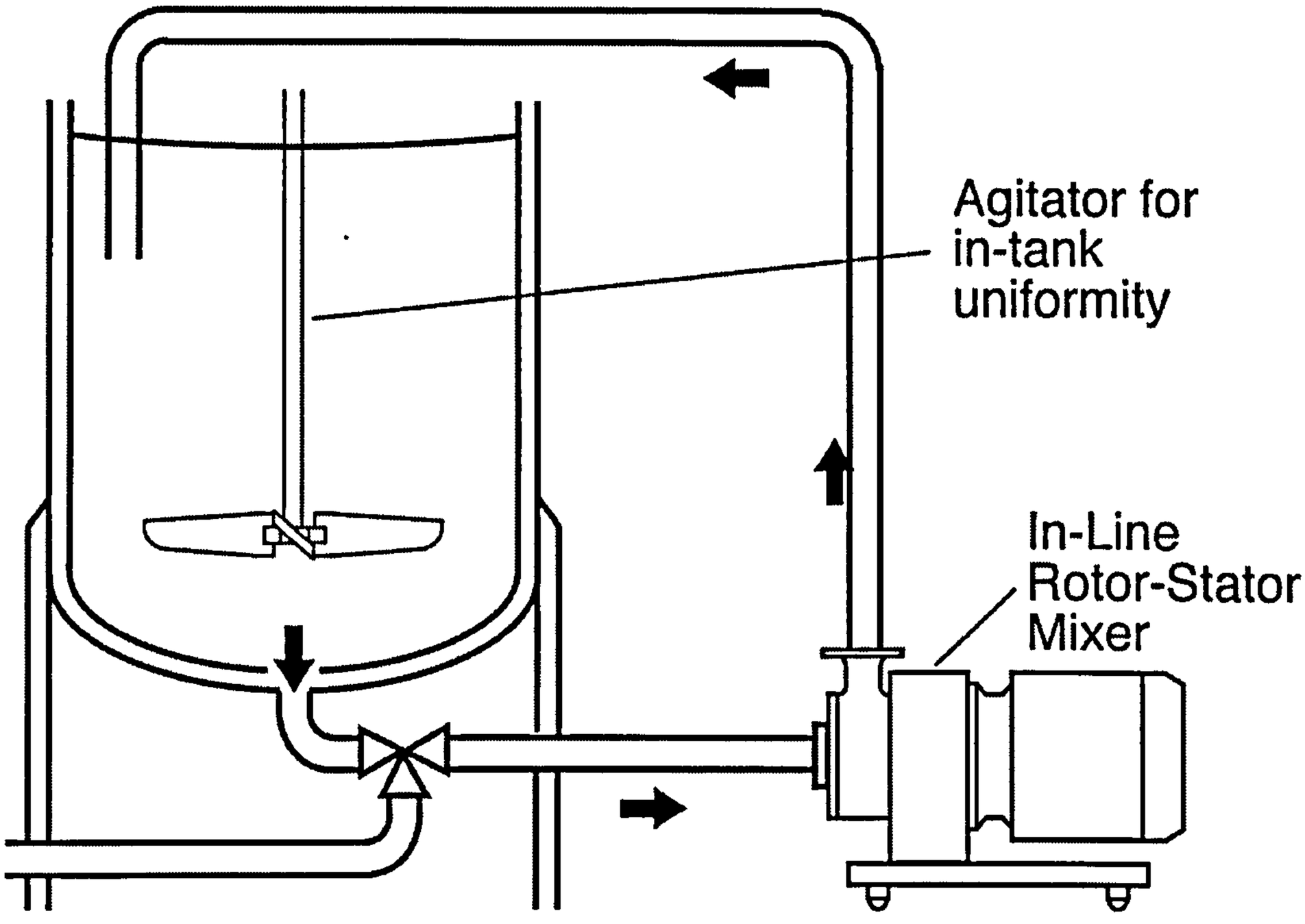

Figure 2.2 In-line mixer used in conjunction with an in-tank device (Courtesy of Silverson Machines Ltd)

The objective of a multi-stage unit is to generate greater total energy input by increasing the number of shearing events that each particle or droplet experiences, with each pass through the mixer. Some designs involve several single-stage units lined up in series, other designs have the same effect but as a single stage (Figure 2.3).

These single stage units are made up of multiple rotor-stator pairs arranged concentrically. The theory behind these units is that, as the mixture moves outwards from the centre, it undergoes a quick succession of shearing events, which generates a shorter processing time and a smaller droplet size. However, due to the lack of correlations relating droplet size to mixer type and size there is no definitive way of

knowing whether an equilibrium droplet size has been attained. Thus, regular testing of the product is required.

It is clear that the in-line rotor-stator mixer is the more versatile of the two main configurations, (the multi-stage can be considered to be an adaptation on the single-stage unit). The in-line mixer popularity can also be attributed to its ability to be incorporated within a recirculating loop ensuring a greater percentage of the fluid (in some cases 100%) is exposed to areas of high-energy dissipation. The fact that numerous passes are required in many applications (Figure 2.1.) leads to the assumption that during a single-pass all of the fluid may not be subjected to areas of high energy dissipation.

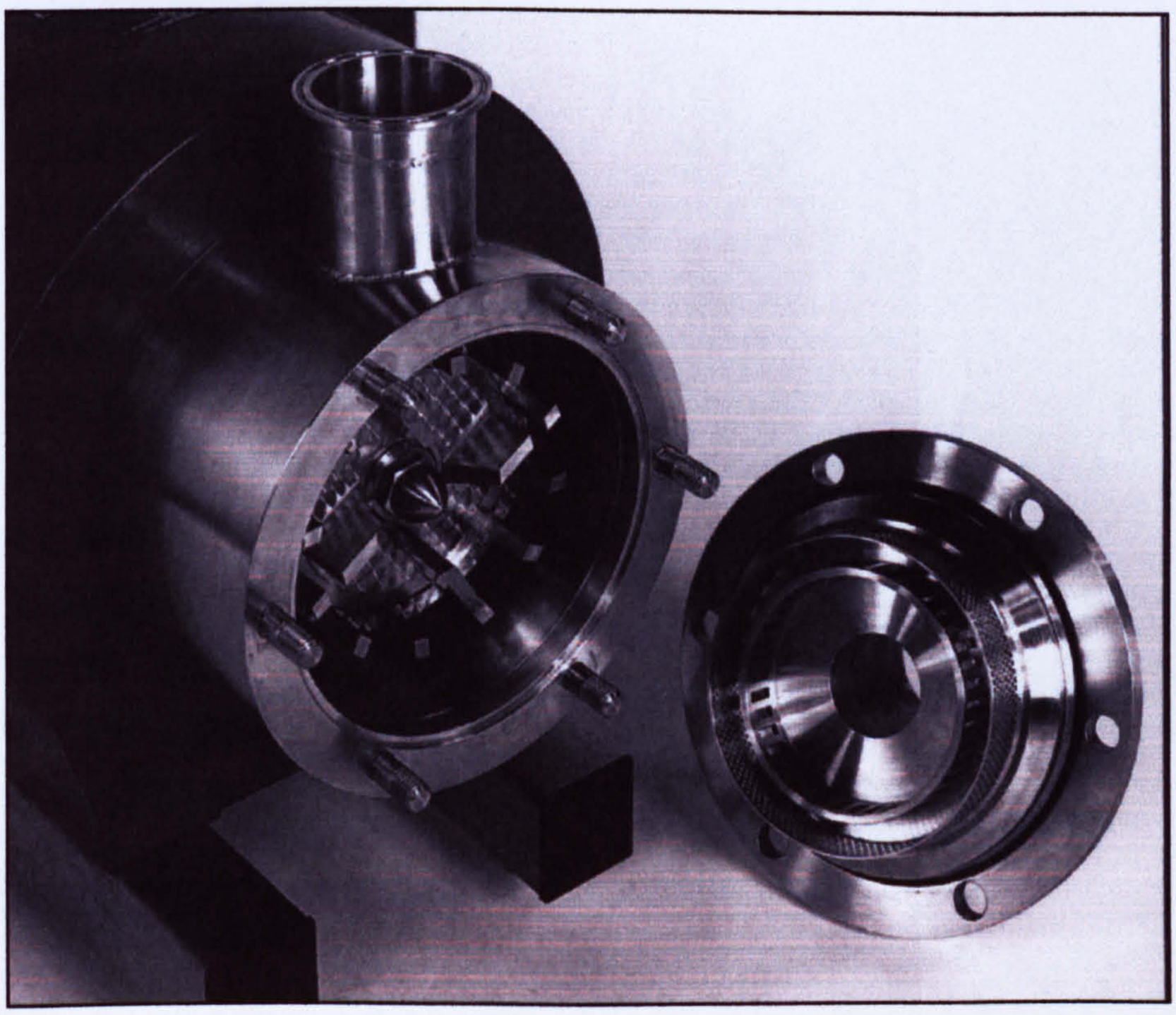

Figure 2.3 Multi-stage In-line mixer (Courtesy of Silverson Machines Ltd)

The focus of this research, therefore, was specific to single stage in-line rotor-stator devices. Sparks (1996) defined an in-line rotor-stator mixer as one that can be incorporated into a process pipeline, similar to a centrifugal pump, often contributing a pumping effect.

2.1.3. In-line rotor-stator mixers

The main advantages of an in-line rotor-stator mixer are:

- A small low-powered unit can handle a batch of any size by recirculating material until the process is completed.
- They are ideal for process lines that require frequent changeover.
- Solids and liquids can be injected directly into the mixing head, which is the area of highest shear.
- They also offer more accurate control, easy and reliable sampling of mixed product and better controlled recirculation, than batch systems (Cohen, 1998).

The in-line rotor-stator can pump liquids with viscosities up to 5 Pa.s, but with pump assistance, can handle greater than 100 Pa.s (Dietsche, 1998). Cohen (1998) reported viscosities from 10 Pa.s up to 1000 Pa.s with a supplemental pump, emphasising the variance in performance of different designs.

They can also cope with a wide range of flow capacities from as low as 4 litres/min to more than 4000 litres/min. The amount of shear, milling, and particle disintegration is determined by the high speed of the rotor, which also supplies flow. The stator design varies with manufacturer and has an influence on the effectiveness of the mixer.

2.1.4. In-line rotor-stator mixer designs available on the market

In-line rotor-stator mixers are supplied with various designs of rotor and stator. In general these designs can be grouped into three categories:

(a) Mixers that are supplied with swept blade rotors combined with stators (basically cylinders with perforations). These mixers are the most common design available and will be referred to in this report as a Silverson design (Figure 2.4.).

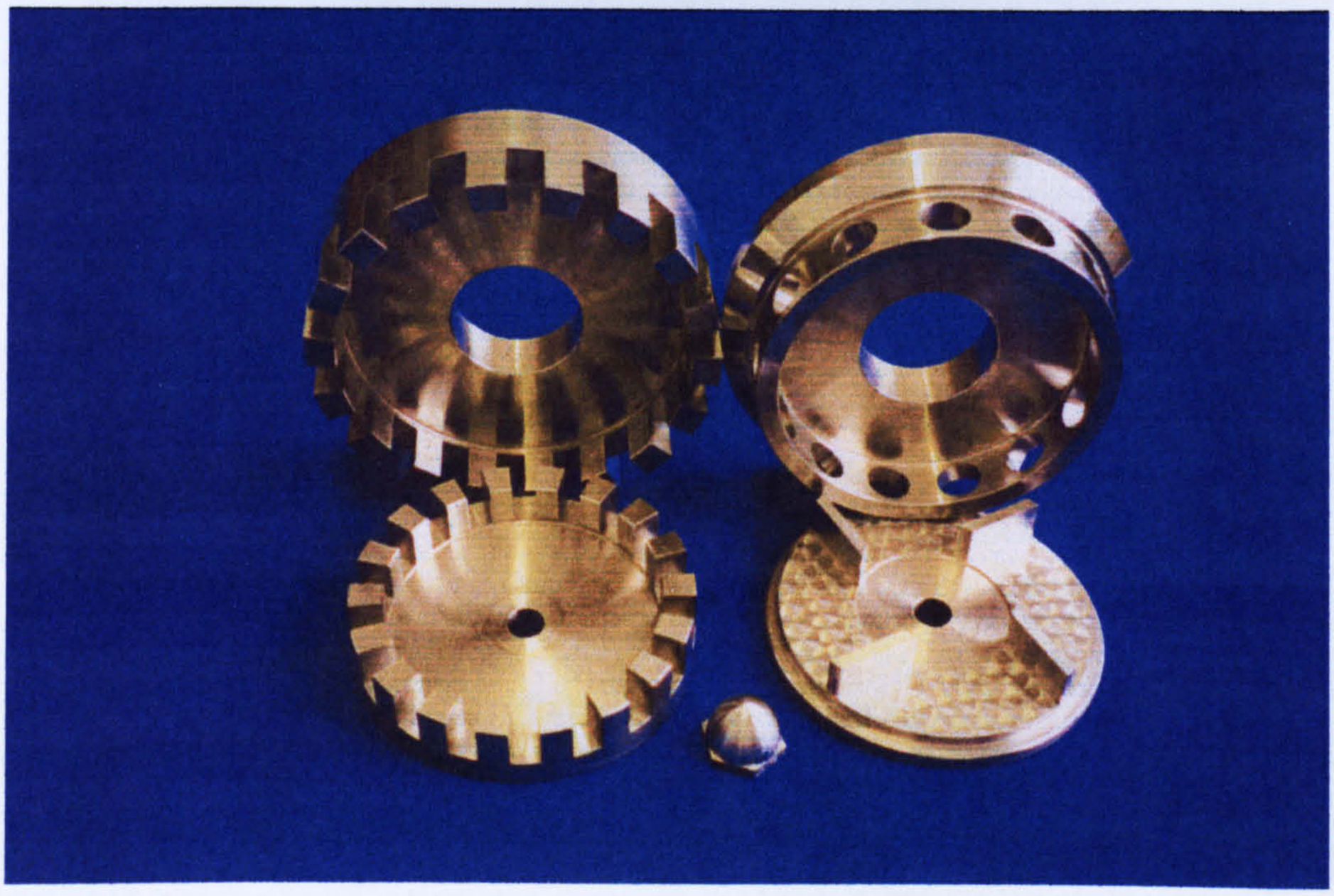

Figure 2.4 A Silverson type mixer (Right) and a toothed mixer (Left) the stators are at the top and the rotors are below

(b) A toothed design is one in which the rotor and stator are discs with a number of approximately trapezoidal teeth around their circumference (Figure 2.4.). These units are typical of ones produced by German and Swiss manufacturers.

(c) The third design is an axial flow device, an example of which is the Greerco pipeline mixer (Figure 2.5).

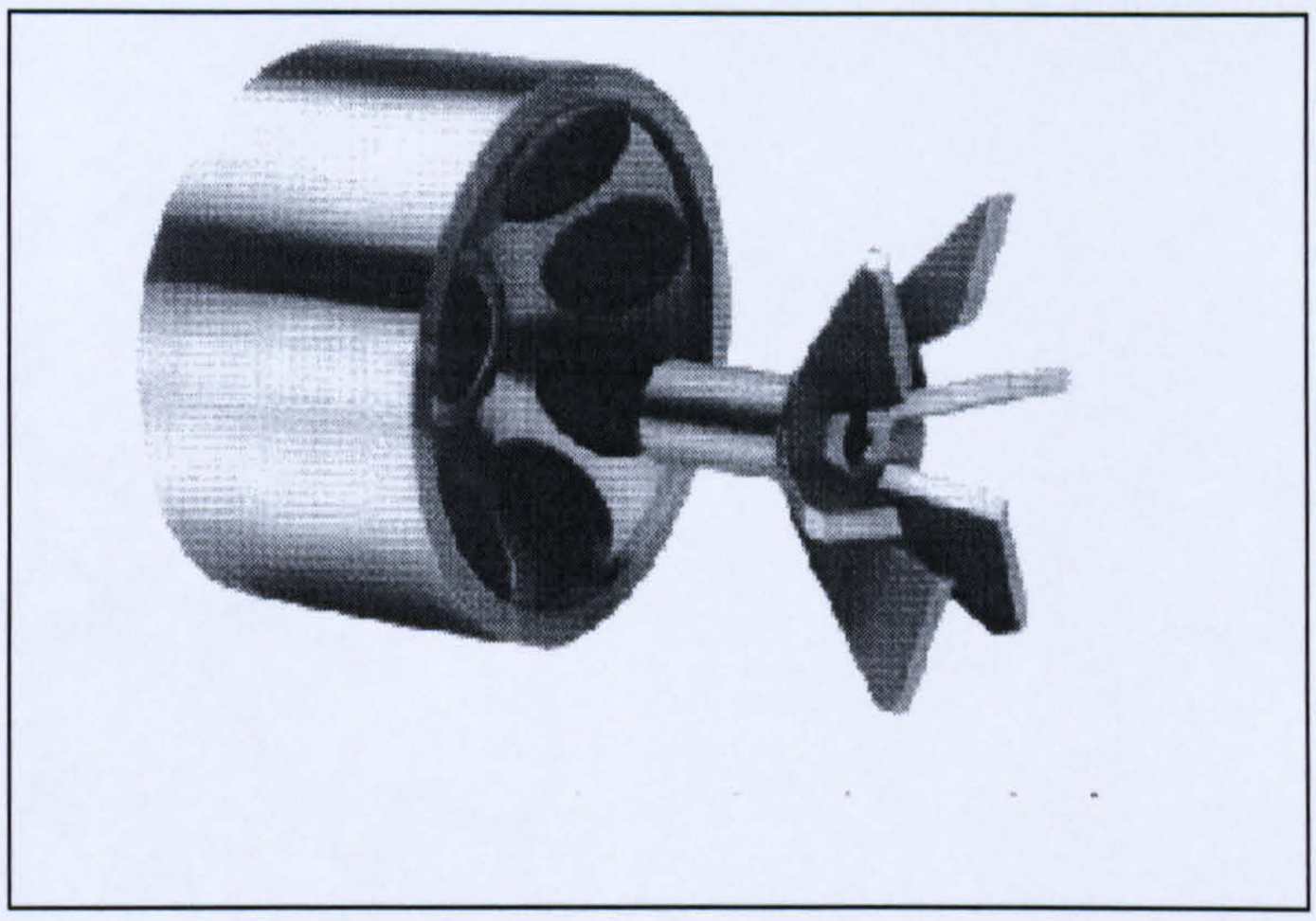

Figure 2.5 A standard single-stage Greerco mixer

2.1.5. Operation of an in-line rotor-stator mixer

The operation of a Silverson mixer is described below. The fundamentals are true for all in-line rotor-stator mixers. The basic operation of a rotor-stator mixer can be divided into three main stages:

i. Suction
ii. Milling
iii. Intense hydraulic shear

The high-speed rotation of the rotor blades creates suction, which draws the material to be mixed into the mixing head. The material is then forced, by the centrifugal force, towards the edge of the mixing head and into the gap between the tips of the rotor blade and the stator wall, (the shear gap). The flow of material approaching the stator is tangential. The mixture is then exposed to intense hydraulic shear as it is forced, at high velocity, through the perforations in the stator. The flow of material out of the stator is radial.

2.1.6. Industrial applications

Examples of rotor-stator applications can be found in the food, chemical, pharmaceutical and cosmetics industries. As this project is predominantly concerned with liquid-liquid systems, the majority of the following examples concentrate in this area.

Food, Cosmetics and Toiletries Industries:

Table 2-2 gives a brief review of liquid-liquid applications that can be found in each of these sectors.

Table 2.1 Typical Liquid-Liquid Applications that have benefited by using Rotor-Stator Mixers (Silverson Machines, 1999)

Industry	Application (Liquid-Liquid)	Manufacturing Problems Solved by Rotor-Stator mixers
Food	• Salad Dressing • Flavour emulsions	• Formation of agglomerates • Unstable emulsions • Long process times
Cosmetics and Toiletries	• Creams and Lotions • Deodorants and Antiperspirants • Sun Tan Lotions	• Formation of agglomerates • Unstable emulsions • Long process times • Homogenous product • Reduced aeration • Increased shear

Other examples that are not liquid-liquid processes include:

Food Industry:

- The preparation of isinglass finings for the brewing industry.
- Dispersion of Pectin (a polysaccharide obtained from fruit) for jams and preserves.

Cosmetics and toiletries industry:

- The dilution of high activity surfactants.

The oil and gas industry

Saadevandi & Zakin (1996) investigated the use of rotor-stator mixers in the petroleum industry. In particular they were concerned with the mixing of heavy crude oil with an aqueous surfactant solution to form an oil/water emulsion. This enabled the easy transportation of the otherwise heavy crude, resulting in reduced pumping costs.

Chemical & pharmaceutical

The following are not examples of liquid-liquid processes, but list other chemical and pharmaceutical processes that have benefited from using rotor-stator mixers.

Nikiforov, et al (1990) reported the use of rotor-stator mixers in the production of aqueous polyacrylamide (PAA) solutions. PAA is used to enhance the strength of paper. The mixer was a modified centrifugal pump. This was done to investigate an alternative method to a conventional stirred tank for producing a PAA solution. It was found that the stirred vessel had problems attaining the ideal specific energy rate, ε, (= 10 W/kg) and also had difficulties producing a uniform PAA solution due to the formation of stagnant areas. The modified pump not only generated a value of $\varepsilon = 1015$ W/kg but after two passes, formed a uniform solution in less time than the stirred vessel.

Other examples include (Silverson, 1999):

- The production of polymer modified bitumen for road surfacing.
- The re-dispersion of filter cake.
- High-speed dispersion of filter cake.
- High-speed dissolving of viscosity index improvers in luboils
- The production of cough mixtures and pharmaceutical syrups.
- Manufacture of pharmaceutical tablet coatings

2.1.7. Summary

There are a large number of different rotor-stator designs available on the market, each with its own unique geometric variation. They can be classified into three main categories:

i. Radial flow devices (Silverson design)
ii. Toothed type mixers
iii. Axial flow devices

However there is very little academic data available on any of these designs.
The diversity of the in-line rotor-stator mixer is highlighted by the fact that they are used in a broad range of industries that include liquid-liquid mixing applications.

Although the high-pressure homogeniser and the colloid mills are traditionally used to produce fine emulsions, there are disadvantages associated with these large energy consuming units with high capital and operating costs. The work of Schubert (1997) and manufacturers experience (Dietsche, 1998 & Cohen 1998) has shown that the rotor-stator mixer can be made to produce fine emulsions for some applications.

It is thought that the droplet generating properties of these mixers is very much dependant on the physical properties of the fluid, the mixer geometry and rotational speed. The main advantages of the in-line rotor-stator mixer over these other mixers are:

(a) Cheaper to run and maintain.
(b) They can handle higher throughputs (up to 4000 litres/min).
(c) They are suitable for high viscosities (up to 1000 Pa.s).
(d) They are relatively easy to incorporate into existing processes.
(e) It is possible to pass the entire fluid mixture through the regions of high-energy dissipation by increasing the number of passes (stages).

2.2. Liquid-Liquid Theory

Liquid-liquid dispersions are made up of two immiscible liquids one of which is suspended in the other in the form of droplets. The liquid that is present in the form of droplets is called the dispersed phase and the liquid in which these droplets are suspended is the continuous phase. Dispersions can exist in two forms, an oil suspended in water (O/W) or the reverse, water suspended in oil (W/O). The term emulsion generally covers dispersions with small and relatively stable droplets, usually with the addition of a stabilising agent (Becher, 1966).

Most stabilising agents are surfactants which consist of a hydrophilic group (attracted to the aqueous phase) and a lipophilic group (attracted to the organic phase). The lipophilic group is attracted to the oil droplet leaving the hydrophilic group exposed to the aqueous phase. The hydrophilic groups sticking out of the droplet repel similar groups in other drops, thus preventing coalescence. In addition to their stabilising qualities, surfactants also exhibit interfacial effects and in many cases decrease the interfacial tension.

The process of making droplets is a simple one. In a large number of cases, simple shaking proves to be sufficient. However, a large amount of energy is required to break down the drops further.

The suspension of the dispersed phase in the continuous phase is caused by the direct action of shear stresses exerted by the continuous phase on the dispersed phase. There are two sources for these shear stresses, those due to velocity gradients, (i.e. laminar flow conditions) and those due to inertial forces, (i.e. turbulent flow conditions).

In addition to the break-up stresses imparted to a drop there are forces that oppose deformation. Various models have been developed to attempt to describe the scaling of the stresses that deform a drop against those that resist drop break-up. These models form a foundation for correlating experimental data and provide a method for confidently extrapolating experimental conditions for scale-up purposes.

Whilst the process of drop break-up is taking place, at the same time drops are colliding with each other. In turbulent conditions droplets that are smaller than the micro-scale of turbulence are completely contained within the eddies whereas larger drops are acted upon by the turbulent eddies. The collision of drops below the micro-scale of turbulence is caused by two different mechanisms depending on whether the drop has a density similar or different from that of the surrounding fluid. Droplets with similar densities follow the motion of the fluid completely and the droplet velocity fluctuations can be described by the fluid velocity function. Droplets with significantly different densities are not completely entrained by the turbulent eddies and drops with differing diameters move at different velocities resulting in collisions.

If the drops remain together long enough, so that the separating continuous phase film thickness reaches a minimum, then the film ruptures and the drops coalesce. There are many factors that determine whether a collision will result in coalescence including, surfactants, mass transfer, surface tension gradients, physical properties and Van Der Waals forces. For coalescence to occur, contact time must be greater than coalescence time. A review of various models developed to describe the drop coalescence rates is given by Tavlarides and Stamatoudis (1981).

Tackling drop break-up and coalescence together is far too complicated and as a result the role of coalescence can be limited by considering dilute dispersions, or by adding a stabilising agent. Also, in dilute systems the continuous phase can be described using concepts developed for a single-phase fluid (Calabrese 1992).

Although this research uses dispersions with high concentrations, Calabrese (1992) stipulated that theories developed for dilute systems can be applied to more concentrated systems that have been stabilised. This is because the presence of a stabiliser would inhibit coalescence. This statement, can therefore, be extended to incorporate systems that do not readily coalesce. It has been shown both in this work (Chapter 3) and work performed by Brown and Pitt (1971) that the kerosene-water system (used in this work) can be described as such.

Both kerosene and water are liquids of relatively low viscosity (Chapter 3), therefore, the flow in a rotor-stator mixer is expected to be predominantly turbulent. Sparks (1996), assumed that the power supplied by the rotor to the fluid was dissipated in a small region of the rotor-stator surrounding the rotor teeth, stator teeth and the gap between the two. Calculating the Reynolds number (Re) using the gap width as the characteristic length scale and the tip speed as the characteristic velocity (see Section 2.3.1) for rotational speeds from 3000rpm to 12000rpm (with water) gives values of Re ranging from 3.5×10^6 to 7×10^6 (respectively) which would indicate turbulent conditions.

However, it has also been reported that the energy dissipation within the mixer is highly inhomogeneous and there may be regions within the mixer that may not exhibit turbulent characteristics, (Sparks, 1996; Pedrocchi and Widmer, 1988; Kroezen & Wassink, 1987). Furthermore, Pedrocchi and Widmer (1988) found that the gap width had little or no affect on the droplet size distribution. This would suggest that Spark's (1996) assumption may not hold true and other factors may be more important for drop break in a rotor-stator mixer. This is discussed in more detail in Section 2.3.

Most of the work on modelling dispersed phase dynamics such as droplet breakage is based on models developed from isotropic turbulence. The main concepts are outlined in the following sections.

2.2.1. Forces affecting drop stability

Models that have been developed from theories of droplet break-up are based on balancing the disruptive force that acts on the drop with the forces that resist disruption. It is, therefore, important to have an understanding of the forces that affect the stability of a drop.

If the force acting on the surface of a single drop is due to turbulent pressure fluctuations then the disruptive force per unit area, τ_c, is given by Equation (2.1).

$$\tau_c = \rho_c \overline{U^2(d)} \qquad (2.1)$$

Where ρ_c is the density of the continuous phase

$\overline{U^2(d)}$ is the mean square velocity difference across the surface of the drop with diameter d.

If the disruptive force is due to mean velocity gradients rather than turbulent pressure fluctuations, then Newton's law of viscosity will apply (Calabrese, 1992):

$$\tau_c = \mu_c U' \qquad (2.2)$$

Where μ_c is the viscosity of the continuous phase

U' is the characteristic mean velocity gradient in the system.

It should be noted that Equation (2.2) is only applicable when the turbulence intensity is low and the instantaneous velocity gradient averaged over the time-scale of a single breakage event is well approximated by that for mean flow.

The effect of shear is counteracted by the interfacial and viscous forces, which act to maintain the most compact droplet shape. Equation (2.3) is an expression for the resistive force per unit area, τ_s, due to interfacial tension.

$$\tau_s \propto \frac{\sigma}{d} \qquad (2.3)$$

Where, σ is the interfacial tension.

The dispersed phase viscosity, μ_d, provides a resistive force per unit area, τ_v, within the drop and is given by:

$$\tau_v \propto \left(\frac{\mu_d}{d}\right)\left(\frac{\tau_c}{\rho_d}\right)^{1/2} \tag{2.4}$$

Where the term $(\tau_c/\rho_d)^{1/2}$ is the characteristic velocity inside the drop as determined by balancing the kinetic energy on the drop's surface.

Calabrese (1992) reasoned that the interfacial tension provides a restorative force on the drop whilst the dispersed phase viscosity dampens any deviations from a spherical shape.

Equation (2.1) shows that the disruptive force is dependent on the diameter of the droplet and it can be seen from Equations (2.3) and (2.4) that the cohesive forces decrease with increasing diameter. This leads to the realisation that there exists a maximum stable droplet diameter, d_{max}. The cohesive forces on drops with diameter larger than d_{max} are insufficient to prevent droplet break-up. If the drop diameter is below d_{max} then the hydrodynamic forces acting on the drop are insufficient to cause break-up. The maximum stable drop size can then be defined as the drop diameter for which disruptive and cohesive forces are in balance (Equation (2.5)).

$$\tau_c(d_{max}) = \tau_s(d_{max}) + \tau_v(d_{max}) \tag{2.5}$$

It is important to note that breakage is a rate dependent process and the concept of d_{max} and Equation (2.5) only apply when correlating mean drop size at equilibrium conditions.

In addition to equilibrium conditions, it is further assumed that:

1) Both phases exhibit Newtonian fluid behaviour
2) No mass transfer occurs between the two and there is no surfactant present.
3) Dispersion is fully turbulent.
4) Density difference between the two phases is small to avoid buoyancy effects.

2.2.2. Drop break-up in turbulent flow

Theoretical prediction of droplet size distributions has traditionally been based on the assumption of homogenous isotropic turbulence, more commonly referred to as the Kolmogorov theory (Kolmogorov, 1949). Another important assumption of this theory is that the role of coalescence is unimportant.

Turbulent flow can be considered to be made up of the random flow of eddies superimposed on the overall average flow. In fully developed turbulence the velocity at any point within the fluid varies continually about some mean value and the amplitude of the variations about the mean may not be small compared with the magnitude of the mean itself. A similar random variation exists between two points within the fluid. The instantaneous point velocity in space, U, is given by Equation (2.6):

$$U = iU_x + jU_y + kU_z \tag{2.6}$$

Where, U_x, U_y and U_z are the scalar co-ordinates along the unit vectors i, j, k respectively.

It is convenient to break down the instantaneous velocity U, into the sum of the mean value over a time interval, $\overline{U}$, and the superimposed fluctuation u':

$$U = \overline{U} + u' \tag{2.7}$$

The magnitude of u' provides a qualitative indication of the degree of turbulence of the flow. The time average value of this component is zero, as no net motion arises from the eddies. However, the average of the squares of the fluctuations ($\overline{u'^2}$) will not be zero and thus the root mean square (rms), $\sqrt{\overline{u'^2}}$, value is used to calculate an average.

In order to simplify the mathematical treatment of turbulent flow the assumption that the flow is homogenous and isotropic is often made. Homogenous turbulence occurs when the time averaged velocity components are independent of position (this rarely applies in

practice except over short distances). The flow is termed isotropic if the magnitude of the fluctuating velocity component is the same in each of the three principle directions (i.e. $\sqrt{\overline{u_x^2}} = \sqrt{\overline{u_y^2}} = \sqrt{\overline{u_z^2}}$).

Turbulent flow can be described as a spectrum of eddy sizes and each eddy has its own energy associated with it, Figure 2.6. The energy spectral density function E(k) describes the total turbulent kinetic energy contained within a range of eddies. (Where k is the wave number and is the reciprocal of eddy size (1/d), such that E(k) represents the energy contained in eddies of size k to k + dk).

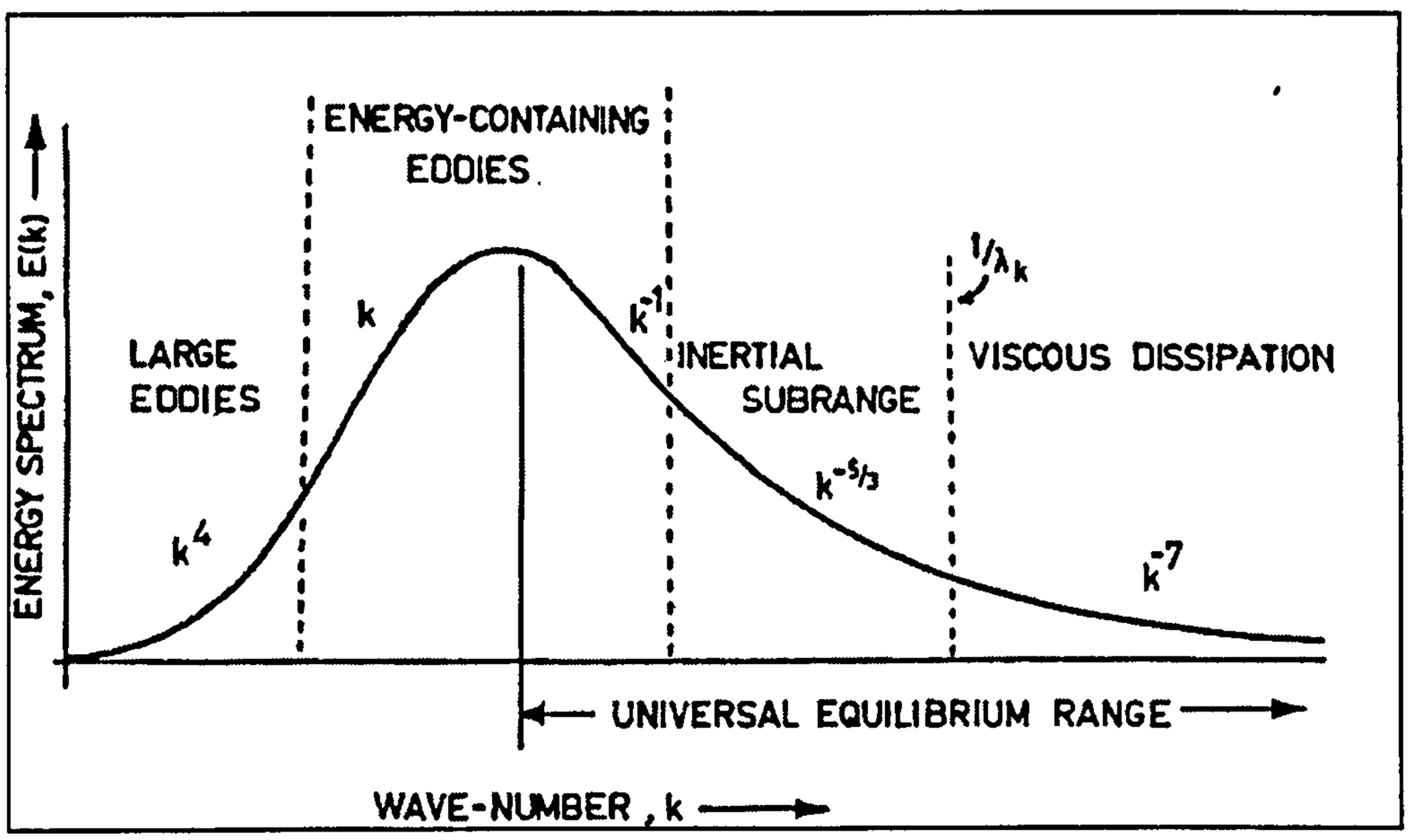

Figure 2.6 General shape of the energy spectrum (its Fourier Transform), Keey (1967)

The larger eddies (which are effected by external forces such as the impeller blade in a stirred vessel) transfer their energy to the smaller ones until the smallest eddies dissipate kinetic energy into heat through viscous shear. The smaller eddies become statistically

independent from the larger ones. For steady state to be maintained there must be an input of energy, provided for example by an impeller.

There is thus a range of frequencies that are not excited by external forces and are instead created by inertial interactions of larger scale motions. This range of eddie sizes, where the energy is self adjusting through inertial forces, is known as the Universal Equilibrium Range, as turbulence is uniquely determined by the energy dissipated per unit mass ε, and the kinematic viscosity, ν. The universal equilibrium range is made up of two sub-ranges: the inertial sub-range where the energy spectrum is independent of ν, and only dependent on ε, and the viscous dissipation range where the energy spectrum is dependent on both (Figure 2.6).

If the assumptions are made that break-up is due to turbulent pressure fluctuations and that the droplet size is small compared to the macro-scale of turbulence, L, Kolmogorov (1949) and then later Hinze (1955) argued that the flow could be characterised in terms of the energy dissipation.

The largest scale of turbulence is the integral length scale of the velocity correlation function (Hinze, 1955) and is generally assumed to be proportional to impeller diameter, D, which for rotor-stators can be assumed to be analogous to the rotor diameter. The size of the smallest eddies is called the Kolmogorov micro scale, λ_k.

$$\lambda_k = \left(\frac{\nu^3}{\varepsilon}\right)^{1/4} \tag{2.8}$$

ν Kinematic viscosity (m^2/s)

ε Mass specific local energy dissipation rate (W/kg)

The characteristic velocity and time scales in this range can be defined respectively by:

$$u_k = (\nu\varepsilon)^{1/4} \quad \text{and} \quad \tau_k = \left(\frac{\nu}{\varepsilon}\right)^{1/2} \tag{2.9}$$

The region between eddy sizes of D and λ_k is the inertial sub-range where the assumption of homogeneous isotropic turbulence can be applied (Kolmogorov, 1949). For stirred vessels it is postulated that drop sizes, as a result of turbulent pressure fluctuations, are much larger than λ_k. Therefore, it can be said that eddies in the inertial sub-range are predominantly responsible for drop break-up. It is worth mentioning that many workers have reported droplet sizes from a rotor-stator mixer an order of magnitude smaller than in a stirred vessel. Values for λ_k in a rotor-stator mixer will help to determine which energy region is predominant for drop break-up in rotor-stator mixers.

In industrial applications it is difficult to determine local energy dissipation rates and hence average energy dissipation rate, ε_{av}, is taken over the whole volume of a vessel. The local energy dissipation rates vary considerably throughout an in-line rotor-stator mixer and the majority of researchers have estimated values for the highest local energy dissipation rates, (Sparks, 1996; Pedrocchi and Widmer, 1988; Kroezen & Wassink, 1987).

(a) Drop break-up in the inertial sub-range

Kolmogorov (1949) and later Hinze (1955) developed a model of drop-break in the inertial sub-range. The model assumes that the disruptive stress on a drop is due to turbulent eddies in the inertial sub-range and viscous forces of the dispersed phase are considered to be negligible.

If the Reynolds number is high, the motion of the fluid in a very small volume are determined solely by the energy dissipation rate, ε (i.e. local isotropy). This assumption

holds true if the macro-scale of turbulence (the length scale of the energy containing eddies), D, is large compared to the smallest scale, λ_k.

If the turbulent fluctuations across the drop are isotropic, then the mean square velocity difference across the surface of the drop, $\overline{U^2(d)}$, can be related to the total kinetic energy using the energy spectrum (Equation (2.10)).

$$\overline{U^2(d)} = \int_{1/d}^{\infty} E(k)dk \tag{2.10}$$

The scaling of the E(k) in the inertial sub-range is then given by:

$$E(k) = \beta\varepsilon^{\frac{2}{3}}k^{-\frac{5}{3}} \tag{2.11}$$

Where β is commonly called the Kolmogorov constant.

Substituting Equation (2.11) into Equation (2.10) and then the result into Equation (2.1) yields:

$$\tau_c = 1.5\beta\rho_c\varepsilon^{2/3}d^{2/3} \tag{2.12}$$

Equation (2.12) describes the magnitude of the inertial stresses acting on a drop of diameter, d and is valid for $D >> d >> \lambda_k$. This equation can be combined with the expressions for the resistive force Equations (2.3) and (2.4) to give a value for d_{max}. As d_{max} is determined by the maximum local energy dissipation, ε should be replaced by ε_{max}.

The maximum stable diameter of a drop, d_{max}, in a turbulent field is then given by:

$$d_{\max} \propto \left(\frac{\rho_c}{\sigma}\right)^{\frac{3}{5}} \varepsilon_{\max}^{-2/5} \tag{2.13}$$

Shinnar (1961) extended Hinze's theory to stirred vessels by relating ε_{max} to the mean energy dissipation rate (power draw) per unit mass, ε_{avg}. In an agitated vessel it can be assumed that the local energy dissipation rate is proportional to the average energy dissipation rate, ε_{av}, over the whole vessel for all sizes of mixing vessel (geometric similarity).

Therefore ε_{max}, can be expressed as:

$$\varepsilon_{\max} = B_1 \varepsilon_{avg} \tag{2.14}$$

The constant of proportionality was defined as the energy concentration factor, B_1. The concentration factor is dependant on the geometry of the vessel and impeller.

In a stirred vessel, for sufficiently long residence times all the drops in the dispersion will experience the full range of energy dissipation. Therefore, it can be safe to assume that d_{max} will be determined by the largest values of ε. ε_{max} can be assumed to be the total power draw of the mixer. For fully turbulent conditions the power draw, P, can be determined from drag coefficient analysis which gives:

$$P = P_0 \rho_c N^3 D^5 \tag{2.15}$$

Where P_0 is the power number (a dimensionless group that is a function of geometric, kinematic and dynamic properties of the system).

Substituting Equation (2.15) into (2.14) yields:

$$\varepsilon_{avg} = B_2 N^3 D^5 \tag{2.16}$$

Where B_2, the constant of proportionality, incorporates the geometric factors including the power number, P_0.

Hinze (1955) suggested that the drop size could be related to the droplet Weber number, *We*, the ratio of inertia force (or kinetic energy) acting on the surface of the drop to opposing interfacial forces. This term has a critical value, We_{crit}, above which the drop becomes unstable. As ε_{avg} is a function of the impeller diameter and the impeller tip speed (πND) the Weber number can be expressed in terms of impeller speed and impeller diameter for mixing vessels:

$$We = \frac{\rho_c N^2 D^3}{\sigma} \tag{2.17}$$

Equation (2.16) can be inserted into (2.13) and simplified using the definition of *We*, to give the Weber number correlation:

$$d_{\max} = A_1 We^{-3/5} \tag{2.18}$$

It should be noted that this correlation is only applicable when the droplets are of a similar density/viscosity to the continuous phase and inertial stresses created by eddies in the inertial sub-range are responsible for drop break-up. Also, it is assumed that the residence time in the vessel is sufficient to ensure that all the droplets in the dispersion are exposed to the full range of energy dissipation (i.e. d_{max} is determined by the largest values of ε).

(b) Drop break-up in the viscous sub-range

The stress mechanism by which a drop breaks up is dependent on the drop size and location in the mixing vessel. If the drop passes through a region of high-energy dissipation, it is possible that drop sizes below λ_k will be generated. In such cases the previous definition for the functional form of E(k) would not be appropriate. Alternative definitions for E(k) were presented by Shinnar (1961) and Chen and Middleman (1967).

These expressions can be substituted into Equation (2.7), which then allows a similar analysis to be performed to yield a correlation in terms of d_{max} for the viscous sub-range for turbulence.

Shinnar (1961) used the following functional form for E(k), ($d < \lambda_k$):

$$E(k) \propto \varepsilon \upsilon^{-1} k^{-3} \tag{2.19}$$

Which gives Equation (2.20):

$$d_{\max} \propto \sigma^{1/3} \rho^{-2/3} \upsilon^{1/3} \varepsilon^{-1/3} \tag{2.20}$$

Equation (2.20) can then be simplified in terms of We and Re:

$$\frac{d_{\max}}{D} \propto (We\,\mathrm{Re})^{-1/3} \tag{2.21}$$

The Reynolds number is the ratio of inertial forces to viscous forces and is defined as:

$$\mathrm{Re} = \frac{\rho_c N D^2}{\mu_c} \tag{2.22}$$

Chen and Middleman (1967) used the following functional form for E(k), ($d << \lambda_k$):

$$E(k) \propto \varepsilon^2 \upsilon^{-4} k^{-7} \tag{2.23}$$

Which gives:

$$d_{\max} \propto \sigma^{1/7} \rho^{-5/7} \upsilon^{4/7} \varepsilon^{-2/7} \tag{2.24}$$

Equation (2.24) can then be simplified to:

$$\frac{d_{max}}{D} \propto \left(We\,\mathrm{Re}^4\right)^{1/7} \tag{2.25}$$

Equation (2.21) and (2.25) both apply to the viscous sub-range of turbulence and assume that break-up is caused by inertial stresses. The differences in the two can be attributed to the definition of the functional form of E(k).

However, Shinnar (1961) suggested that for drops smaller than λ_k, shear forces would be more significant than inertial stresses acting on the drop. The viscous shear force responsible for break-up was given by ($d < \lambda_k$):

$$\tau_D \propto \mu\gamma' \tag{2.26}$$

Where the shear rate, $\gamma' \propto (\varepsilon/\nu)^{1/2}$

This then gives the following expression for d_{max} to represent the magnitude of the forces causing drop break-up below the Kolmogorov micro-scale:

$$d_{max} \propto \sigma^1 \rho^{-1/2} \upsilon^{1/2} \varepsilon^{-1/2} \tag{2.27}$$

Simplifying in terms of We and Re:

$$\frac{d_{max}}{D} \propto We^{-1}\,\mathrm{Re}^{1/2} \tag{2.28}$$

It is clear that expressions for d_{max} show different dependencies on system parameters. The definitions of the main stresses that are responsible for d_{max} depend upon the mode of droplet deformation or the stress mechanism, which vary depending upon location in the

vessel and the droplet diameter. Many workers have reported that the rotor-stator mixer exhibits inhomogeneous energy dissipation and it is probable that the stress mechanisms that cause break-up will vary throughout the mixer region. However, a comparison of these models will establish which stress mechanisms are dominant in the generation of dispersions in a rotor-stator mixer.

Shinnar (1960) assumed that We was dependant on the energy dissipation as described by Equation (2.16). As this has not been established for rotor-stator mixers, (for the range of rotational speeds to be studied) and to ensure that this assumption is valid, the energy dissipation will be measured (Section 2.4).

The definition of Reynolds number above (Equation (2.22)) is the impeller Reynolds number often used for stirred vessels. This definition takes the impeller diameter as the characteristic length scale and the impeller tip speed as the characteristic velocity (to determine the inertial forces created by the rotor). However, Sparks (1996) observed that various regions in the mixer had different flow patterns (Section 2.3.1). In each of these regions the characteristic length scale and the associated velocities causing turbulence may change, these are discussed in further detail in Section 2.3.1.

2.2.3. Mean drop size correlations

The correlations presented previously are all based on the maximum stable droplet size, d_{max}. However, most of the correlations available in literature substitute the Sauter mean diameter for d_{max}. Many previous authors have used image-capturing techniques to determine droplet size distributions, which require tedious drop size counting. The accurate determination of d_{max} requires the measurement of a large sample of droplets. It has been shown that the Sauter mean diameter can be determined accurately for a smaller sample size and therefore offers a practical replacement.

The Sauter mean diameter, d_{32}, is defined as the quotient of the second and third moment of the size distribution:

$$d_{32} = \frac{\sum_{i=1}^{n} d_i^3}{\sum_{i=1}^{n} d_i^2} \tag{2.29}$$

The Sauter mean diameter is important in mass transfer and reaction systems as it is related to the interfacial area per unit volume, a_s:

$$a_s = \frac{6\Phi}{d_{32}} \tag{2.30}$$

Where, Φ is the dispersed phase volume fraction.

In addition to its design value, d_{32} gives a better representation of the small as well as large droplets, since it takes volume and surface area into account.

The Sauter mean diameter is often assumed to be directly proportional to d_{max}, which was shown to be true for inviscid dispersed phases by Chen and Middleman (1967) and also for non-coalescing systems by Brown and Pitt (1971). They made the assumption that break-up was due to a single mechanism. Calabrese (1992) generalised their derivations to state that d_{max} is proportional to any convenient mean diameter, provided break-up is due to a single mechanism.

Calabrese (1992) suggested the use of the volume mean diameter, d_{43}, which better represents the larger drops in the distribution. It was reasoned that the larger drops should undergo the same stress mechanisms as d_{max} and would therefore act as sensible replacement. It was also stressed that more than one mean diameter should be tested for suitability in models.

It is important to note that it is possible for two dispersions to have the same mean diameter but have very different droplet size distributions. Therefore, although mean

drop diameters are useful in design correlations the droplet size distribution should always be considered when assessing a dispersion.

Tavlarides and Stamatoudis (1981) provide a comprehensive summary of correlations based on the d_{32} developed by various authors.

2.2.4. The effect of dispersed phase volume fraction, Φ, on turbulence

A large number of papers confirm the inference that Φ has little or no effect on the mean drop size (Middleman, 1974; Chen & Libby, 1978; and Streiff, 1977). However, Tavlarides & Stamatoudis (1981) and El-Hamouz et al (1988) reported models that had been developed for droplet size distributions (in stirred tanks) fitted experimental data better by taking into account a damping effect on turbulence by the dispersed phase.

This agreed with findings by Brown and Pitt (1971) who observed that an increase in dispersed phase concentration resulted in an increase in d_{32}. As the system they were using was a non-coalescing one, they attributed the increase to turbulence damping. Brown and Pitt (1971) and later Streiff et al (1997) showed that d_{32} could be related to Φ in the following form:

$$d_{32} = C(1 + k\Phi) \tag{2.31}$$

Where C and k are constants determined from experiments.

Doulah (1975) derived an expression that accounted for the increase in drop size with the dispersed phase concentration.

$$d_{32} = \left(\frac{\rho_c}{\rho_e}\right)^{6/5} (1 + 2.5\Phi)^{6/5} d'_{32} \tag{2.32}$$

Where ρ_e is the density of the dispersion and d'_{32} represents the Suater mean diameter of drops in a dilute dispersion (as opposed to that in the concentrated dispersion, d_{32}). Equation (2.32) can be expressed in terms of the energy dissipation:

$$\varepsilon_e = \varepsilon\left(\frac{\rho_c}{\rho_e}\right)^3 (1+2.5\Phi)^{-3} \qquad (2.33)$$

ε_e denotes the energy dissipation available in a dispersion of high Φ and ε represents the energy dissipation in the dilute system. Francis (1999) suggested the use of Equation (2.33) in the derivation of the expressions for d_{max} (or d_{32}) described previously to account for the effect of Φ.

2.2.5. Summary

Traditionally the theoretical prediction of droplet size has been based on the assumption of homogenous, isotropic turbulence. By extending the theories of Kolmogorov (1945) and Hinze (1955) to stirred vessels, various correlations for d_{max} or d_{32} have been developed (Chen and Middleman, 1967; Shinnar, 1961; Tavlarides & Stamatoudis, 1981). These correlations are based on mechanistic models that balance the forces that cause drop disruption and those that oppose it. The correlations have been simplified to exclude the effects of coalescence and drop viscosity and therefore only apply to inviscid, dilute dispersions (only interfacial effects resist drop deformation). The most important correlations are summarised in Table 2.2.

The Sauter mean diameter, d_{32}, has been shown to be proportional to d_{max} and has a greater design value than d_{max}. d_{32} can, therefore, be substituted into the correlations for d_{max} listed in Table 2.2.

The majority of authors report that the dispersed phase, Φ, has little or no effect on droplet size. There are a few exceptions, however, who all report a linear relationship between mean drop size and Φ (Equation (2.31)).

Table 2.2 A summary of theoretical correlations to predict droplet size

Authors	Correlation	Equation	Exp^{t} on N	Stress Mechanism	Range
Kolmogorov & Hinze (1955)	$d_{max} \propto \sigma^{3/5} \rho^{-3/5} \varepsilon^{-2/5}$ $\frac{d_{max}}{D} \propto We^{-3/5}$	(2.13) (2.18)	-6/5	Inertial Sub-Range	D>>d >>λ_k
Shinnar (1961)	$d_{max} \propto \sigma^{1/5} \rho^{-2/5} \nu^{1/3} \varepsilon^{-1/5}$ $\frac{d_{max}}{D} \propto (We\,\mathrm{Re})^{-1/3}$	(2.20) (2.21)	-1	Viscous Sub-range	d < λ_k
Chen and Middleman (1967)	$d_{max} \propto \sigma^{1/7} \rho^{-5/7} \nu^{4/7} \varepsilon^{-2/7}$ $\frac{d_{max}}{D} \propto (We\,\mathrm{Re}^{4})^{-1/7}$	(2.24) (2.25)	-6/7	Viscous Sub-range	d << λ_k
Shinnar (1961)	$d_{max} \propto \sigma^{1} \rho^{-1/2} \nu^{1/2} \varepsilon^{-1/2}$ $\frac{d_{max}}{D} \propto \left(We\,\mathrm{Re}^{-1/2}\right)^{-1}$	(2.27) (2.28)	-3/2	Turbulent Viscous Shear	d < λ_k

2.3. Rotor-stator mixers

2.3.1. Flow patterns and Reynolds numbers in an in-line rotor-stator mixer

An understanding of the flow patterns within the rotor-stator mixer will give an appreciation of the areas of high energy dissipation and the types of break-up mechanisms that would be induced as a result. At this point it is worth clarifying the basic geometry of an in-line rotor-stator mixer. In doing so, attention is drawn back to Figure 2.4 which shows an example of a toothed and Silverson design of rotor and stator.

The basic principle (as outlined in Section 2.1.5.) is that the rotor spins at high speeds within a motionless stator (with very small clearances). This creates a suction force which draws material directly into the rotor region and is in turn forced by the pumping action of the blades through the perforations or holes in the stator.

The rotor-stator mixer exhibits complex flow patterns that make direct visualisation very difficult. The flow within a rotor-stator mixer has been reported to be unsteady and periodic (Kroezen & Wassink, 1987; Pedrocchi and Widmer, 1988; Korshakov et al 1990; Sparks 1996). The fixed stator will experience a pulsating force as the rotor spins. A small element of fluid experiences a large acceleration as it enters the rotor region followed by a sudden deceleration as it proceeds to hit the stator wall.

Sparks (1996) performed some flow visualisation tests on a Perspex toothed rotor-stator mixer and an acid-base decolourisation scheme (hydrochloric acid and sodium hydroxide with bromo thymol blue tracer). The rotor-stator was broken down into sections and the flow of tracer was observed through each of these sections. These sections included; (a) the inlet pipe; (b) the rotor region; (c) the shear gap; (d) the stator region; (e) the volute.

The Reynolds number, Re, (Equation (2.22)) is the ratio of inertial forces to viscous forces present in a system. The relevant forces are considered over an area of flow and this area can be simplified to a characteristic linear dimension of the system. In stirred vessels the characteristic length scale is usually chosen as the impeller diameter, D and

the representative velocity of flow is taken to be the impeller tip speed, πND. This gives the impeller Reynolds number defined in Equation (2.22). This dimensionless parameter provides an indication of the level of turbulence in a system, the higher the value the greater the likelihood of turbulent flow. In mixing applications the Re provides a criterion for dynamic similarity for scale-up.

The flow visualisation work performed by Sparks (1996) showed the flow patterns to be very different in the various regions of the rotor-stator mixer. Also, it has been widely reported that the energy dissipation in a rotor-stator mixer is highly inhomogeneous. This would indicate that the turbulent energy would differ greatly throughout the mixer.

This would imply that the impeller Reynolds number may not be a true reflection of the flow characteristics throughout the whole of the mixer. Each section in the mixer will have its own characteristic length scale and characteristic velocity. The various characteristic length scales and velocities within the mixer will shed some light on where in the mixer the turbulent energy dissipation is focussed. Taking this in to consideration would allow the identification of regions that are operating in the turbulent and laminar regimes.

The following is a review of the findings of Sparks (1996) and the various regions in the mixer and the corresponding length scales and velocities will be defined for each section of the in-line rotor-stator mixer.

(a) Inlet Pipe

The inlet pipe was found to contain swirling fluid caused by the effects of the spinning rotor drawing the fluid up the inlet pipe. There was no change in flow pattern observed with operating condition (rotor speed, flowrate).

This swirling flow would result in a small degree of pre-mixing which might be beneficial in the generation of dispersions. However, there is also the possibility of phase separation. The degree of pre-mixing will be determined by the turbulence characteristics

in the in-let pipe which can be assessed simply by taking into account the pipe Reynolds number, Re_{pipe}:

$$\mathrm{Re}_{pipe} = \frac{\rho d u}{\mu} \tag{2.34}$$

Where, the characteristic length scale is the inlet pipe diameter and the velocity is given by the flowrate divided by the cross sectional area of the pipe.

(b) Rotor

Fluid entering the rotor region was accelerated tangentially and the flow pattern upstream of the rotor teeth could be characterised by swirl generated as the fluid followed the rotor face. The flow pattern again showed little dependence on the operating condition.

The tracer was seen to follow the rotor teeth for a considerable distance (along the rotor circumference) leading to interaction with tracer plumes from consecutive feeds.

The injection of sodium chloride tracer into the rotor teeth and monitoring of the conductivity upstream revealed little or no back flow into the region.

The flow in this region was considered to be predominantly tangential, with a much lower radial component. As the fluid was seen to follow the rotor teeth the velocity of the fluid at the rotor tip, v_{tip}, was considered to be the same as the tip speed of the rotor:

$$v_{tip} = \pi N D \tag{2.35}$$

Where, N is the rotational speed (s^{-1}) and D is the rotor diameter (m).

Sparks (1996) went on to describe the trajectory of the fluid through the rotor region as being indicated by v_{tip} and the nominal radial velocity, v_{RADIAL}, which was defined as:

$$v_{RADIAL} = \frac{Q}{A} \tag{2.36}$$

Where, A is the open area of the rotor (m^2) and Q is the flowrate (m^3/s).

If v_{RADIAL} can be calculated and the radial length, D_{RADIAL}, that the fluid must travel in a particular region can be determined. In the case of the toothed rotor D_{RADIAL} in the rotor region is the length of a rotor tooth, for a Silverson type rotor (a swept blade) this length will be the length of one of the blades. The nominal residence time of the fluid in that region can be estimated using Equation (2.37).

$$\tau = \frac{D_{RADIAL}}{v_{RADIAL}} \tag{2.37}$$

It is worth pointing out that the open area of a toothed rotor is considerably smaller than that of a Silverson rotor (i.e. a swept blade type), Figure 2.7. This would lead to smaller radial velocities and greater nominal residence times in the rotor region. A similar calculation can be applied to other regions within the mixer (e.g. the stator).

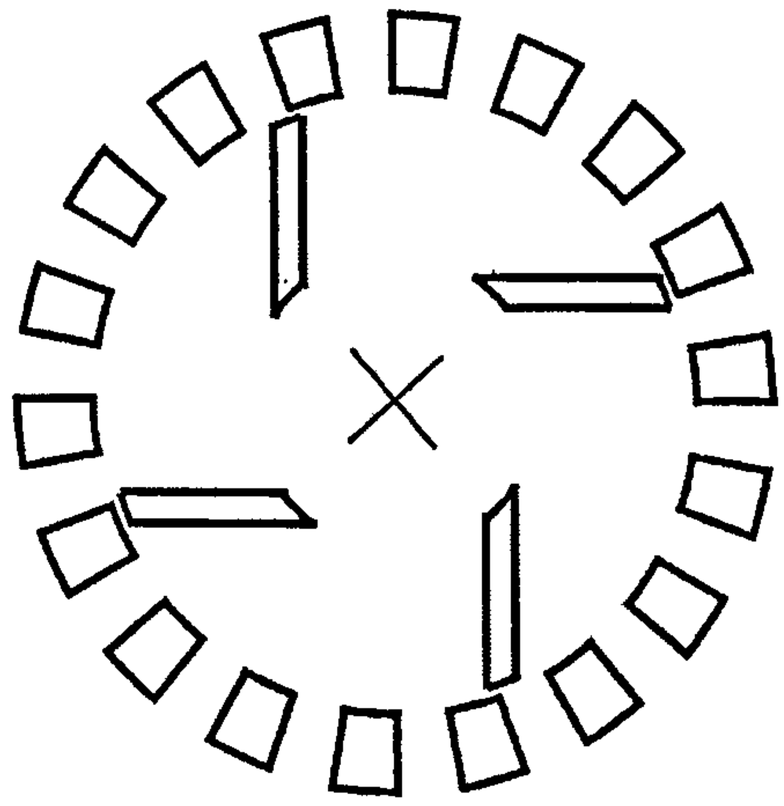

Figure 2.7 A Silverson type rotor and stator configuration

Hence, two characteristic length scales can be determined for fluid movement in the rotor region. That for tangential flow, where the rotor diameter, D, will be the characteristic length and the rotor tip speed, v_{tip}, the characteristic velocity; and that for radial flow, where corresponding length scales and velocities will be D_{radial} and v_{RADIAL}.

The former results in the impeller Reynolds number (Equation (2.22)) and the latter is given by:

$$\mathrm{Re}_{RADIAL} = \frac{\rho D_{RADIAL} v_{RADIAL}}{\mu} \tag{2.38}$$

(c) Shear Gap

The scale over which effects in the shear gap occur (less than 1 mm) coupled with the high rotor-speeds made observations of the flow pattern in the shear gap region difficult.

The characteristic length scale in this region will be the gap between the rotor and the stator, δ, although the characteristic velocity in this region will remain the rotor tip speed, v_{tip}. Therefore the shear gap Reynolds number will be:

$$\mathrm{Re}_{\delta} = \frac{\rho \delta v_{tip}}{\mu} \tag{2.39}$$

The shear rate in this region is determined by δ and v_{tip} and the Re_{δ} will provide an indication of the dissipation in the gap due to viscous shear.

The values for δ and v_{tip} can be inserted into Equation 2.37 to estimate the nominal residence time in the shear gap.

(d) Stator

(d) Stator

Fluid discharging from the rotor was abruptly turned by the upstream face of the stator teeth and emerges radially. A fast stream followed the leading edge of the stator and a region of recirculation accompanied this (Figure 2.8).

The tangential kinetic energy given to the fluid by the rotor was transformed into pumping power, skin friction losses and turbulent losses. It was suggested that the point where the abrupt turn in the flow takes place is where the losses are greatest.

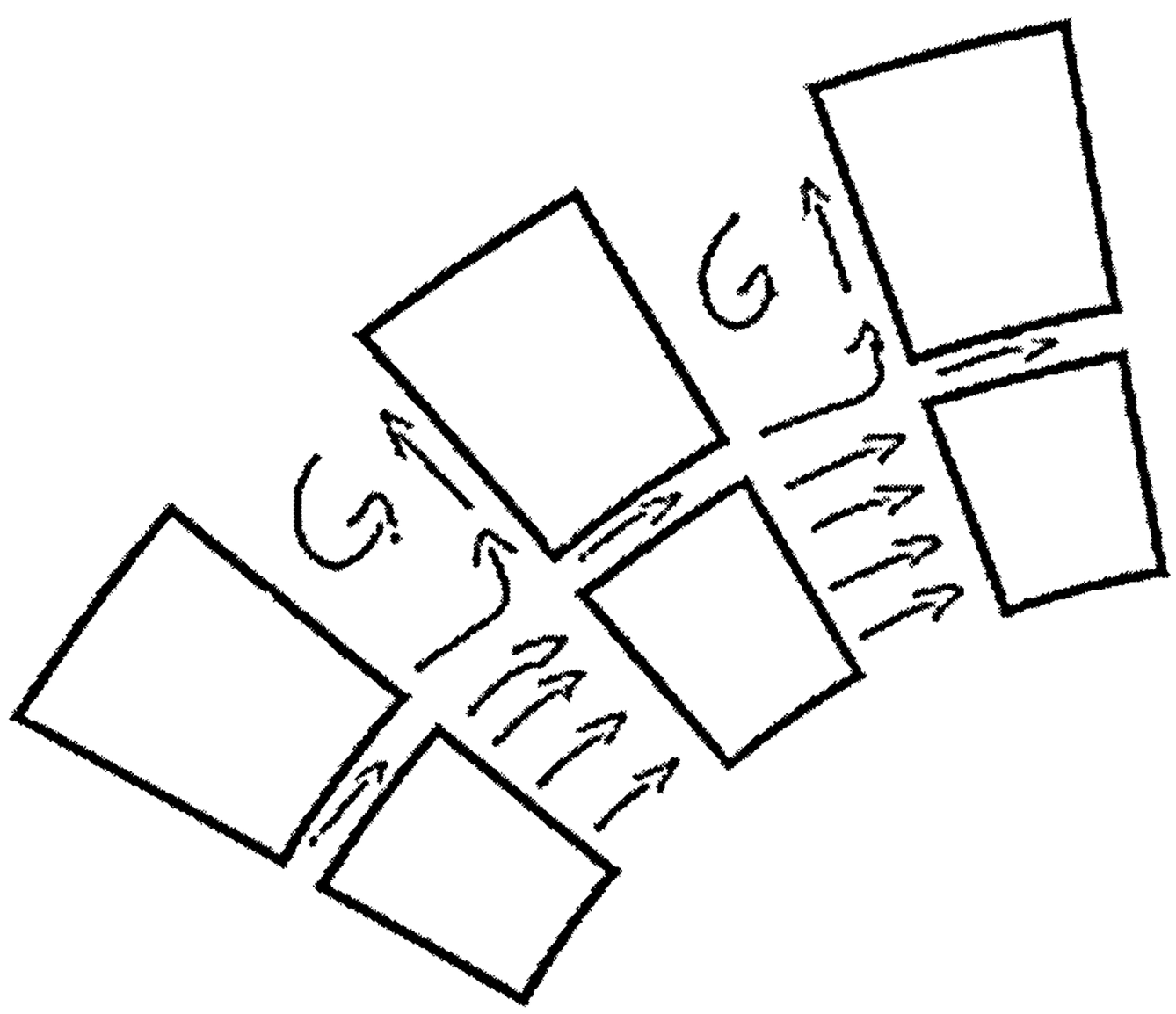

Figure 2.8 Flow pattern through a stator (Sparks 1996)

A certain degree of back-mixing may also be evident as the rotor creates an area of low pressure on the blade following edge, which may draw liquid back into the slot/hole.

The various shapes of the holes/slots in the stator screens make it appropriate, for turbulent flow, to specify a hydraulic mean diameter, D_{hyd}, as the characteristic length scale in this region. The hydraulic mean diameter is defined as four times the cross-sectional area divided by the wetted perimeter. The velocity of the fluid moving radially through the stator holes/slots can be defined as the bulk flowrate divided by the open area of the stator screens and will be the velocity of the fluid jets emanating from the screens, v_{jets}. The definition of Reynolds number in the stator region is given by:

$$\mathrm{Re}_{stator} = \frac{\rho D_{hyd} v_{jets}}{\mu} \tag{2.40}$$

The nominal residence time in the stator holes/slots can be estimated by using the thickness of the screen (the depth of the hole/slot) and v_{jets} in Equation 2.37.

(e) Volute

Sparks (1996) divided the flow in the volute into three main sections (Figure 2.9). Recirculating flows were observed behind the rotor (A). The flow directly out from the stator was radial (B) and the outlet pipe contained swirling flow (C). Again no change with operating condition was detected.

It is very difficult to characterise the length scale in this region as the shaft and rotor and the shape of the volute will influence the flow characteristic. It is safe to assume that the bulk of the flow in this region and the resultant turbulent energy in the volute will be as a direct result of the jets emanating from the stator holes/slots. It is also safe to assume that all of the fluid eventually finds its way to the outlet. Therefore, the characteristic linear length scale for the flow in the volute can be taken as the distance between the volute wall and the stator, which will be referred to as D_{volute}

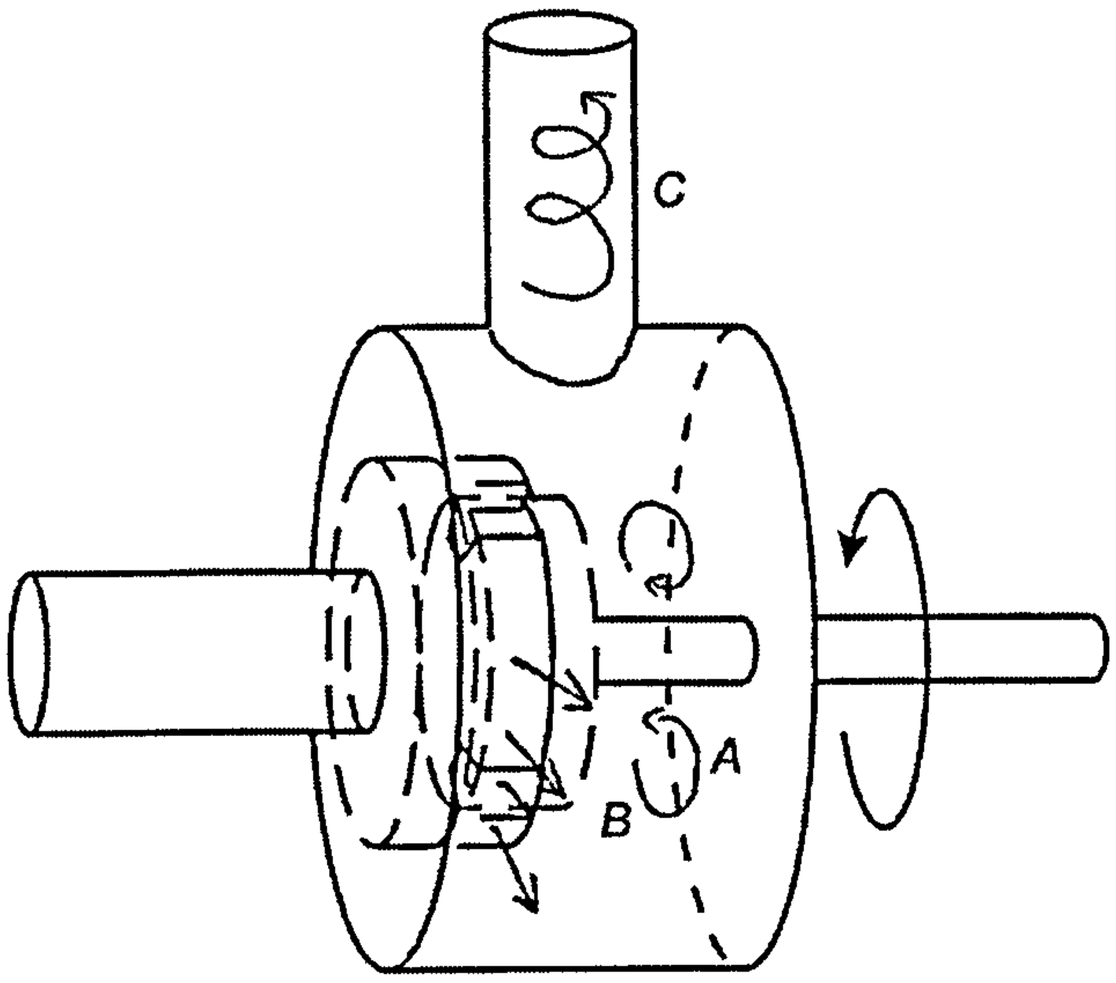

Figure 2.9 Flow pattern in the volute (Sparks, 1996)

Hence, the Reynolds number in the volute can be defined as:

$$\mathrm{Re}_{volute} = \frac{\rho D_{volute} v_{jets}}{\mu} \tag{2.41}$$

Sparks (1996), suggested that the overall residence time distribution characteristics of the mixer were determined by the flows in the volute. This seemed a reasonable statement as he found that the residence time distribution curves were similar for a Silverson type mixer and a toothed type. This is also reasonable as the volume of the volute is much greater than the volume of the inlet and outlet pipes and the rotor-stator region.

A nominal residence time of the fluid in this region can be estimated by dividing the volume of the volute by the bulk flowrate.

2.3.2. Drop Break-up in shear and elongated flow fields

Up to this point drop break-up in turbulent flow has been reviewed, however it is reasonable to assume that there are regions within the mixer where these theories will not apply. It has been reported that the assumption of local isotropy is only fulfilled locally within the mixer. For this reason the following section will review the main theories behind droplet break-up in highly sheared flows.

When one immiscible liquid is added to another the dispersion process can be considered to occur in stages. Initially the two liquids are at present in bulk as the mixing process develops the bulk fluid gets broken up into chunks which in turn get broken into smaller parts or globules. Hinze (1955) provided a summary of the various modes a single drop (or globules) could break-up. He explained that a globule could split (due to hydrodynamic forces) in a number of different ways depending on the flow pattern around them and generalised them into three types (Figure 2.10).

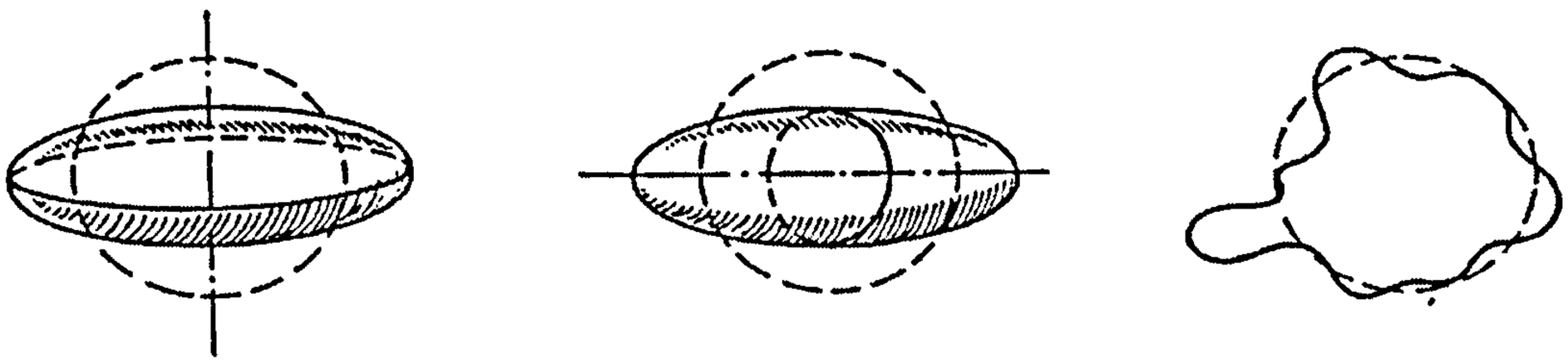

Figure 2.10 Basic types of globule deformation (Hinze 1955)

Type 1 is where the globule is flattened to form an oblate ellipsoid. How the globule is broken depends on the magnitude of the forces causing deformation. Type 2 occurs as the globule becomes more and more elongated and forms a cylindrical thread which then breaks into drops. Type 3 occurs as a result of local deformations on the surface of the globule resulting in small drops breaking off the main body. Hinze (1955) went on to classify six different flow patterns that may cause drop break-up, five of which are shown diagrammatically in Figure 2.11.

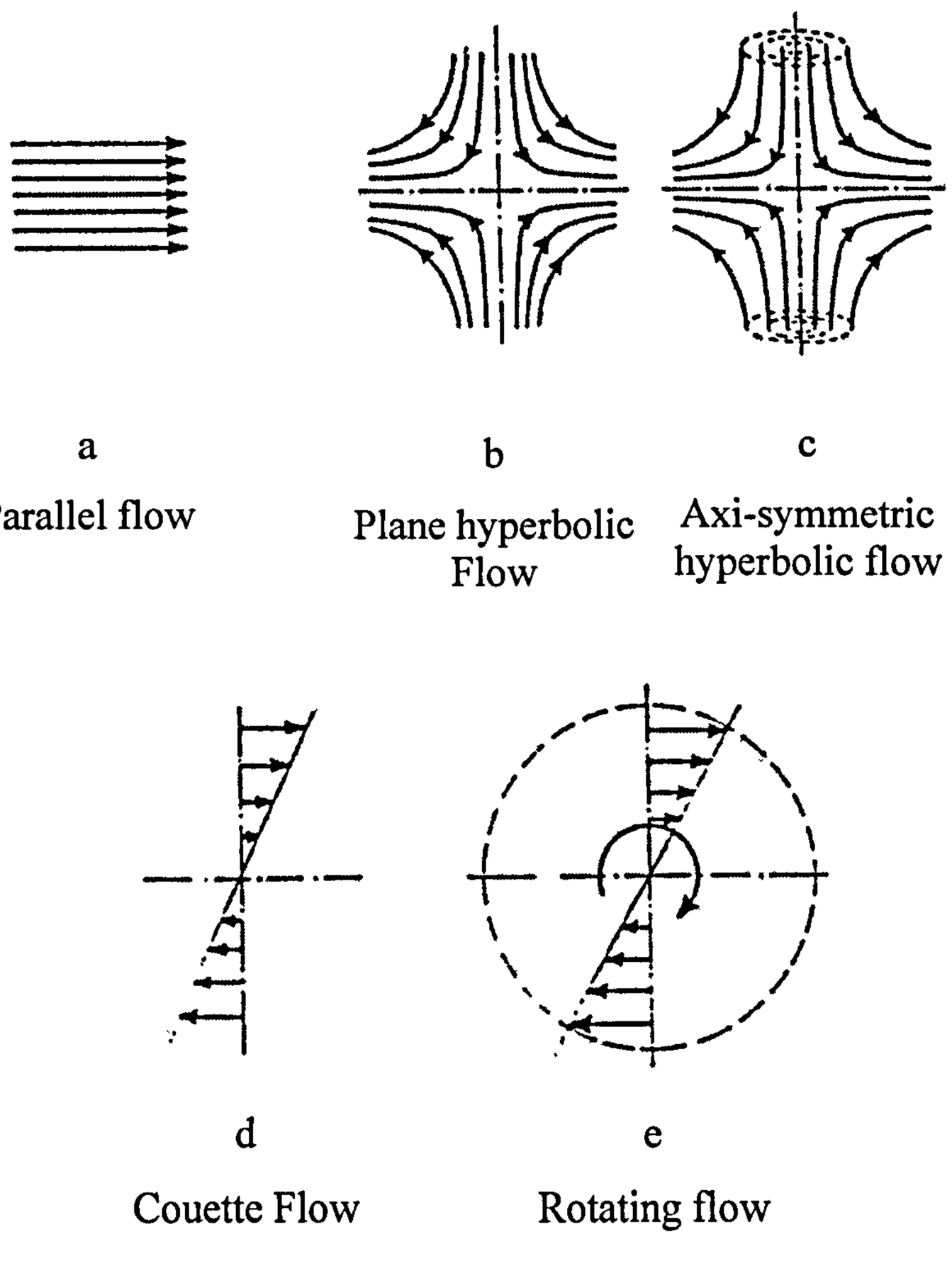

Figure 2.11 Flow patterns that can cause one of the basic types of globule deformation.

The sixth flow pattern that was described was an Irregular flow field (f) occurring in turbulent flow.

It was assumed that for the rotating flow pattern (e) the fluid rotates bodily. The flow patterns were also assumed to be large compared to the globule size but still local within the whole flow field.

It is possible to distinguish between deformation by inertial forces and that by viscous forces. Table 2.3 summarise each deformation mode and the particular flow patterns that may cause them. For example, it can be seen that Lenticular deformation can arise if the globule is subjected to inertial or viscous forces produced by parallel, axi-symmetrical and rotating flow patterns (a, c and e in Figure 2.11).

Table 2.3 Flow patterns that cause each deformation mode

	Type 1 Lenticular	**Type 2 Cigar-Shaped**	**Type 3 Bulgy**
Inertial forces	a, c, e	b, d	f
Viscous Forces	a, c, e	b, d	-

The globule will break-up if the flow pattern is large enough to sustain the globule and if the globule is exposed to this flow pattern for a sufficient amount of time. The type of deformation and break-up was found to depend on the local flow patterns around the drop and the physical properties of the liquids.

In turbulent dispersions, inertial forces were thought to be dominant since at relatively high Reynolds numbers, the local regions of viscous flow were assumed to be small compared with the size of the drop. In viscous flows the likely deformation modes were plane hyperbolic and Couette flow, whereas, in turbulent flow it was deemed likely that

Couette, axi-symmetrical and plane hyperbolic flow and perhaps irregular flow were responsible for drop deformation.

Karam & Bellinger (1968) observed drop break-up in simple shear flow in a Ćouette device. They found that drops rarely broke-up into two equal droplets and the majority of the cases break-up resulted in a number of smaller drops. They concluded that under simple shear flow a uniform droplet size is unlikely and that a range of sizes is more likely. Figure 2.12 shows a summary of their observations.

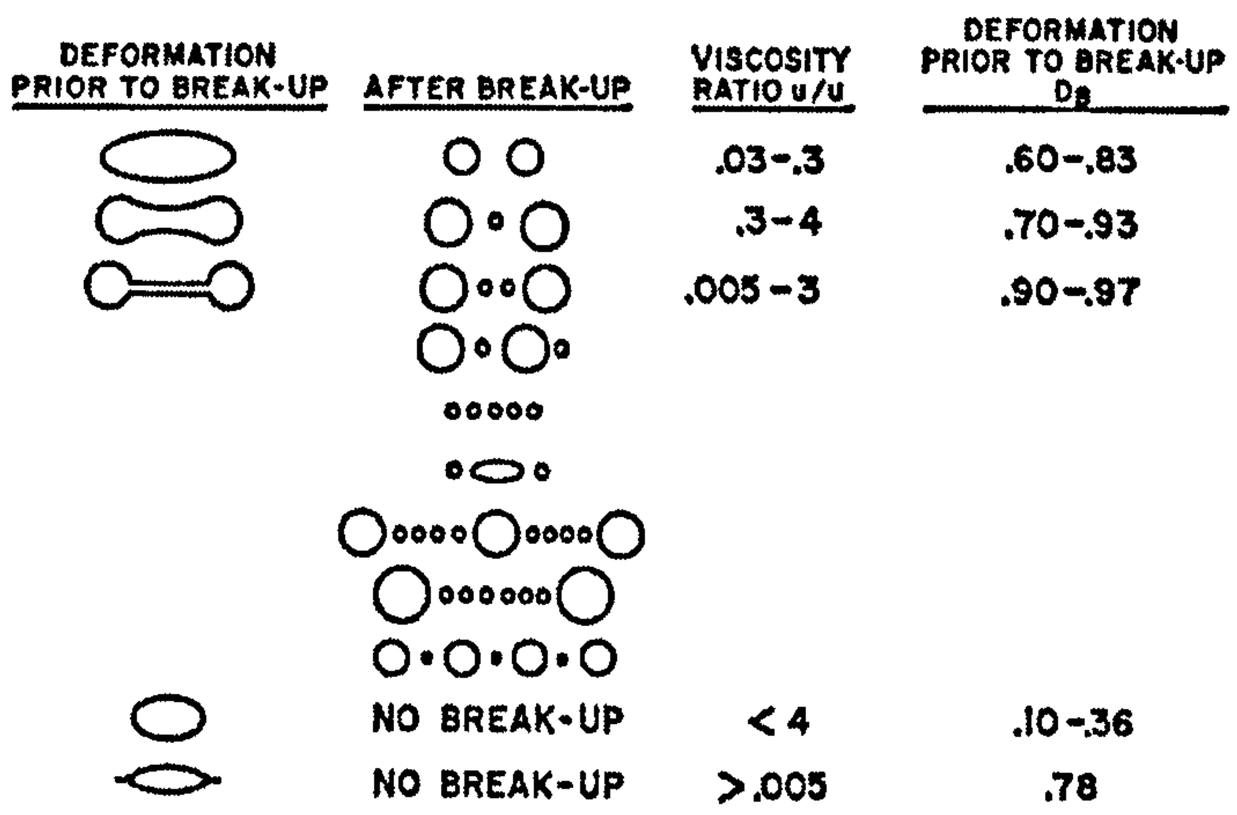

Figure 2.12 Break-up of droplets in Couette flow field (Karam & Bellinger, 1968)

Typically, in Couette flows drops form ligaments that break into smaller drops, the number and size of these smaller drops is dependant on the length of the ligament before break-up (the longer the ligament the greater the number of smaller drops). In Extensional flow the drops will deform into a thin filament with dumb bells at each end which on break-up will form tow separate drops and several satellite drops.

Taylor (1934) investigated droplet deformation in the laminar flow regime (simple shear field) over a range of viscosity ratios, μ_d/μ_c, (where, μ_d is the dispersed phase viscosity,

and μ_c is the continuous phase viscosity) 0.0003 to 20. Single drops approximately 1mm in diameter were observed to deform and break-up in both Couette and hyperbolic flow. Taylor formulated a theory of droplet deformation and break-up. In doing so he made the following assumptions; that the drops are small so that they remain spherical when deformed, small deformations, no slip at the drop interface and a continuous shear stress across the interface.

He found that drop break-up occurred at lower shear rates in a hyperbolic flow field compared with the Couette flow. At the highest viscosity ratios no break-up was observed in the Couette flow. For both types of flow patterns, higher shear rates were required to deform and break-up drops at the viscosity ratios both considerably higher and lower than one.

Karam & Bellinger (1968) discussed the concept of internal circulation within a liquid drop, which stabilised a droplet when deformed in a simple shear flow. Interfacial tension acting on a drop under deformation will cause the drop to pinch off and divide. Internal circulation prevents this from happening by building up pressure within the drop against the dimple and pushing outward. Internal circulation was used as an explanation for why the observed drop size was approximately three times the calculated size (using the theories of Taylor, 1934).

There have been numerous studies that have furthered the work of Taylor (1934). Karam & Bellinger (1968) studied single drop break-up in Couette shear flow fields. However, the most comprehensive work done in this area was by Grace (1982) who studied the deformation and break-up of droplets in various simulated shear flow fields, including Couette and plane hyperbolic flow fields. A wide range of liquids were studied which enabled μ_c from 5 to 300 kg/ms, σ up to 0.025 N/m and μ_d/μ_c from 10^{-6} to 950. The particle Reynolds numbers were in the range from 10^{-2} to 10^{-6}.

The following is a summary of the findings of Grace (1982). A number of plots and correlations were formulated using experimental data from simulated Couette (Rotational Shear field) and Extensional flow (plane hyperbolic shear fields).

For small deformations Taylor (1934) showed theoretically that the deformation at burst, D_B, is equal to E_B (referred to by Grace as the reduced shear required for break-up). The drop deformation D equals the length of an elongated drop minus breadth over length plus breadth, ($= \frac{L-B}{L+B}$). E_B is defined by Equation 2.42.

$$E_B = \frac{G_B r_d \mu_c f(p)}{\sigma} \tag{2.42}$$

Where, G_B is the shear rate (s^{-1}), r_d is the drop radius, $f(p)$ is a theoretical function of the viscosity ratio suggested by Taylor (1934), Equation (2.43). Values for $f(p)$ vary from 1 to 1.2 for viscosity ratios from 0 to infinity.

$$\text{Viscosity ratio, } p = \frac{\mu_d}{\mu_c}, \quad f(p) = \frac{19p+16}{16p+16} \tag{2.43}$$

Couette Flow (Shear Flow)

Firstly, considering drop deformation and break-up in a uniform Couette shear field.

Figure 2.13 shows a plot of E_B, the ratio of viscous forces and interfacial forces necessary for drop bursting versus μ_d/μ_c. This correlation allows the prediction of G_B, required to break a drop of radius r_d, at known μ_c and σ for a viscosity ratio from 10^{-6} to 3.5 in uniform rotational shear.

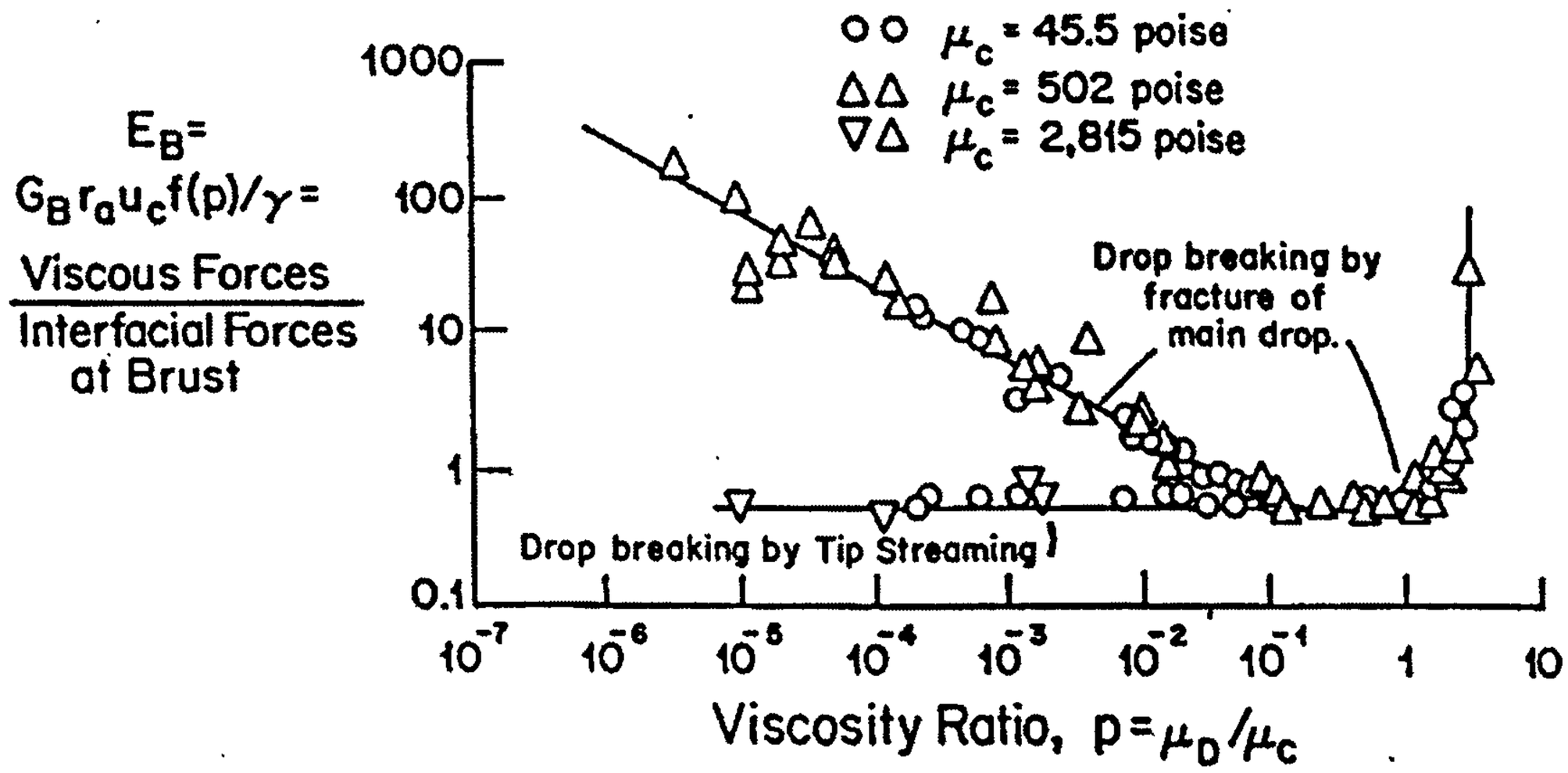

Figure 2.13 Effect of viscosity ratio on E_B in simple shear flow field (Grace, 1982)

It can be seen that the viscosity ratio has a significant effect on E_B, in Couette shear and a minimum occurs in the range of viscosity ratios from 0.1 to 1.0. The critical shear gradient increases significantly either side of this range. It was claimed that the horizontal section below a viscosity ratio 0.1, represents tip streaming (small drops that are broken off from the tips of a drop that assumes a sigmoid shape) and does not represent actual drop break-up. It can be seen that it is not possible to break drops in a simple shear field if the viscosity ratio exceeds 3.5.

Figure 2.13 is similar to that reported by Karam & Bellinger (1968), who also saw a minimum in a similar viscosity range. However, Grace showed that drops could be broken at viscosity ratios as low as 10^{-6}, whereas Karam & Bellinger (1968) indicated that this was not possible below 5×10^{-3}. They also showed a minimum value of reduced shear of approximately 2 compared to 0.6 of Grace (1982). Grace (1982) attributed these differences to limitations in equipment and lower values of μ_c used by Karam and Bellinger (1968) and also the values of interfacial tension used (Grace used the dynamic interfacial tension between to pure components).

The data was also plotted in terms of drop draw ratio required for break-up at the critical shear gradient. The drop draw ratio was defined as the length required for break-up over the original drop diameter. Figure 2.14 shows a plot of drop draw ratio versus viscosity ratio. The general correlation is similar to that shown in Figure 2.13, in that a minimum occurs in a viscosity ratio range of 0.2 to 1.0 with a rapid increase either side of this minimum. For break-up to occur at the critical value of reduced shear, both a critical drop draw ratio and a critical time under shear must be attained.

Figure 2.14 shows the data in terms of reduced burst time, t_b, versus viscosity ratio. The reduced burst time is a dimensionless term and is represented as $\frac{t_b \sigma}{2 r_d \mu_c}$.

Figures 2.13 to 2.15 can be used to predict the required critical shear, drop draw ratio and the required shear time for break-up over a 10^6 range of μ_d/μ_c. However, in most dispersion applications there will be a range of droplet size distributions and Grace (1982) discussed the effects of exceeding the critical shear for larger size drops to break the smaller drops.

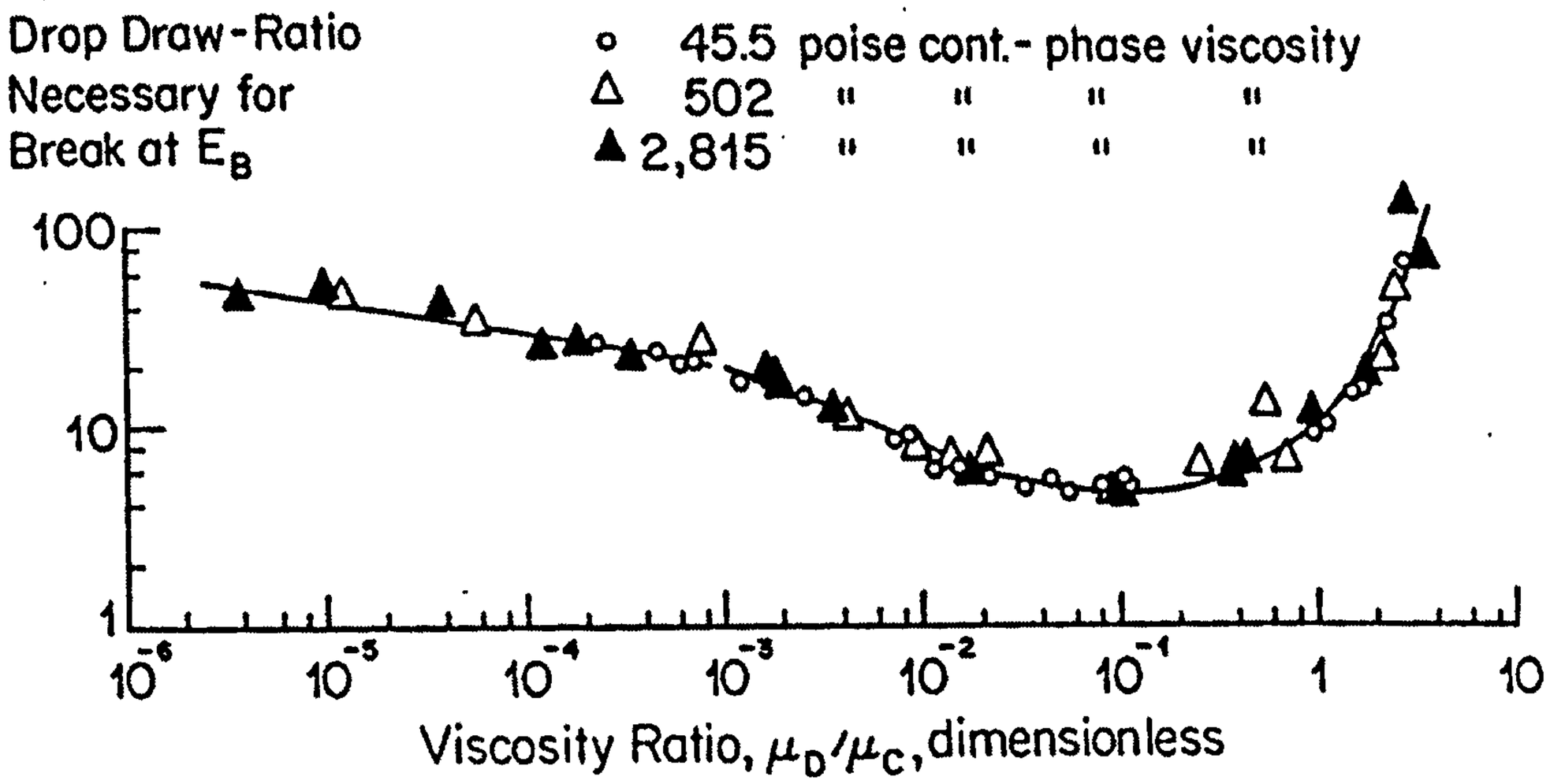

Figure 2.14 Effect of viscosity ratio on drop draw ratio necessary for break-up at E_B (Grace, 1982)

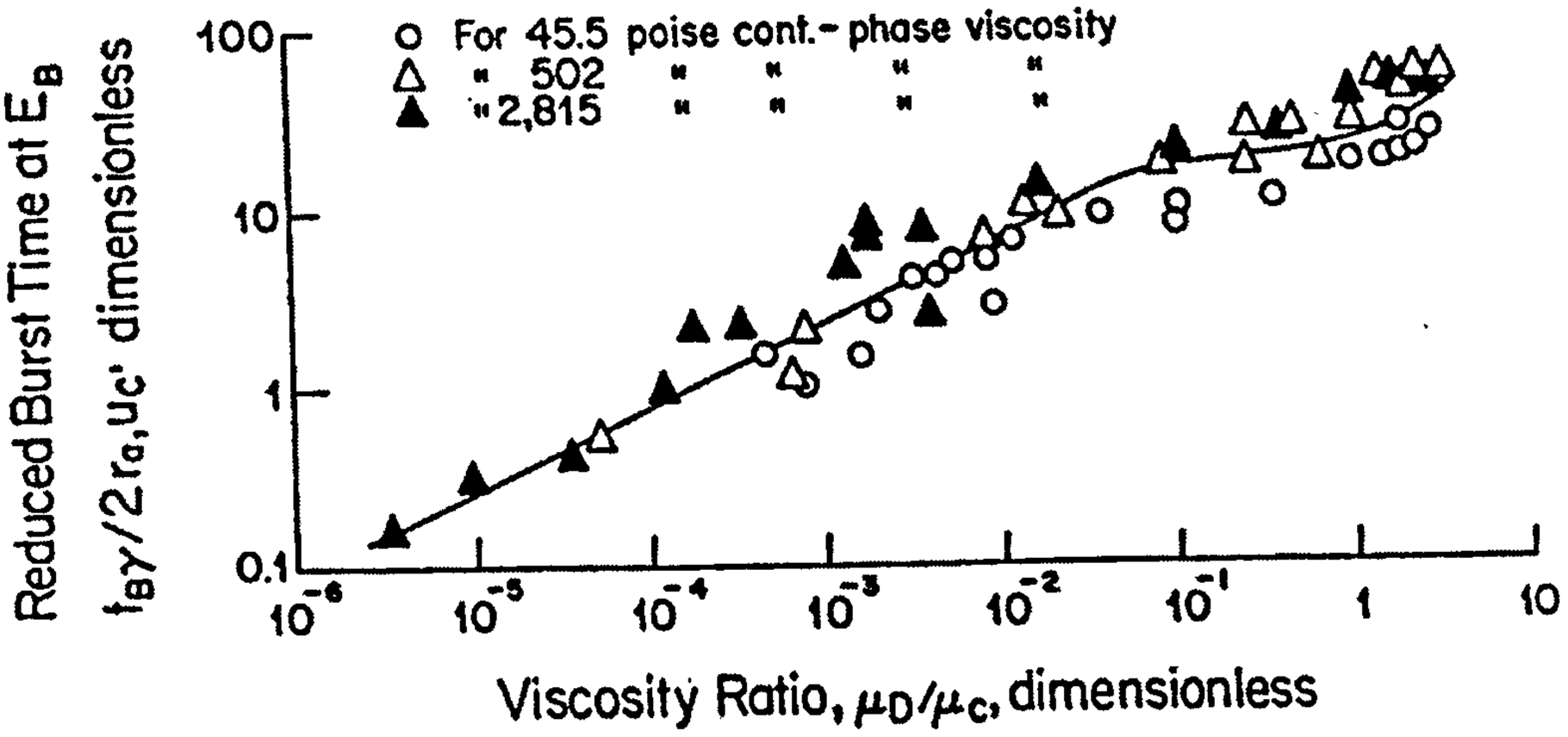

Figure 2.15 Effect of viscosity ratio on reduced burst time at E_B (Grace, 1982)

Grace discussed his results in terms of the ratio of actual shear over critical shear (E/E_B), his main findings were as follows:

1. As E/E_B is increased the drop draw ratio ($L_B/2r_d$, where L_B is the length of the drop at bursting point) increases rapidly.
2. The number of drop fragments produced is only dependant on μ_d/μ_c when E/E_B is equal to one. As E/E_B increases the number of fragments increases rapidly reaching values in the order of 10,000 fragments at E/E_B in the order of 100 and the break-up behaviour becomes much more dependant on E/E_B.
3. As E/E_B increases beyond one the reduced burst time decreases rapidly. This decrease was seen to be less than proportional to the increase in E/E_B implying that the energy input is increasing quite rapidly.
4. Exceeding the critical shear gradient results in a broader droplet size distribution.
5. Increasing E/E_B beyond approximately 4 to 10 times does not result in a significant reduction in the ratio of fragment over original drop diameter.

The last point (5) above led to the inference that to achieve a large drop size reduction, shear should be applied stage-wise, with sufficient low shear hold-up between stages to permit break-up of already deformed drops, in order to minimise energy consumption and heat generation. It was suggested that the product of shear rate and shear time should be kept constant with low shear rate and long shear time at the feed end and high shear rate and short shear time at the discharge end of a dispersion device.

Extensional (Hyperbolic) Flow

Both Grace (1982) and Karam & Bellinger (1968) found a maximum viscosity ratio (3.5 and 4 respectively) beyond which drops were not broken in simple shear flow. For this reason Grace (1982) also looked at single drop break-up in a simulated extensional shear field.

Figure 2.16 shows a plot of shear required for drop deformation and break-up, E_B, in extensional flow field versus viscosity ratio. Grace (1982) also included data points from other workers, which showed good agreement with his data.

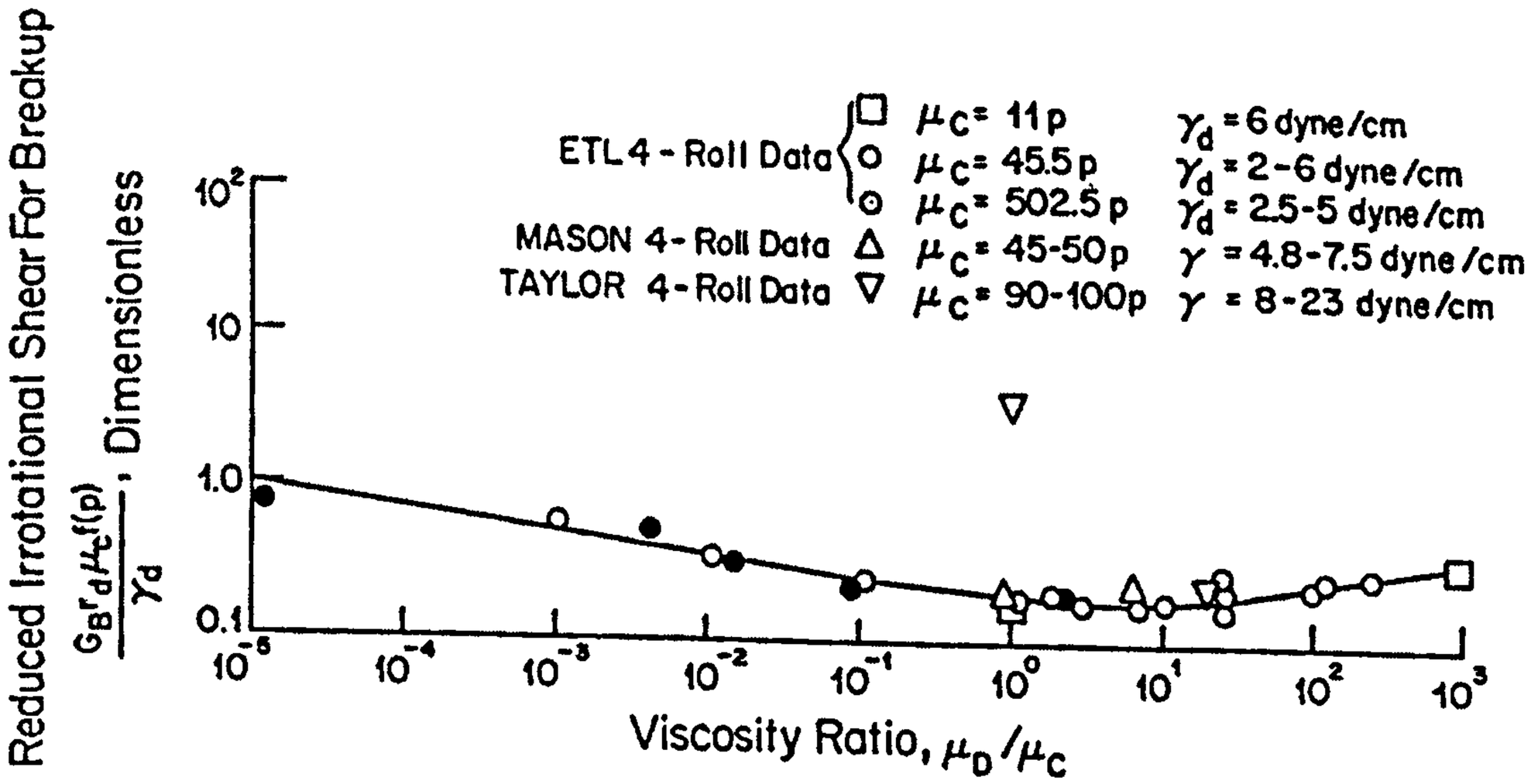

Figure 2.16 Effect of viscosity ratio on E_B in hyperbolic flow field (Grace, 1982)

It can be seen in Figure 2.16 that the curve exhibits a minimum at viscosity ratios between 1 and 5. Either side of this minimum the shear required to break up drops increases slowly with a maximum and minimum viscosity ratio in the order of 900 and 10^{-5}.

The value of shear required for drop break-up at the minimum of the curve is 0.2. This value is a third of that seen for a simple shear field (Figure 2.13) which showed a value of 0.6 at the minimum. Thus, it can be said that for equal shear rates, extensional shear is more effective for drop break-up than simple shear field (Couette), even at low viscosity ratios.

It is important to be able to determine the shear stress and shear time needed to exceed a maximum stable drop deformation for drop-break to occur in extensional flow (Figure 2.17). It is important to note that exceeding this maximum deformation does not ensure drop break-up but makes it possible with the right combination of shear stress and shear time.

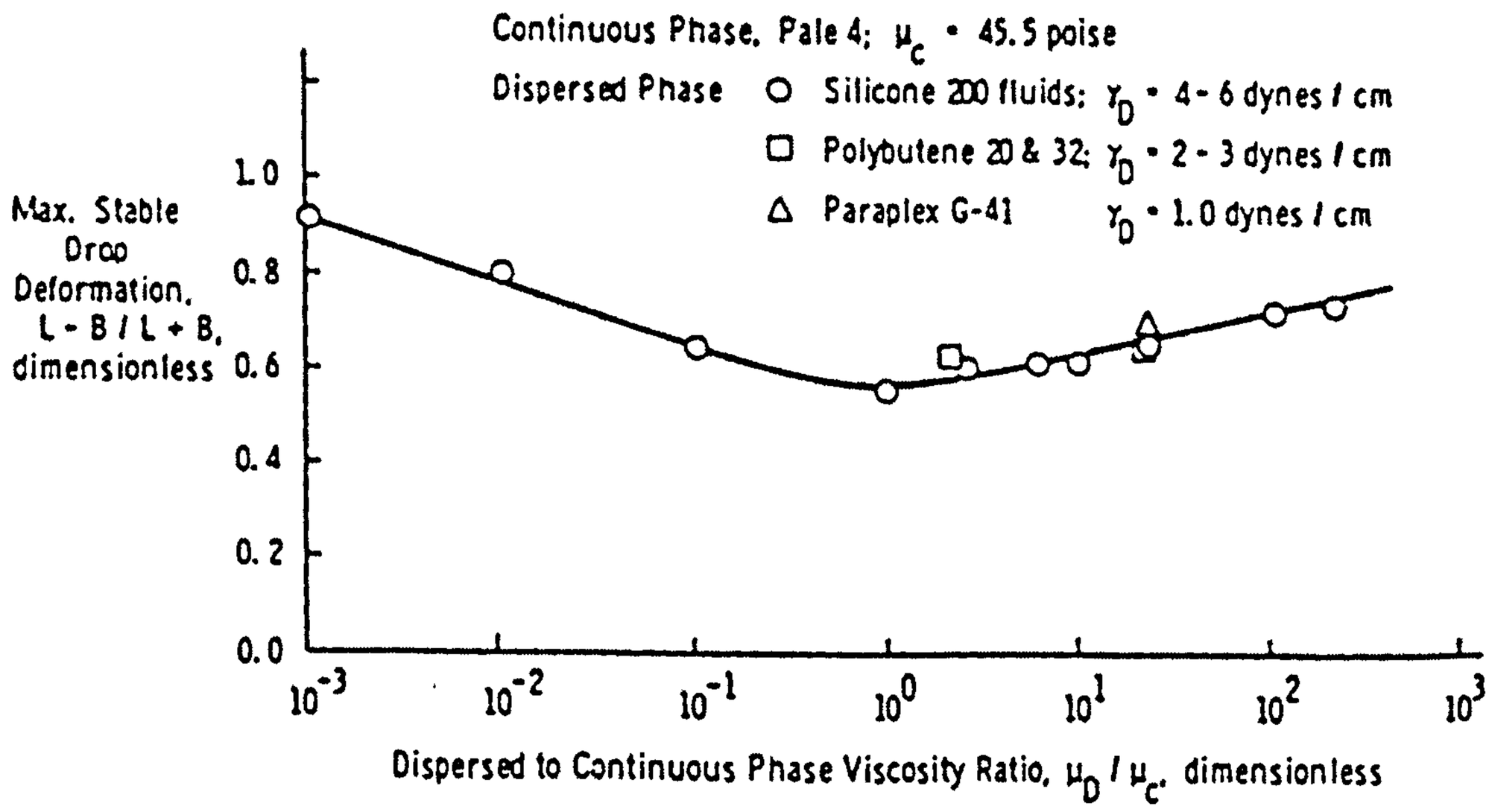

Figure 2.17 Maximum stable drop deformation in extensional shear field versus viscosity ratio (Grace, 1982).

Grace (1982) showed that a critical drop deformation existed below which the removal of shear would not result in break-up but would return the drop to its original shape. The critical drop deformation is defined in Figure 2.18. The critical deformation values are large compared with the maximum stable drop deformation (Figure 2.17).

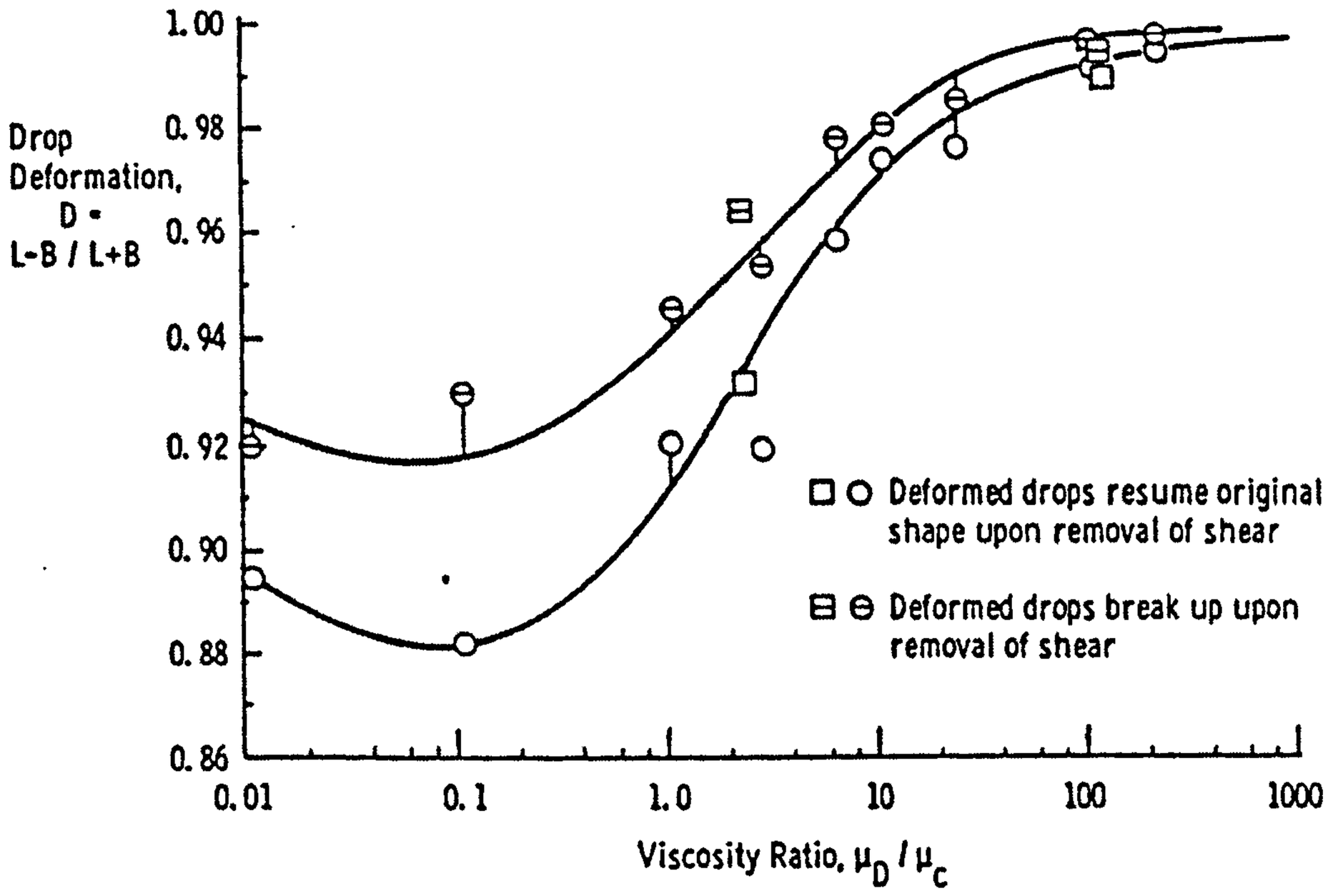

Figure 2.18 Drop deformation for burst at critical shear in extensional shear (Grace, 1982)

Figure 2.19 shows the critical burst time required to ensure break-up upon application and removal of the critical extensional shear. The critical burst time for extensional shear was shown to be similar to that for simple shear (Figure 2.15).

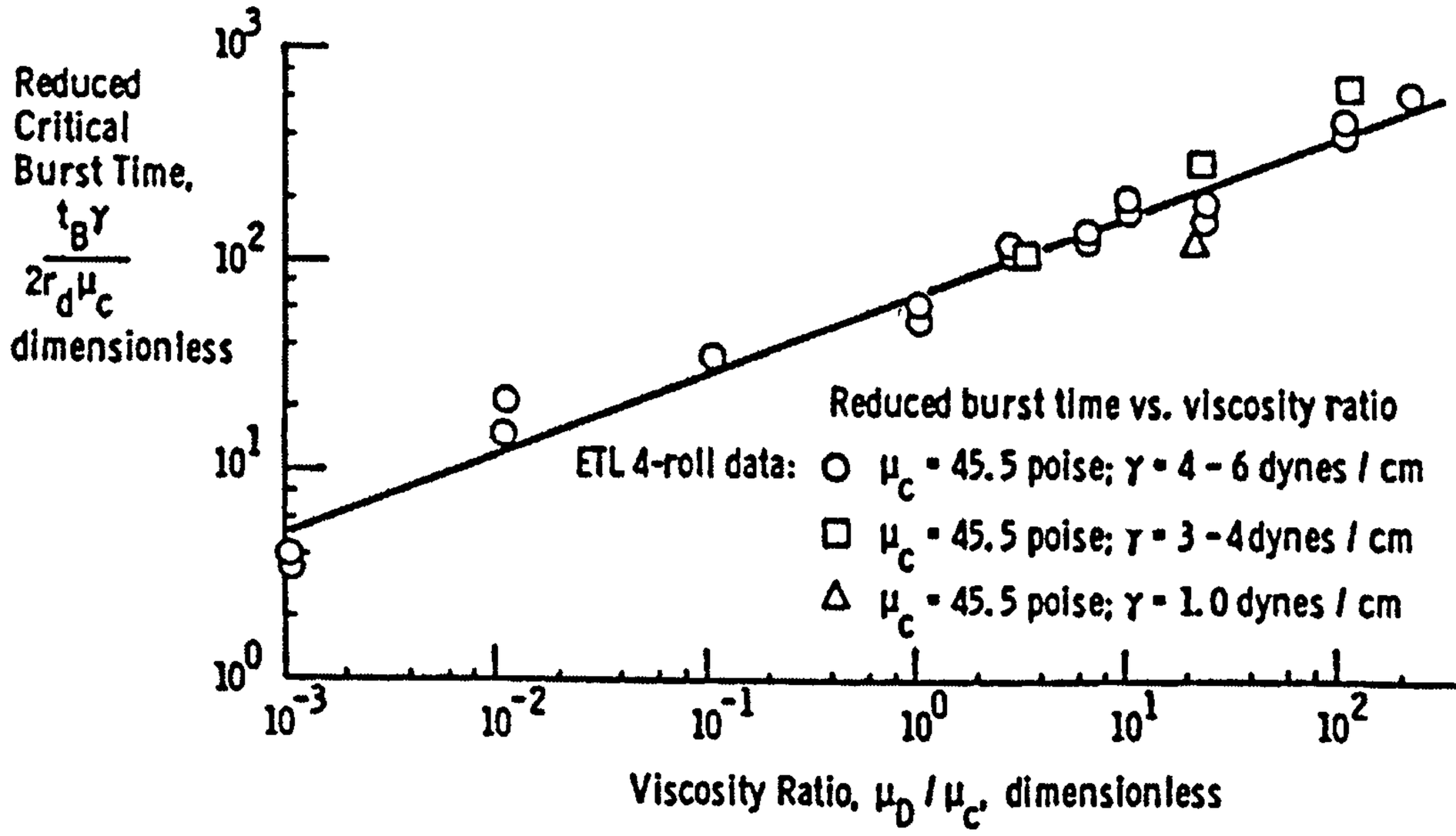

Figure 2.19 Effect of viscosity ratio on critical burst time for extensional shear (Grace, 1982)

The critical shear required for drop break-up was shown to be lower for extensional shear compared to simple shear, with equal critical burst times required. This indicated that under extensional shear field a lower total energy was required for break-up compared to simple shear conditions.

2.3.3. Drop break-up in a rotor-stator mixer

The models discussed previously (Section 2.2) have been tested extensively for liquid-liquid dispersions in stirred vessels (Tavlarides & Stamatoudis, 1981). However, their application to rotor-stator mixers has been few and far between. This section provides a review of the limited work performed on rotor-stator mixers and discusses the application of the models for the design of rotor-stators for liquid-liquid systems.

In the past, many manufacturers and operators have assumed that, due to the complex flow patterns and the high rotational speeds of the rotor-stator mixer, the device is operating within the turbulent regime. However, Levine (1994) states that this assumption is often misguided and that the machine is often operating in the laminar regime (when mixing highly viscous fluids). This may explain the discrepancies in performance of these types of mixers when scaling up from laboratory trials to full-scale production.

This reasoning highlights the importance of being able to predict whether the machine is operating in laminar or turbulent regimes. The identification of scale-up parameters that may influence the transition between the two regimes is of paramount importance to designers.

Levine (1994) went further to suggest that in turbulent flow the strong dependency of power (i.e. energy dissipation) on rotational speed leads to the deduction that volume throughputs and geometric variables would not have a significant influence on the mixing performance of the machine. Therefore, the most influential parameter when scaling-up in the turbulent regime is the rotational speed (N). This opinion is echoed by those of Kroezen and Wassink (1987), who investigated the use of rotor-stators as foam mixers. They found N to be the parameter that had the greatest effect on bubble size distribution.

In laminar flow, viscous shear would be the more prominent break-up mechanism. The longer a drop is exposed to the region of high shear the greater the likelihood of the drop elongating and splitting. Schubert (1997) found that for equal magnitudes of energy dissipation per unit volume, viscous shear caused the greatest droplet disruption. In viscous shear, break-up is controlled by the shear rate (Equation (2.23)) and the residence time in a high shear zone is dependent on the geometry of the mixer. Therefore, for the purposes of scaling up mixers that operate in the laminar regime, geometric similarity as well as rotational speed would have to be considered.

A method of determining the flow regime is to determine the dependency of the power draw of the unit on rotational speed. If the power is found to be proportional to rotational speed raised to the power of 3, then turbulent conditions will apply. If the power is related to rotational speed raised to the power of 2, then the flow will be laminar.

Averbukh et al (1988) presented the following correlation, to determine a mean droplet size in an in-line rotor-stator mixer:

$$d_{av} = C\Phi^{0.135}\left(\frac{\sigma}{\rho_c}\right)^{0.15}\frac{\nu_c^{0.7}}{\delta^{0.25}N^{0.8}Q^{0.08}} \qquad (2.44)$$

Where, Φ, is the dispersed phase volume fraction, σ is the interfacial tension, ν_c is the kinematic viscosity of the continuous phase, Q is the volume throughput, δ is the shear gap, N is the rotor speed and C is a constant determined from experiments.

The results calculated using Equation (2.31) compared favourably with experimental results. They described the unit as a centrifugal pump with a perforated ring mounted on the impeller and which rotated in a second fixed perforated ring. Experimental test were performed using three types of oil in water emulsions and also three different rotor diameters (with variable shear gaps and number of slits, and constant slot dimensions). This enabled them to quantify the effects of various physical and geometrical parameters indicated in Equation (2.42). However, it was highlighted that this correlation was applicable only within the limits of their experimental conditions. No further details of experimental work were given.

It is worth noting that the parameters show similar dependencies to the correlation derived by Chen and Middleman (1967) for drop break-up in the viscous sub-range. Equation (2.31) also includes the effects of Q, Φ and δ on the mean diameter.

2.3.4. Turbulent energy dissipation rates, ε

Schubert (1997) compared different mixers based on their energy dissipation rates, he defined the energy dissipation as the power per unit volume:

$$\varepsilon = \frac{P_{Fluid}}{V} \tag{2.45}$$

Unfortunately, a definition of the volume was not provided and it is assumed that V represents the volume of the whole mixer.

The correlations discussed in Section 2.2 all show different dependencies of ε on the system variables. Bourne and Garcias-Rosas (1986) studied the micro-mixing performance (diazo-coupling experiments) in an in-line X-20 Ystral mixer (a toothed type). They found that the product distribution decreased with rotor speed indicating an increase in turbulent energy dissipation rates.

They estimated energy dissipation rates of between 5 and 700 W/kg and correlated their data with:

$$\varepsilon = 4\times10^{-10} N^3 \tag{2.46}$$

Sparks (1996) assumed that the power was supplied to the fluid in a small region of the rotor-stator (that included the rotor and stator teeth and the shear gap). He further assumed that a proportion, a third of this power was dissipated through turbulence. This estimation for the turbulence energy dissipation was considered a conservative guess compared to the values quoted for static mixers (80%). However, it was deemed reasonable due to the extra frictional losses that may arise from the larger surface area in a rotor-stator mixer.

Values in the order 1 kW/kg were quoted for the mixer as a whole. If the above assumptions were made and the volume of the rotor-stator region was considered this value increased by 5 times.

However, values for turbulent energy dissipation rates were also estimated from Diazo-coupling experiments and only a small proportion of the power supplied to the fluid by the rotor in the rotor-stator region was found to be dissipated as turbulent energy. It was suggested that bypassing occurred through the rotor-stator region, resulting in significant in-homogeneity in the turbulence field.

This agrees with findings by Kroezen & Wassink (1987) who used a rotor-stator mixer for producing foams (gas-liquid dispersions, with dispersed phase concentrations greater than 50%). They reported that the shear rate was highest during rotor-stator interaction, and for longer residence times, an equilibrium bubble size was obtained.

Sparks (1996) proposed two methods of ensuring that a higher proportion of fluid experienced the higher dissipation rates. Firstly, the rotor-stator can be designed to reduce the inhomogeneity. The Silverson design that was used had a lower nominal radial velocity than the toothed designs, which may have reduced short-circuiting. Secondly, the process fluid can be recycled through the device, in semi-batch mode (Figure 2.2). A multi-stage rotor-stator mixer (discussed in Section 2.1.2) is an alternative way of implementing the second solution.

Pedrocchi & Widmer (1989) found that up to 50 passes through the rotor-stator unit was required to reach an equilibrium drop size distribution. The number of passes will be dependent on the design of the mixer and also the physical properties of the liquid-liquid system being used. A degree of caution is advised when operating in this mode, as continual recirculation would result in a temperature rise, which would effect the physical properties of the fluids involved.

2.3.5. Energy dissipation and droplet size

It is desirable to be able to provide the minimum amount of energy needed to form a stable emulsion with desired characteristics. Power is the principle operating cost for any agitation system.

It can be observed from the models discussed previously that in the generation of dispersions the principle parameter that can be varied to influence the final dispersion properties is total energy input. The mean drop diameter can be related to the energy dissipation by Equation (2.47):

$$d_{mean} \propto \varepsilon^{-b} \tag{2.47}$$

The constant b is dependent on the mixer geometry (stator design). Values of b for rotor-stator mixers were evaluated to be between –0.54 to –0.76 (Pedrocchi & Widmer, 1988) and –0.2 to -0.4 in turbulent flow (Schubert, 1997).

According to the Kolmogorov-Hinze theory the exponent b should be –0.4 (Equation 2.13), which is close to the values quoted by Schubert. Unfortunately neither author provides any further details of the stator dimensions and design or reasons as to why the values differ from those according to the theory of Kolmogorov-Hinze.

Calabrese et al (2000) found the value for exponent b to be –0.48, which is close to -0.5 from the Shinnar model for break-up due to viscous sub-range eddies (Equation (2.25)). They also found that their mean drop size data correlation, Equation (2.35), closely matched Equation (2.22), (Chen and Middleman, 1967). Consequently, they suggested that the break-up mechanisms for drop diameters near λ_k were due to eddies in the inertial sub-range or viscous sub-range.

$$\frac{d_{32}}{D} = 0.040We^{-0.58} \tag{2.48}$$

It must be noted, however, that the work performed by Pedrocchi and Widmer (1988) and Calabrese et al (2000) were done using a laboratory scale batch rotor-stator mixers.

Saadevandi & Zakin (1996) studied the affect of mixing intensity and time on the mean droplet size. It was observed that for a given time, an increase in mixing intensity produces a smaller mean droplet size. However, it was also observed that beyond a critical energy input the mean droplet size started to increase. An explanation for this phenomenon was not given. However, it is possible that an increase in turbulent energy dissipation would increase the probability of drops colliding and coalescing. Another factor to consider is that as drops become smaller, the total concentration of drops within a dispersion increases (i.e. greater surface area), this would also increase the likelihood of collision.

2.3.6. Turbulent break-up in the shear gap

It is commonly believed that the power dissipated in the shear gap is responsible for drop break-up. Pedrocchi and Widmer (1988) and later Calabrese et al (2000), found that varying the dimension of the shear gap (width and height) had little affect on the volume specific energy dissipation and droplet size. Both workers argued that the geometry of the inlet and the outlet of the shear gap had a greater affect on ε and drop size. Calabrese et al (2000) postulated that the stator holes (slots) and the resulting turbulent jets were mainly responsible for drop break-up.

It was suggested that only a small percentage of the total energy input was dissipated in the shear gap and the assumption of isotropic turbulent flow is only fulfilled locally in the mixer.

Bourne and Garcias-Rosas (1986) looked at rotor-stator mixers for rapid micromixing. They performed diazo-coupling experiments and found that removal of the stator had little or no effect on the product distribution. Two possible explanations were given for this observation. Firstly, it is possible that the turbulent energy dissipation rate in the

shear gap and the stator region were not significantly higher than in the rotor region. Alternatively, the reaction may have been complete before the shear gap and stator was reached. The findings of Calabrese et al (2000) and Pedrocchi and Widmer (1988) would favour the former explanation.

2.4. Power consumption in a rotor-stator mixer

In-line rotor-stator mixers are analogous to centrifugal pumps and an in-line rotor-stator mixer is often referred to as an inefficient pump. Nikiforov et al (1990), modified a centrifugal pump by attaching two perforated rings, one fixed to the pump impeller (simulating a rotor), the other fixed permanently in the volute to emulate a stator.

Sparks (1996) identified the main differences between a rotor-stator mixer and centrifugal pump as follows:

(a) In a rotor-stator mixer the gap between the rotor and the stator, the shear gap, is very narrow. The impeller in a centrifugal pump rotates with a large clearance from the stationary volute wall.
(b) The pump impellers have swept blades to transmit momentum to the pumped fluid, while minimising separation and recirculation losses (i.e. minimise turbulence generation). The rotor in a rotor-stator mixer is not usually optimised for pumping.
(c) The volute (or impeller discharge collection region) in a rotor-stator mixer is not optimised. Pumps usually have a spiral volute to minimise head loss through gradual pressure recovery.

2.4.1. Total power supplied to fluid

Sparks (1996) presented a power balance for pumps (Stepanoff, 1957 and Anderson, 1980):

$$P_{SHAFT} = P_{PUMP} + P_{MECH} + P_{DISC} + P_{LEAK} + P_{HYDRAULIC} \qquad (2.49)$$

The individual components are discussed in the following sections.

2.4.2. Shaft power - P_{SHAFT}

This parameter is important to the designer so that the correct motor can be specified. Sparks (1996) stated that this is analogous to the shaft power in a stirred tank, which for a fully baffled stirred tank is given as (Rushton et al, 1950):

$$P_{SHAFT} = P_O \rho N^3 D^5 \tag{2.50}$$

P_O is the power number and differs with impeller type.

Sparks (1996) investigated the effect of rotor-stator design on the shaft power for toothed and Silverson design mixers, in all cases the shaft power increased with both shaft speed and flowrate. He found the exponents on N and D to be 2 and values for P_0 to be approximately 10, for all rotor-stator geometries.

The exponents on N and D were explained by the fact that the flow visualisation showed the fluid in the rotor region followed the rotor teeth, at a speed v_{tip} (=πND). Therefore, the kinetic energy of a fluid element at the rotor tip, of mass m (=ρQ), could be expressed as Equation (2.51).

$$P_{fluid} = \frac{1}{2}\pi^2 N^2 D^2 Q \tag{2.51}$$

The effect of the number of teeth on the rotor was found to have little or no effect on shaft power. The effect of stator design was also found to have little effect on shaft power.

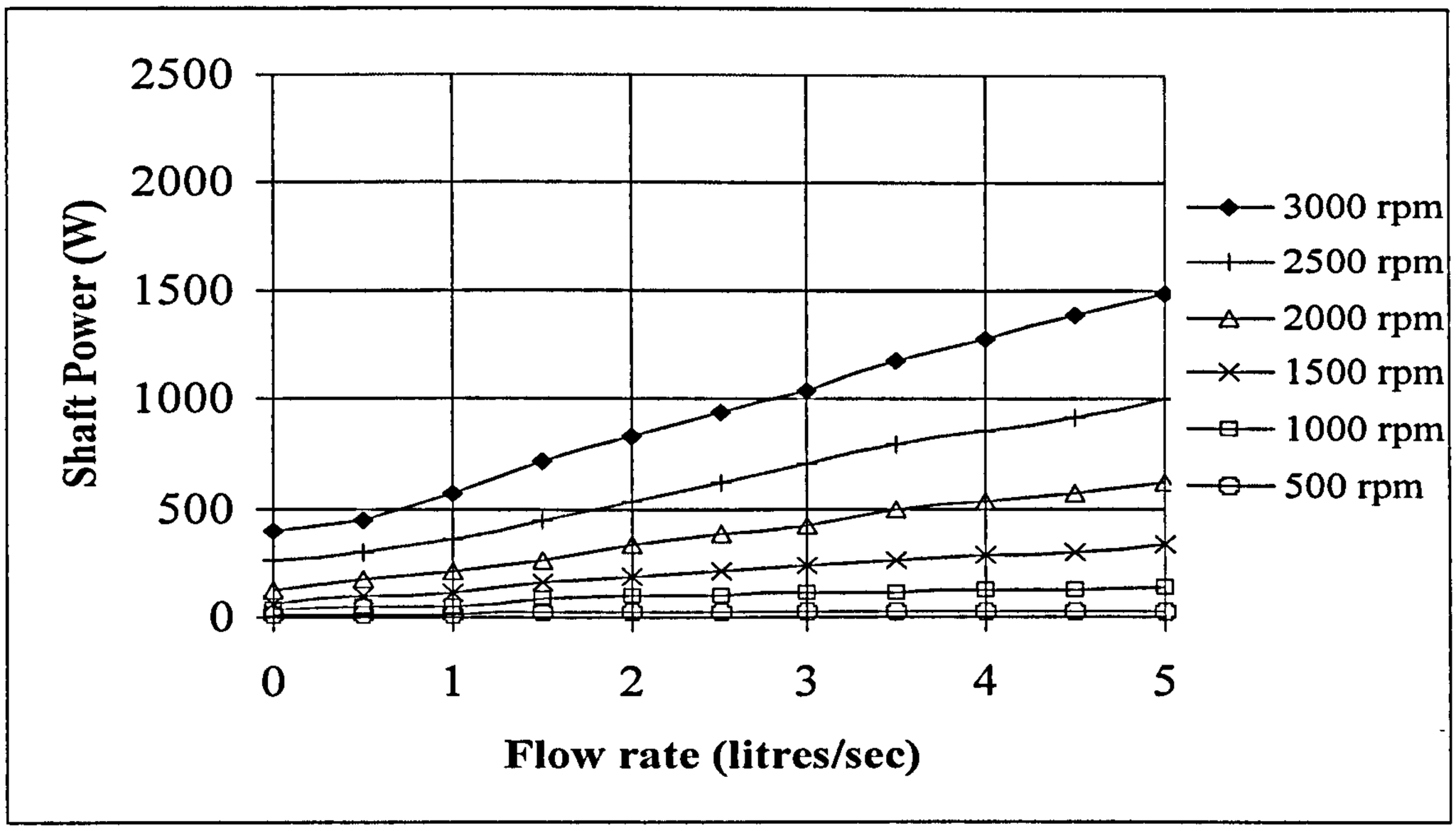

Figure 2.20 Shaft power versus flow rate for a range of shaft speeds for a Silverson mixer (Sparks, 1996)

Shaft power was determined by measuring the shaft torque and the rotational speed and calculated using:

$$P_{SHAFT} = 2\pi N\Lambda \tag{2.52}$$

Where, Λ is the shaft torque (Nm).

2.4.3. Pumping power - P_{PUMP}

A designer would require the magnitude of pumping power in order to assess whether a supplemental pump is required.

The pumping power output is defined as:

$$P_{PUMP} = Q\Delta p \tag{2.53}$$

Sparks (1996) found that the Silverson mixer had a greater pumping efficiency than the toothed designs, as the Silverson blades resembled the impeller blades in a centrifugal pump more closely.

Expectedly, the pumping efficiencies obtained from the rotor-stator mixers were low compared to that for centrifugal pumps. The rotor-stators inefficient pumping was attributed to the fact it had not been optimised for pressure recovery process.

In the rotor-stator, the flow straightening effect of the stator produces some pressure recovery. If significant pumping was required, this process does not occur without large losses, principally to turbulence and friction losses. This is because the fluid being discharged tangentially by the rotor, impacts onto and then exits the stator in a radial direction.

Sparks (1996) found the pressure recovery process to be sensitive to rotor-stator interaction as the shear gap thickness was reduced. It was suggested that if the pressure recovery step were sensitive to rotor-stator interaction then the turbulence generating process would be as well.

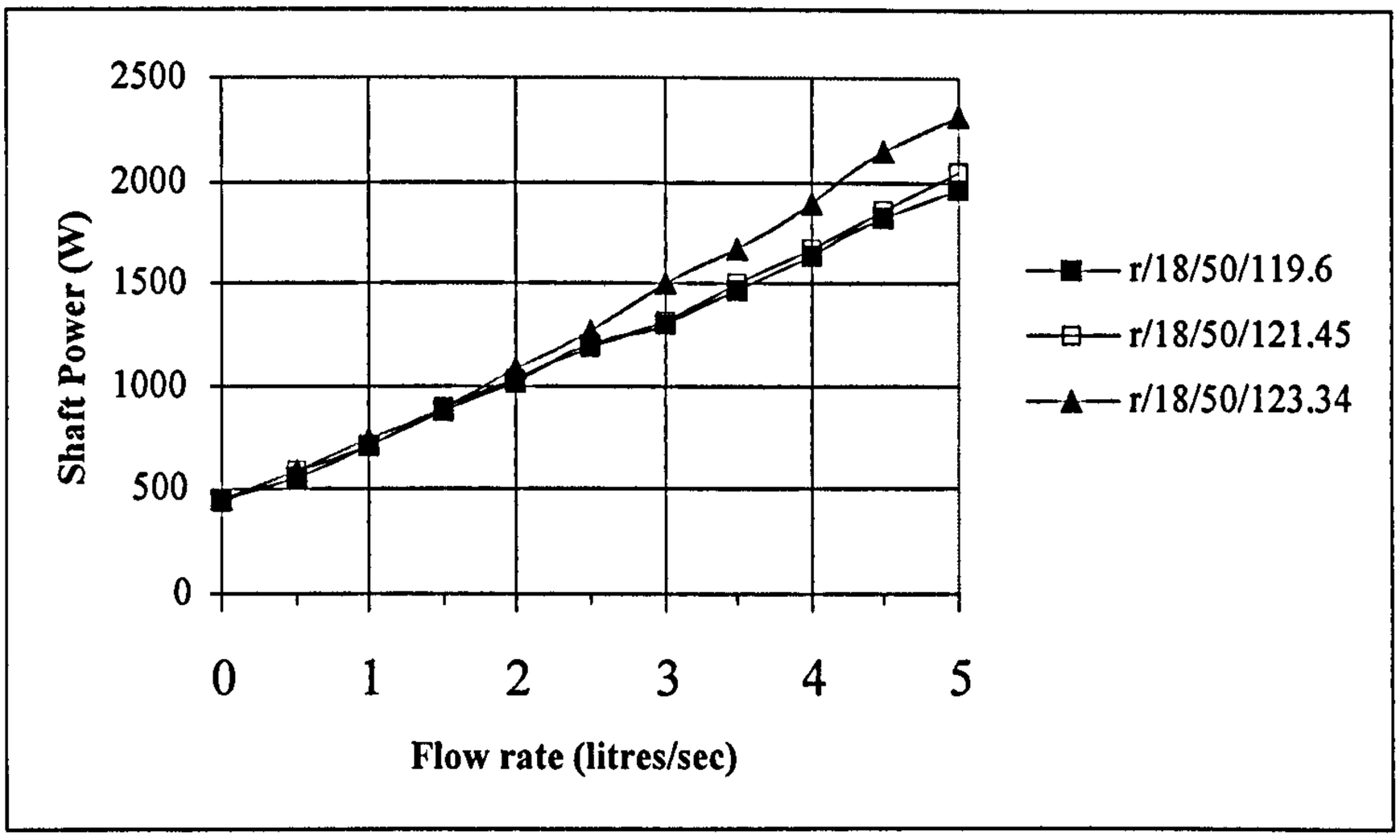

Figure 2.21 Shaft power versus flow rate for a range of shear gap thickness for a Silverson mixer (Sparks, 1996)

The effect of stator design on pumping performance was also discussed and the results from the toothed design suggested that the pumping efficiency was more dependent upon stator open area than rotor-stator interaction. The superior pumping efficiency of the Silverson mixer, which had an open area of approximately 35%, further, supported this deduction.

It was also reported that pressure recovery was affected by rotor-stator interaction significantly which also implied that turbulence and skin friction losses must be affected as well. This suggests that stators might be designed to optimise for turbulence production.

2.4.4. Mechanical losses – P_{MECH}

The mechanical losses are the losses due to friction in the seals and bearings (Stepanoff, 1957). Sparks (1996) found that the mechanical losses accounted for approximately 2.5% of the shaft power.

2.4.5. Disc friction losses – P_{DISC}

Disc friction losses are caused by the frictional drag on the solid surfaces of the rotor and are analogous to the skin friction losses in motionless mixers. These losses tend to be significant in pumps. Sparks (1996) used the following equation to predict disc friction loss (Karassik et al, 1986):

$$P_{DISC} = KN^3 D^5 \tag{2.54}$$

2.4.6. Leakage (recirculation) losses – P_{LEAK}

The leakage loss can have two meanings, firstly (and most obviously) it can refer to leakage through seals. Secondly it can mean loss due to the fluid not passing through in the right direction. For example when fluid passes back from the high-pressure (downstream) side of the impeller to the low-pressure (upstream) side.

2.4.7. Hydraulic losses – $P_{HYDRAULIC}$

Centrifugal pumps are very poor mixers (Hearn, 1992) and hydraulic losses (including turbulent losses) are very small in relation to the energy balance at or near the best efficiency point.

When considering the design of a rotor-stator mixer the rotor should be designed to increase hydraulic losses as this will increase turbulent energy dissipation. An opposite approach, to that of centrifugal pump design, should be adopted (Sparks 1996).

Sparks (1996) did not measure hydraulic and leakage losses, but instead assumed that the remainder of the power balance that was not accounted for was the hydraulic and leakage loss combined.

$$P_{LEAK} + P_{HYDRAULIC} = P_{SHAFT} - (P_{PUMP} + P_{MECH} + P_{DISC}) \tag{2.55}$$

It was found that approximately 70% of the shaft power input was dissipated through hydraulic and leakage losses.

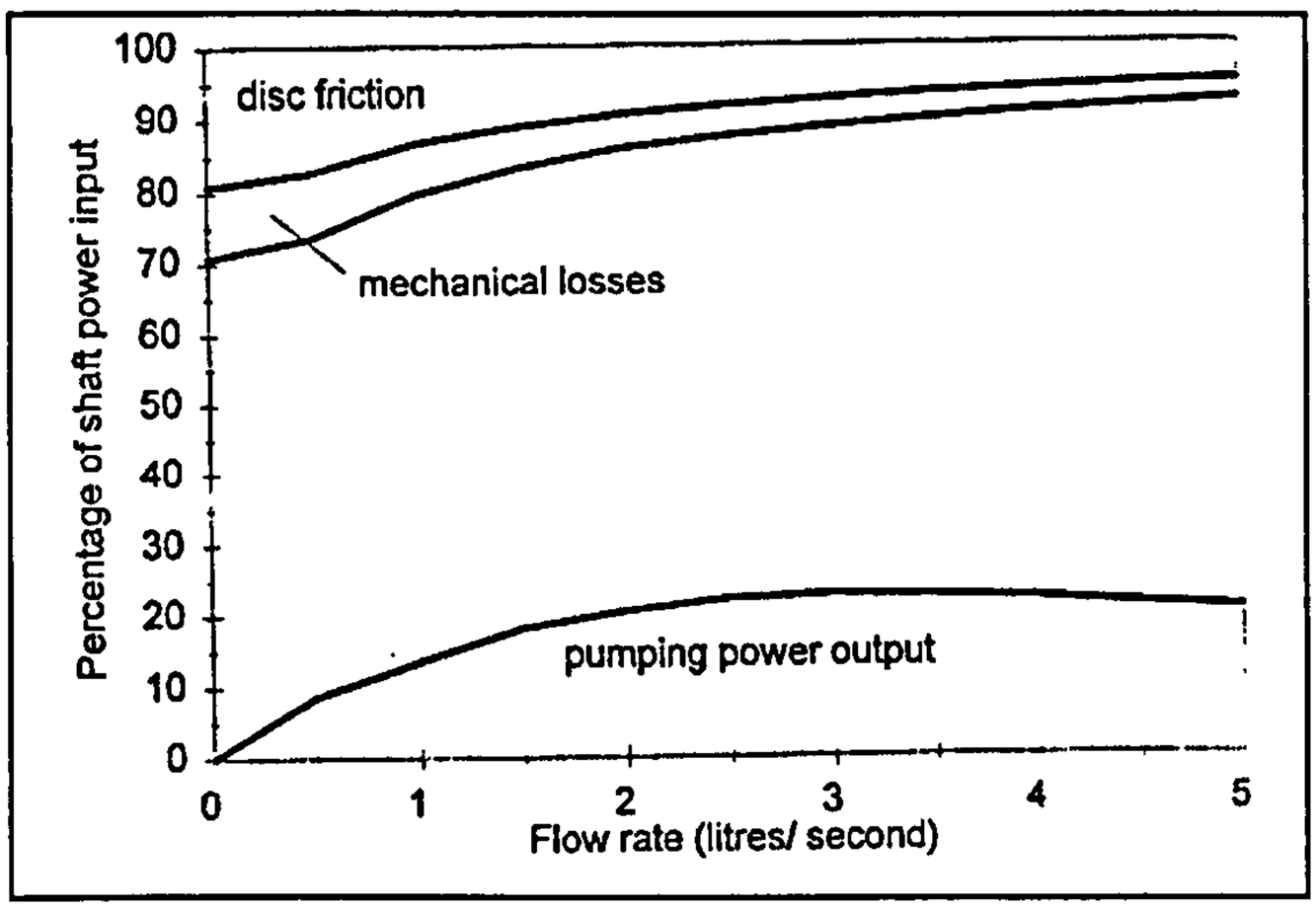

Figure 2.22 Overall power balance for a Silverson Unit (Sparks, 1996).

The energy balance (Figure 2.22) showed that the combination of hydraulic and leakage power was relatively insensitive to small changes in flowrate and appeared to be more dependant on shaft speed.

2.5. Droplet size measurement techniques

There are a number of different droplet size measurement techniques reported in literature. The following is a brief review of the ones most commonly used. The details of the measurement and sampling technique employed in this research are discussed in the next chapter.

Measurement techniques can be divided into two categories, in-line and off-line. The in-line techniques are preferred for the majority of liquid-liquid systems, as off-line techniques require the need for sampling, giving rise to problems associated with coalescence and sample disruption.

2.5.1. On-line drop size measurement techniques

The main on-line drop size measuring technique that has been reported throughout literature is image capturing (Middleman, 1974; Brown & Pitt, 1974; Chen & Libby, 1978; Pacek et al, 1994; Pacek & Nienow, 1995, Calabrese et al, 2000). Despite the popularity of this technique for use in liquid-liquid work it has a number of limitations:

- Only suitable for low dispersed phase concentrations.
- It is not suitable for opaque fluids.
- Cannot accurately measure droplets below 20 μm, this makes it inapplicable for measuring small droplet sizes ($d < \lambda_k$).
- Difficulty in getting enough light to take pictures in small diameter pipelines.
- Data acquisition is time consuming
- The results are operator dependent (as the manual measurement of drop sizes is required).

Another technique reported to have been used on-line, is the measurement of electrical conductivity, Coulter counter, (Wachtel and La Mer, 1961; Becher, 1964, Saadevandi and Zakin, 1996). The dispersion is forced through a small aperture between two electrodes and drop sizes are measured by changes in the conductivity of the continuous phase.

Drops can be measured in the range of 10 to 250 microns. However, this technique is only suitable for dilute systems to prevent blockage of the aperture and also to lower the probability of two drops passing through at the same time. This technique also requires the addition of an electrolyte to enhance conductivity, which may effect the physical properties of the system and will affect the likelihood of coalescence occurring.

2.5.2. Off-line drop size measurement techniques

There are numerous off-line techniques available. The most common are as follows:

- Light scattering (Averbukh et al, 1988): This techniques utilises the relationship between droplet size and the degree of light that each size scatters (the smaller the drop the greater the scatter). This method is simple to operate and there are instruments available on the market that can make rapid measurements over a wide size range. However, they are not suitable for opaque or concentrated systems.

- Laser diffraction (El-Hamouz et al, 1988, Pedrocchi and Widmer 1988; Streiff et al, 1997): This technique is similar to light scattering, however, the degree of diffraction is related to droplet size. The smaller the droplet the greater the diffraction. Its advantages are it is a rapid measurement device and can measure droplets from 1000μm down to sub-micron sizes. However, instruments that are currently available on the market require the need for considerable dilution. There are several commercially available instruments, the Malvern Mastersizer being the most common.

- Ultrasound: This is a relatively new technique that utilises the relationship between the attenuation of sound as a function of frequency and droplet size. It works on the principle that different sizes attenuate sound at different frequencies. This method is suitable for high dispersed phase concentrations and handles a wide size range (0.01-1000 μm) (Clements, 1996). However, due to it being a relative new technology, instruments on the market (Malvern Mastersizer) tend to be very expensive and its in-line application is still very much in the development stages.

2.5.3. Technique selection

It is apparent that research into liquid-liquid systems has been limited to dilute systems by the constraints imposed by the drop size measurement technique. The measurement technique for use in this research must incorporate the following important factors:

1. Measurement of drop sizes in the order of the Kolmogorov micro-scale and below.
2. The measurement of droplets in high dispersed phase concentrations.
3. The technique must show good repeatability.
4. Availability

The droplet sizes generated by an in-line rotor-stator mixer are expected to be too small for measurement using video techniques. Semi-in-line methods such as laser diffraction (Malvern Mastersizer) and electrical conductivity (Coulter Counter) are limited to low Φ.

However, despite it's limitations the Malvern Mastersizer (laser diffraction) is the only available technique that can successfully measure the small droplet sizes that are expected from the rotor-stator mixer (<10μm). This is the most important criterion for work with high-energy dissipation rates and the validation of mechanistic models for $d < \lambda_k$. As this technique requires considerable dilution at high Φ and is predominantly off-line, a sample has to be extracted and diluted for measurement to be possible.

The sampling procedure can be validated against an in-line video capturing technique that has been developed in-house at BHR group. A detailed description of the two techniques used in this work is given in chapter 3.

2.6. Conclusions

Rotor-stator mixers are used in a wide range of applications and are suitable for processes requiring fast disintegration, homogenisation, solubilisation, emulsification and dispersion. Despite their popularity the literature review reveals that there is a deficiency

in literature openly available specifically regarding correlations of drop size with operating parameters.

The work that has been done discusses the relationship between droplet size and energy dissipation. It has been reported that the mean drop diameter was found to be a power function of ε.

It is uncertain as to whether the assumption of isotropic turbulence is applicable in rotor-stator mixers. A limited amount of work has been done on investigating the main break-up mechanisms in a rotor-stator mixer. It has been suggested that more than one mechanism is responsible for droplet size reduction. Various definitions can be formulated for different regions in the mixer which can be used to determine where in the rotor-stator the flow exhibits turbulent or laminar characteristics.

It is widely reported that energy dissipation in the shear gap is small compared to that due to rotor-stator interactions. However, little is known about the distribution of energy dissipation within the mixer. It is clear that the rotational speed of the mixer is the main parameter that effects droplet size. This is expected, as ε is a direct function of N.

The general consensus is that scale-up should be based on energy dissipation rather than tip speed. The literature is mainly concerned with the small-scale laboratory devices. There has been little work done on industrial sized unit.

Although theories describing the forces causing and resisting break-up is simplified to inviscid dilute systems, they can be extended to high values of Φ if the system studied is non-coalescing (but still inviscid).

CHAPTER 3. Goals, Aims and Objectives

The literature review revealed that the level of understanding of liquid-liquid dispersion formation from rotor-stator mixers is not as great as for stirred tanks or static mixers. Therefore, the main aim of this project was to quantify the behaviour of an industrial sized in-line rotor-stator mixer with regards to its liquid-liquid performance. This research focused on one liquid-liquid system to isolate the influence of the geometrical and mechanical features of the mixer on droplet size. To achieve the main goal, the following objectives were specified:

(a) Design and construction of a liquid-liquid rig that incorporates suitable instrumentation and hygienic fittings for ease of cleaning.

(b) Identify and validate a suitable droplet size measurement and sampling technique.

(c) Determine the effects of rotor speed (N), flowrate (Q), rotor diameter (D), stator geometry and dispersed phase concentration (Φ) on droplet size.

(d) Ascertain the effect of stator design on the droplet size distribution

(e) Develop a technique for measuring power consumption in the rotor-stator mixer.

(f) Explore the relationship between droplet size and turbulent energy dissipation rate.

(g) Analyse the results of the experimental work and correlate the data in terms of d_{mean}.

(h) Attempt to determine the main stress mechanism responsible for drop break-up

CHAPTER 4. Experimental Equipment, Materials and Methods

In order to achieve the goals of this research, it was necessary to construct a liquid-liquid contactor rig. This rig was used to perform the dispersion tests and enabled the operating conditions to be varied easily and rapidly. This meant for a single run, a number of different conditions could be investigated.

A Malvern Mastersizer was used to measure the droplet sizes. This technique required sampling and considerable dilution. A continuous sampling arrangement was developed to overcome problems associated with extracting a sample and diluting. This sampling validation was validated against an image capturing technique.

A separate rig was set-up to perform the power measurements on the in-line rotor-stator mixer.

Details of the equipment used including the methodologies are presented in the following sections.

4.1. Experimental Rig and Instrumentation

An experimental rig was constructed to perform the tests on the in-line rotor-stator mixer (Plate 4.1). Details of the operating procedures and the names and addresses of suppliers can be found in Appendix 1 and 2 respectively. The rig design enabled the flowrates, dispersed phase concentration and rotational speed of the mixer to be varied quickly and easily to investigate their effect on the droplet size distribution.

The rig was designed by N Thapar (HILINE Consortium, BHR Group Ltd) and constructed with the help of Silverson Machines Ltd. The rig was designed with the intention that it could be used to test the performance of static mixers as well as in-line rotor-stator mixers. For this reason it had to be easily interchangeable between the two types of mixers and easy to clean.

4.1.1. Experimental Rig

A schematic diagram of the experimental rig is shown in Figure 4.1 and a general view shown in Plate 4.1. An in-line rotor-stator mixer (based on a Silverson 425 LSM unit, Appendix 2) was fitted in a flow loop between two feed tanks (aqueous and organic) and two settling/waste tanks, each with a capacity of $1m^3$.

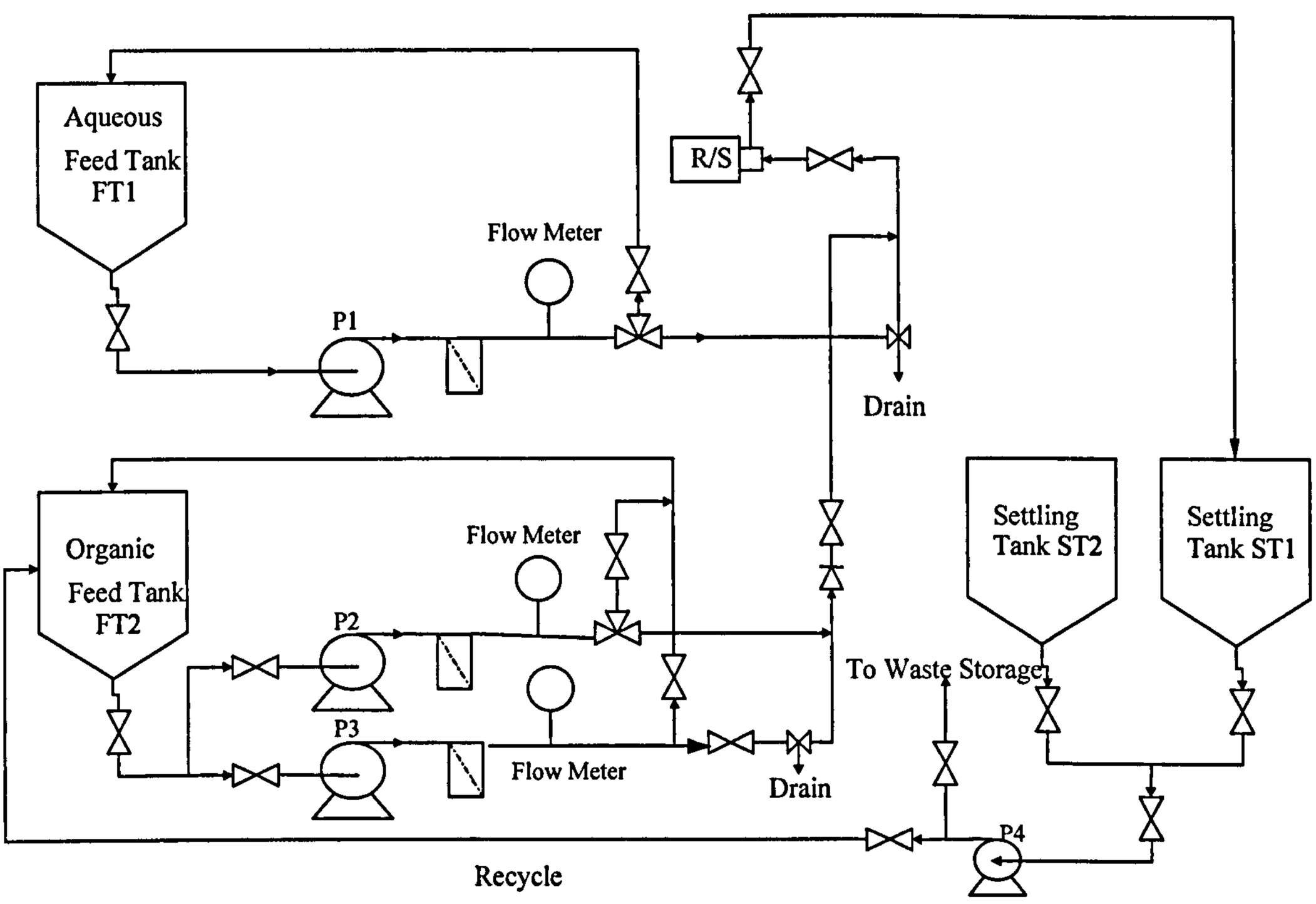

Figure 4.1 A flow diagram of the test rig

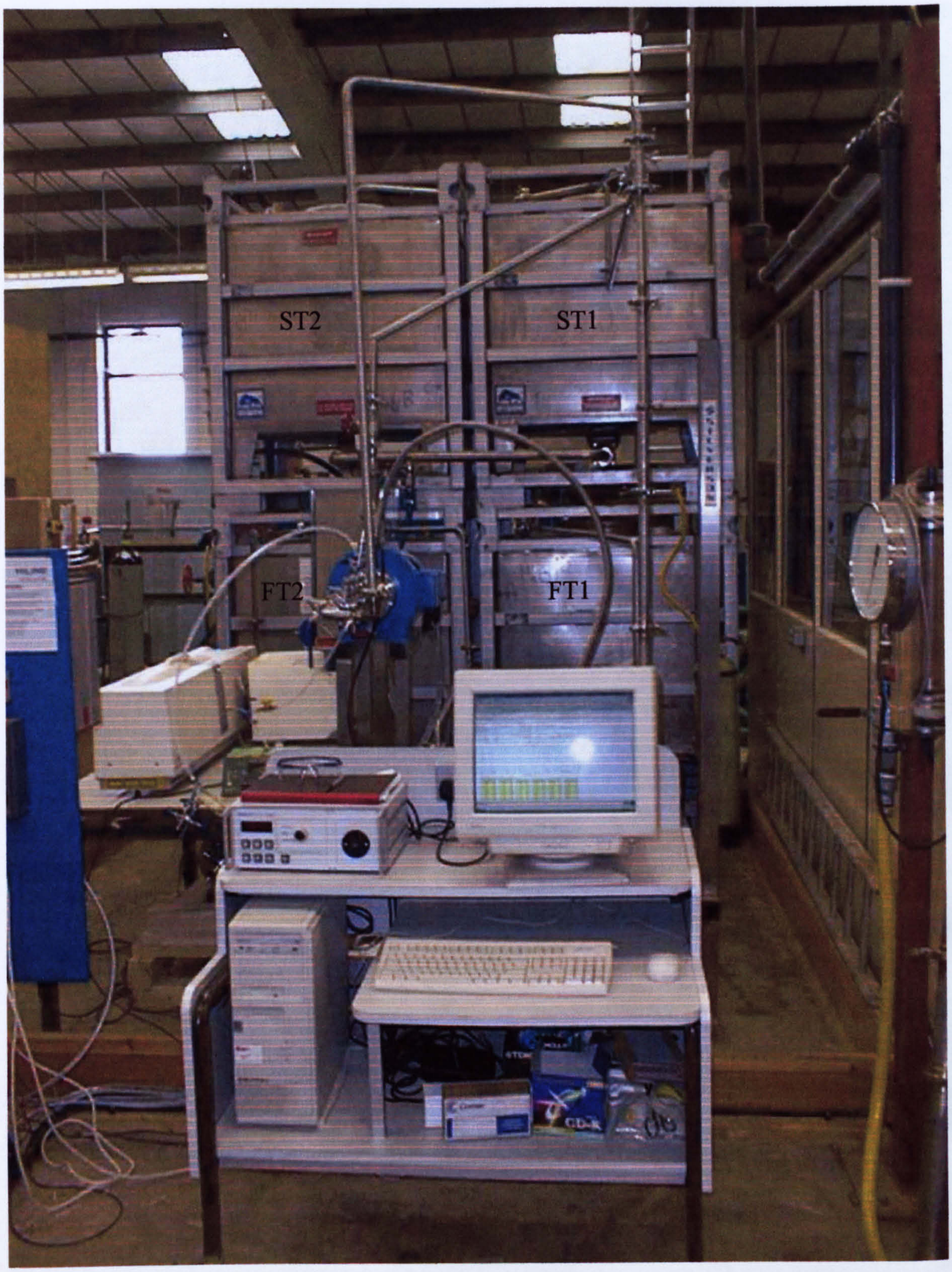

Plate 4.1 Photograph of test rig (Front View)

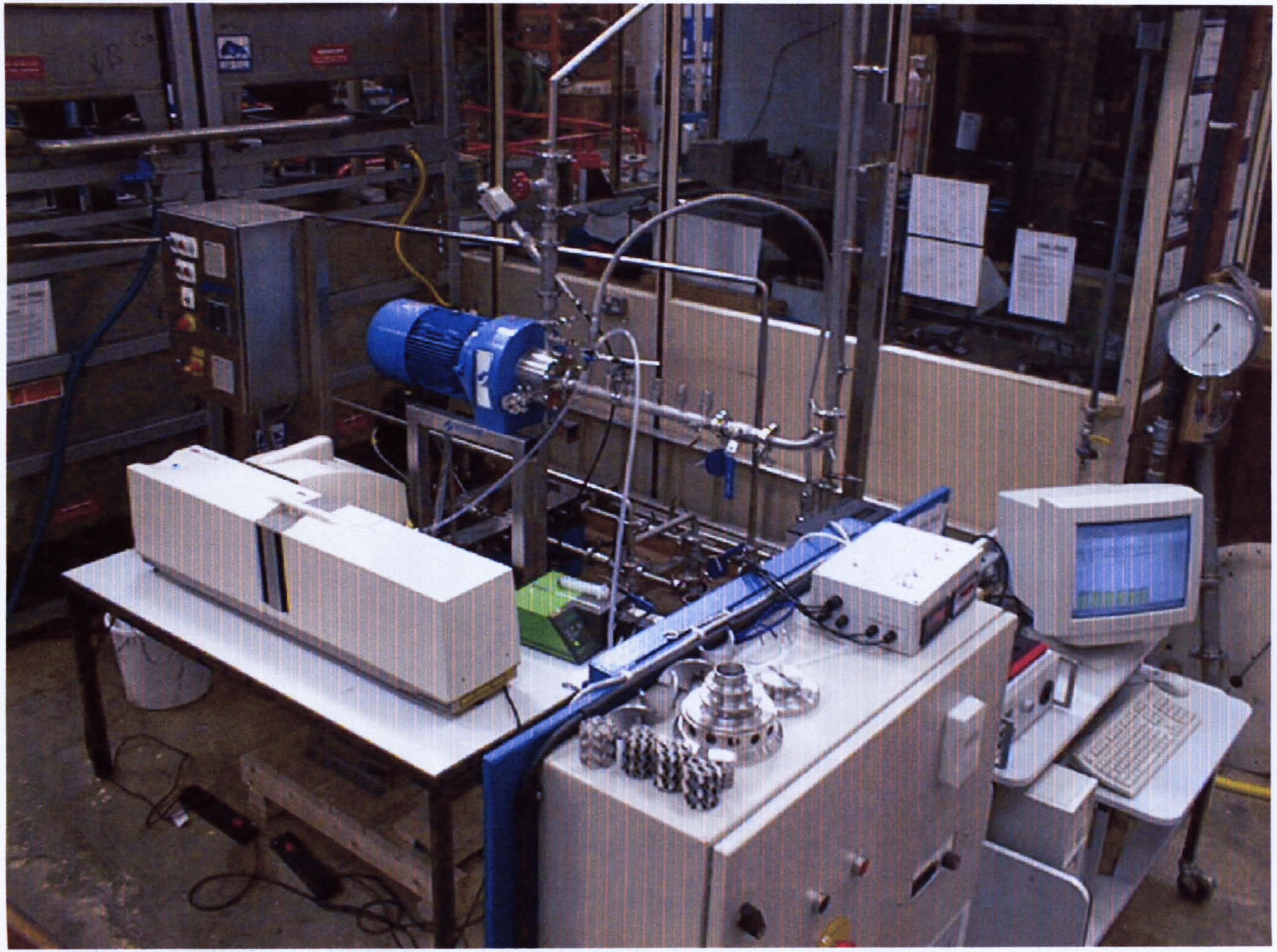

Plate 4.2 Photograph of test rig (side view)

The organic feed was introduced to the aqueous line one pipe diameter up-stream of the rotor-stator mixer via a manifold (a T-piece). Samples were extracted one pipe diameter downstream of the mixer (Section 4.4). The two liquids were supplied to the mixers using centrifugal pumps, one for the continuous phase and two (high flow and low flow) for the dispersed phase, this enabled a wide range of dispersed phase concentrations to be investigated. The pumps were controlled using a flow controller so that a number of different Φ and Q to be investigated in a single run. This enabled rapid measurements and a large quantity of drop measurements.

An inherent problem with working on industrial sized units is the waste product that is generated. The dispersed phase was allowed to settle in the settling tanks and then recycled. Any waste water was pumped into a separate storage vessel (along with waste organic phase) which was periodically emptied and taken away for incineration. This increased the cost of the operation of the rig.

4.1.2. Materials of Construction

The feed and settling tanks were constructed from stainless steel and all the pipe work was hygienic stainless steel (Outer Diameter of 25.4 mm). The fittings were hygienic tri-clover clamps. This enabled the rig to be easily dismantled for cleaning purposes. The tri-clover gaskets were made out of Medium Density Ethylene Propylene Rubber (EPDM) on the aqueous side and Viton on the organic side.

4.1.3. Flowrate and Φ control

The organic and the aqueous feeds were pumped to the in-line mixer using centrifugal pumps. The aqueous feed was pumped using a Grundfos CRN2-40 (1.5 kW) which was capable of delivering flowrates between 0.4–2.7 m^3/h. A similar pump was used on the organic feed in addition to a smaller one, Grundfos CRN8- 40 (0.55 kW) that enabled lower flowrates between 0.14-0.4 m^3/h. This resulted in a wide range of flowrates (0.14-2.7 m^3/h) on the organic line and thus a wider range of Φ.

The desired Φ was achieved by maintaining the flowrates of the organic and aqueous phases in the correct proportions. The flowrates were measured using Quadrina Q-flo turbine meters (types QBL/10B/EP1 & QEL/10B/EP1) all of which gave an error of +/- 0.5%. The flow was controlled using a feedback loop from the flow meters to the pump motor inverters via a Nixon Instrumentation digital flow controller 98RC that controlled the speed of the pumps. The flow controller was used to set the desired flowrates and to select the required organic pump.

A gate valve was placed downstream of the rotor-stator mixer to throttle its pumping effect, thus preventing cavitation and maintaining a constant flowrate. The recycle loops were present on the feed lines for use when commissioning the flow transducers and testing the pumps. The pressured difference across the mixer was measured using a Druck PTX 120/WL pressure transducer connected to fittings located 1 pipe diameter either side of the mixer.

The material in the settling tanks was left to separate for at least 24 hours before recycling the organic phase. The water phase (plus any remaining organic) was pumped out to waste.

4.1.4. Rotor-stator mixer design

Tests were performed on a Silverson 425 LS unit that incorporated a motor specially adapted to produce rotational speeds from 3000 to 12000 rpm. A Vacon inverter (CXS range) was used to drive the motor.

Four different stator designs were investigated, all of which were standard Silverson designs (Figure 4.2).

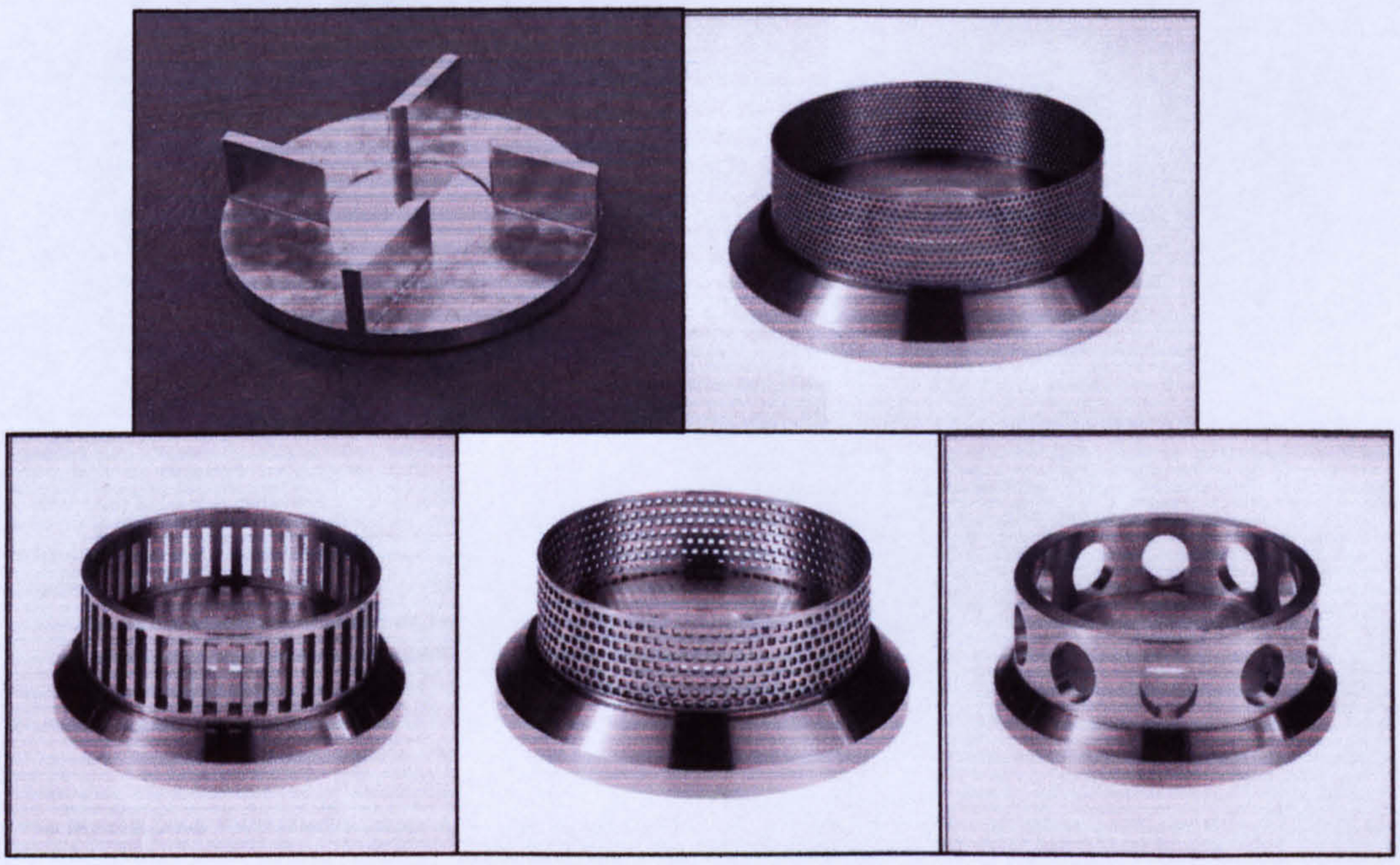

Figure 4.2 Standard Silverson rotor and stators. Clockwise from top left; Rotor; Emulsor screen; General purpose disintegrating head; Slotted Head; Square hole high shear screen.

The Square Hole High Shear Screen (SQHHSS) and the Emulsor Screen (ES) are the two favoured stator designs for liquid-liquid mixing. However, tests were also performed on the Slotted Head (SH) and the General Purpose Disintegrating Head (GPDH) to observe the effects of geometry on droplet size.

The dimensions of the various rotors and stators studied are summarised in Table 4.1. The dimensions listed all represent standard industrial scale Silverson designs. The

clearance is generally made as small as possible, within the limitations of the machinery and material used.

Table 4.1 Dimensions of the rotors and stators investigated

Rotor Size (mm)	Stator Type	Stator I.D. (mm)	Clearance (mm)	Hole/Slot size (mm)	Open Area (%)
69.85	ES	70.80	0.475	1.40	25.9
	SQHHSS	70.10	0.125	2.38	25.5
50.8	ES	51.05	0.125	1.40	31.7
	SQHHSS	51.05	0.125	2.38	31.5
	SH	51.05	0.125	11 _ 3.24	33.0
	GPDH	51.05	0.125	9.53	35.0

The volume of the volute was not changed with each rotor scale. It could be argued that this does not represent a true reflection on scale, as the liquid volume in the volute decreases as the rotor-stator size increases. However, discussions presented in Section 2 suggested that the area of maximum energy dissipation might be in the rotor-stator region. The differences in the volume were small and consequently the affect of these differences on the flow in the volute would also be small.

4.2. Experimental materials

4.2.1. Immiscible liquids

Odourless kerosene, marketed as Alcosol D70, was used as the organic (dispersed) phase. This material is kerosene (C11-C12 hydrocarbon) with all its light aromatic constituents removed, (the name and address of the supplier, Alcohols Limited, can be found in Appendix 2). The main reasons behind this selection are that it is relatively cheap and safe.

The sensitivity of liquid-liquid systems to impurities dictated the quality of the continuous phase to be as pure as possible. For this reason the liquid-liquid rig utilised de-ionised water. Table 4.2 lists the physical properties of Alcosol D70 and water.

Table 4.2 Physical properties of Alcosol D70 and water

	Kerosene	Water
Viscosity (kg/ms)	0.002	0.001
Density (kg/m^3)	800	1000
Interfacial Tension (Portingell, 1989)	0.046 N/m	
Absorption (Malvern, 1997)	0.001	-
Refractive Index (Malvern, 1997)	1.435	1.33

The viscosity of the kerosene was measured using a bob and cup type rheometer (Contraves Rheomoat 115). The value in Table 4.2 corresponds to a shear rate of $5s^{-1}$ at 20°C. The temperature rise from a single pass through an in-line rotor-stator mixer was very small (typically in the order of 10^{-3} °C). The viscosity of water, from steam tables,

decreases from 0.001 kg/ms at 20°C to 0.009 kg/ms at 25°C. Therefore it was assumed that the instantaneous effect on heating on the viscosity of the two liquids was negligible.

The interfacial tension between kerosene and water was evaluated using the pendant drop method, (Portingell, 1989). This was measured each time fresh fluids were added to the test rig. Also, spot checks were performed on material that was recycled. The interfacial tension did not vary more than 5% over the course of the experiments.

4.2.2. Kerosene-Water Stability

Some initial bench top experiments were performed to investigate the stability of the kerosene/water dispersion. These experiments were performed in a glass vessel fitted with a six blade Rushton turbine (the impeller speed being the equivalent of rotor speed) using relatively small volumes of dispersion in order to ensure a high power per unit volume.

The dispersion was generated using a vessel (5.43 litre) fitted with a six bladed Rushton turbine (Figure 4.3) with a rotational speed of 1000 rpm.

A range of dispersed phase concentrations were investigated (0.05 - 5%). The experiments were performed in a water bath and were run for 60 minutes to ensure droplet size equilibrium had been attained.

Samples were extracted from the vessel and placed onto glass slides and viewed under a microscope. Various sampling strategies were employed to assess their effects on the droplet size distribution.

A plastic 10 ml pipette with the end chopped off to increase the diameter of the tube was used to extract samples to observe any differences in droplet size distribution. A syringe was also used with some 2mm Marprene tubing attached. The length of time the sample

remained in the pipette was also varied. This would give an idea of the effects of sampling time on the droplet size distributions.

The results of these experiments were then used to develop a continuous sampling technique on the main liquid-liquid rig. The results and observation of these tests are discussed in Chapter 6.

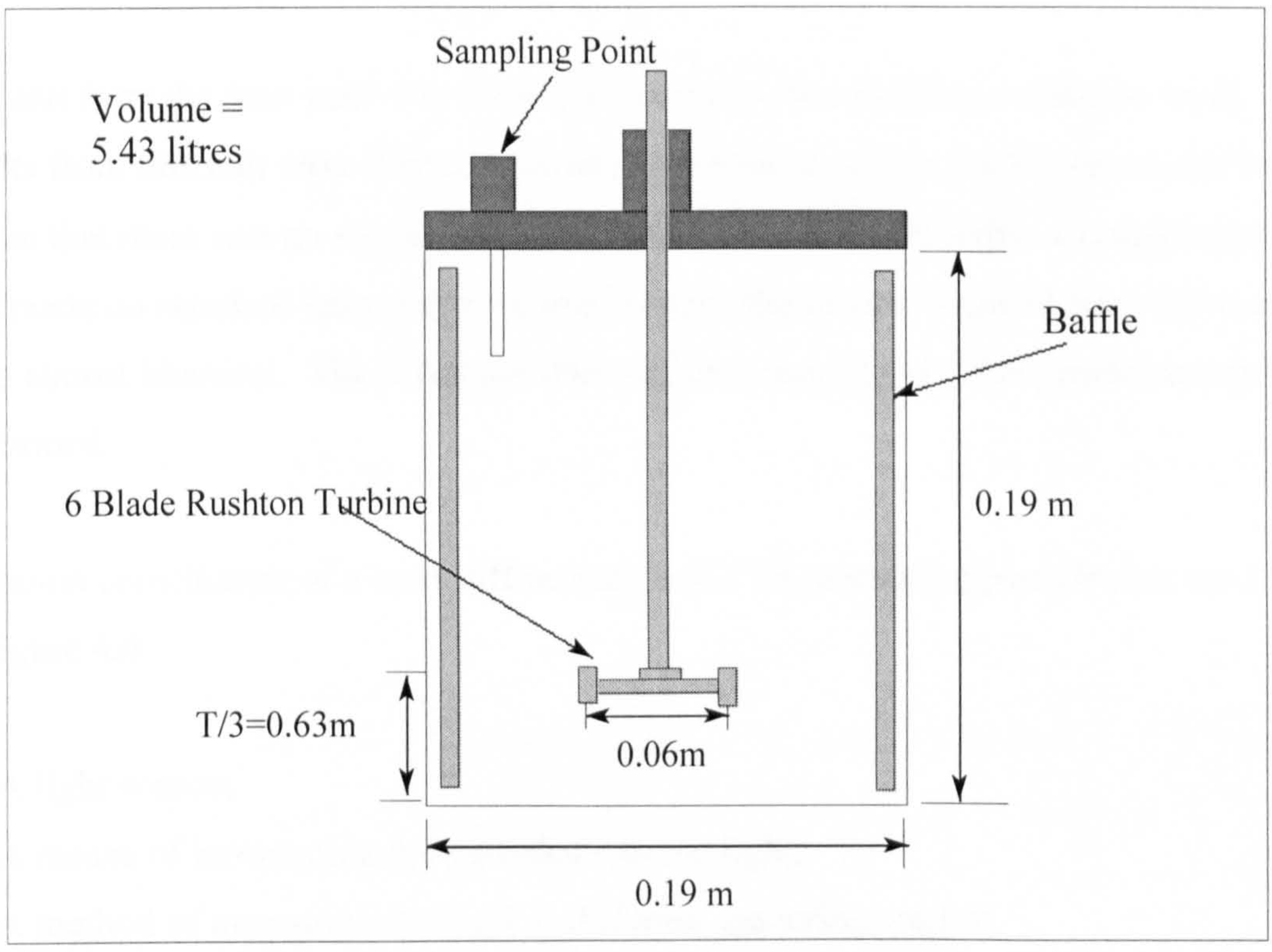

Figure 4.3 Stirred vessel used to create dispersions

4.3. Droplet Size Measurement

4.3.1. Malvern Mastersizer

A brief description of the principles of laser diffraction is given in Appendix 3. In this section the various elements that make up a practical unit are discussed and the general operation is explained.

The Malvern Mastersizer was selected to measure the droplet size distributions from the in-line rotor-stator mixer. A Mastersizer 2000 was used in this research which was supplied courtesy of Silverson Machines and also the EPSRC Loan Pool, (Appendix 2).

The unit from the loan pool was used extensively in the sampling validation work. The results from this unit were then compared (for a similar run) to the Silverson unit to ensure that there was no significant differences in the different units. Comparisons were also made on standard latex particles and between the results obtained from the two units were almost identical. The Silverson unit was then used for all of the performance tests performed.

The main constituents of a laser diffraction device for measuring particle size are shown in Figure 4.4:

(a) A light source;
(b) A means of introducing the particles into the light;
(c) A method of measuring the light at different scattering angles;
(d) A method of converting the scatter pattern to a size distribution.

The Mastersizer can be broken down into three constituents, the optical unit; sampling unit and the computer system. The optical unit is used to collect raw data that is then processed by the software in the computer to give drop sizes. The sample accessories are used to prepare the sample and transfer it to the optical unit

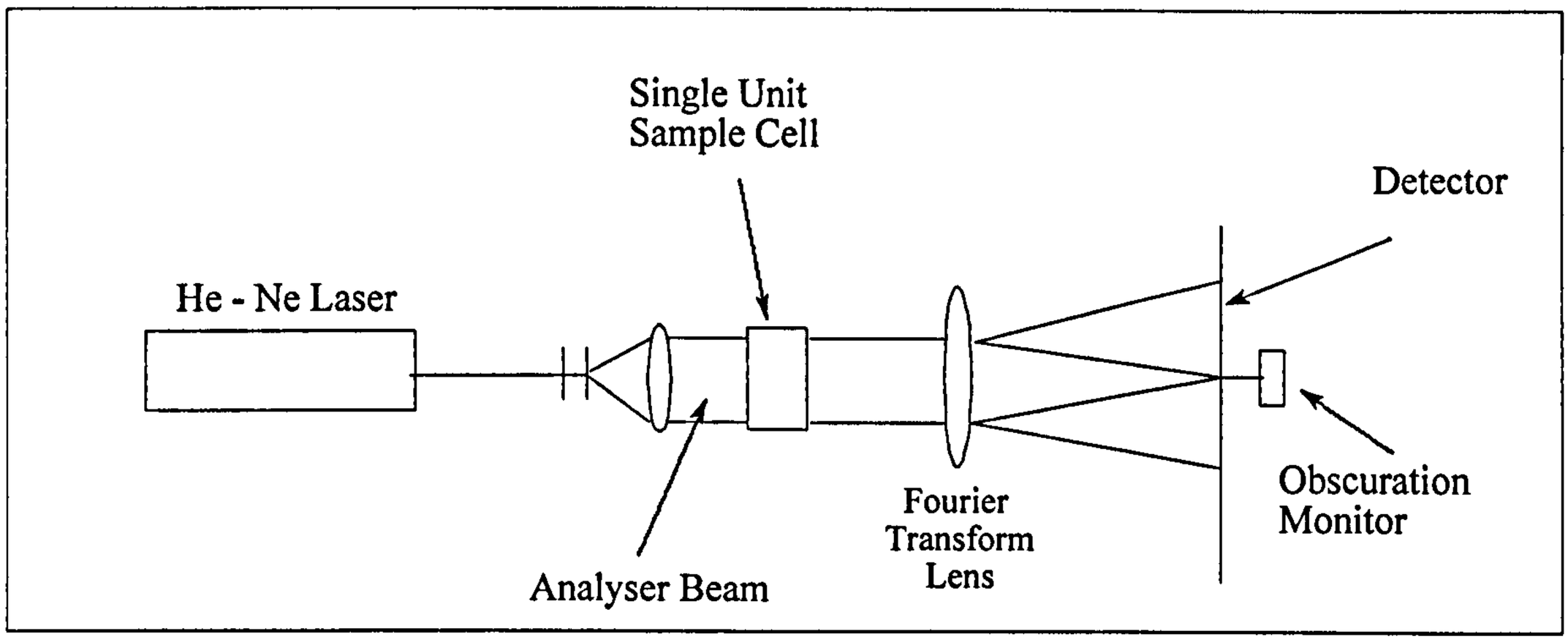

Figure 4.4 A Schematic diagram of a Malvern Mastersizer

The optical unit incorporates three modules that correspond to points (a) - (c) mentioned above:

The Transmitter

The transmitter contains the laser and electronics that generate the laser beam. The Mastersizer uses a Helium-Neon laser to provide a monochromatic light source. The laser beam is passed through a processing unit that comprises of a spatial filter and a beam expander that produces an extended and collimated beam. The expanded beam is then transmitted through the sample cell.

The Sample Cell

The sample area is located between the transmitter and the receiver and is where the laser is passed through the sample. The Mastersizer is supplied with various sampling accessories that allow it to measure both wet and dry samples. The accessories are designed to prepare and deliver the sample to the optical unit for measurement.

The accessory that came with the Mastersizer 2000 was the Hydro 2000G. The Hydro 2000G has a 1 litre vessel that contains a stirrer (to keep the sample in suspension) and a pump that supplies the flow cell with sample. However, a continuous dilution technique, Section 4.4, was developed that avoided the need for this accessory and the Hydro 2000G was only used for cleaning purposes (flushing the cell) and not for introducing the sample to the cell.

A schematic diagram of the flow cell and the Hydro 2000G arrangement is shown in Figure 4.5. During the measurement process V2 was closed and V1 was opened to allow the diluted sample through the flow cell. After the sample had passed through the flow cell it was directed straight to waste by keeping V3 open.

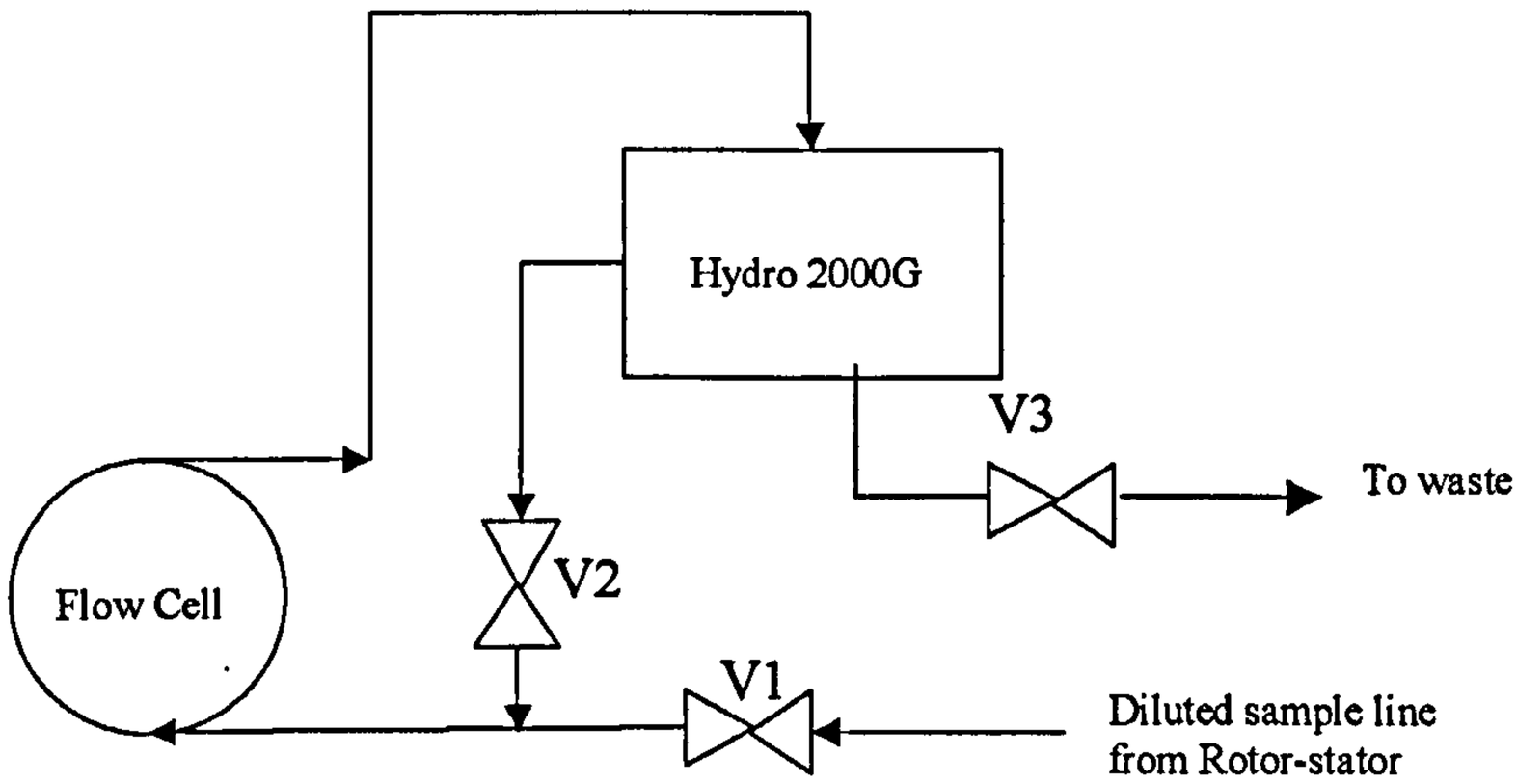

Figure 4.5 A schematic diagram of the flow cell and Hydro 2000G arrangement

Once the measurement was complete, V1 and V3 were closed and V2 was opened and the Hydro 2000G was filled with de-ionised water. The water was then recirculated through the flow cell using the Hydro 2000G pump.

The cleanliness of the cell was monitored using the background reading on the Mastersizer. The cell was flushed through twice after every measurement. If the background readings were too high even after flushing, the cell was taken apart and left to soak in 5% detergent solution (Decon 75) for 2 hours. After 2 hours the cell was flushed thoroughly firstly with warm water and then with de-ionised water, to ensure all of the detergent was removed.

The Receiver

The receiver collects and stores the information received from the diffracted laser light and its main components are a Fourier lens, detector and an obscuration monitor.

The diffracted light is intercepted by the Fourier lens, which maps the scattered light from particles of the same size into a common spatial position in the focal plane. The detector is located in the focal plane and consists of a number of photo-diode elements arranged in a radial pattern. Each of these elements is positioned to correspond to a specific scattering angle. The Fourier lens enables light scattered by a particle to fall on the same part of the detector for as long as the particle is in the laser beam, independent of its position in the laser beam. This makes it possible to measure the intensity of light diffracted by particles of the same size and de-convolute this data to produce a size distribution.

To ensure that the detector takes a representative reading of the scattering pattern the Mastersizer takes over 2000 snaps for each measurement with each snap taking 1 millisecond.

The obscuration monitor is used to measure the amount of laser light lost due to the introduction of the sample into the analyser beam. If there are no particles in the laser

beam, all the light falls onto the obscuration detector. As particles are introduced into the laser beam, they block this light and scatter light onto the detector elements. The obscuration is the ratio of the intensity of the incident light with no sample to that with sample and is used to monitor the concentration of the particle. It is an important parameter as it allows the operator to control the concentration of the sample, as too many particles would result in multiple scattering and therefore erroneous size data.

The collected data is then sent to the computer for analysis. The Mastersizer uses Lorenz-Mie theory to predict the droplet size distribution from scattering intensities. The Mastersizer collects a scatter pattern from a sample and then constructs a rough droplet size distribution. Lorenz-Mie theory is then applied to convert this distribution back to a scattering pattern. The predicted pattern is then compared to the original pattern and if it is a close fit the corresponding particle sizes are accepted. If the comparison is not a good one then the Mastersizer repeats the process until the closest fit is found.

The accuracy of the fit between measured and calculated data is given by the residual, a value less then 1% denoting a good fit. If the residual is greater than 1% then this is a good indication that the correct refractive indices and absorption values have not been used.

4.3.2. Video Probe

The sampling strategy was validated against an in-line image capturing technique that incorporated a video probe that was inserted into the outlet pipe of the rotor-stator mixer.

The ability to measure the droplet sizes on-line enabled a comparison to be made with the off-line measurement technique. It was then possible to determine whether the sampling and dilution technique affected droplet size distribution. However, before being able to make these comparisons an appreciation of the differences between the two techniques had to be gained first. This was done measuring standard latex particles.

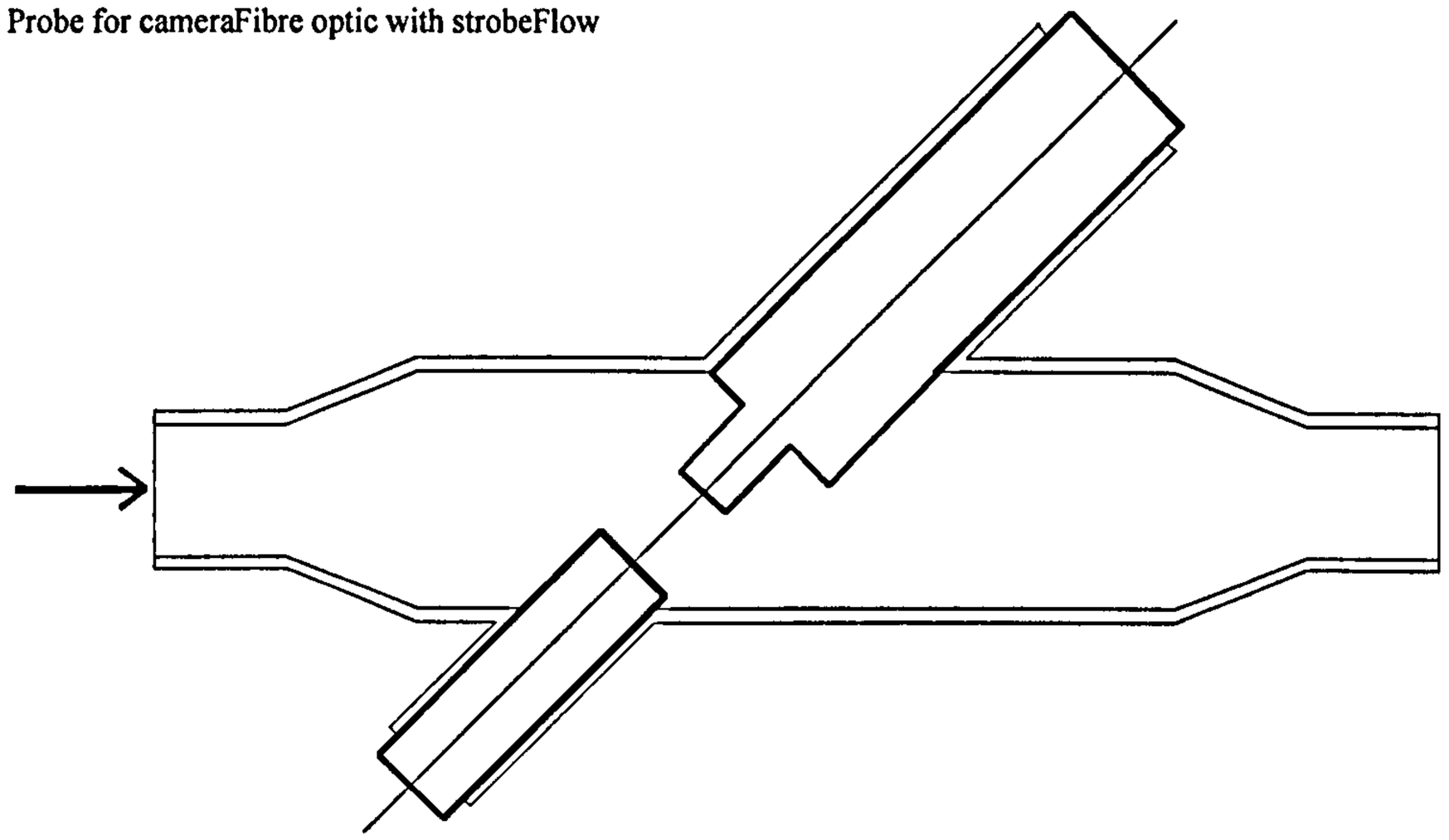

Figure 4.6 Video Probe housing

The Video probe consisted of a lens attached to a CCD camera (Hitachi KP160) that was housed in a purpose built stainless steel casing. The casing was fitted with tri-clover fittings, which enabled the probe to be inserted in-line (Figures 4.6 & 4.7a). The probe housing was designed so that the cross sectional area between the probe and the strobe was equal to that of the inlet and the outlet of the video probe housing.

The probe consisted of a lens that was attached to a CCD camera (HITACHI KP160) which in turn was connected to a computer. The light source was a stroboscope (DRELOscope 3244) and was transmitted inside the pipe via a fibre optic, located on the opposite side of the probe to provide backlighting. The strobe was operated at 50 Hz to correspond with the electronic shutter speed of the camera and had a flash half intensity width of 1 μs and intensity 0.15 J/flash.

The dimensions of the casing and the space restrictions imposed by the positioning of the probe and the fibre optic meant that images were taken 5 pipe diameters downstream of the mixer.

Images were transferred from the CCD to a computer using a Neotech frame grabber, which displayed images continuously on the computer monitor. Ninety-nine bitmap images were captured for each run.

The system was calibrated by taking a picture of a graticule using the Video Probe, one division on the graticule was the equivalent of 50 μm. A computer was then used to draw a straight line on the image. This length of the line (in μm) was known from the divisions on the graticule and the computer was then used to calculate a calibration factor by dividing this distance by the number of pixels that represented the line. The calibration factor was calculated to be 1.2 μm/pixel.

The droplets were sized using a semi-automatic programme developed in-house at BHR Group Ltd using National Instruments LabView software. This involved the operator defining the boundaries of a drop by dragging a circle around it using a mouse. The program counted the number of whole pixels across the diameter of the circle and then used the calibration factor to determine a diameter in μm. Only drops in focus were measured.

When all of the drops in a frame had been measured the software programme counted the number of drops that had been measured and calculated the d_{32}, before moving onto the next frame. The number of droplets measured was dependent on the value of d_{32}, which was monitored throughout the measurement process. The measurement was ended when the value of d_{32} stopped changing significantly (± 1 micron) with each new measured drop. The number of drops required before a stable value of d_{32} was reached was typically around 600 drops. The measured diameters were stored in data files, which were then imported into a spreadsheet package for analysis.

The images captured by the CCD camera were made up of two interlaced pictures (i.e. two frames taken a split second apart). As the images were taken of a dynamic situation the picture quality was not always the best and the drops would often have blurred edges. During analysis, the software program allowed one of these images to be discarded. It then interpolated between the gaps to obtain a full image. This procedure resulted in improved image quality.

A potential problem with this technique is the degree of accuracy displayed when measuring smaller droplet sizes. The calibration factor for this measurement was 1.2 microns/pixel so a true droplet diameter of 5 μm would cover 6 pixels. The size of one pixel was approximately 250 μm, thus the diameter of the circle that would have to be drawn around a 5 μm drop would be 1500 μm (or 1.5 mm). The resolution of this technique was 2.4 μm (as the thickness of the circle drawn around a drop was the equivalent of 2 pixels).

In order to eliminate errors due to individual subjectivity, the same operator was used to measure all the drop sizes.

Another inherent problem with this technique is that the larger droplets have a tendency to obscure the smaller ones and thus make it difficult to spot smaller ones. This gives rise to inaccuracies in the droplet size distribution. However, this technique is useful in identifying the larger droplet sizes, which are more likely to be affected by the sampling arrangement.

4.3.3. Droplet size distributions

The Mastersizer collects a scatter pattern from a particular sample and uses Lorenz-Mie theory to determine the size distribution. The main assumption in the use of Mie theory is that all the particles are spherical and the results are expressed in terms of equivalent spheres. The Mastersizer, therefore, determines the volume of the particle and relates this

back to a diameter of a sphere with an equivalent volume. It is important to note that the size distribution derived by this technique is volume based.

The analysed distribution from the Mastersizer is expressed in a set of size classes, which are optimised to match the detector geometry and optical configuration giving the best resolution. The standard Mastersizer has 72 analysis size bands and are created by equal logarithmic spacing between the limits of the instrument. All parameters are derived from this fundamental distribution using the summation of the contributions from each size band. The representative diameter for each band is taken to be the geometric mean and is generally considered to be more appropriate to the logarithmic spacing of the fundamental size classes.

The droplet size distributions generated by the Malvern Mastersizer are presented as Volume frequency curves. The frequency curve is useful when identifying where the main peaks in the distribution lie and also when comparing results from different measurements. This curve is calculated by differentiating the cumulative volume frequency curve, which in turn is calculated from the initial size bands.

The Mastersizer software allows the volume distribution to be converted to a number distribution. However, as the initial measurement is volume based, this conversion is liable to systematic errors.

The Mastersizer software allows the customisation of the size bands and can switch from a logarithmic x-axis to a linear one to enable comparison of distributions from other techniques.

The droplets that were measured using the video probe were analysed in an Excel spreadsheet that arranged the data in ascending order and then placed the diameters into predetermined bin sizes (which matched those used by the Mastersizer software). The distributions generated by the spreadsheet were both number and volume based. This

enabled the droplet size distributions from the Mastersizer and the Video probe to be plotted on the same axis.

It is important to note that different techniques measure different properties of a droplet. For instance the Malvern Mastersizer measures the volume of a drop, whereas the video probe measures the diameter. It was mentioned previously that the video probe was subject to an error of ± 2 μm on a particle/droplet diameter. Therefore, for droplets below 15 μm, an error greater than ±13% would be exhibited. Therefore, comparisons were made using both number based and volume based distributions to minimise errors that may exist when converting from one to the other.

4.4. Sampling technique

4.4.1. Continuous Sampling

A continuous sampling and dilution system was developed (Figure 4.7) that eliminated the need for the sampling accessories on the Malvern Mastersizer. This allowed a larger volume of sample to be measured at higher concentrations and also aided the process of making rapid measurements.

Figure 4.7a shows the video probe in the outlet of the mixer and the sampling point. The technique involved the extraction of a continuous stream of sample from the outlet of the rotor-stator mixer. This sample was introduced into a water line, the flowrate of which was controlled using a peristaltic pump (Figure 4.7b). The diluted stream was fed directly into the sampling unit of the Mastersizer (Figure 4.7d).

The sample was extracted using two sections of 2mm stainless steal tubing both with one end curved (Figure 4.7c & Figure 4.8). The angle of curvature was kept as large as possible to minimise flow irregularities. The sampling inlet was positioned in the centre of the rotor-stator outlet pipe. The two tubes were connected using 2mm Marprene tubing, a distance was kept between the two tubes to accommodate the lab clamp valve.

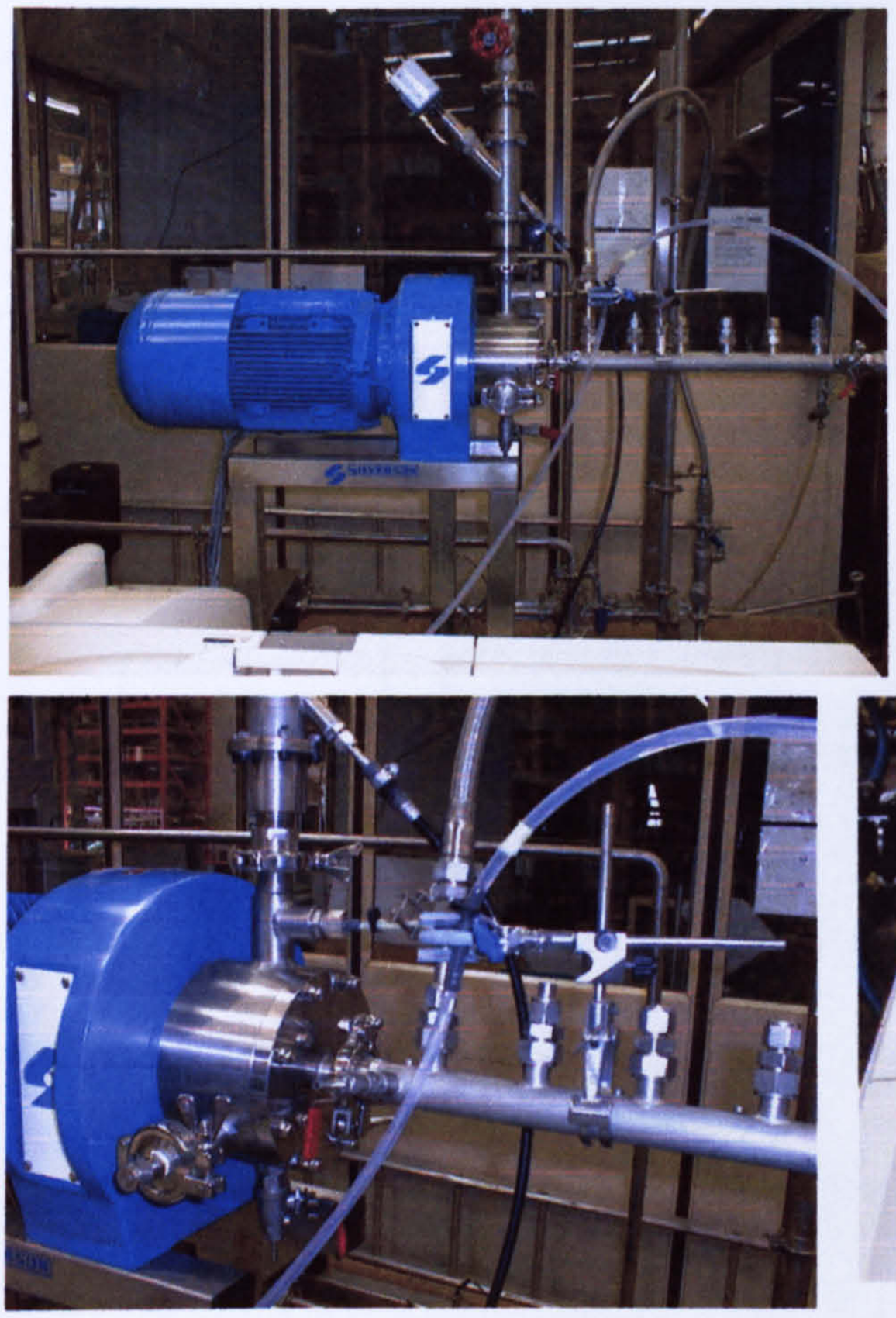

Figure 4.7 Sampling arrangement. Clockwise from top left; (a) The inline rotor-stator with sample point and Video probe in place; (b) Watson Marlow pump used for supplying diluent; (c) Inlet to Mastersizer flow cell and pump and stirrer unit used for flushing the cell; (d) Sample point with sampling arrangement.

There was a danger that as the sample flows through the valve arrangement, further drop break-up may occur giving rise to erroneous results. The lab clamp valve arrangement was selected because it eliminated any sharp surfaces or edges that would exist if a ball or

needle valve were used and minimised the effect of sampling on the droplet size distribution.

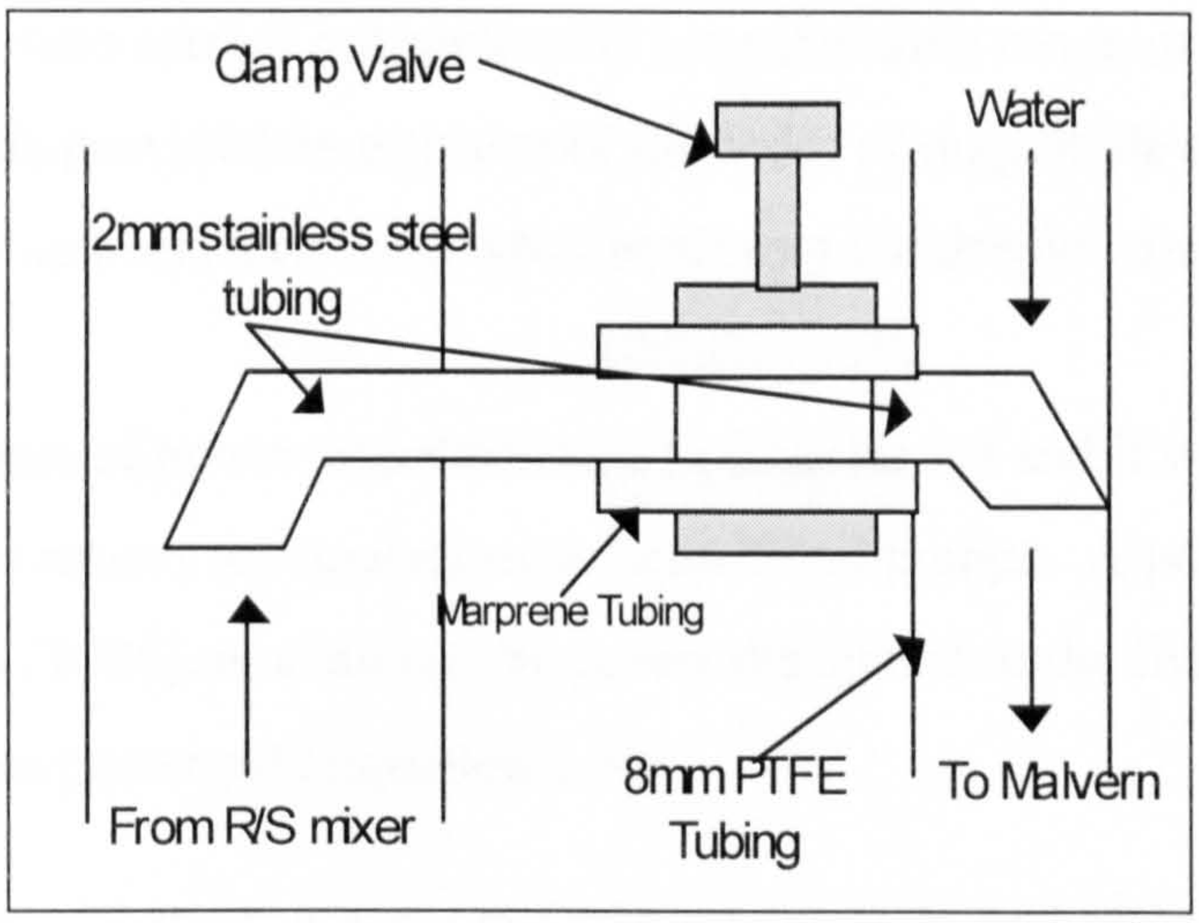

Figure 4.8 A schematic of the continuous sampling system.

The sensitivity of the Mastersizer to air bubbles led to de-ionised water (that had been left to de-aerate over night) being used as the diluent. The correct dilution rate was achieved by adjusting the laboratory clamp valve and also by varying the flowrate of the water. The concentration (or obscuration, see Appendix 3) was monitored by the Mastersizer software program and a measurement was made only when the correct level was achieved. The sampling technique was validated against the Video Probe described previously the results of which are discussed in Chapter 6.

4.5. Measurement of Power supplied to the fluid

The various mechanistic correlations, discussed previously, are dependent on the scaling of the droplet sizes with the Kolmogorov length scale. The Kolmogorov length scale, therefore, is important in the interpretation of the droplet size data.

Although it was not possible to monitor the power during the dispersion tests, measurements were carried out separately over the same range of experimental conditions. This provided an estimate of the order of magnitude of the Kolmogorov length scale, which was then used when analysing the droplet size data.

The measurement of power was discussed in Chapter 2.4 and it was mentioned that in-line rotor-stator mixers are analogous to centrifugal pumps. A power balance for pumps, used by Sparks (1996), to evaluate the power dissipated to the fluid in an in-line rotor-stator mixer was presented (Equation 2.36).

Traditionally, the method of determining total power in stirred vessels is to measure the shaft torque. The shaft power is calculated from the torque using Equation 2.38. This method is dependent on the accurate measurement of the shaft torque and many instruments, such as torque transducers and strain gauges are available to do this.

Sparks (1996) used this technique to calculate the shaft power on an in-line rotor-stator mixer. The motor shaft was extended to allow a torque transducer to be fitted between the motor and the mixing head. He reported values of torque from 1 to 4 Nm at 3000 rpm, (the highest rotational speeds investigated). However, it was found that these values were at the lower limits of the torque transducer used and thus at the limits of accurate measurement. An inherent problem with strain gauges and torque transducers is that their resolution decreases as the rotational speed increases.

Adopting a similar approach was difficult for this work due to the high rotational speeds of the rotor-stator mixer. Instrumentation designed for high rotational speeds did not have adequate resolution to measure the low values of torque expected from the in-line

rotor-stator mixer. In addition, the cost and safety implications of extending the motor shaft to rotate at 12000 rpm meant it was impractical to pursue this technique. As a result alternative techniques were investigated and it was found that the best option available was to use a thermometric technique.

4.5.1. Thermometric method of power measurement

The thermometric technique for measuring pumping efficiencies is one that has been used extensively in the water industry (Brown, 1991). It is based on the fact that the majority of losses in a pump are dissipated into the fluid as heat.

These losses result in a small increase in temperature, typically in the order of a few hundredths of a degree, between the inlet and the outlet of the pump. Therefore, the technique requires the accurate measurement of temperature to within a few thousandths of a degree.

This method was adapted to measure power in the in-line rotor-stator mixer. The problems associated with measuring the small temperature rises were overcome by inserting the mixer into a recirculation loop and monitoring the temperature rise over a period of time. The numerous passes through the mixer heated the fluid sufficiently to enable accurate temperature measurement. The time was measured allowing the calculation of the theoretical number of passes and therefore the temperature rise for one pass.

4.5.2. Recycle loop and instrumentation

The rotor-stator mixer was fitted into a recycle loop using a 100 litre stainless steel vessel with a 1 inch outlet (Figure 4.9). The low volume vessel was chosen, as it was easier to lag and limit heat losses through the vessel wall. In addition, for a lower volume, large temperature rises were possible in a shorter time.

The pipework from the vessel to the inlet of the mixer and immediately after the outlet was 1 inch. A 3 inch Endress and Hauser Promag 33 flowmeter was fitted downstream (10 pipe diameters) of the mixer and as result the pipework was gradually enlarged from 1 inch to 3 inches. A 3 inch butterfly valve was located downstream of the flow meter and was used to control the flowrate. The pipework was gradually reduced from 3 inch back to 1 inch at the inlet of the vessel. The inlet to the vessel was submerged below the liquid level in the vessel.

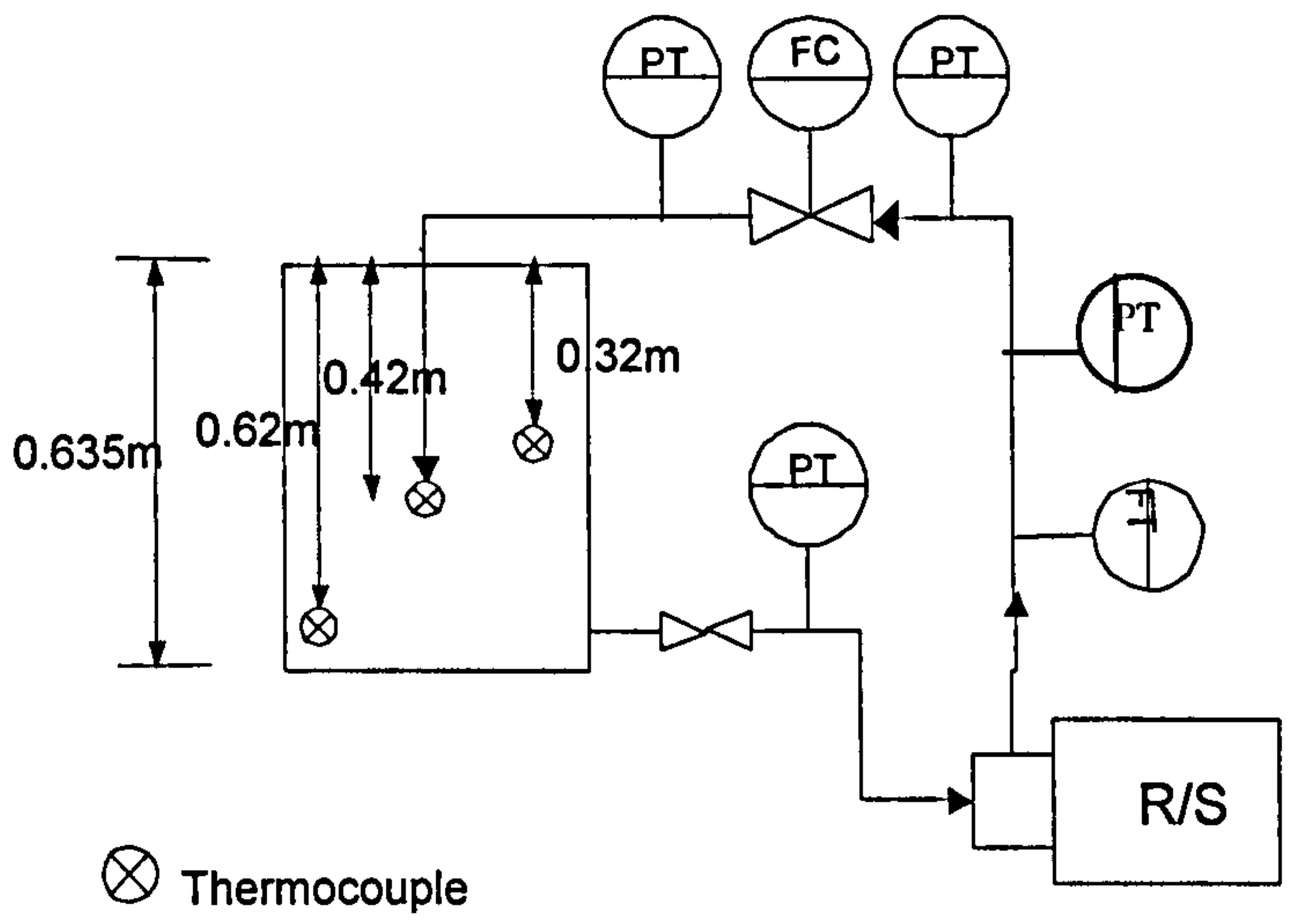

Figure 4.9 Flow loop set-up for thermometric power measurement

To monitor the losses across the control valve, pressure gauges (Wika Bourdon Tube Pressure Gauges Type 213.53) were fitted 1 pipe diameter either side of it. A pressure gauge was also fitted one pipe diameter up-stream of the mixer.

The flow from the inlet to the vessel was used to mix the fluid and to ensure homogeneity the temperature was measured at different locations in the vessel. Three type K fine wire thermocouples were located near the top, at the mixer outlet and near the bottom of the vessel. The temperature was monitored using a Fluke 50S handheld digital thermometer connected to a Type K 6-way bench selector switch (although only three of the connections were used). The mixer was run until the temperature of the water had risen by 10 °C. This gave an error in measurement of ± 0.1°C.

The vessel, the inline rotor-stator mixer and all the pipework was fully lagged using 150 mm fibreglass insulation. After everyone run the temperature of the water was monitored with the mixer turned off. After 24 hours the temperature of the water was found to have only decreased by approximately 1-2 °C, therefore, the heat losses to the surroundings were considered to be negligible.

4.5.3. Experimental procedure

The vessel was calibrated to hold 100 litres of de-ionised water and fresh water was used for every run. To ensure that the volume of water was kept constant the outlet valve was kept shut while the vessel was being filled. Once the correct volume had been reached the valve was opened to fill the pipe work and the mixer.

The temperature was noted at time zero for all three thermocouples. It took a few minutes for all three thermocouples to read the same temperature (± 0.1 °C), once this had been achieved the mixer was started at the appropriate rotational speed. The butterfly valve was adjusted to control the flowrate. After the first run the speed and the valve were set for the next run before the mixer was switched off.

The temperature was monitored until a total rise of 10 °C had been achieved. This temperature difference was considered high enough to obtain a reading within the desired accuracy ((± 1%). Typically, this temperature rise was observe over a period of 3-6

hours. The initial temperature of the water ranged from 12 °C to 14 °C and the final temperature was between 22 °C to 24 °C. The density of water varies by less than 0.5% over this temperature range.

The vessel and the pipework were drained using a drain valve that had been fitted into the bottom of the mixing head.

4.5.4. P_{SHAFT}

The power supplied to the fluid from heat dissipation can be defined as:

$$E = \dot{m} C_p \Delta T \tag{4.1}$$

Where, E = Energy supplied to the fluid (J)

C_p = Specific heat capacity (J/kgK)

$\dot{m}$ = Mass flowrate (kg/s)

ΔT = Temperature rise (K)

The theoretical number of passes is given by:

$$No\ of\ Passes = \frac{\dot{m}t}{M} \tag{4.2}$$

Where, t = the time the mixer was run (s)

M = Total mass of water (kg)

Therefore, the temperature rise over a single pass, ΔT_s, is given by:

$$\Delta T_s = \frac{\Delta TM}{\dot{m}t} \tag{4.3}$$

It can be assumed that all of the power supplied by the shaft is converted to heat energy. Therefore, the energy supplied to the fluid in a single pass, can be considered to be the equivalent of the shaft power giving Equation 4.4:

$$P_{SHAFT} = mc_p \Delta T_s = P_O \rho N^3 D^5 \tag{4.4}$$

4.5.5. P_{PUMP}

The flowrate and the differential pressure across the mixer were measured using the Endress and Hauser flowmeter and the Wika pressure gauges. Equation 2.39 was then used to calculate the pumping power.

4.5.6. P_{MECH}

The mechanical losses were measured by removing the rotor, filling the head with water and blanking off the inlet and the outlet. The shaft was then rotated in the water until a temperature rise of 10°C had been achieved. The temperature inside the head was measured using the Fluke 50S handheld digital thermometer in conjunction with a BSS1843 thermocouple probe (type K) inserted into a 3/4" compression fitting at an additional sampling point located on the side of the mixing head (tangential outlet).

4.5.7. P_{DISC}

Sparks (1996) attempted to measure the P_{DISC} by spinning a smooth disc with the same dimensions as the rotor. The resultant torque readings were found to be low compared to those specified for the torque transducer used. It was suggested that the flow patterns would differ to those for a rotor (due to the absence of teeth) and therefore a theoretical calculation would be just as reliable. The theoretical power loss due to disk friction was, therefore, calculated using eqn 2.40.

4.5.8. P_{LEAK} and $P_{HYDRAULIC}$

P_{LEAK} and $P_{HYDRAULIC}$ were not directly measured but it was assumed that they accounted for the remainder of the shaft power, once all the other losses had been deducted.

$$P_{LEAK} + P_{HYDRAULIC} = P_{SHAFT} - (P_{PUMP} + P_{MECH} + P_{DISC}) \qquad (4.5)$$

4.5.9. Losses through the control valve and pipe work

The heat input caused by the losses associated with the valve and the pipework were also calculated. The pressure was monitored across the valve and along the pipework using the Wikon gauges. This enabled the head loss across the valve to be calculated.

The losses in the pipe were expected to be small in relation to the heat input from the rotor-stator mixer. However, the heat contribution of the control valve would be significant.

CHAPTER 5. RESULTS

The rotor-stator liquid-liquid contactor rig was used to perform a range of tests that investigated the affects of N, Q and Φ on the droplet size. These tests were done on two different rotor-stator sizes as well as four different stator designs.

The high rotational speeds of the rotor-stator mixer made it difficult to measure power during the tests. Therefore, a separate rig was set-up that utilised a thermometric technique described in Section 4.5. These measurements were done on the 69.85 mm rotor with the Square Hole High Shear Screen and the Emulsor Screen, for which the most comprehensive range of droplet size data was collected.

The details of the experiments and the location of the results are presented below and discussed in Chapter 6.

5.1. Measurement technique validation

The sampling technique employed on the liquid-liquid contactor rig was validated using a Video probe. This involved performing initial tests in a laboratory scale stirred vessel to investigate the stability of the kerosene-water system. This was done to determine whether sampling was a viable option.

Tests were also performed comparing the Malvern Mastersizer with the Video Probe by measuring standard latex. The results from these tests were then used to interpret the results from the sampling validation.

The validation tests involved inserting the video probe at the outlet of the rotor-stator mixer and comparing the results against the Malvern Mastersizer. The results and observations of this work are presented in Section 6.1.

5.2. In-line rotor-stator performance tests

The performance tests involved the investigating the effects of rotational speed on droplet size at two different Q (0.4 l/s and 0.8 l/s) and four different Φ (5%, 10%, 20%, 30%). A small number of tests were also performed at 40%.

The main focus of these tests were on the 69.85 mm rotor with the Emulsor screen, (ES), and the Square Hole High Shear Screen, (SHHSS). This rotor size was the standard for the unit supplied and these two stator designs are recommend by the manufacturer for use with liquid-liquid systems.

A limited number of experiments were also performed using the 50.8 mm rotor. These tests looked at the effect of rotor speed on droplet size at a constant flowrate (0.4 l/s) and dispersed phase concentration (10%). The effect of dispersed phase concentration was also investigated for this rotor size (at 7000 rpm at 0.4 l/s). These tests were done to gain some insight into the effects of stator design on the droplet size distribution.

The volume size distributions from these results can be found in Appendix 4. The distributions are discussed in Section 6.2. The influence of the important parameters on droplet size are discussed in Section

5.3. Power Measurement

The power input to the fluid was measured separately to give an idea of the Kolmogorov length scale. The power was measured for the 69.85 mm rotor with the ES and SHHSS. This was because the most comprehensive droplet size data was collected for this rotor size and two screens.

The power was measured for a range of flowrates, 0.4 to 1.2 l/s in 0.2 l/s increments for rotor speeds form 5000 rpm to 11000 rpm. A discussion of these results are given in Section 6.4..

CHAPTER 6. Discussion

6.1. Measurement technique and Sampling validation

6.1.1. Kerosene-Water Stability

The Kerosene-water stability was investigated in a stirred vessel described in Section 4.2.2. A dispersion was created and samples were taken and placed on a glass slide and viewed under a microscope (Figure 6.1).

It was observed that the droplets in a globule of sample from a 5% dispersion placed on a glass slide moved around considerably (drop sizes ranged from 10 to 100 μm). This motion could be attributed to the droplets, due to their density, ascending to the highest point of the globule. At the highest point, the greatest rate of coalescence would be expected due to droplets getting closer together.

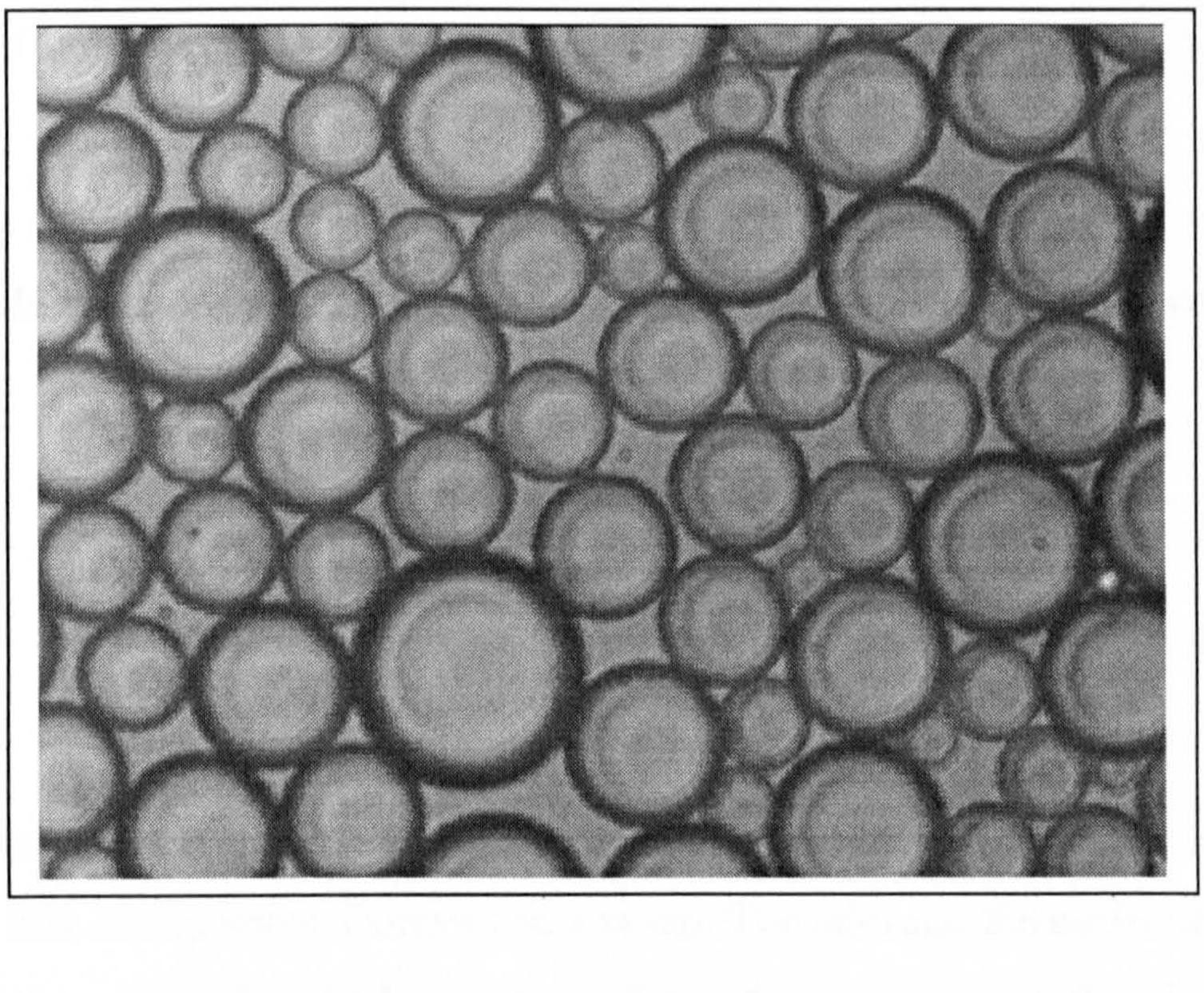

Figure 6.1 Droplets collecting at the top of the sample under a microscope (5% dispersed phase concentration, undiluted)

However, it can clearly be seen, in Figure 6.1, that there appears to be no evidence that the drops are coalescing, (no bursting of interface and no further drainage of the continuous phase). This appeared to be the case after observing periodically for up to an hour.

These findings support those of Brown and Pitt (1971) that the kerosene-water system is not a readily coalescing system. Droplets that would be generated in a rotor-stator mixer are expected to be significantly smaller than those generated by a stirred tank. The smaller droplet diameters would lead to an increase in the interfacial forces resisting drop break-up (Equation 2.3) resulting in increased stability.

6.1.2. Comparison of measurement techniques

The Malvern Mastersizer and the Video Probe were both used to measure standard latex beads with known diameters. Two sets of latex standards, supplied by Bangs Laboratories (Appendix 2), were used with different mean diameters (Table 6.1).

Table 6.1 Latex beads tested using the Mastersizer and the video probe.

Mean Diameter (μm)	Standard deviation (μm)
98	90 - 106
113	75 - 150

Measurements were made using the Mastersizer sampling accessory (Hydro 2000S/G, Figure 4.7c) that incorporated a stirrer and a pump. The inlet and the outlet of the accessory were connected to the Mastersizer, simulating a continuous flow loop (closing valves V1 and V3 in Figure 4.5). The Video probe was inserted into the flow loop (in place of V2 in Figure 4.5), so that measurements could be made simultaneously with the Mastersizer.

The Latex beads were introduced to 1 litre of water in the Hydro 2000S/G, and the stirrer was used to keep the particles in suspension. The latex beads were then passed through the video probe and the measurement cell of the Mastersizer. The measurements were repeated using a fresh set of beads and the results compared favourably to within 5% for the video probe and almost identical for the Mastersizer.

The volume and number based particle size distributions for the 98μm and the 113μm beads are shown in Figures A.2 & A.3 (Appendix 4) respectively.

The 98μm particles have the narrowest distributions (Figure A.2), which is expected as these beads exhibited the lowest standard deviation (Table 4.4). This observation is consistent with both the volume and number distributions generated by the two techniques. The main observation for the two sets of particles is that the distributions do not match, with the Mastersizer favouring the smaller particle sizes. This is true for both the volume and the number distributions.

Figure A.2 shows that the distributions from the Mastersizer appear to have shifted approximately 5μm to the left of those generated by the data from the Video probe, with peaks at 96μm with the Mastersizer and 100μm with the video probe. Comparing this to the average diameter (mode) specified by the manufacturer of the beads, 98μm, suggests that both techniques are within ± 2% the acceptable limit.

The volume curve generated by the Mastersizer in Figure A.2 exhibits a small secondary peak between 75-90μm. This smaller peak is not apparent when viewing the number distribution and the number curves from the two techniques appear to follow the same shape. It is possible that this secondary peak is smoothed out on the number curve as there are a larger number of particles that make up a small percentage of the volume.

In Figure A.3 the distributions from the video probe consistently give larger sizes. The average value (mode) for this set of beads should be 113μm. However, the Mastersizer shows a peak at 95μm and the Video Probe shows a peak at 103μm.

Another interesting observation is that both techniques appear to be measuring particles outside of the range of the standard deviation for the sets of beads. This highlights the potential for variability. The manufacturer of the latex beads used a sieving technique to measure the latex beads, which would also contain a certain degree of error. So it is possible that the Mastersizer and the Video probe are measuring the beads more accurately than technique employed by the manufacturer.

The importance in realising that different techniques measure different parameters is clearly evident. One would not expect a perfect match between the two techniques, as there are systematic errors involved in them both. The Mastersizer measures volume and the video probe measures the diameter. However, the Mastersizer appears to have more of a bias towards smaller sizes and the video probe appears to show more of a bias towards larger particles.

The differences are more apparent for the larger and wider distributions (75-150μm). It can be seen that the video probe is seeing a greater number of particles larger than 100μm. This could be due to the fact that the larger particles are easier to see during measurement and that they also tend to obscure the smaller ones. This phenomenon would be less obvious for a narrower size distribution.

In general the distributions although not identical were close enough for comparative purposes. It is also believed that the sampling arrangement for which the video probe would be used to validate, would be more sensitive to the larger drops. Therefore, this technique can be used to determine whether the sampling arrangement is having an effect on the droplet size.

6.1.3. Sampling technique validation

The sampling technique was validated against the in-line video probe. The probe was inserted into the outlet of the in-line rotor-stator mixer (5 pipe diameters down stream) and images were captured simultaneously with the sampling.

The video probe could only be used at the lowest rotor-speed (3000 rpm) and the lowest Φ (5 %) at a total throughput of 0.8l/s, (Figure 6.2). Images at values higher than these were not possible, due to the increase in smaller droplets and consequently increased light scattering and resultant focussing problems.

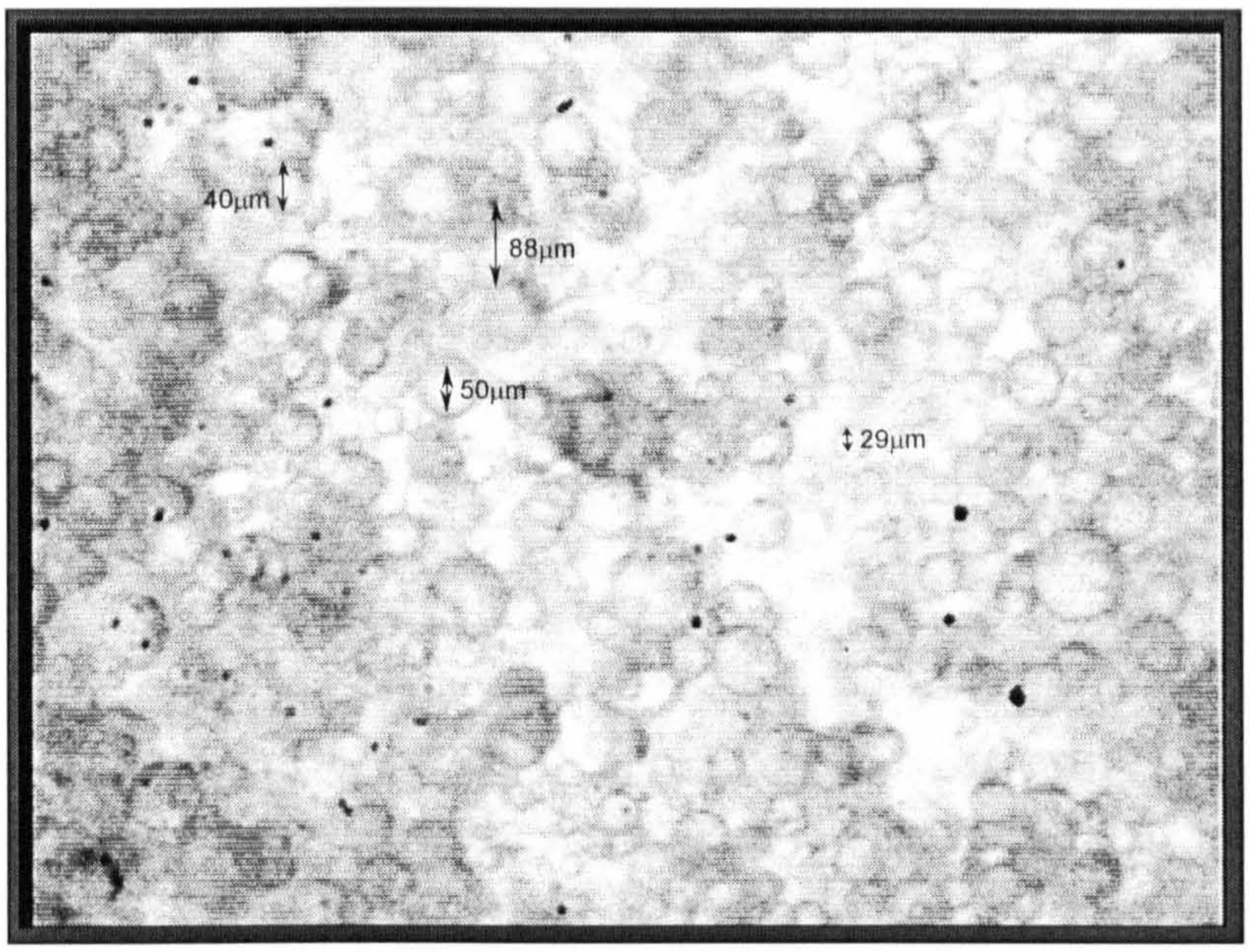

Figure 6.2 Image at 3000 rpm and Φ = 5%

It can be seen from Figure 6.2 that the quality of image obtained at the lower rotational speed is at the limit of acceptability. This is due to the large number of droplets that are below the minimum size range for this technique (20 μm), images become increasingly out of focus below this size range (due to increased light scattering).

Figure 6.3 shows a comparison of the volume distributions generated by the Mastersizer and by the Video Probe at the outlet of the rotor-stator mixer. As expected, the distributions are broader than those obtained from the latex beads and the main peaks from both techniques lie in approximately the same region (40-60μm).

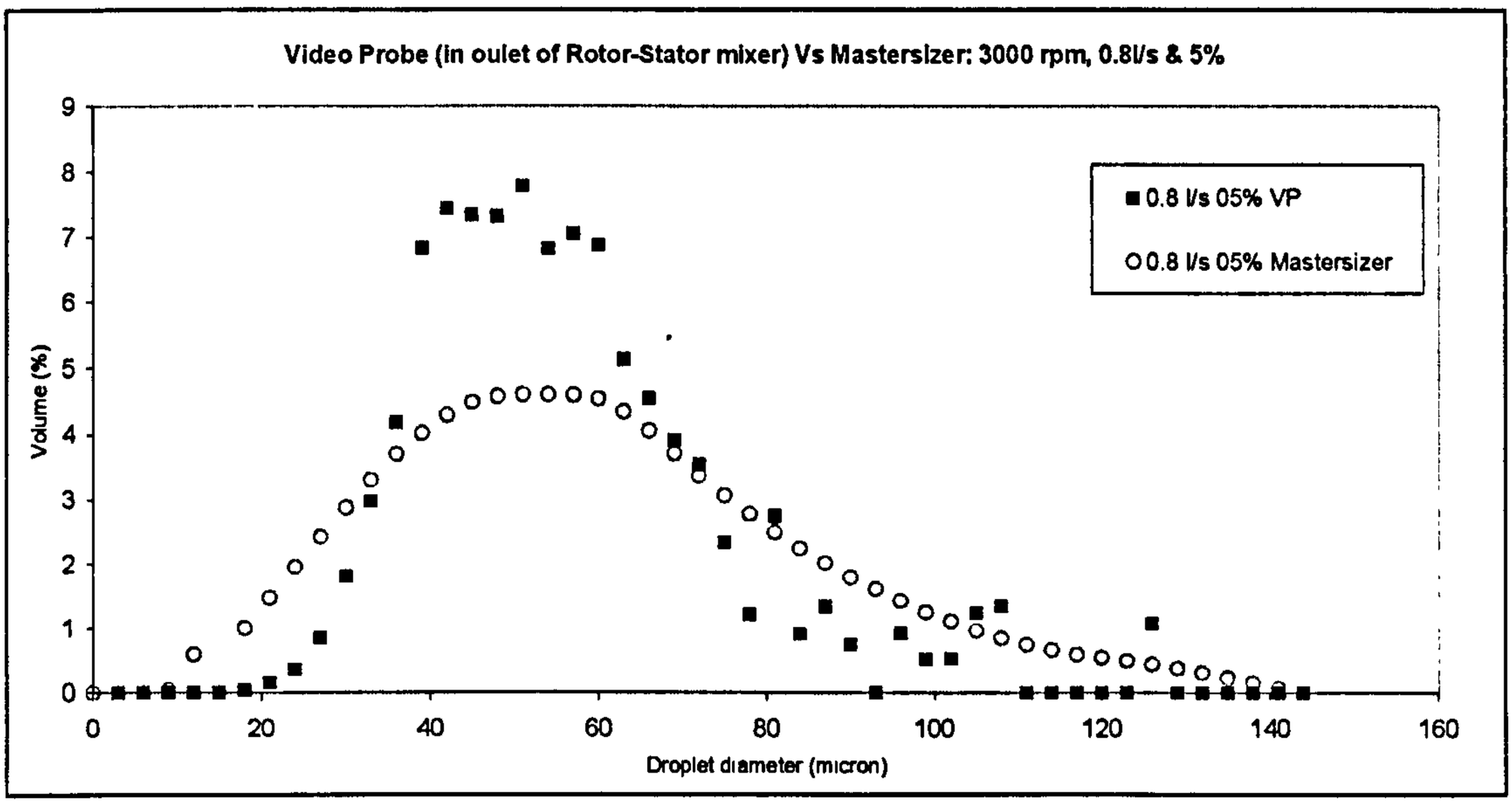

Figure 6.3 A comparison of DSD measured using the Mastersizer and the Video Probe for a rotor speed of 3000 rpm and $\Phi = 5\%$ at 0.8l/s

As well as seeing smaller droplets, the Mastersizer seems to have measured a greater number of larger droplets. Only a small percentage of the droplets measured by the Video Probe appear to be at the larger scale. However, the maximum size measured was 130μm. This led to the conclusion that droplets of sizes up to 140μm could be successfully sampled using the continuous sampling arrangement.

6.2. Drop Size Distributions

Tests were performed on a Silverson in-line rotor-stator mixer investigating the effects of rotor-speed, dispersed phase concentration, flowrate and the stator design on droplet size. The following section reviews the trends in the droplet size distributions and the mean diameters calculated from them. The effects of the individual parameters are then discussed paying particular attention to the scaling of the various parameters against d_{32}.

6.2.1. Volume frequency curves

The droplets size distributions generated by the 69.85 mm rotor with the Emulsor Screen (ES) can be found in Figures A.4 to A.12. Figures A.13 to A.18 show the distributions generated by the 69.85 mm rotor with the Square Hole High Shear Screen (SHHSS). The distributions are shown as volume frequency curves for a constant Q and Φ for varying N. The volume distributions from the 50.8 mm can be found in Figures A.18 to A.25.

The distributions are fairly broad, with drop sizes ranging from below 10 μm up to 100 μm. This is indicative of the inhomogeneous energy dissipation and by-passing within the rotor-stator mixer. The majority of the distributions exhibit a long tail at the smaller size end and a truncation of the drop size at the larger end of the size spectrum. The truncation at the larger end is due to the distributions being plotted on a logarithmic axis.

The shape of the distributions appears similar for each of the rotor speeds but the peak shifts towards the smaller droplet sizes as the speed increases. This shift is less significant at speeds greater than 7000 rpm.

At some of the lower rotational speeds a bi-modal distribution is evident, with a secondary peak at the smaller droplet sizes. This is more apparent for runs performed at the higher Φ. The secondary peak appears to smooth out as N is increased.

The main bulk of the droplet sizes are below 100μm for the runs performed at the lowest values of Φ, 5% and 10%. The main peaks lie at approximately 50 μm. This peak shifts towards the larger droplet sizes with an increase in dispersed phase concentrations.

An additional peak, at the larger size ranges, is observed for some of the higher dispersed phase concentrations (Figures A.6, A.7 and A.13). This peak represents droplet sizes up to 1000 μm at the maximum measurable size limit of the Malvern Mastersizer. The peaks appear to cut off at these points suggesting that droplets exist that are too large for measurement. However, these additional peaks disappear as the rotational speed increases. Due to the curtailing of the size distributions the corresponding mean diameters were not used in any of the subsequent analysis.

6.2.2. The relationship between d_{32} and d_{max}

There are many correlations available in literature that have substituted d_{32} for d_{max} (Tavlarides and Stamatoudis, 1981). The relationship between d_{max} and a mean diameter was discussed in Section 2.2.3. It was stated that in addition to its greater design value, for a small sample size d_{32} could be determined more accurately than d_{max}.

It was also suggested that d_{max} was proportional to any convenient mean diameter, provided break-up was due to a single break-up mechanism. Figure 6.4 shows a plot of experimentally measured d_{32} versus d_{max} for the full range of tests performed using the liquid-liquid contactor rig described in Section 4.1. The average diameters were those determined by the Malvern Mastersizer. The measurement time was increased to 10 seconds to ensure a large sample size was measured (the Mastersizer took approximately 10,000 snapshots of the sample with each snap taking one millisecond), which meant that the number of drops measured was in the order of thousands.

Although there is considerable scatter in the data, a linear trend can be seen. The best fit through all the data points gives a constant of proportionality of 0.13. This is lower than those reported in literature; Brown and Pitt (1972) reported a value of 0.72 for a 6-bladed

disc turbine, whereas Chen and Middleman (1967) reported a value of 0.6 for a Rushton turbine; Francis (1999) using a laboratory batch rotor-stator reported a value of 0.44.

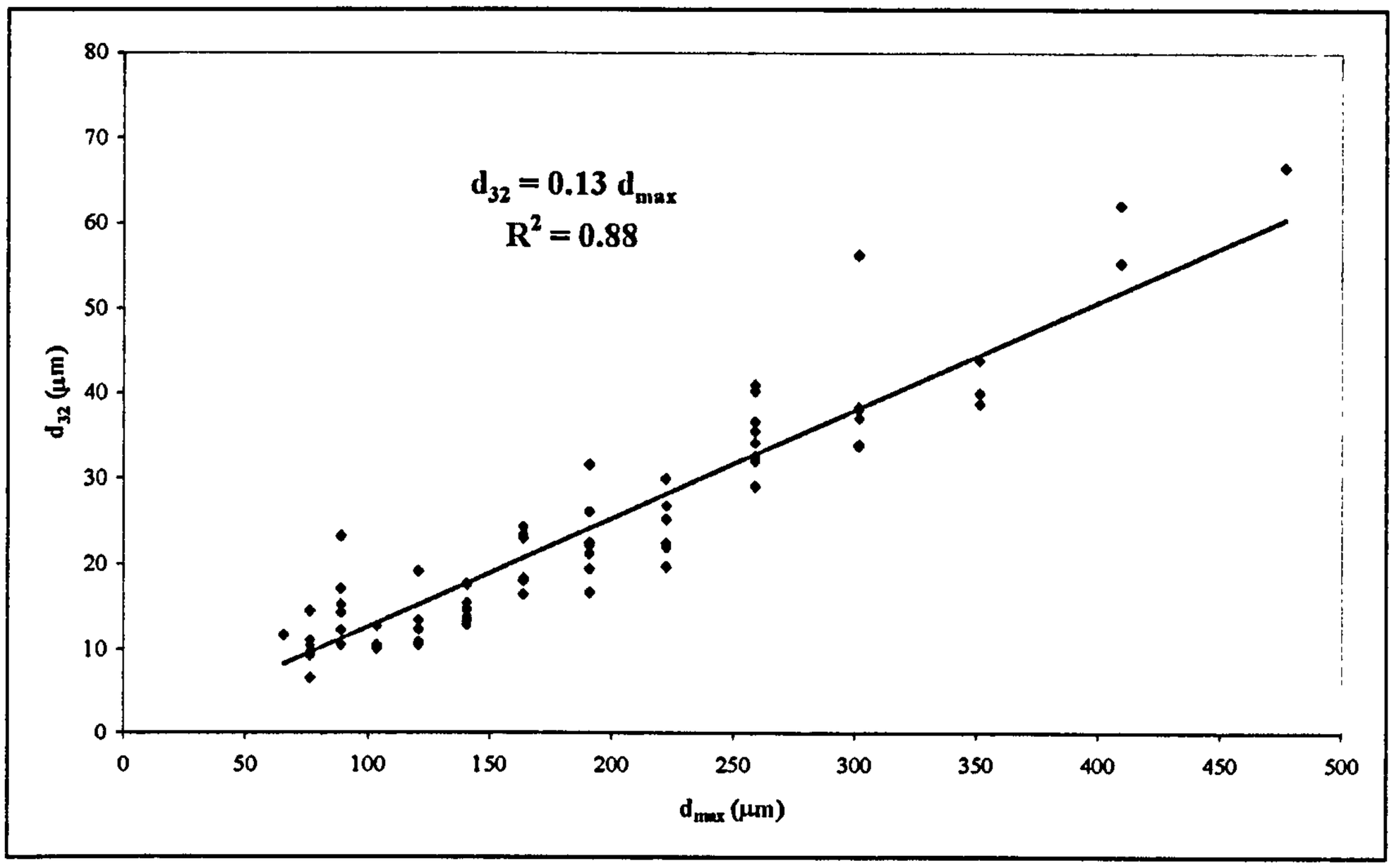

Figure 6.4 Correlation between d_{32} and d_{max}.

The low constant of proportionality maybe due to the long tailing of the droplets at the smaller size range. Although, these droplets may be significant in number, in terms of their volume they are small. Their influence on d_{32}, therefore is also smaller than the larger droplets.

At this point it is important to note that the theories of droplet break-up rely on the prediction of mean drop size at equilibrium conditions. Due to the inhomogeneous nature of the energy dissipation in an in-line rotor-stator mixer (nominal residence times in the shear gap, the region of highest shear rate, are in the order of 10^{-5} s) it is unlikely

that equilibrium drop size has been attained after a single pass. Therefore, the significance of d_{max} can be rebutted.

However, the fact that the kerosene-water system has been shown to be a non-coalescing system leads to the assumption that coalescence is not affecting the droplet size distributions. Also, the sampling technique should show no affect on the droplet size distribution.

It can, therefore, be assumed that transient effects are negligible (as there is no further break-up and coalescence) and that the correlation of mean drop size based on equilibrium drop-size can still be applied.

Also, the spacing between the size bands created by the Mastersizer is logarithmic. This bin spacing is designed to match the detector geometry and provide the best resolution. This implies that the resolution of d_{max} decreases as the droplet sizes increase, due to the bin sizes increasing. For droplet sizes above 140μm the bin sizes ranged from 20μm to 50μm.

The Mastersizer generates curves by mathematically finding the size data that best fits the light scatter data, this almost always results in smooth curves. A test for the accuracy of such a plot is to ensure that the values of residual calculated by the Mastersizer software are close to the value of 1.

Therefore, the d_{max} data, although useful in determining whether the assumption that break-up is due to a single mechanism is valid, should only be used qualitatively.

6.2.3. The effect of rotational speed, N, on droplet size

Figure A.4 shows the volume frequency curve for a flowrate of 0.4l/s and Φ of 10%. The distribution can be seen to shift towards the smaller size range as N increases. It is interesting to see that there is a significant change in the distributions between 3000rpm

and 6000rpm, with the main peak shifting from approximately 100μm to 50μm. However, rotational speeds above 6000rpm exhibit only a small change in droplet size. This trend is consistent with the majority of the tests performed for both the ES and the SHHSS.

Figure 6.5 shows the d_{32} plotted against rotor speed for a range of dispersed phase concentrations. The droplet size decreases with rotor-speed, however they begin to level off after 7000 rpm.

It is clear that the rotor-speed is only influential down to a certain droplet size below which further size reduction is not evident.

A similar trend was observed for the data collected for the 50.8 mm rotor, Figure 6.6. The droplet sizes, although still appearing to level off (especially for the GPDH and SH) it is not as prominent as that exhibited by the drop sizes from the 69.85 mm.

When considering the power supplied to the fluid, for a fully turbulent system, the power should scale with N^3 and should therefore increase. If the energy supplied to the fluid by the rotor was predominantly responsible for drop break-up the droplet sizes would continue to decrease with rotor speed. This would indicate that there are other factors that influence drop break-up.

It is interesting to note that in Figures 6.5 and 6.6 there are no significant differences in droplet size from the ES and the SHHSS for both rotor sizes.

Figure 6.6 shows that with the 50.8 mm rotor the ES and the SHHSS give the smallest droplet sizes and the largest come from the GDH. The GDH has the largest open area out of all the screens (35%) in addition to the largest hole size. However, the hole sizes of the

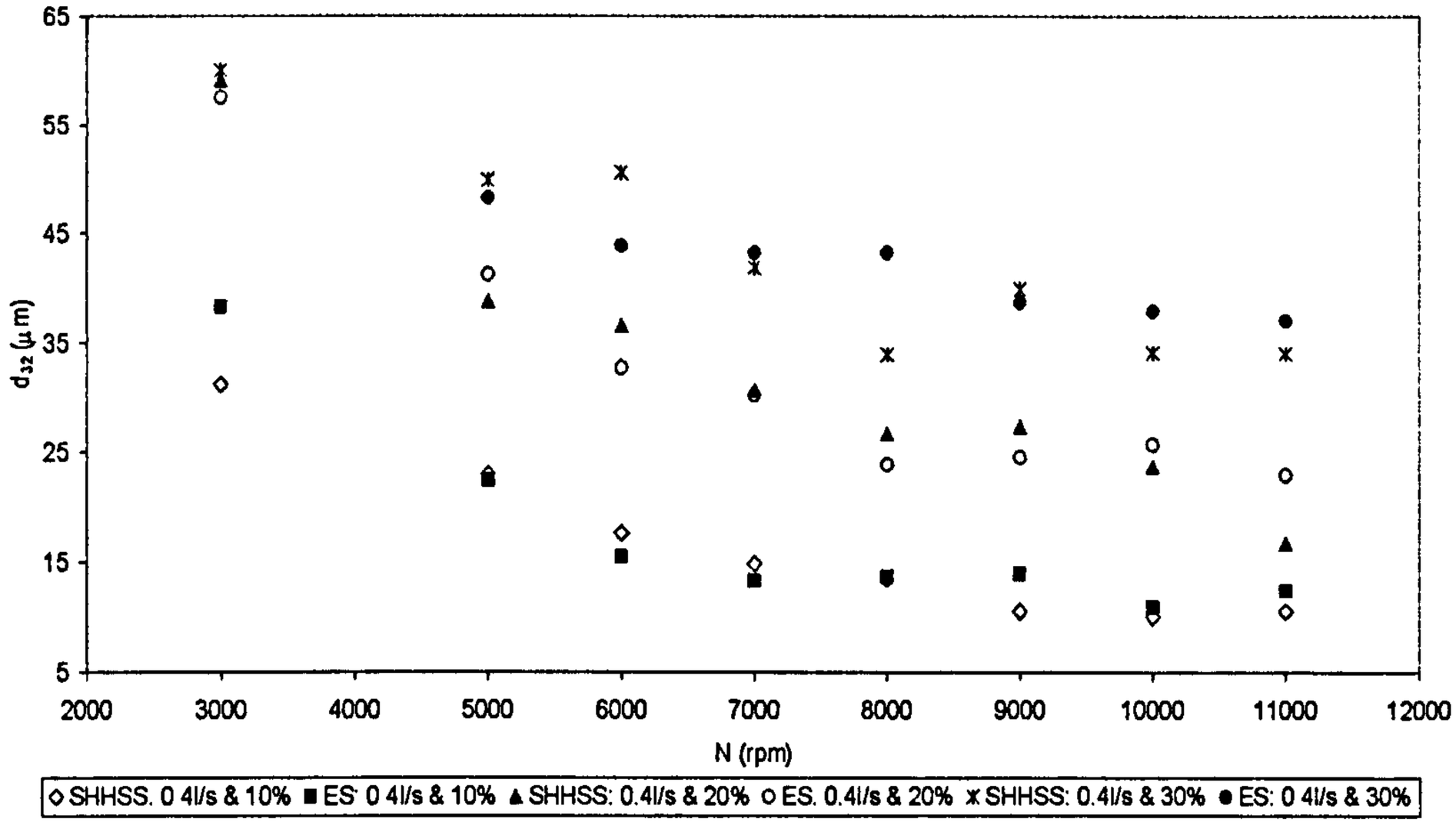

Figure 6.5 d_{32} versus N (RPM) for the ES and SHHSS (69.85 mm rotor) for varying Φ

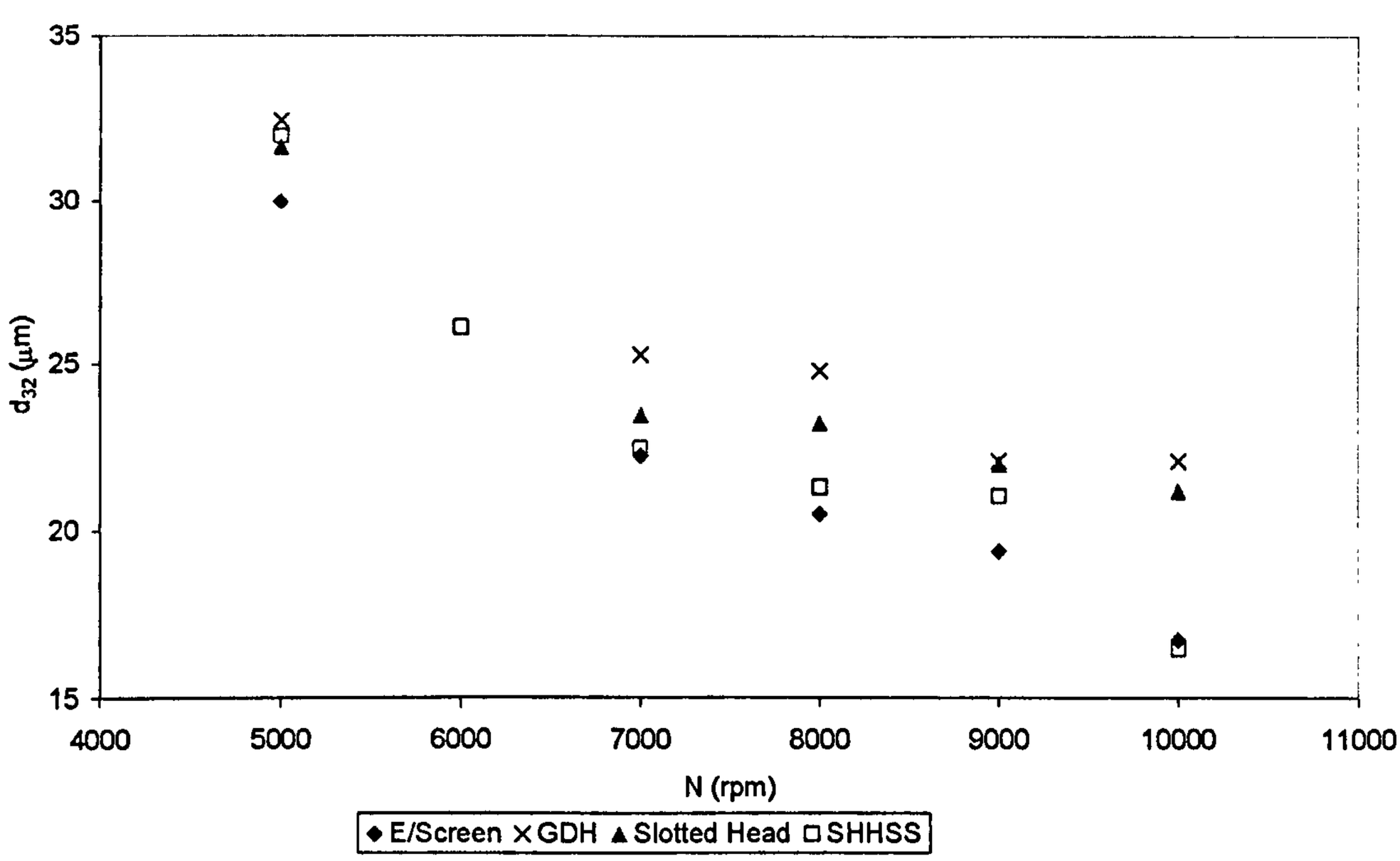

Figure 6.6 d_{32} versus N (RPM) for four different screens (50.8 mm rotor), 0.4 l/s and Φ = 10%

ES (1.4 mm) and the SHHSS (1.2 mm) are different and both these screens give similar droplet sizes. As the only variant is the open area of the screens it can be reasoned that open area has an influence on the droplet size distribution.

It is also worth noting that, in Figure 6.5, the droplet sizes increase with dispersed phase concentrations.

6.2.4. The effect of dispersed phase concentration, Φ

In Figure 6.5 the droplet size was seen to increase with Φ, this effect is further evident in the droplet size distributions (Appendix 4). The distributions can be seen to shift towards the larger droplet size spectrum as Φ is increased.

Figure A.7 and Figure A.11 show the distributions from the ES at 0.4 l/s (Φ = 40%) and at 0.8 l/s (Φ = 30%) respectively. The distributions do not change significantly with an increase in rotor speed.

Both Brown and Pitt (1971) and Streiff et al (1997) reported the effects of Φ on the droplet size distribution. Brown and Pitt (1971) also looked at a non-coalescing kerosene-water system, they attributed this effect to a form of turbulent damping. Both researchers showed that d_{32} could be related linearly with Φ (Equation 2.28).

In Figure A.7 an additional peak exists at the larger droplet sizes. This peak is curtailed due to the limits of the size measurement technique, however it is clear that droplets of sizes above 1000 μm exist.

It is unlikely that this peak is due to coalescence. It is possible that at the lower rotational speed and high Φ there is a formation of kerosene globules in the feed line. These globules may be passing through the mixer without being dispersed effectively in the continuous phase. The low flowrates in the inlet pipe and also the effect of the swirling

flow at the inlet (see Section 2.3.1) is not enough to ensure that the two phases are entering the mixer in the correct proportions.

As the dispersed phase concentration increases, the large globules (or a sausage like flow) of dispersed phase enter the mixing head and pass through it without coming into contact with the continuous phase. The smaller droplet sizes may be produced by the rotor chopping parts of the sausage as it passes through the stator hole and also the effect of the mixture being pumped through small holes (a type of jet mixing effect) into the volute. The jets would also cause turbulence in the volute and drops may undergo further break-up under a different mechanism. This is discussed in greater detail in Section 6.5.

It is worth noting that the dispersed phase is being injected one pipe diameter (0.0254m) up-stream of the mixer. The pipe Re number at the lowest flowrate, 0.4l/s, is approximately 15000 (at 30% dispersed phase concentration) which can be considered to be turbulent flow. However, the nominal residence time in the inlet pipe is 0.03s (at 0.4 l/s) which would suggest that the two phases are not exposed to the turbulent region for a significant period of time to allow any significant pre-mixing to occur.

This would point to the importance of feed strategy for high dispersed phase concentration. In batch systems, where an in-line rotor-stator mixer is used in conjunction with an agitator in a vessel, the agitator would create a pre-mix. Also, in many practical applications a static mixer can be inserted up-stream of the rotor-stator mixer to reduce the effect of feed injection.

This theory was not tested in greater detail for this work. However, varying the length between the mixer and the dispersed phase injection point and measuring the resulting droplet size distribution would provide further insight into the effect of feed strategy. A further discussion into the effects of flow regimes on the droplet size in the inlet is presented in Section 6.5.

6.2.5. The effect of flowrate, Q, on droplet size

The flowrate was not varied significantly in these tests. However, to obtain an appreciation of the effect of Q on the droplet size tests were performed at two different flowrates (0.4 l/s and 0.8 l/s).

Figure 6.7 shows d_{32} versus N for 0.4 l/s and 0.8 l/s at two different Φ. The drop sizes for 0.8 l/s are smaller than for 0.4 l/s at the lower rotational speeds. However, the droplet sizes appear to come together as the rotational speed is increased.

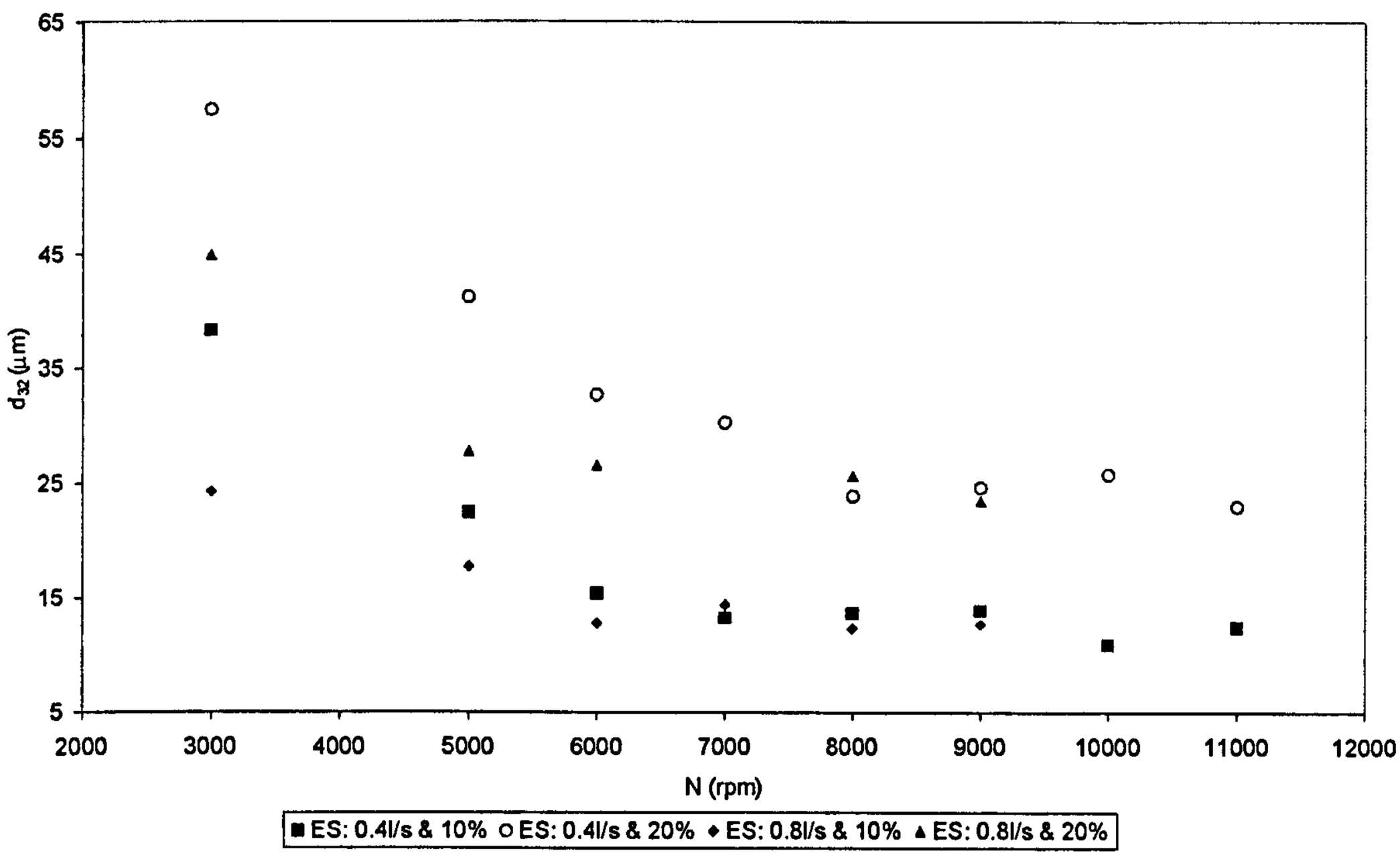

Figure 6.7 d_{32} versus N for 0.4 l/s and 0.8 l/s (at Φ = 10% & 20%)

Two possible explanations for this occurrence follow. Firstly, going back to the comments made previously on feed strategy, the higher flowrate may create a better pre-mix in the inlet pipe. This would ensure that the two fluids are entering the mixer in the

correct proportions at the lower rotational speeds (when the swirling effect of the flow was less).

Secondly, if the power draw of the mixer is proportional to N^3 then the energy input to the fluid by the rotor should increase significantly as the rotor speed is increased. It is possible that at the lower speeds an increase in flowrate would increase the velocity of the jets emanating from the holes in the stator. It can be assumed that the velocity of the fluid out of the jets is the ratio of flowrate and the open area (of the stator). The energy input of these jets in the volute coupled with the impinging fluid on the stator, maybe greater than that of the rotor at the lower speeds.

This second explanation would lead to the possibility that the mixer is operating with drowned suction (when the pumping effect of the rotor is overrun by the pump upstream of the mixer) at the lower speeds.

Sparks (1996) reasoned that when the mixer is operating drowned the energy dissipation would result from the losses associated with the rotor and from static losses similar to a motionless mixer.

Averbukh et al (1988) incorporated Q into their correlation for calculating mean droplet size in an in-line rotor-stator mixer (Equation 2.31). However, the mean drop size only showed a small dependence on Q (an exponent of -0.08). For the limited range of Q studied, there only appears to be an effect on droplet size at the lower rotor speeds. For this reason Q was assumed to have little or no effect on the droplet size.

6.2.6. The correlation of d_{32} with N

Four different correlations for d_{32} were discussed in Section 2.2.3 and are summarised in Table 2.3. These correlations are based on mechanistic models that balance the forces causing and opposing drop break-up.

The following section attempts to determine the dominant break-up mechanism by determining the correlation of d_{32} with the rotor-speed, We and Re.

Previous discussions have highlighted that there are no significant differences in droplet size from the ES and the SHHSS. For this reason data from both these screens is considered together in the following analysis.

Figure 6.8 shows d_{32} versus rotor speed on a log-log plot for the different Φ. A linear regression was performed on each of the data set to determine the scaling of d_{32} with N.

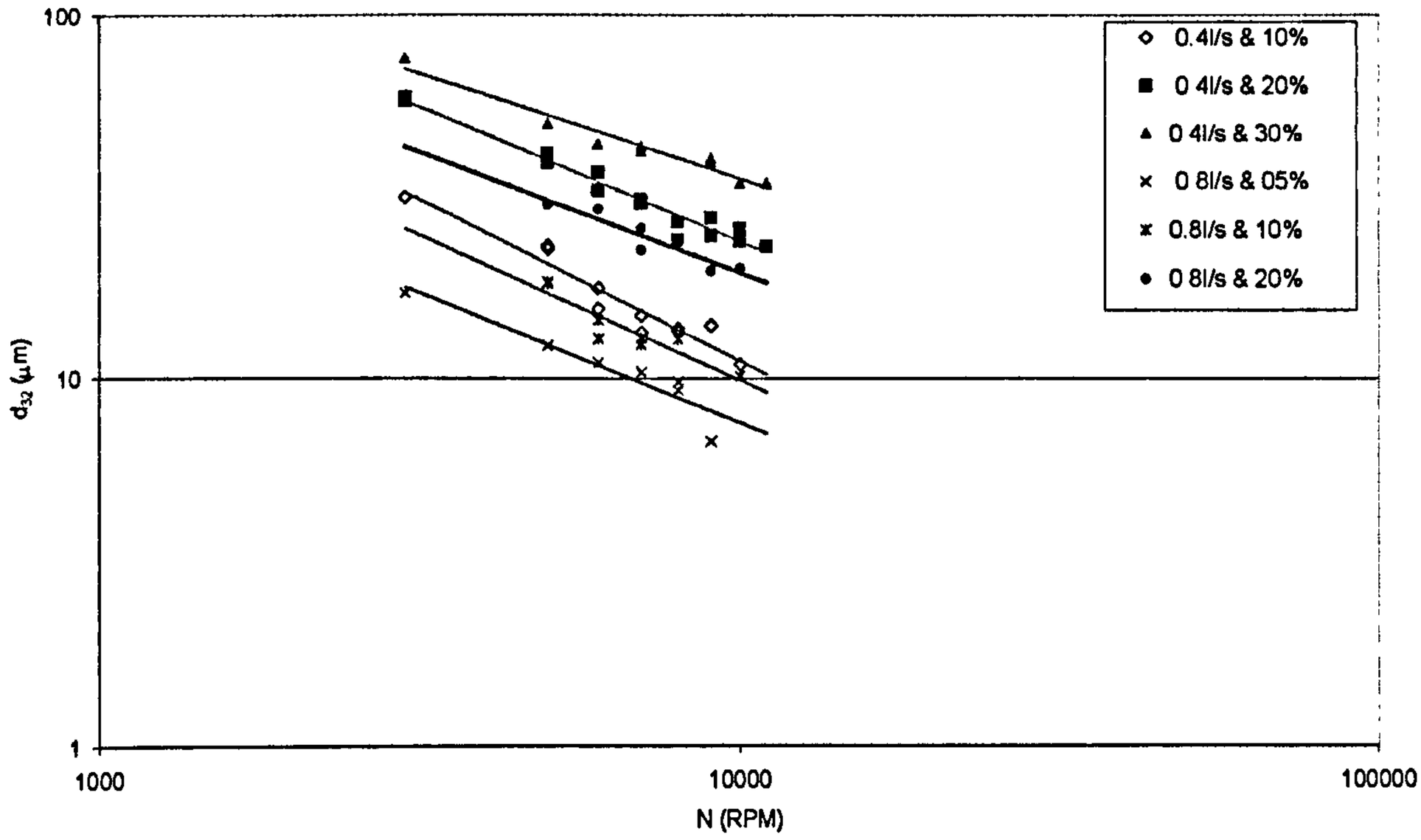

Figure 6.8 d_{32} versus rotor speed for the SHHSS and the ES at different Φ and Q

Table 6.2 shows that the exponent on N for the data collected best match the Chen and Middleman correlation, -0.86 (Equation 2.22). This would suggest that inertial stresses are responsible for droplet break-up and that the drop sizes are below the Kolmogorov length scale.

Table 6.2 The best fit exponents on N for varying Φ

Q (l/s)	Φ (%)	N^x	R^2
0.4	10	-0.88	0.92
	20	-0.82	0.85
	30	-0.58	0.95
0.8	05	-0.82	0.88
	10	-0.79	0.86
	20	-0.66	0.88
Average		-0.77	
Standard Deviation		0.11	

The drop sizes can therefore be correlated by:

$$d_{32} \propto N^{-6/7} \tag{6.1}$$

From Table 2.3 it can be seen that for this correlation to hold true the droplet sizes must be significantly smaller than Kolmogorov length scale. An estimation of the Kolmogorov length scale is given in Section 6.3.6 and the comparison with d_{32} is discussed in Section 6.4.

The correlation of d_{32} with N enables a relationship to be determined that incorporates the effect of Φ.

6.2.7. Correlation of d_{32} with We and Re

Equation 6.1 gives the scaling of d_{32} with the rotor speed. The general form of the Chen and Middleman correlation relates d_{32} scaled with rotor diameter proportionally to $(WeRe^4)^{-1/7}$. The constant of proportionality would be dependent on the mixer geometry and from Figure 6.8 the dispersed phase concentration.

However, for the data set shown in Figure 6.8 the rotor diameter is constant and the geometry of the stator did not have a significant effect on the droplet sizes produced. Therefore, it can safely be assumed that the dispersed phase concentration is the only parameter, in addition to the rotor speed, that affects the droplet size. This allows the following analysis to be performed.

Although, the majority of the data in table 6.2 correlate well with Equation 6.1 it is apparent that there are some deviations at the higher values of Φ, with the largest occurring for $\Phi = 30\%$. For this reason the data for $\Phi = 30\%$ was not considered in the subsequent analysis.

Brown and Pitt (1971) and Streiff et al (1997) showed that Φ could be related to d_{32} linearly in the form shown in Equation 2.31. An attempt is now made to show a similar relationship for the data in Figure 6.8.

As a result of the general relationship in Equation 6.1 the d_{32} can be plotted against $(WeRe^4)^{-1/7}$ for each of the dispersed phase concentrations, Figure 6.9. A straight line can be drawn through the origin and the size data for each of the dispersed phase concentrations, (using a linear least squares fit).

Table 6.3 lists the gradients of the lines for the different values of Φ. If the slopes are plotted against Φ then a linear relationship can be determined that takes the form of Equation 6.2.

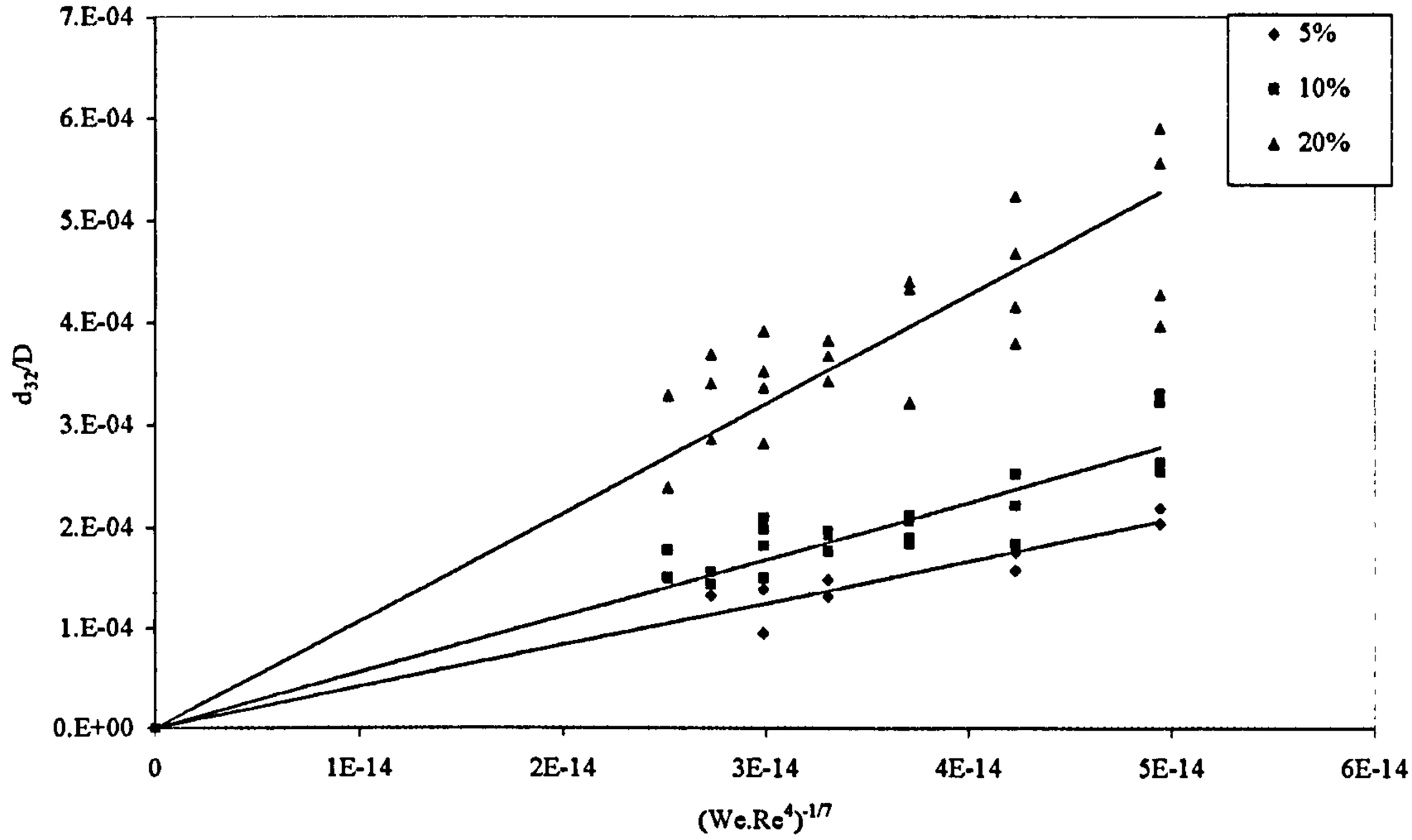

Figure 6.9 d_{32}/D versus $(WeRe^4)^{-1/7}$ for different Φ

Table 6.3 Gradients of the lines in Figures 6.11

Φ	5	10	20
Gradient, m	4×10^9	6×10^9	1×10^{10}

$$m = 4x10^{10}\Phi + 2x10^{9} \qquad (6.2)$$

The general correlation for d_{32} for an in-line rotor-stator mixer (with a constant geometry) in a turbulent system for Φ up to 20% is given by:

$$d_{32} = 2x10^{9}(1+20\Phi)(We\,\mathrm{Re}^{4})^{-1/7} \qquad (6.3)$$

It must be noted that this correlation does not take into account the rotor diameter or stator geometry (e.g open area, hole dimensions). The reason for this is the diameter was not varied for this data set and the screens showed no difference in d_{32} values.

Figure 6.10 shows the d_{32} values determined experimentally against those calculated using Equation 6.3. Although there appears to be certain degree of scatter in the data the correlation shows a reasonable fit.

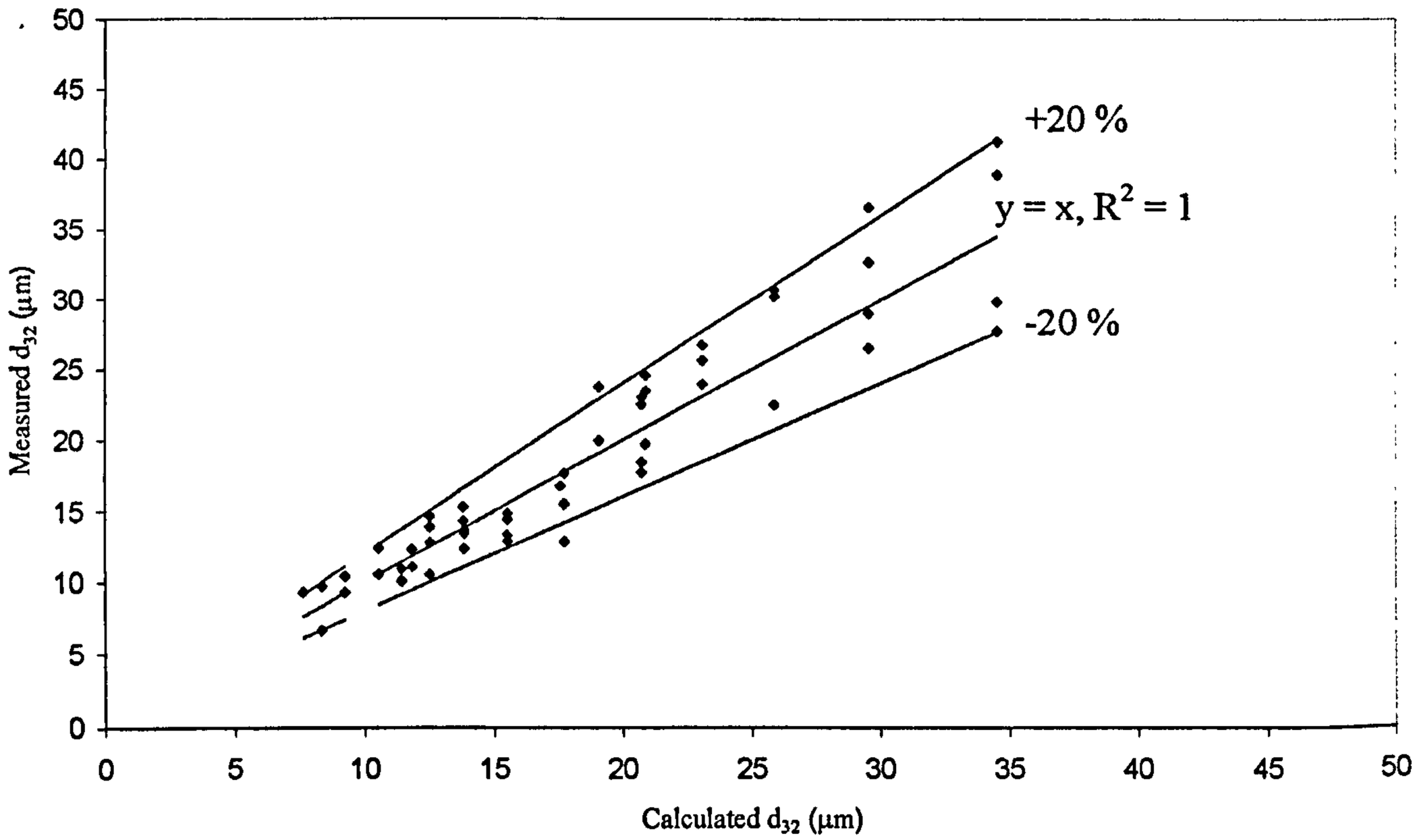

Figure 6.10 Measured d_{32} versus calculated d_{32}

The scatter appears to be more evident at the larger droplet sizes resulting from the higher dispersed phase concentrations. This is not surprising as these values showed the greatest deviation from Equation 6.1. However, Figure 6.10 shows that the scatter is within 20% of the predicted value and it can therefore be said that Equation 6.3 provides a reasonable estimate of d_{32} values.

The scaling of d_{32} with $N^{-6/7}$ should only apply when drop sizes are significantly below the Kolmogorov Length scale. This should occur in the regions of high energy dissipation, which should be in the shear gap where skin friction and turbulent losses are the greatest (Section 2.3.1).

In order to determine an estimate of the Kolmogorov length scale and also the scaling of d_{32} with energy dissipation power measurement were undertaken. The findings of these results are presented and an explanation of the trends in drop size based on power measurements is given in Section 6.4.

6.2.8. Summary

Droplets size data was collected using the Emulsor Screen, ES and the Square Hole High Shear Screen, SHHSS, with a 69.85 mm rotor. The resultant droplet size distributions were relatively broad which is indicative of inhomogeneous energy dissipation and also the occurrence of by-passing.

The droplet sizes decreased with N, however, the droplet size distribution did not change significantly at speeds of 7000 rpm and above. There were no significant differences in the droplet sizes from the ES and the SHHSS. Furthermore, the flowrate, Q, only had an effect on droplet sizes at the lower rotational speeds. Droplet sizes were seen to increase with dispersed phase concentration.

A small number of tests were performed on a 50.8 mm rotor, with four different screens (Slotted head, SH, General Purpose Disintegrating Head, GPDH in addition to the ES and

the SHHSS). The droplet size distributions from the SHHSS and the ES were found to be similar. The GPDH (with the largest open area) gave the largest droplet sizes.

The Sauter mean diameter, d_{32}, was related to d_{max} in the following way:

$$d_{32} = 0.13 d_{\max}$$

The linear relationship validated the assumption that drop break-up was due to a single mechanism and enabled the analysis of the drop size data based on mechanistic correlations.

As the distributions were similar d_{32} values from the ES and SHHSS were considered together. The d_{32} was found to correlate with N with an exponent of approximately -0.8, which was closest to the Chen and Middleman correlation. This implied that the dominant break-up mechanism was due to inertial stresses in the viscous sub-range.

A linear relationship was found between dispersed phase concentration and d_{32} and the following correlation was developed:

$$d_{32} = 2x10^{9}(1+20\Phi)(We\,\mathrm{Re}^{4})^{-1/7}$$

6.3. Power Measurement

The most comprehensive droplet size data was collected using the 69.85 mm rotor with the SHHSS and the ES. For this reason power data was collected over the same experimental conditions for both these screens. To investigate the effects of flowrate on power draw the experimental matrix was expanded for the ES to include a wider range of flowrates.

The following sections discuss the results from the individual components that make up the power balance (Equation 2.49). This data is then used to calculate the total power supplied to the fluid, which in turn is used to determine energy dissipation and the Kolmogorov length scale.

6.3.1. Losses across the control valve and the pipework

The differential pressure was measured across the valve and also before and after each of the pipe reducers and enlargers. This enabled the calculation of the losses in the pipework and across the valve.

The head loss in the pipework was low, a typical value at the highest flowrate investigated was approximately 15W. This value was less than 1% of the corresponding value for total power input. These losses considered to be insignificant relative to the total power input and were incorporated into the losses across the valve.

Figure 6.11 shows the power input associated with losses across the control valve for varying flowrate and a range of rotor speeds. The power input to the fluid by the valve is high and increases with rotor speed and also flowrate. These values were deducted from the total power to give the power contributed to the fluid from the shaft.

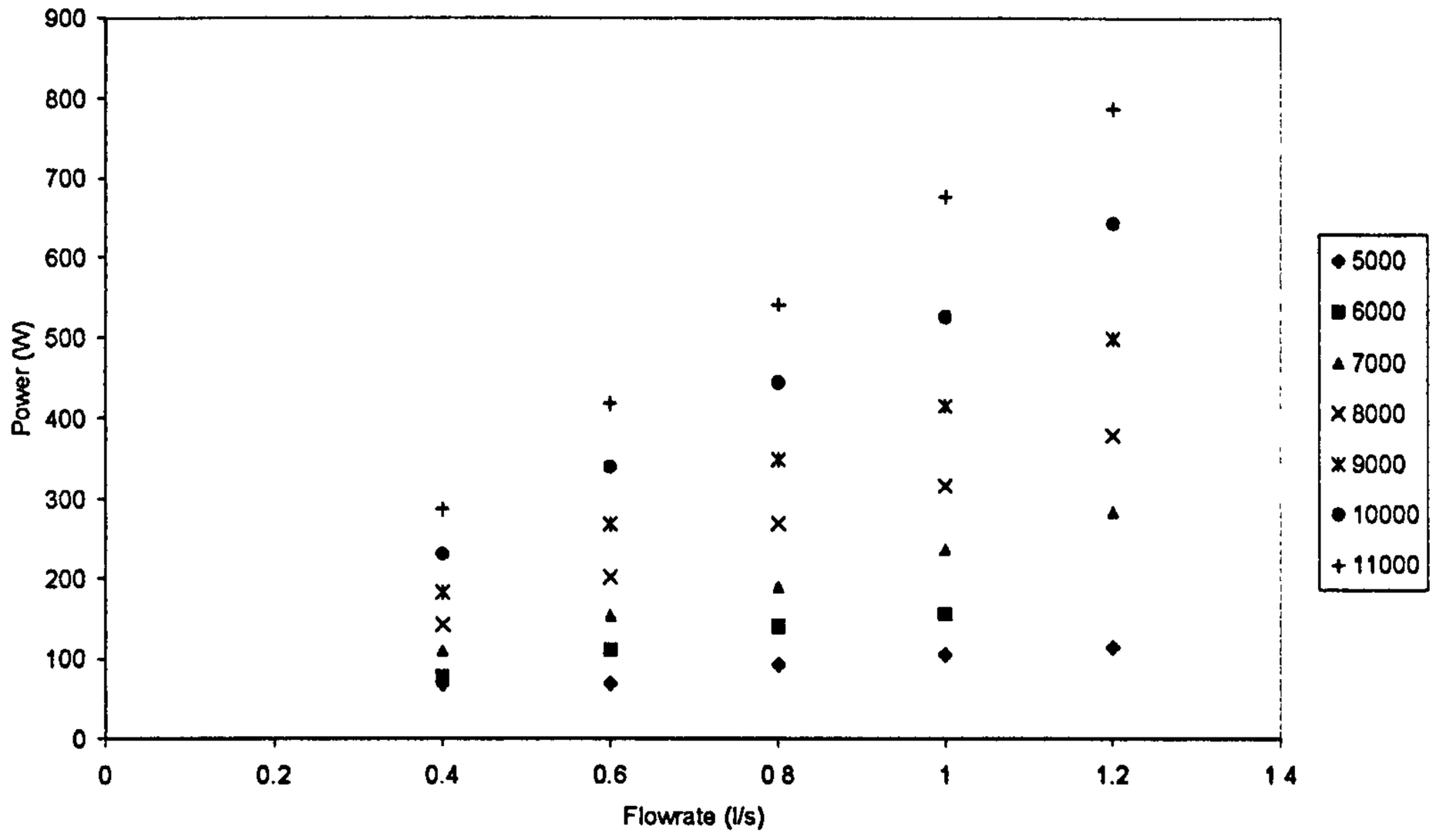

Figure 6.11 Power input across the control valve versus flowrate.

6.3.2. P_{SHAFT}

The results of the shaft power measurements are shown in Figures 6.12 and 6.13 for the Emulsor Screen and the Square Hole High Shear Screen respectively. Figure 6.14 shows a comparison of the power drawn by the two screens at similar flowrates.

As expected, the shaft power increases with rotational speed and there also appears to be greater power draw at the higher flowrates. The influence of flowrate on power draw appears to be more significant at the higher rotational speeds.

There does not appear to be a significant difference between the power drawn by the two different screens (Figure 6.14). There is some scatter at the highest rotational speed, however no valid inferences can be made on this single data set.

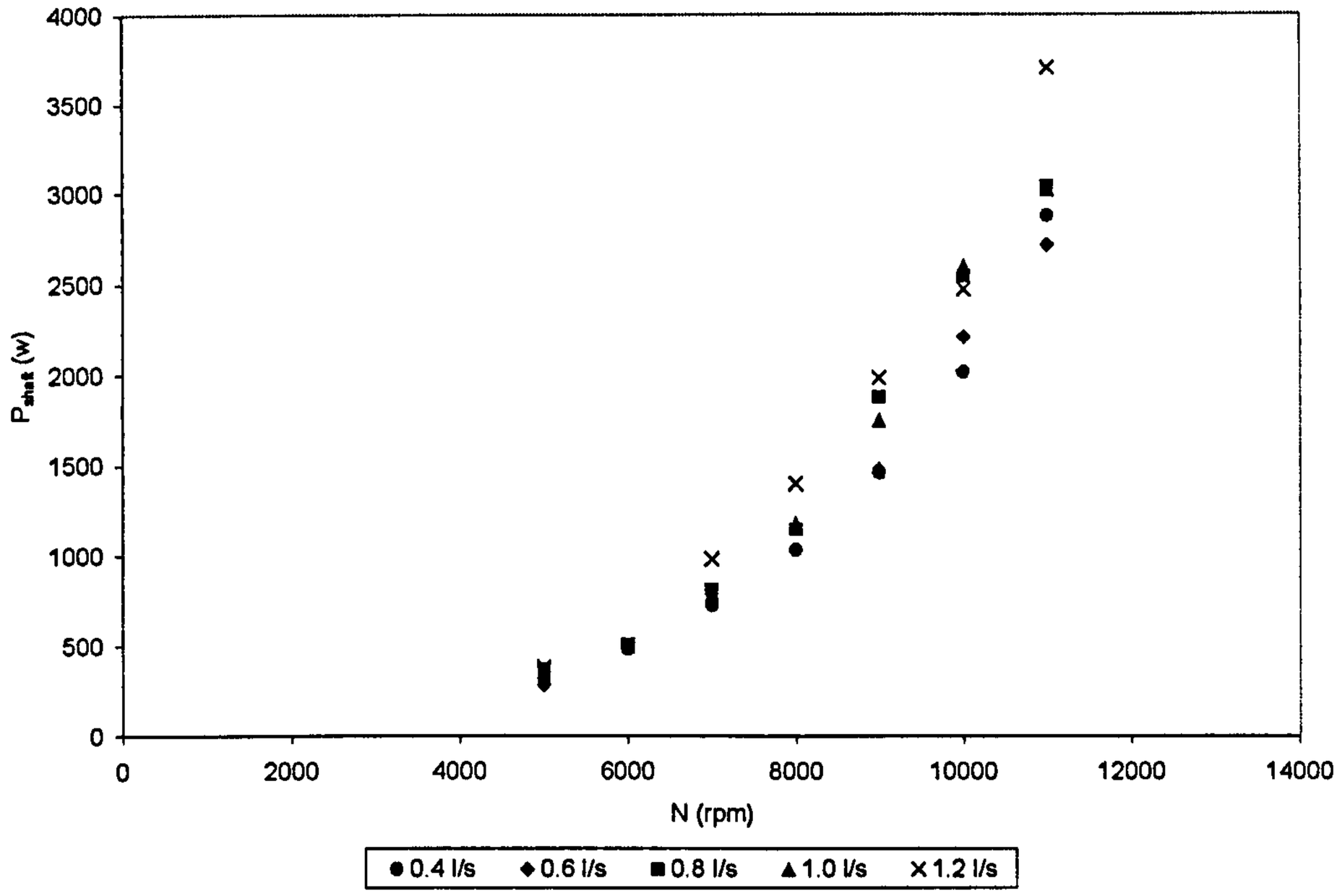

Figure 6.12 Shaft power (W) versus rotational speed (RPM) for the Emulsor Screen

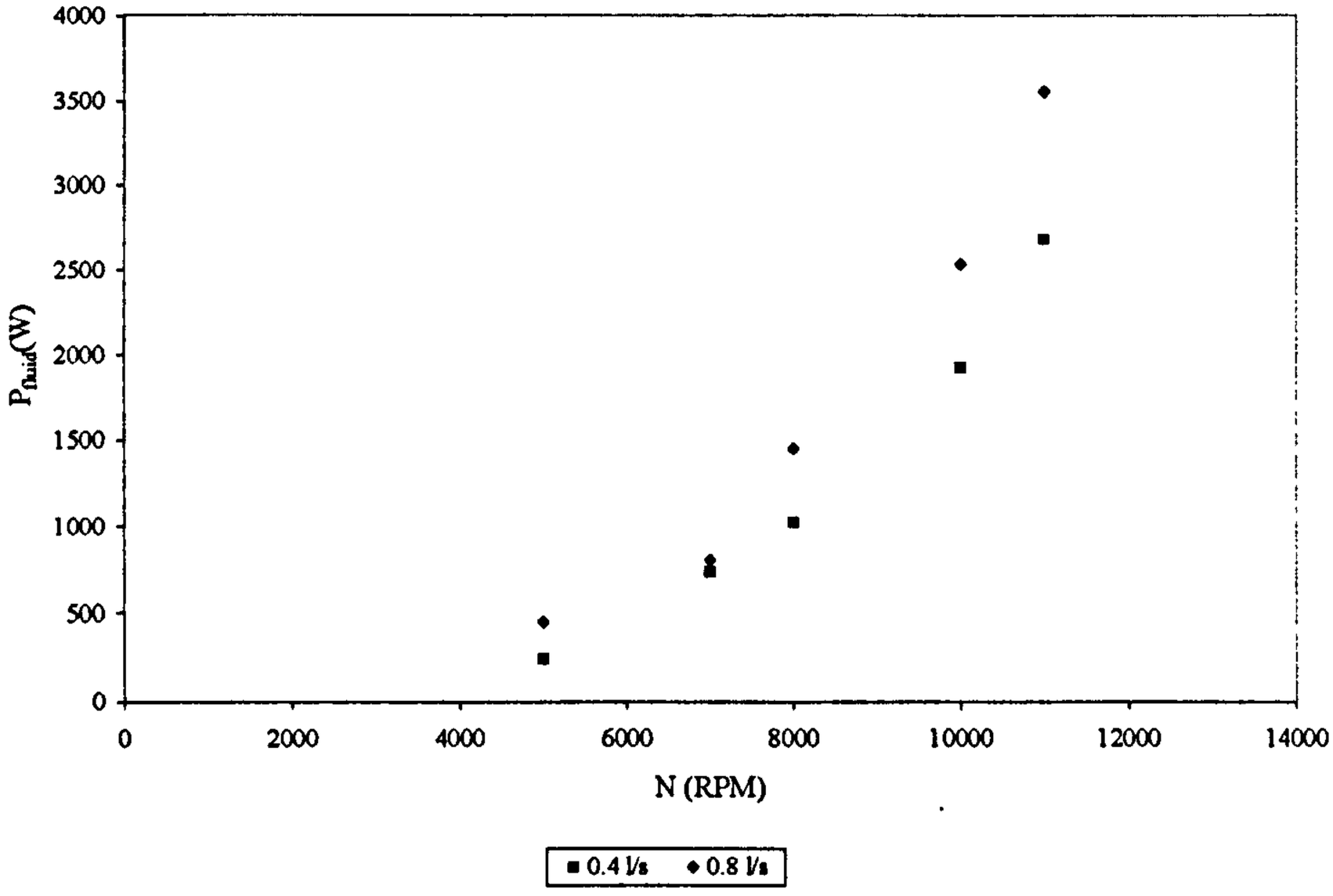

Figure 6.13 Shaft power (W) versus rotational speed (RPM) for the Square Hole High Shear Screen

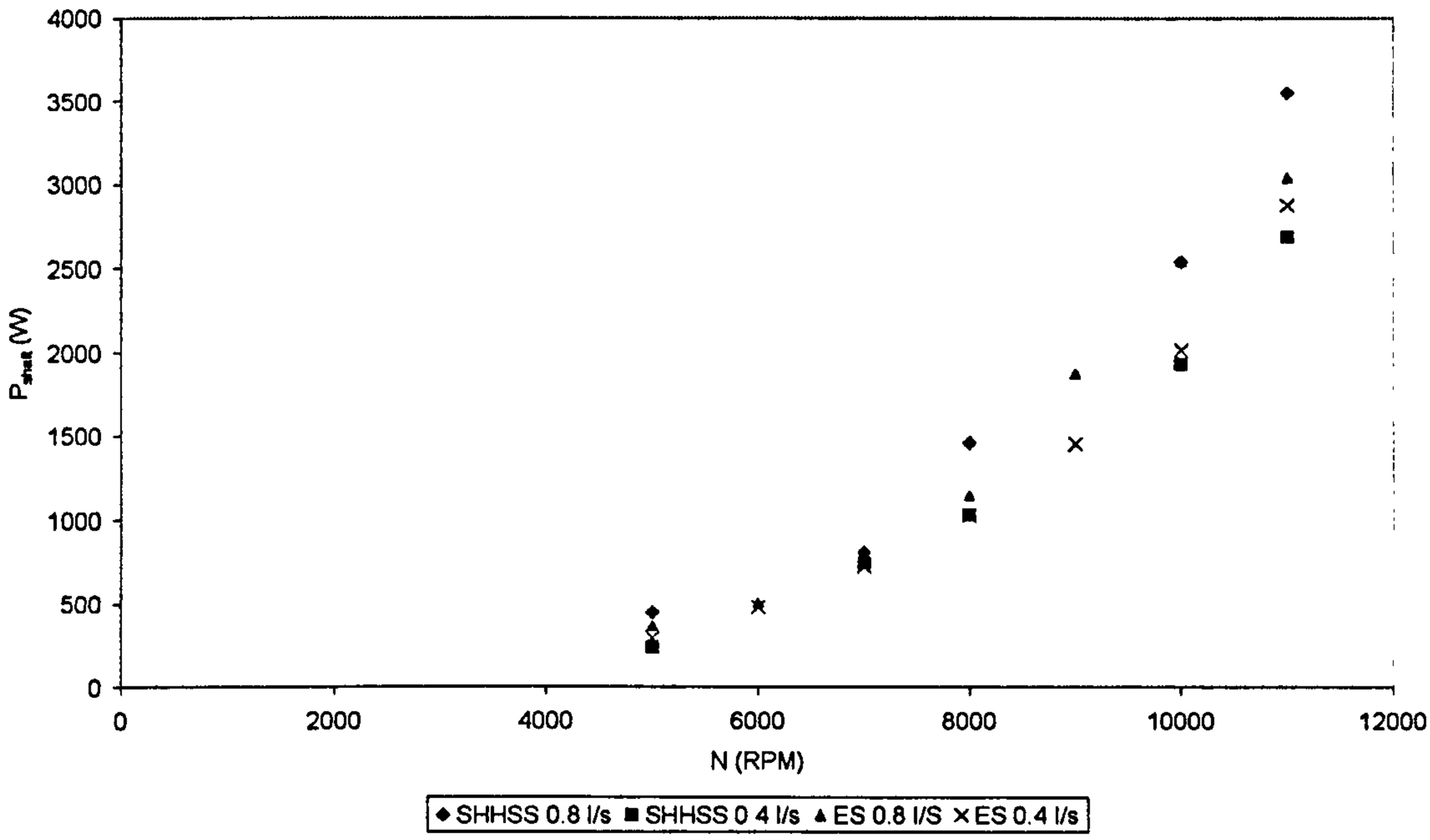

Figure 6.14 A comparison of values for P_{shaft} from the ES and the SHHSS at 0.4l/s and 0.8l/s.

Figures 6.12 to 6.14 shows that shaft power increases with rotational speed and flowrate, the rotor diameter was not varied in these tests. The similarities in the power draw for the two screens suggest that the main parameters effecting power draw in a rotor-stator mixer are the rotational speed and perhaps the diameter of the rotor.

It is also a reflection on the effect of shear gap on power draw, as the clearance between the rotor and the stator are markedly different (0.475 mm for the ES and 0.125 mm for the SHHSS). This suggests that losses due to mean velocity gradients in the shear gap are insignificant supporting claims made by Pedrocchi and Widmer (1988) and Calabrese et al (2000).

It is interesting to note that the open area is similar for both screens (Table 4.1). It was mentioned that the stator performed a flow straightening effect as fluid discharged tangentially by the rotor impacted into the stator wall. This results in a transformation of high kinetic energy into pumping power, skin friction losses and turbulent losses. It was suggested that these losses were greatest where the fluid turned abruptly in the stator hole.

Increasing the number of holes in the stator would effectively increase these losses. The fact that the open area is a direct function of the number of holes suggests that it would display an influence on the power draw of the mixer. This effect was not investigated further in terms of power dissipation but the droplet size data collected for all the different screens for the 50.8 mm rotor seemed to favour this theory.

It can be assumed that the power would depend on the rotational speed and the flowrate by the following relationship:

$$P_{SHAFT} = P_n N^a Q^b \tag{6.4}$$

Where, P_n is analogous to the power number although this equation is not dimensionless.

The effect of rotational speed and flowrate was analysed by performing a multiple regression on all the data collected. Values for P_n, a and b were found to be 0.008, 3.0 and 0.25 respectively with an R^2 value of 0.98, showing good correlation.

Sparks reported values between 2 and 2.5 for the exponent on N and 0.8 to 1 for the exponent on Q. Values ranging from 14.6 to 62.5 were given for P_n.

The lower value of the exponent on Q could be due to the fact that the flowrates investigated in this work are significantly lower than those used by Sparks (1996). Values for P_n would be dependent on a number of variables including the geometry of the mixer.

Figure 6.15 shows the values calculated using Equation (6.4) plotted against measured values. It can be seen that the calculated values match the measured values well and that Equation (6.4) provides a good prediction for the values of P_{SHAFT}.

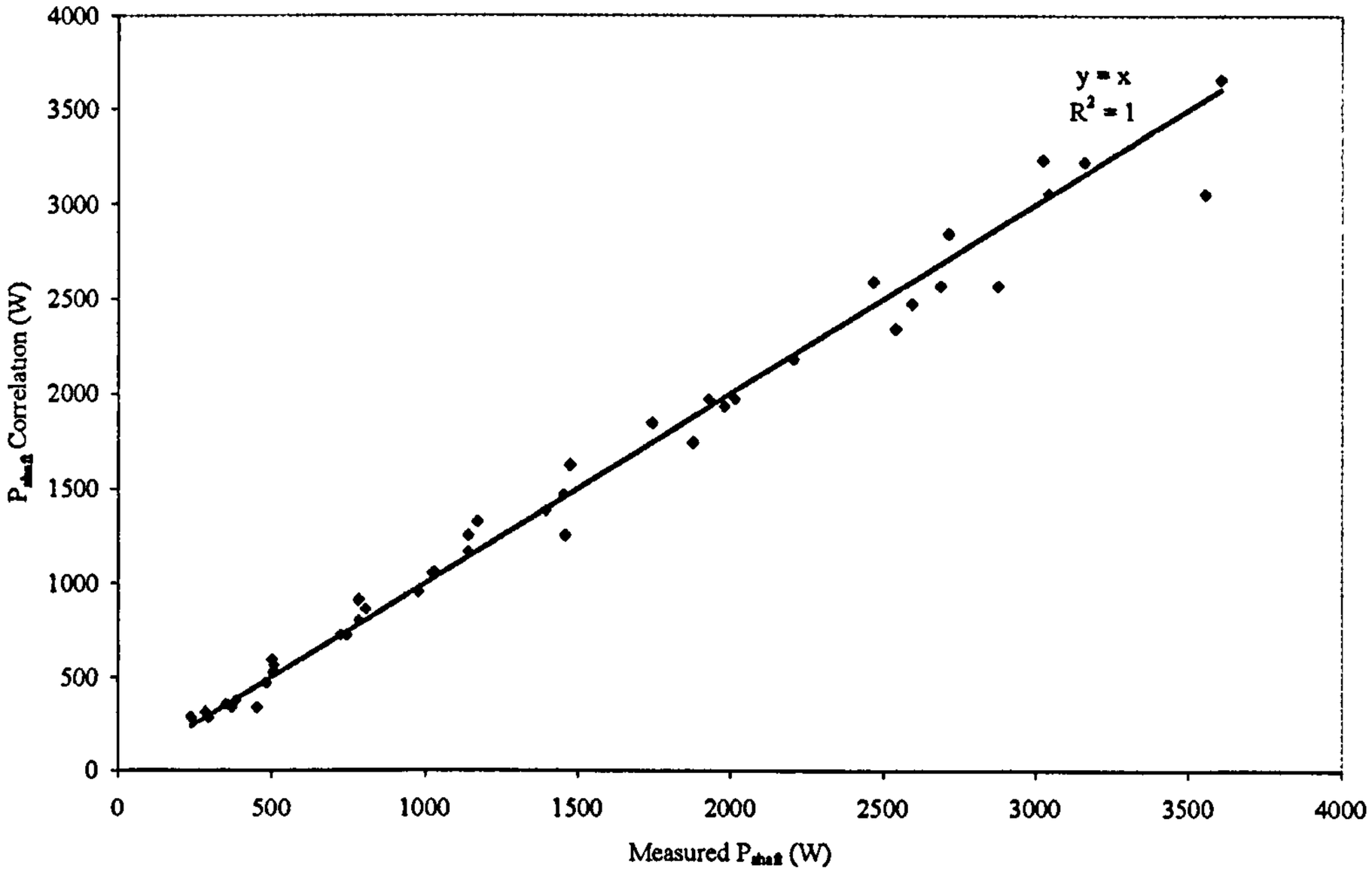

Figure 6.15 Measured P_{SHAFT} data versus correlation

6.3.3. P_{PUMP}

It has previously been stated that in-line rotor-stator mixers can be considered as inefficient pumps. It is important to note that although the pumping effect of these mixers may help in reducing pumping requirements of a process they are not designed for pumping.

Figure 6.16 shows the pumping power plotted against flowrate for the ES. Predictably, the pumping power increases with flowrate and rotational speed. The curves for the lower rotor speeds are flatter than that for the higher rotor speeds. Also, the effect of rotor speed is greater at the higher flowrates.

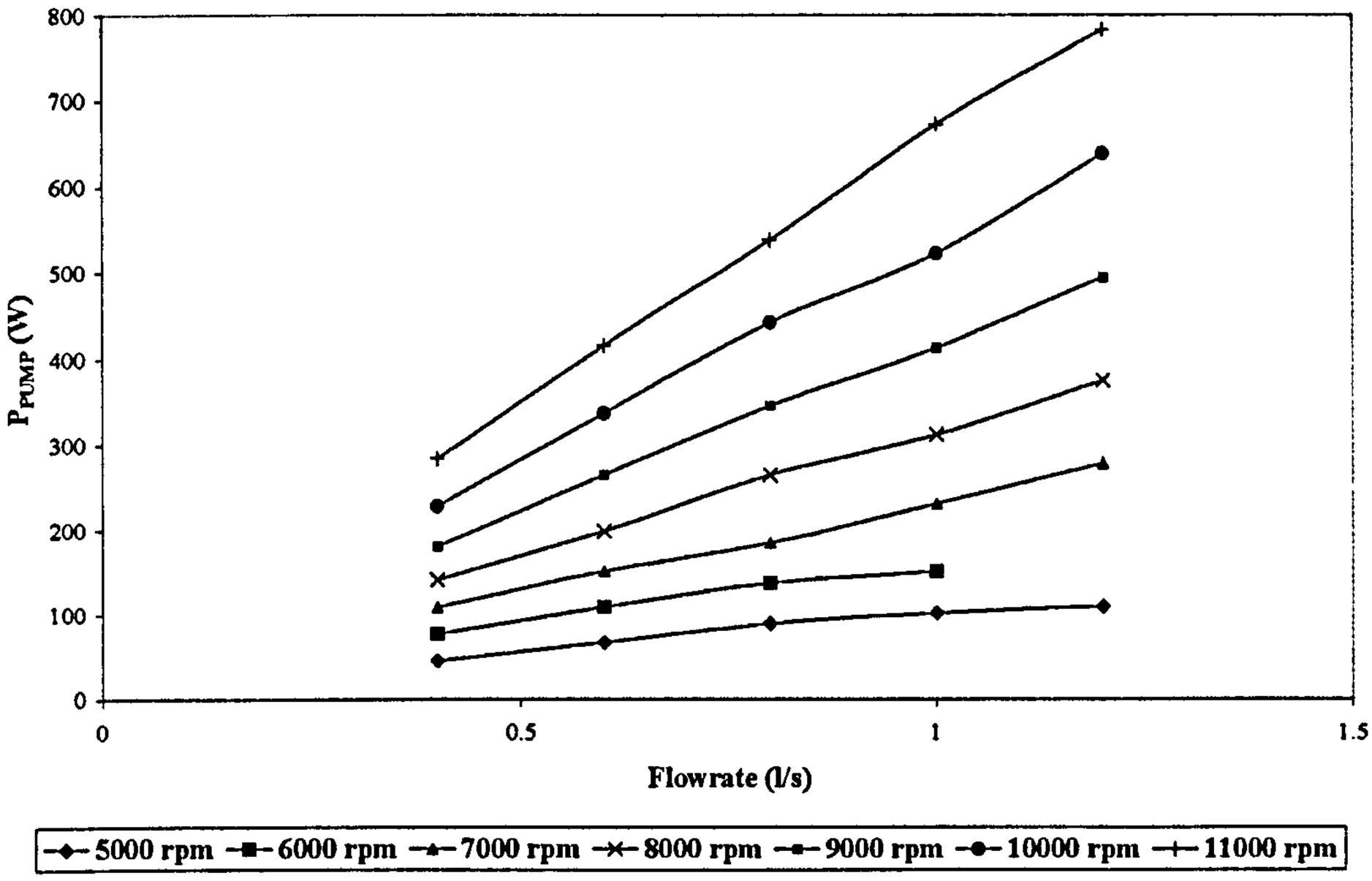

Figure 6.16 Pumping Power versus Flowrate for a range of shaft speed, 69.85 mm rotor and Emulsor screen.

The shape of the curves for rotational speeds of 8000 rpm and above appears to be increasing. This suggests that higher flowrates are possible and that the mixer is operating at the lower end of the pumping curve (i.e. the best pumping efficiency point has not been reached).

The pumping efficiencies were calculated to be between 15% and 20%, these figures are very low compared to centrifugal pumps, for which efficiencies close to 100% are possible. This is an encouraging sign when considering the mixing performance, as in this region of operation the losses useful to mixing (hydraulic and leakage) are greater.

Figure 6.17 shows a comparison of values of pumping power from both the SHHSS and the ES. It can be seen that there is no significant difference in pumping power values for both these screens. The corresponding values for P_{pump} from both screens at constant flowrate and varying N are very close to each other.

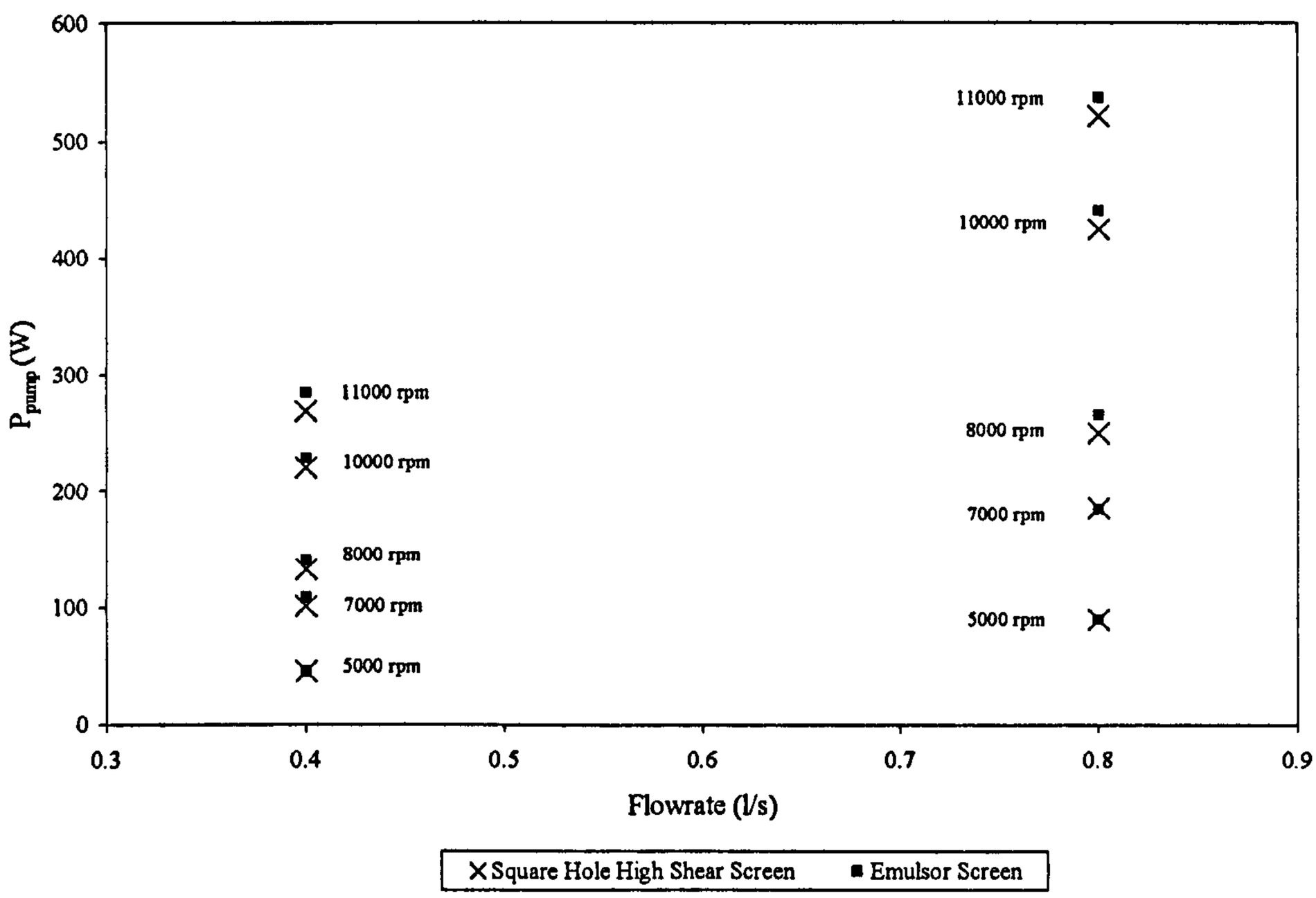

Figure 6.17 A comparison of pumping power values from both the ES and the SHHSS at different flowrates (for increasing N).

Again, this similarity points to the rotor diameter and possibly the open area, in addition to rotational speed, as being the main influences on power draw. Although power data was not collected for different open areas, it is reasonable to believe that the open area may have a significant effect on pumping power. Centrifugal pumps are designed for optimum pressure recovery (the process of converting kinetic energy from the rotor to pumping output), however rotor-stator mixers are not.

The pressure recovery process in a rotor-stator mixer comes from the flow straightening effect of the stator, which does not occur without significant turbulent and frictional losses (Sparks, 1996). This is because fluid is transmitted tangentially with high kinetic energy by the rotor blade. It then impacts on the stator and exits in a predominantly radial direction.

Therefore, the main losses in a rotor-stator mixer are due to the acceleration of the fluid in the rotor and the abrupt deceleration of the fluid in the stator. A smaller open area would increase the amount of fluid that impacts on the stator and thus reduce the power contributed to pumping. The amount of these losses should then depend on the stator design and open area. It would seem reasonable to believe that these losses are advantageous in the generation of dispersions as they would contribute to the turbulent energy dissipation.

The benefits are reflected to a certain degree by Figure 6.6 which showed d_{32} values from the dispersion tests performed on the 50.8mm rotor with the four different screens. Smaller droplet sizes were seen from the Square Hole High Shear Screen and the Emulsor Screen (with the smallest open area), whereas, the GPDH (with the largest open area) produced the largest droplets.

6.3.4. P_{MECH} and P_{DISC}

The mechanical losses were measured by spinning the shaft without the rotor attached. The mixing head was filled with water and the inlet and the outlet was blanked off. The temperature of the water and the time was measured. The resultant temperature rise of the

water was due to friction within the seal and the bearing and also the drag on the shaft and spring.

It was not possible to measure the losses associated with disc friction and therefore an empirical correlation (Equation 2.54) was used to calculate them (Karassik, 1986).

Figure 6.18 shows the measured values for P_{MECH} and P_{DISC}. It can be seen that both these losses increase with rotational speed. The highest value of P_{MECH} is close to 40 W (for 12000 rpm) which, compared to the equivalent shaft power, approximately 3 kW. Therefore, it can be said that at the highest shaft speeds, where the mechanical losses are greatest, they account for approximately 1% of the total shaft power. The corresponding value for disc friction (≅ 300 W) was approximately 10% of the total shaft power input.

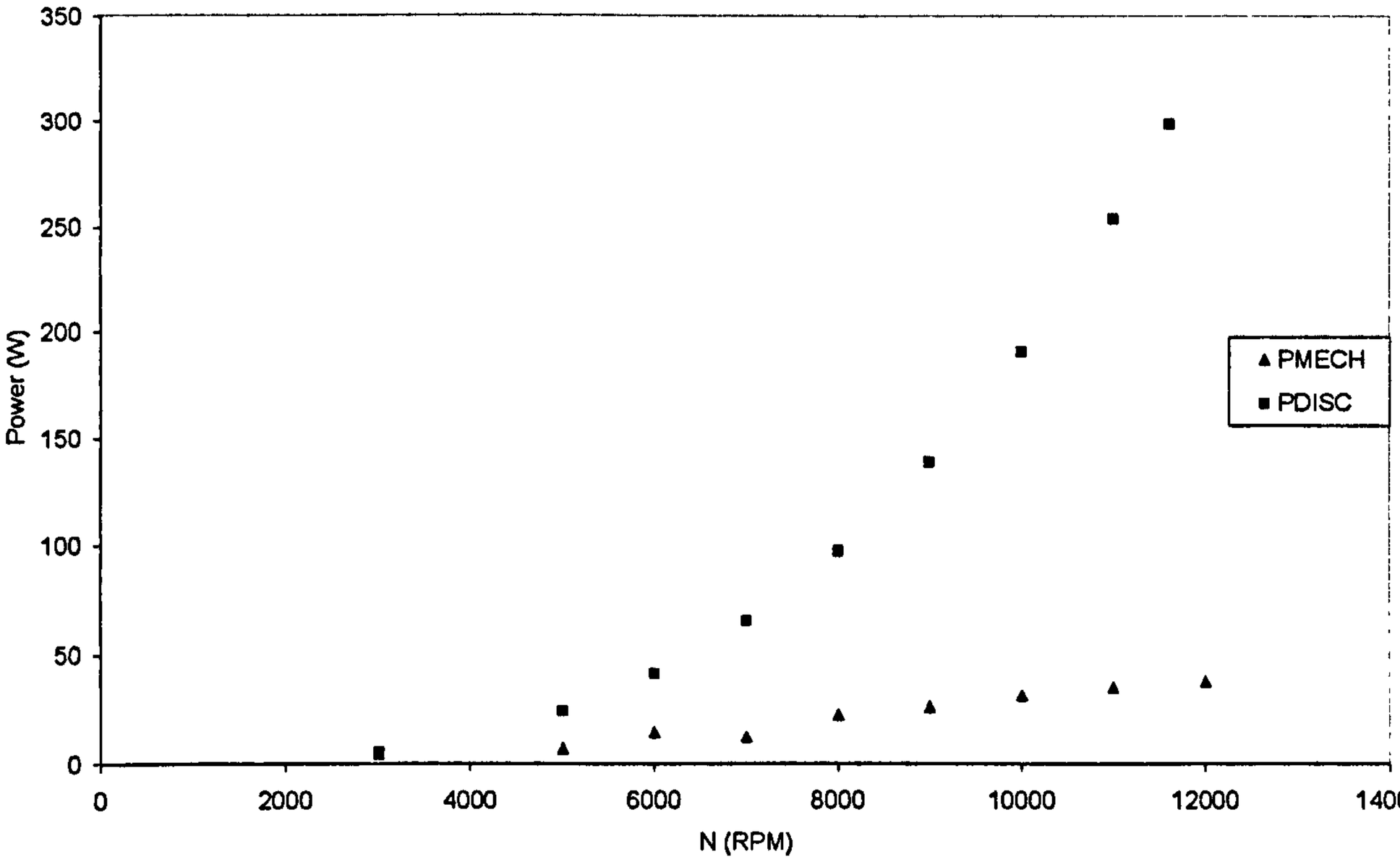

Figure 6.18 Mechanical and Disc frictional losses versus rotational speed.

6.3.5. Power supplied to the fluid by the rotor, P_{FLUID}

The contribution of the mechanical and disc friction losses to mixing and pumping in a rotor-stator mixer is negligible. The total power supplied to the fluid associated with pumping and mixing, P_{FLUID}, is the remainder of the power balance (i.e. energy supplied to the fluid by Hydraulic and Leakage losses):

$$P_{FLUID} = P_{LEAK} + P_{HYDRAULIC} + P_{PUMP} = P_{SHAFT} - (P_{MECH} + P_{DISC}) \tag{6.5}$$

As values for shaft and pumping power were not significantly different between the ES and the SHHSS, all the power data collected was considered in the following analysis.

As there is very little information on power draw for rotor-stator mixers the following analysis was done in terms of power number, (similar to that for an impeller in a stirred tank). For turbulent systems the power dissipation would be expected to be proportional to N^3.

Flow visualisation work done by Sparks (1996) showed that the fluid at the tip of the rotor blade follows the rotor at the same velocity as the tip speed, v_{tip}. Therefore, the kinetic energy imparted to the fluid, of mass m, at the rotor tip is given by:

$$KE = \frac{1}{2} m v_{tip}^2 \tag{6.6}$$

The equivalent power is then:

$$P = \frac{1}{2} \rho Q v_{tip}^2 \tag{6.7}$$

However, v_{tip} can be expressed as πND giving:

$$P_{FLUID} = \frac{1}{2}\pi^2 \rho Q N^2 D^2 \tag{6.8}$$

When the rotor-stator mixer is operating without a supplementary pump, the flowrate can be expressed as (Sparks, 1996):

$$Q \propto ND^3 \tag{6.9}$$

Therefore, the following expression can be obtained for power supplied to a fluid in an in-line rotor-stator mixer:

$$P_{FLUID} = P_o \rho N^3 D^5 \tag{6.10}$$

Where, the constant of proportionality P_o is the power number, a dimensionless group that is a function of the geometric, kinematic and dynamic properties of the system.

Figure 6.21 shows a plot of P_{FUID} versus rotational speed and the corresponding results from the regression performed on all of the data. The exponent on N is 3 (with an R^2 value of 0.94 showing a good correlation) which is what would be expected for fully turbulent conditions. Equation (6.10) can therefore be used to determine the power number and hence calculate the power supplied to the fluid by the rotor.

From Equation (6.10), the power number is:

$$P_o = \frac{P_{FLUID}}{\rho D^5 N^3} \tag{6.11}$$

As the values for P_{FLUID} scale with N^3, the power number can be determined from Figure 6.19.

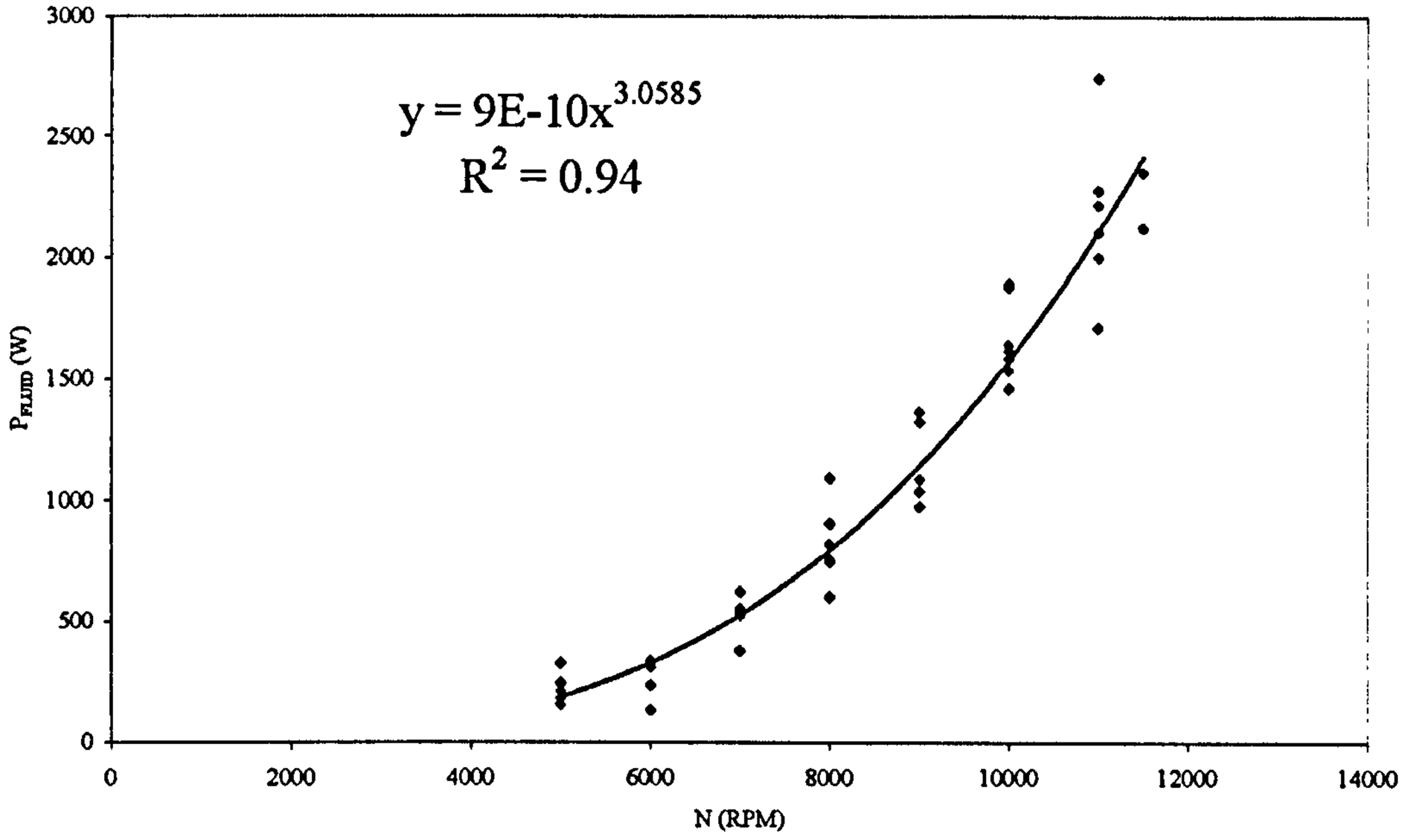

Figure 6.19 P_{FLUID} versus N and the dependency of P_{FLUID} on N.

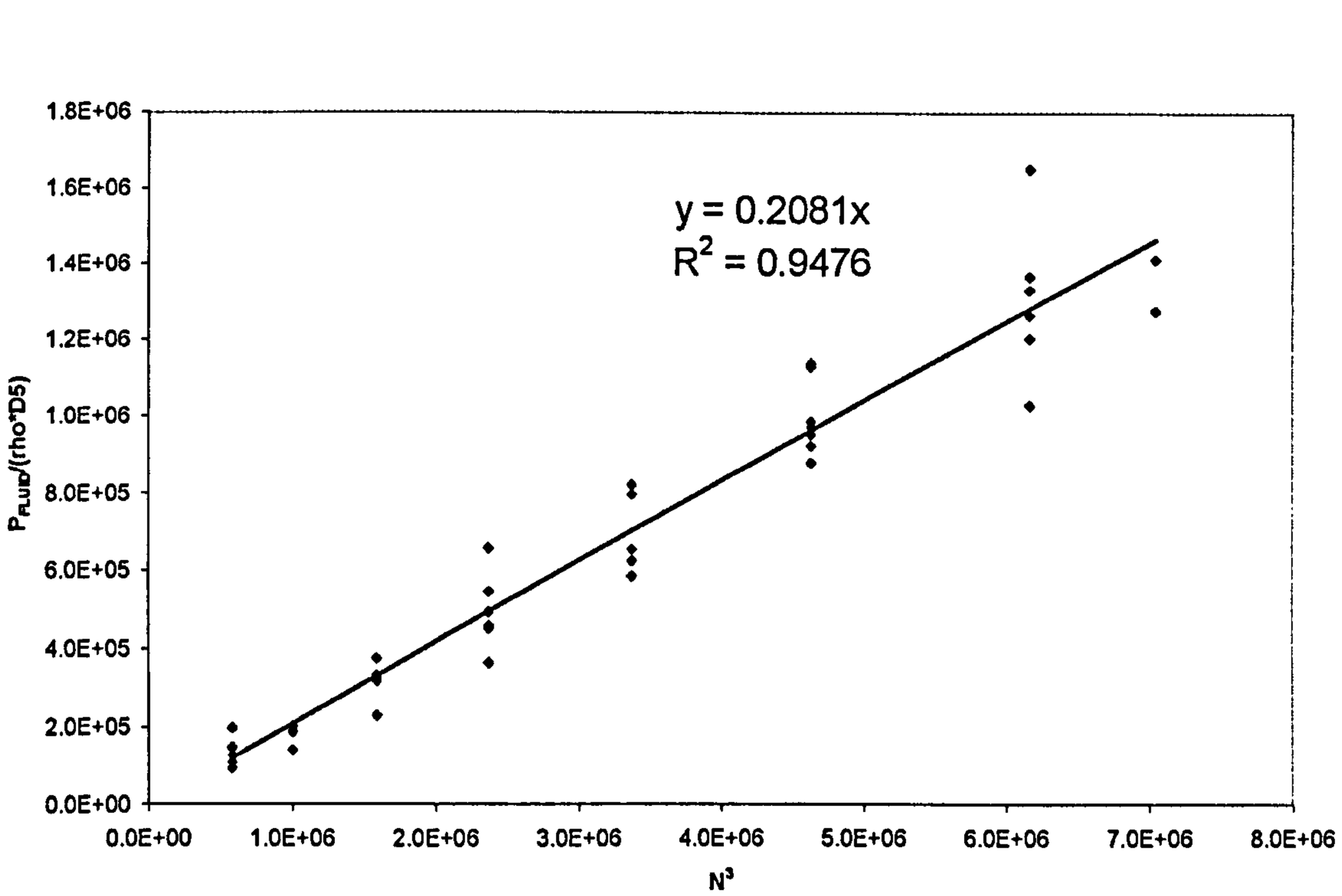

Figure 6.20 $P_{FLUID}/\rho D^5$ versus N^3.

Figure 6.20 shows the power number to be 0.2 which is low compared to values quoted by Sparks (1996) who evaluated power numbers in the region of 10 for both the Toothed design and the Silverson design. Francis (1999) reported values between 2.5 and 4.5 in a laboratory scale batch rotor-stator with various stators (none of which were similar to the ones studied in this power work).

In fully turbulent conditions the power number is constant and is dependent only on the geometry of the rotor. A possible reason for this low power number is that a valve is used to control the flow, reducing the pumping required of the mixer. The shaft power was seen to increase with flowrate suggesting that power draw would increase if the mixer was left to pump by itself.

Equation (6.10) defines the energy dissipated to the fluid by the rotor in the rotor chamber. It is in this region of the mixer where it is thought that the maximum turbulent energy will be dissipated

Figure 6.19 show that it is reasonable to assume that the mixer is exhibiting turbulent characteristics, at least within the rotor chamber. The energy dissipation rates will vary throughout the rotor-stator mixer with a maximum value around the stator region (where the fluid impinges on the stator).

The broad droplet size distributions generated by a single-pass through the mixer adds further weight to this observation. This also leads to the conclusion that the majority of the droplets are not exposed, either at all or for long enough, to the regions of high energy dissipation.

6.3.6. Energy dissipation and the Kolmogorov length scale

The energy dissipation rate, ε, was discussed in Section 2.3.4 and it was defined as the power supplied to the fluid by the rotor divided by the mass of the fluid. It can be assumed that the pumping power has little influence on mixing. It can also be assumed

that the hydraulic losses would be responsible for the majority of the turbulent mixing that occurs in a rotor-stator mixer. Therefore, referring back to the power balance (Equation (2.49)) the power contributed to useful mixing is represented by $P_{HYDRAULIC}$ + $P_{LEAKAGE}$.

Various researchers have used different definitions of the mass (or volume) of fluid depending on the area in the mixer considered to have the maximum energy dissipation. The rotor supplies energy to a small region of the rotor-stator mixer encompassing the rotor, the stator holes and the shear gap. Consequently, the total volume of this region of the mixer (0.064 litres) was used when calculating the energy dissipation rates.

Sparks (1996) estimated, from diazo-coupling experiments that less than 3% of the power supplied to the fluid was dissipated as turbulent energy, ε. This would appear to be a very small percentage, however he reasoned that there was considerable by-passing and inhomogeneity in the turbulence field meaning that a proportion of the fluid passing through the mixer may not experience the highest energy dissipation rates.

Subsequently, the values calculated for energy dissipation rates ranged from 70 W/kg at 5000 rpm to 800 W/kg at 11000 rpm. These values were then used in Equation 2.6 to determine the Kolmogorov length scale, λ_k. Figure 6.21 shows λ_k versus rotational speed for all the power data collected.

In a stirred tank ε is an undetermined function of the spatial coordinates of the tank. For sufficiently long residence times all drops in a dispersion will sample the full spectrum of energy dissipation. Therefore, D_{max} will be determined by the largest values of ε. It is worth noting that the energy dissipation rates will vary throughout the rotor-stator mixer, with a maximum value around the stator region (where the fluid from the rotor impinges on the stator). The values for λ_k would be smaller in this area than those calculated for the mixer volume as a whole.

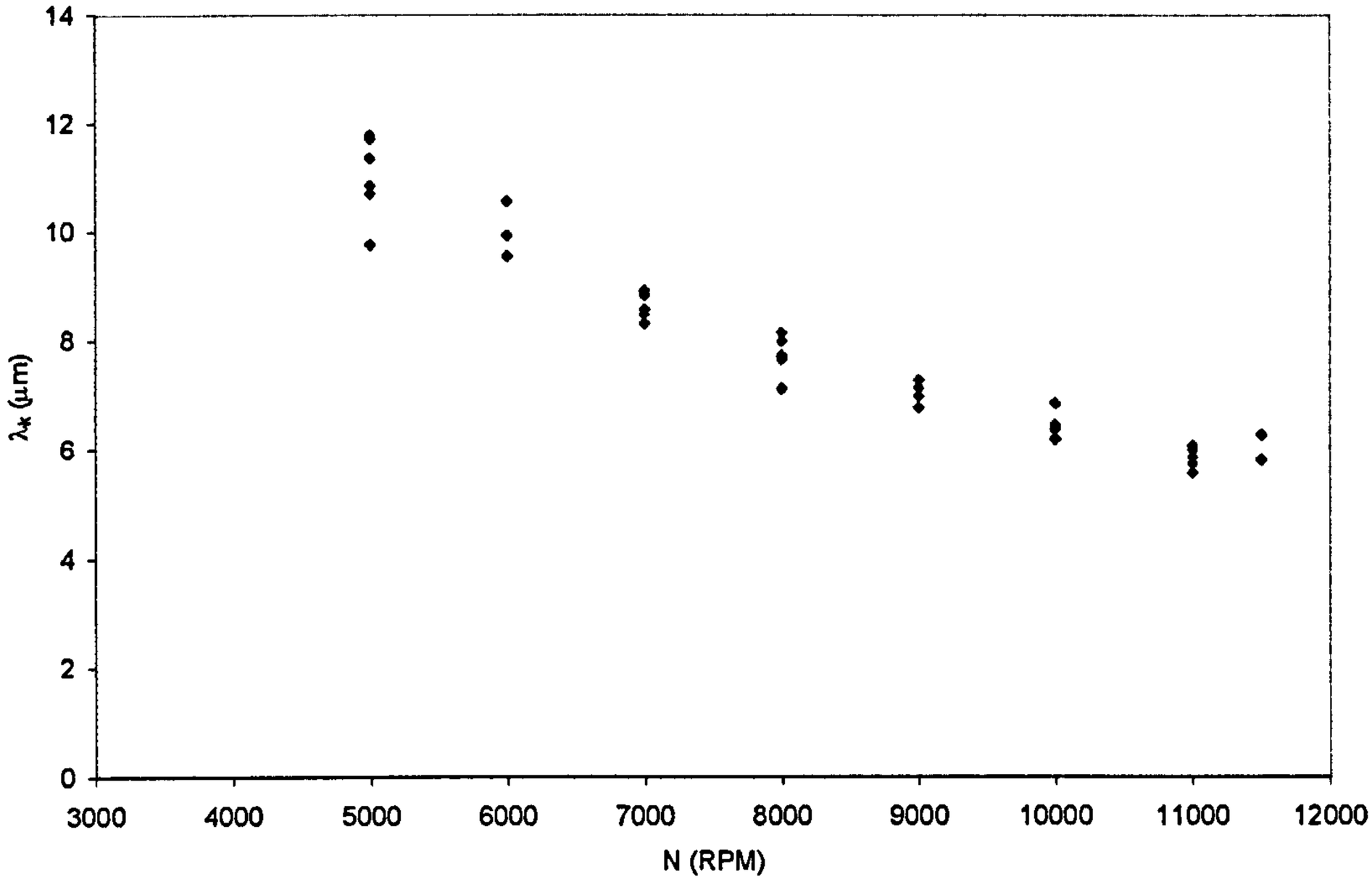

Figure 6.21 The Kolmogorov length scale versus impeller speed

6.3.7. Summary

A thermometric technique was employed to determine the power the in-line rotor-stator mixer supplied to the fluid. This then enabled values for ε to be estimated which in turn were used to estimate λ_k.

P_{shaft} was found to increase with N and Q. The SHHSS and the ES showed very similar power characteristics, which led to the inference that the effect of shear gap was insignificant. Also, it was reasoned that the open area of the screen was an important factor in the power of the mixer.

This was supported by the droplet size data collected from the 50.8 mm rotor. The GPDH (largest open area) generated the largest sizes and the SHHSS and the ES (smallest and similar open areas) created the smallest droplets.

A general correlation to estimate P_{shaft} (which would be useful in sizing motors) was developed for flowrates ranging from 0.4l/s to 1.2l/s:

$$P_{shaft} = 0.008xN' xQ^{0.25}$$

The pumping power of the rotor increased with Q and N and as for P_{shaft}, the open area was also thought to be influential.

The power supplied to the fluid in terms of pumping and hydraulic losses, P_{FLUID} was found to scale with N^3. This led to the deduction that the mixer was operating in the turbulent regime and the power number was 0.2.

Values for ε were determined by assuming a proportion (<3% as reported by Sparks, 1996) of P_{FLUID} was converted to turbulent energy. Consequently, values ranged from 40 W/kg at 5000 rpm and 800 W/kg at 11000 rpm. The corresponding values for λ_k were then estimated to range from 12μm (at 5000 rpm) to 6μm (at 12000 rpm).

6.4. An explanation of the trends in droplet size based on energy dissipation

Figure 6.21 shows that values of λ_k range from approximately 12μm down to 6μm as the rotational speed varies from 5000 rpm to 11500 rpm. Figure 6.22 shows a comparison of these values to d_{32} (from Figure 6.5).

Figure 6.22 shows that values of d_{32} are approximately twice the size of λ_k at $\phi = 10\%$ and up to 5 times at $\phi = 30\%$. This suggests that $D > d_{32} > \lambda_k$ which are more appropriate conditions for drop break-up due to the inertial sub-range eddies rather than the viscous

sub-range as implied by Equation (6.3). It would appear that d_{32} at the lowest dispersed phase concentrations generates droplets closest to λ_k. This again points to the fact that an increase in dispersed phase concentration dampens the formation of turbulent stresses.

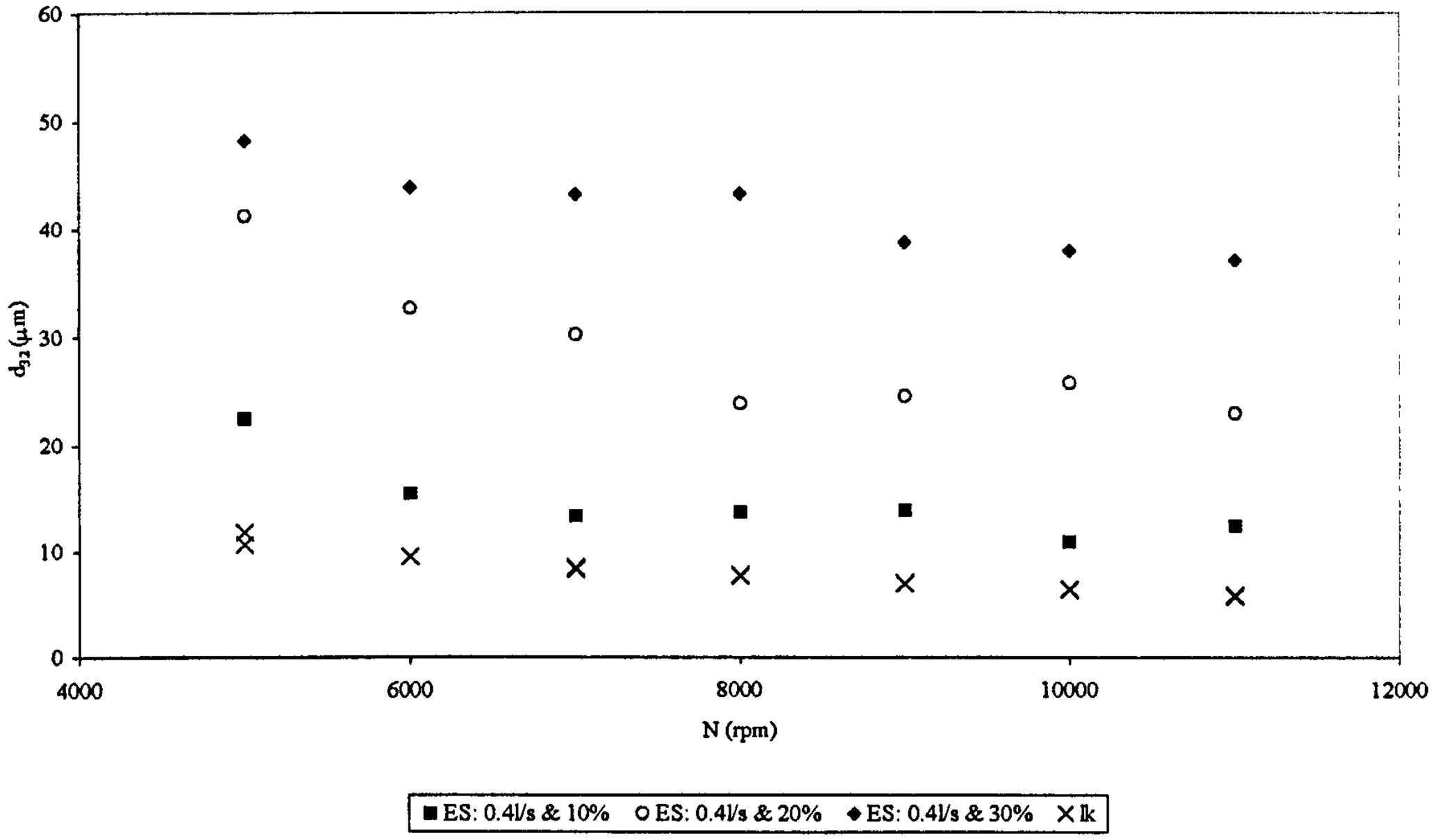

Figure 6.22 A comparison of d_{32} and λ_k versus N (at 0.4l/s for ES)

Droplets ranging from approximately 100 μm with the main peak at around 50 μm and the smaller range below the 10 μm were observed in the volume frequency curves (Figure A.4 and A.12). The broad size distributions and the fact a percentage of the distributions are below the smallest scale of turbulence would suggest that not all of the droplets are passing through the areas of high energy dissipation (that determine the

Kolmogorov length scale). This would further suggest that break-up is more than likely caused by more than one mechanism.

The determination of the dominant drop break-up mechanism can also be based on the dependency of d_{32} on energy dissipation rates, ε, (Equations, 2.10, 2.17, 2.21, 2.24). The results of a regression performed on d_{32} plotted against ε are presented in Table 6.4.

Table 6.4 The best fit exponents on ε for varying Φ

Φ (%)	ε^x	R^2
05	-0.21	0.82
10	-0.22	0.75
20	-0.19	0.74
30	-0.13	0.80

Although, there is a certain degree of scatter in the results (the R^2 values show a significant deviation from 1) the exponents on ε closely match -0.2 similar to that in the Shinnar correlation for droplet break-up in the viscous sub-range. This also corresponds with values reported by Schubert (1997).

When correlating the size data with energy dissipation rates the dominant drop-break mechanism is found to be inertial stresses in the viscous sub-range. This was similar to observations made when correlating against rotor speed (albeit with a different form of the energy equation). However, as highlighted previously, both these models should only hold if d_{32} is lower than λ_k.

It is worthwhile to draw further attention to the values of λ_k for a possible explanation in the discrepancies between the correlations and the drops sizes relative to λ_k. The Kolmogorov length scale was calculated using the average energy dissipation rate. The smallest eddy sizes would be generated in the region of the mixer that exhibits the highest energy dissipation rates.

It has previously been discussed that the energy dissipation in the rotor-stator mixer exhibits inhomogeneous tendencies. The number of droplets that would come into contact with this region, in a single pass would be small. This high localised ε would account for the droplet sizes below 10 μm. This would suggest that d_{32} is not a result of the highest energy dissipation rate and may be the reason for the possible discrepancies in the models relative to the applicable size ranges.

Figure 6.22 shows that the droplet sizes closest to λ_k are generated at the lowest dispersed phase concentrations. It is possible that at this dispersed phase concentration, larger droplets are being more effectively broken up before they enter the region of high energy dissipation rates (as there is more turbulent flow throughout the rotor region). This would mean that the number of droplets will grow, increasing the likelihood of them coming into contact with the high ε zones.

It must be emphasised that the approach used to identify the dominant break-up mechanism is a simplistic method of determining an understanding of the complexities of the drop break-up process. At any given point and time in the mixer one mechanism may be responsible for droplet break-up, however it is more than likely that more then one mechanism is responsible for the final distribution. By comparing λ_k with the droplet size distributions it can reasoned that macro-scale eddies, inertial stresses and turbulent viscous shear are responsible for droplet break-up.

The following section is an analysis based on Reynolds numbers and residence times (as defined in Section 2.3.1) to determine which regions in the mixer are most likely to determine the droplet size distribution.

6.5. Flow regimes in the rotor-stator mixer: Re analysis

The following section discusses the flow in the various regions of the mixer (as defined in Section 2.3.1). An attempt is made to determine whether the time scales would allow turbulent or viscous stresses to cause drop break-up in region of the mixer.

The in-line rotor-stator mixer is divided into the following sections, as defined in detail in Section 2.3.1; the inlet pipe, rotor region, shear gap, stator and volute. A summary of the calculated results can be found in Table A.2, Appendix 5.

6.5.1. Inlet pipe

The effect of inlet flows on the droplet size distribution was first discussed in Section 6.2.4. It was found that the droplet size distributions showed bi-modal tendencies with drop diameters observed above 1000 μm, which is beyond the measurement range of the Malvern Mastersizer. A possible explanation for this occurring was that the inlet flows to the mixer were not well mixed and therefore large globules of dispersed phase were passing through the mixer without coming into contact with the continuous phase and the areas of high energy dissipation.

The pipe Re number was estimated using Equation (2.34) and values in the order of 20,000 and 40,000 were calculated (at 0.4 l/s and 0.8 l/s respectively). This would indicate the flow in the inlet pipe is fully turbulent.

In turbulent flow, if drop break-up is due to viscous shearing action the un-deformed drop and resulting elongated drop must be small compared with the local regions of viscous flow (Hinze, 1955). However, when the Re is relatively high, such as in the inlet pipe, the spatial dimensions of such local regions would be very small compared with the largest drops in the system. Therefore it would be a reasonable assumption that inertial stresses are responsible for the maximum droplet sizes in the inlet pipe.

The following is a crude analysis to determine whether it is feasible for turbulent eddies to be the main cause of drop break-up. The assumption of homogenous local isotropy is valid over the volume of pipe containing a turbulent liquid (Davies, 1985, Hinze, 1955). Equation (2.18) can therefore be used in order to estimate the maximum stable drop size that would exist in the in-let pipe before entering the mixer. (The velocity of the bulk fluid in the pipe and the pipe diameter were used as the characteristic scales in the calculation of We and the constant of proportionality was assumed to be 1).

Values for d_{max} were calculated to be 800μm and 400μm (at 0.4l/s and 0.8l/s respectively). Predictably a 2 fold increase in pipe velocity results in a 2 fold decrease in d_{max}. These calculated values of d_{max} can be inserted into Equation (2.13) to back calculate the energy dissipation rate required to create droplets of this size. The values for ε were calculated as 20 W/kg at 0.4 l/s and 150 W/kg at 0.8 l/s.

The time scale of the duration of an eddy causing drop break up can be estimated by assuming that the eddy length is the same size as d_{max} and the instantaneous velocity acting on the drop is the maximum velocity in the pipe. Therefore, the time scale of an eddy responsible for drop break-up (d_{max}/u) is in the order of 10^{-6}s. This is significantly smaller than the nominal residence times in the pipe which are in the order of 10^{-2}s.

Hinze (1955) reasoned that in turbulent flow the area around the drop, plane hyperbolic (extensional), axi-symmetric and Couette flow are most likely to be responsible for breaking up the largest drops. The length of time a drop must be exposed in the Couette and Extensional flows (for a Kerosene/water viscosity ratio of 2) for break-up to occur can be determined from the plots developed by Grace (1982). The high $\frac{\mu_d}{\mu_c}$ of 2 would indicate that drops are less likely to break in simple shear flows (Couette flows).

Values of reduced burst time can be evaluated from Figures 2.15 and 2.19, and the calculated values of d_{max} can be used to back calculate the shear times required for break-

up (Table A.2). Thus, the corresponding shear times in Couette flow and Extensional flow are in the order of 10^{-3}s.

Again, these values are smaller than the nominal residence time in the pipe but significantly larger than eddy length times. Thus, it would seem reasonable to believe that there is not any significant stretching of the drops before break up by turbulent eddies. Also, it can be concluded that inertial stresses are predominantly responsible for drop break up.

The value of d_{max} for a flowrate of 0.4l/s was calculated to be 800μm. This is close to the maximum measurable size limits of the Malvern Mastersizer. Droplet sizes were observed in this size range and above at the lower rotor speeds and higher dispersed phase concentrations (Figures A.6; A.7; A.11; A.13 & A.14). This figure would initially seem a reasonable estimate of d_{max} being fed to the mixer.

However, the effect of the swirling flows should increase with an increase in rotational speed and as a result an increase in the suction created by the rotor (Sparks, 1996). This should lead to increased turbulent energy at the inlet of the mixer and thus the globule sizes entering the mixer should decrease.

Also, Equation (2.18) does not take into account the dispersed phase concentration. However, it was seen that the droplet sizes increased with an increase in Φ, as observed by Brown and Pitt (1971); Streiff et al (1997) and Doulah (1975). An in increase in ϕ is thought to dampen turbulence and it would seem reasonable to believe that the inlet would contain larger globules than 800μm.

This would seem reasonable as μ_d is twice that of μ_c and as ϕ increases the flows can no longer be described by the continuous phase. The inertial stresses at high ϕ would therefore be reduced by the higher viscosity of the dispersed phase. Therefore, at higher dispersed phase concentrations drop break-up would occur due to both viscous and inertial forces.

6.5.2. Rotor region

Sparks (1996) described the flow of fluid entering the rotor region as being accelerated tangentially and the flow pattern upstream of the rotor teeth could be characterised by swirl generated as the fluid followed the rotor face. The flow in this region was considered to be predominantly tangential, with a much lower radial component. As the fluid was seen to follow the rotor teeth the velocity of the fluid at the rotor tip, v_{tip}, was considered to be the same as the tip speed of the rotor.

The Silverson rotor used in this work has a greater open area than the toothed designs used in the flow visualisation work of Sparks (1996). This will result in a lower radial component of the velocity (Q/A) in this region. Also, the rotor blades on the Silverson mixer (close in design to a pump impeller) are significantly longer than the teeth on the unit investigated by Sparks (1996). This will increase the residence time of the fluid in this region.

The Reynolds numbers in this region, as defined by Equation (2.38) were calculated to be 4000 and 8000 (at 0.4l/s and 0.8 l/s respectively). These, relatively low Reynolds numbers would suggest that turbulence levels are low and the assumption of local isotropy may not be applicable. In addition, at low Reynolds numbers the spatial dimensions of the viscous flow will be larger and therefore drop break-up due to viscous shearing action is possible as well as inertial forces.

However, the droplet size was seen to decrease with rotational speed up to approximately 7000rpm after which no significant change was observed. The definition of Re as given in Equation (2.38), is only dependant on the bulk flowrate and open area of the rotor (as $v_{radial} = Q/A$), as well as the physical properties of the liquid system.

Therefore, if drop break-up was due to inertial stresses or viscous forces in the rotor region, Equation (2.38) would indicate that an increase in flowrate would result in a decrease in droplet size. However, the affect of flowrate appeared to be insignificant compared to the rotor speed. Thus, it can be concluded that the rotor speed is more likely

to affect drop break-up and that the definition of Re in terms of v_{radial} is not a true reflection of the flow velocities in this region.

This is not totally unexpected as Equation (2.38) is an over simplification of the flow in the rotor, as in addition to the radial component there is also a tangential component of the velocity. In Section 2.3.1 a second definition of Re in the rotor region was discussed for tangential flow, where D_{RADIAL} remains the characteristic length but the rotor tip speed, v_{tip}, is used as the characteristic velocity. This then results in the impeller Reynolds number (Equation (2.22)) divided by a factor of 2, as $D_{RADIAL} \approx D/2$.

If the two velocity components are considered to be vectors, the sum of the two vectors gives a resultant velocity close to v_{tip}. This is because v_{RADIAL}, (0.12 ms^{-1} at 0.4 l/s) is significantly smaller than v_{tip}, (10.97 ms^{-1} at 3000rpm). It would thus seem reasonable to assume v_{tip} is a more appropriate characteristic velocity in the rotor region. This then results in significantly larger values for Re ($4x10^5$ at 3000rpm) which would then infer greater turbulence and the likelihood of drop break-up by inertial stresses. It must also be noted that these larger values of velocities would also lead to greater nominal shear rates (from $300s^{-1}$ at 3000rpm up to $1300s^{-1}$ at 12000rpm).

The general trend in the droplet size data (Figure 6.5) showed that droplet size decreases with N up to 7000rpm with only small changes in droplet size distributions at rotor speeds above this. Hence, as Re becomes greater the sizes are seen to decrease, however once turbulence is fully generated at speeds of 7000rpm and above no significant change in droplet size is observed. This would imply that break-up due to inertial stresses is only prominent at speeds below 7000rpm as above this higher Re do no correspond with significant changes to the droplet size distribution.

Further explanation into the effects of this possible flow affect on the droplet size distribution can be obtained by considering the droplet size data more closely. The droplet size data from the Emulsor screen at 0.4l/s and $\phi = 10\%$ is shown in Figure 6.24.

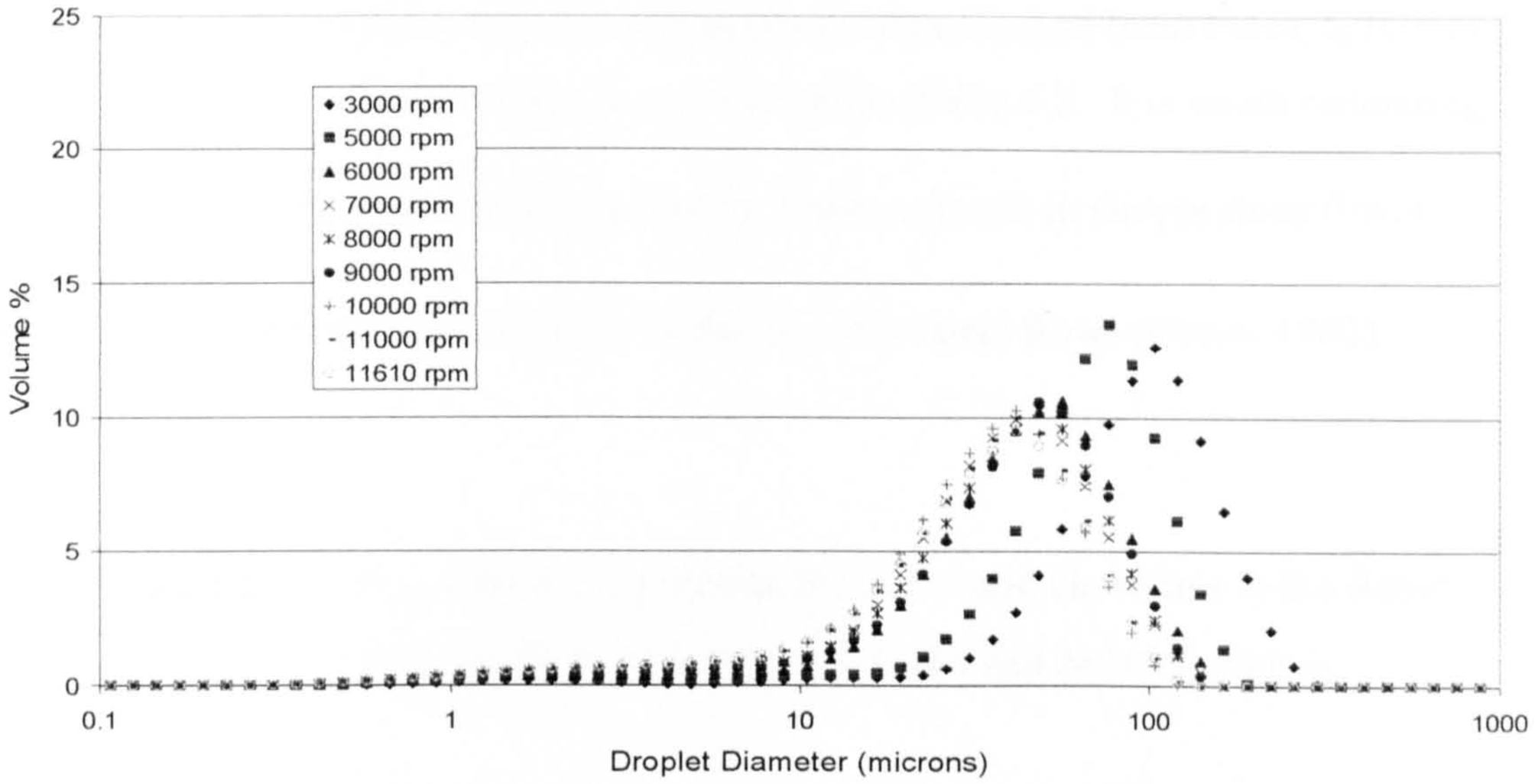

Figure 6.23 Volume DSD generated by the 67.85mm rotor with the Emulsor Screen at $Q = 0.4$ l/s and $\Phi = 10\%$, for varying N (rpm).

As rotor speed increases (and thus Re) values of d_{max} appear to decrease from approximately 300μm at 3000rpm down to 150μm at 7000rpm. At speeds above this there is no significant change in the droplet sizes at the larger end of the droplet size distribution (i.e. d_{max} appears to level off at approximately 150μm). However, rotational speeds above 7000rpm have more of an effect on the smaller droplet sizes in the size distribution (< 10μm).

If viscous stresses are responsible for drop break-up the values of critical shear rates required to produce droplet sizes equivalent to d_{max} can be determined using the plots of Grace (1982), (Figures 2.13 and 2.16 & Equation (2.42)).

The nominal residence time at 0.4 l/s in this region is 0.3s and nominal shear rates for varying N and the corresponding Re, critical shear rates, G_B and burst times, t_B (Grace, 1982) for d_{max} (0.4l/s and ϕ=10%) are summarised in Table 6.5. It is worth reiterating that $\frac{\mu_d}{\mu_c} = 2$ would indicate that drops are less likely to break in simple shear flows (Couette flows) and more likely to break due to extensional flows (Grace, 1982).

Table 6.5 d_{max} with corresponding Re and γ' and G_B values in the Rotor Region (69.85mm rotor, ES, 0.4l/s and ϕ=10%) with λ_k

N (rpm)	v_{tip} (m/s)	Re	γ' (s^{-1})	d_{max} (μm)	Extensional		λ_k (μm)
					Critical shear, G_B, (s^{-1})	t_B (s)	
5000	18.29	1.3E+06	524	191	171442	0.037	4.70
6000	21.94	1.5E+06	628	141	232703	0.028	4.20
7000	25.60	1.8E+06	733	141	232703	0.028	3.73
8000	29.26	2.0E+06	838	141	232703	0.028	3.40
9000	32.92	2.3E+06	942	141	232703	0.028	3.07
10000	36.57	2.6E+06	1047	121	271079	0.024	2.80
11000	40.23	2.8E+06	1152	121	271079	0.024	2.53

Values for the critical extensional shear rate are significantly higher (up to 300 times) than the nominal shear rates in this region. It is worth noting that Grace (1982) found that calculated critical shear rates under extensional flows were proportional to the square root of the wall shear rate in a static mixer.

d_{max} appears to level off at the higher rotational speeds, suggesting that a maximum eddy length scale of ≈150μm may exist in this region. This is despite an increase in turbulent

energy dissipation rates. Furthermore, there is an increase in the number of smaller drops in the order of, if not smaller, than the Kolmogorov scale of turbulence.

These smaller drops could be attributed to the fact that if the drops were breaking due to Couette or Extensional flows they would break into more than two separate drops (Figure 2.12). If the drops underwent large enough deformation they would split into more than two drops and the resultant drops will be smaller than if they underwent smaller deformations (Grace, 1982).

This analysis assumes that the velocity of a drop is well defined by the tip speed. However, the rotor can be considered similar to an agitator in a stirred vessel. Consequently, it can be reasoned that turbulent vortices would exist at the trailing edges of the rotor blade. The local energy dissipation rates in this region would be high. The distance the droplet will travel tangentially in an equivalent time, at a speed v_{tip}, (10.97 ms^{-1} at 3000 rpm) will therefore be approximately 3m. This would suggest that the path by which a droplet travels through the rotor region would be close to a spiral.

Also, the larger open area of the Silverson rotor may result in a certain amount of back mixing as material is being drawn back into the rotor region to replace the fluid displaced by the rotor. This would indicate that the flow through this region is highly inhomogeneous.

It can therefore be concluded that drop break-up at the lower rotational speeds (up to 7000rpm) is due to inertial and viscous stresses. As the speed is increased the inertial stresses is fully formed and inertial stresses then become more dominant. The largest eddy length scales will be in the order of d_{max}. However, it is evident that the number of smaller drops, in the order of or below λ_k, continues to increase at these higher speeds suggest that break-up also occurring due to viscous forces.

The values of Re in this region would suggest that it is more likely that inertial stresses are responsible for the smaller drops. However, the turbulent length scales will be

smaller and the shear rates will be greater in the shear gap. It seems more likely that the smaller droplets would be generated in this region of the mixer. This is discussed in further detail in the following section.

6.5.3. Shear Gap

The Emulsor Screen shear gap, (0.475 mm) is almost 4 times the size of the Square Hole High Shear Screen shear gap (0.125). The Reynolds numbers (Equation 2.39) in this region are low compared to those calculated in the rotor region (as δ is $<< D_{RADIAL}$). Consequently, the shear rates are significantly higher in this region of the mixer.

The Re_δ for the two screens are shown in Table 6.6.

Values for Re_δ for the ES range from 5000 (at 3000rpm) to 20,000 (at 12000 rpm). Whereas for the same N values for the SHHSS range from 1400 to 5000. This would indicate that the viscous forces are more prominent in this region of the mixer. The corresponding nominal shear rates range from 23,000s^{-1} to 90,000s^{-1} and 90,000s^{-1} to 300,000s^{-1} respectively.

Despite the large difference in δ between the two screens, the droplet size distributions generated by the two screens are quite similar. This implies that the size of the shear gap has little effect on the overall droplet size distribution.

However, the inferences made regarding the flows in the rotor region suggested that the higher rotor speeds had a greater affect on the smaller droplet sizes. For break-up of the smaller drops to occur, either the turbulence length scales have to be small enough (in the order of or smaller than the drop) or the shear rates have to be high. Also the relevant times scales have to be sufficient to cause break-up. This would suggest that it is more likely that break-up of the smaller droplets would occur in the shear gap region of the mixer.

Table 6.6 Re_δ for the ES and SHHSS (69.85 mm)

N (rpm)	Re_δ	
	ES	SHHSS
3000	5212	1372
5000	8686	2286
6000	10423	2743
7000	12161	3200
8000	13898	3657
9000	15635	4115
10000	17372	4572
11000	19110	5029
12000	20847	5486

The determination of whether it is the shear forces or inertial stresses that are dominant in the shear gap follows. The values of critical shear rates and burst times for drop diameters equivalent to d_{max} and d_{32} from both the ES and SHHSS (at 0.4l/s and ϕ=10%) can be determined from Figures 2.13 and 2.16 & Equation (2.42) and are summarised in Table 6.7.

Let us first consider the break-up of drops of sizes similar to d_{max} in both Couette and Extensional flow. In the ES the values of critical shear rates (G_B) calculated (Table 6.7) are approximately 10 times and 4 times the nominal shear rates (γ') in this region for Couette and Extensional flows respectively. The corresponding values in the SHHSS are 3 times and 1 times γ'.

Table 6.7 Critical shear rates, G_B, and burst times, t_B, for drop diameters equivalent to d_{max} and d_{32} and the corresponding nominal shear rates (γ') from both the ES and SHHSS (at 0.4l/s and ϕ=10%)

ES	d_{32}	d_{max}	G_B (s^{-1}) for d_{32}		G_B (s^{-1}) for d_{max}		t_B for d_{32} (s)		t_B for d_{max} (s)		Nominal γ'
RPM	(μm)	(μm)	Couette	Ext	Couette	Ext	Couette	Ext	Couette	Ext	(s^{-1})
5000	22.51	190.8	3.6E+06	1.5E+06	4.3E+05	1.7E+05	1.47E-03	4.40E-03	1.24E-02	3.73E-02	3.85E+04
6000	15.5	140.57	5.3E+06	2.1E+06	5.8E+05	2.3E+05	1.01E-03	3.03E-03	9.17E-03	2.75E-02	4.62E+04
7000	13.32	140.57	6.1E+06	2.5E+06	5.8E+05	2.3E+05	8.69E-04	2.61E-03	9.17E-03	2.75E-02	5.39E+04
8000	13.7	140.57	6.0E+06	2.4E+06	5.8E+05	2.3E+05	8.93E-04	2.68E-03	9.17E-03	2.75E-02	6.16E+04
9000	13.92	140.57	5.9E+06	2.3E+06	5.8E+05	2.3E+05	9.08E-04	2.72E-03	9.17E-03	2.75E-02	6.93E+04
10000	10.92	120.67	7.5E+06	3.0E+06	6.8E+05	2.7E+05	7.12E-04	2.14E-03	7.87E-03	2.36E-02	7.70E+04
11000	12.44	120.67	6.6E+06	2.6E+06	6.8E+05	2.7E+05	8.11E-04	2.43E-03	7.87E-03	2.36E-02	8.47E+04

SHHSS	d_{32}	d_{max}	G_B (s^{-1}) for d_{32}		G_B (s^{-1}) for d_{max}		t_B for d_{32} (s)		t_B for d_{max} (s)		Nominal γ'
RPM	(μm)	(μm)	Couette	Ext	Couette	Ext	Couette	Ext	Couette	Ext	(s^{-1})
5000	23.03	163.77	3.6E+06	1.4E+06	5.0E+05	2.0E+05	1.50E-03	4.51E-03	1.07E-02	3.20E-02	1.46E+05
6000	17.62	140.58	4.6E+06	1.9E+06	5.8E+05	2.3E+05	1.15E-03	3.45E-03	9.17E-03	2.75E-02	1.76E+05
7000	14.86	140.58	5.5E+06	2.2E+06	5.8E+05	2.3E+05	9.69E-04	2.91E-03	9.17E-03	2.75E-02	2.05E+05
8000	13.45	120.67	6.1E+06	2.4E+06	6.8E+05	2.7E+05	8.77E-04	2.63E-03	7.87E-03	2.36E-02	2.34E+05
9000	10.53	103.58	7.8E+06	3.1E+06	7.9E+05	3.2E+05	6.87E-04	2.06E-03	6.76E-03	2.03E-02	2.63E+05
10000	10.06	103.58	8.1E+06	3.3E+06	7.9E+05	3.2E+05	6.56E-04	1.97E-03	6.76E-03	2.03E-02	2.93E+05
11000	10.52	88.91	7.8E+06	3.1E+06	9.2E+05	3.7E+05	6.86E-04	2.06E-03	5.80E-03	1.74E-02	3.22E+05

The critical shear values for the SHHSS are close to the nominal shear rates. This would suggest that the shear rates in this region of the mixer are sufficiently large to determine d_{max}. This statement would only hold if the exposure times of the drops to the critical shear rates are long enough to cause break-up.

The nominal residence times (τ) at 0.4l/s in the shear gap region are approximately 4 ms for the ES and 1ms for the SHHSS. Comparing these values to the estimated critical shear times (t_b) shows that for ES the values for t_b are twice τ in Couette flows and 6 times τ in Extensional. The equivalent values in the SHHSS were found to be 7 times and 20 times greater than τ in Couette and Extensional flow (respectively).

Thus, it would appear that the nominal residence times are not large enough for d_{max} to be determined by shear forces in the shear gap.

Performing a similar analysis on values of d_{32} shows values of G_B in the ES are approximately 100 times and 40 times γ' in Couette and Extensional flows (respectively). Interestingly, the corresponding values for t_b are 5 times and 2 times less than τ. In the SHHSS G_B is 25 times greater than γ' for Couette and 10 times in Extensional flows. The corresponding values for t_b in the Couette flow are equivalent to τ. However, for Extensional flows t_b is less than τ ($\approx$0.5 times).

Hence, with the exception of Extensional flows in the SHHSS, the nominal residence times are sufficient for drops in the order of and less than d_{32} to break due to viscous forces. The effects of the viscous forces in the shear gap would increase as the droplet sizes decreased below d_{32}. t_b will decrease increasing the chances for a drop to break in Couette and Extensional flows. However, the fact that the droplet size distributions did not show significant differences between the two screens would indicate that it is turbulent energy dissipation that is more prominent in this region of the mixer.

The areas of highest energy dissipation would be expected in this region where fluid accelerating at high speeds undergoes a rapid deceleration as it impacts against the stator

wall (or edges of the holes). The turbulent length scales will be very small in this region. This would explain why larger quantities of smaller droplets are observed at the higher rotor speeds. This effect will be dependant on tip speed and also the open area of the screens.

The large differences in shear rates and Re_δ of the two screens did not result in significant difference in the droplet size distribution. Therefore, in fully turbulent conditions the effects of the gap size can be assumed to be negligible. However, its influence will increase as the continuous phase viscosity increases (μ_d/μ_c becomes smaller).

This is evident when the droplet size distributions from the two screens are compared at different values of ϕ (Figure 6.24).

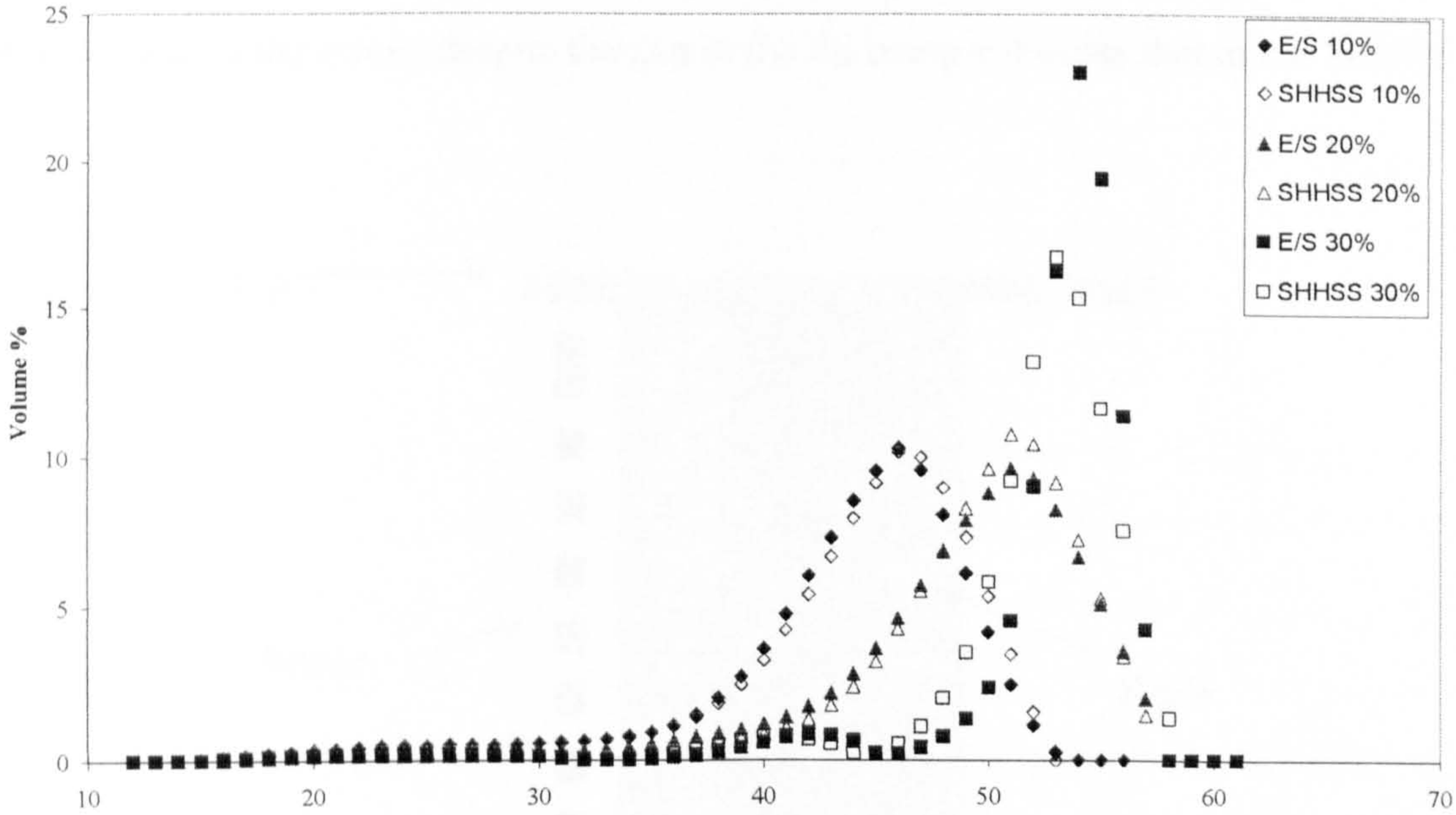

Figure 6.24 Comparison between E/Screen and SHHSS: 8000rpm & 0.4l/s (69.85mm rotor)

The droplet size is seen to increase with an increase in ϕ and this was attributed to turbulence damping. As ϕ increases the system can no longer be defined by the physical parameters of the continuous phase and it is logical to believe that the viscosity of the resultant dispersion will increase.

Figure 6.24 shows that the droplet size distributions from the two screens are similar up to ϕ =20%. However, there is significant change at 30% with the SHHSS generating smaller droplets than the ES.

It is worth noting that the leakage flows that were observed by Sparks (1996) were also negligible. This can be explained by the fact that toothed mixer had an open top gap (i.e. no "Lip" covering the gap). However, the Silverson rotor does have a "Lip" (Figure 6.25) which will reduce the amount of leakage that occurs.

This seems a reasonable deduction as there was no significant difference in the performance of the screen despite the gap in the ES being ≈ 4 times that in the SHHSS.

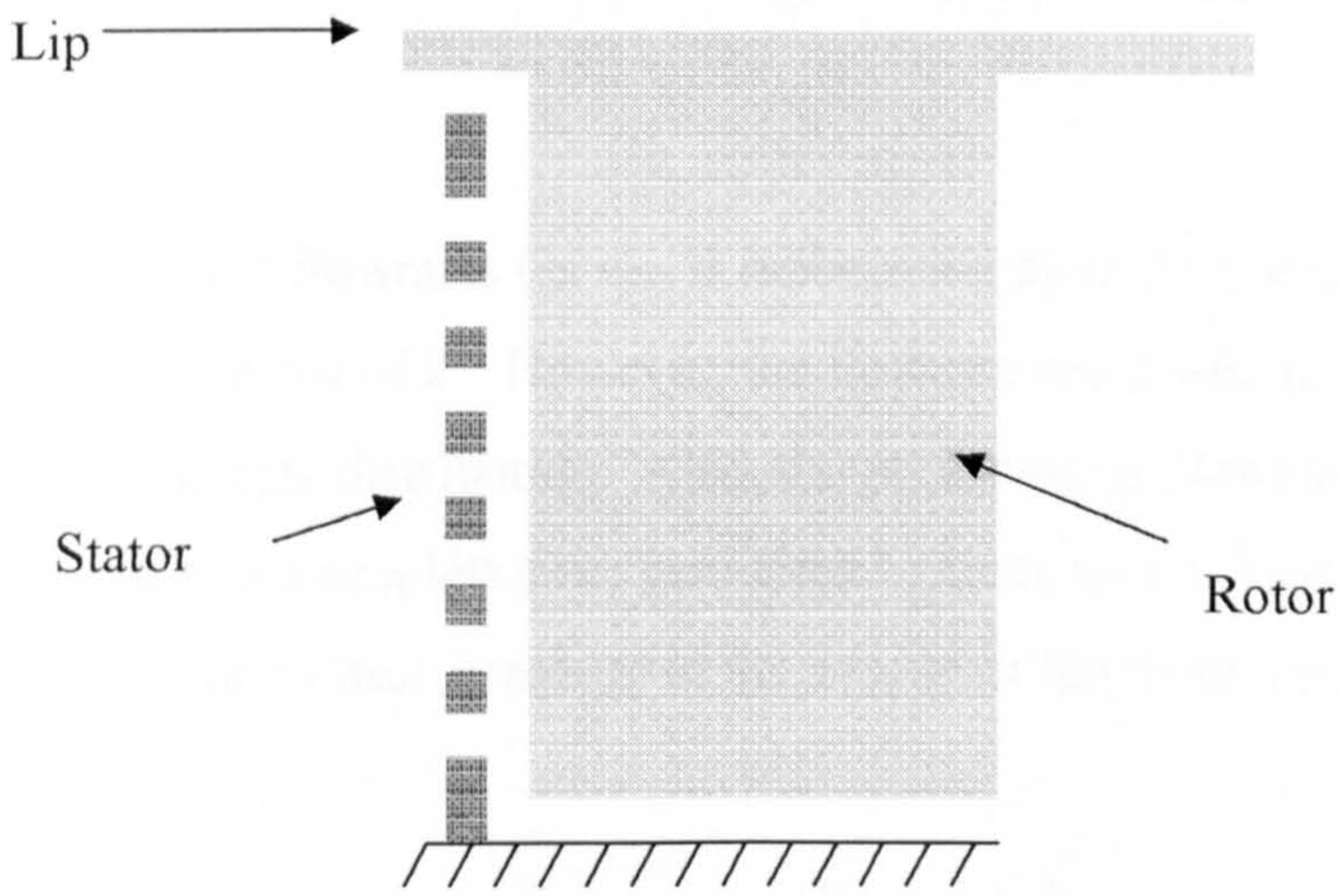

Figure 6.25 Schematic showing the "Lip" at the top of the Silverson rotor

6.5.4. Stator

The Reynolds number in the holes in the stator is defined by Equation (2.40) and the values, along with the nominal τ and γ' are summarised in Table 6.8

Table 6.8 Re_{stator} in the stator holes and corresponding τ and γ'

	D_{hyd} (m)	Q (m^3/s)	v_{jets} (m/s)	Re	τ (s)	γ' (s^{-1})
ES	0.0014	0.0004	0.42	584	0.0034	298
		0.0008	0.83	1168	0.0017	596
SQHHSS	0.0024	0.0004	0.42	1010	0.0048	175
		0.0008	0.84	2020	0.0024	351

The flow through the stator holes will be laminar as the values for Re in the stator holes are very low. This also indicates that viscous stresses will play a more significant role in breaking up drops.

Re_{stator} is a function of the flowrates (as v_{jets} is determined by Q/A) and doubling Q also increases τ and γ' by a factor of 2. However, the flowrate was found to have a little or no effect on the droplet size distribution. Also, the performance of the two screens was similar (with regards to the droplets sizes generated by them both). This would suggest that there is very little or no drop break up in this region of the mixer (at least due to viscous stresses).

Comparing the values of τ and γ' to the values of critical shear rates and burst times for drop diameters equivalent to d_{max} and d_{32} (Table A.2). It can be determined that γ' is significantly smaller than values for G_B, (up to 10^4 times).

The equivalent values of t_b for d_{max} were again compared to τ and were found to be larger. Implying that drops of size d_{max} and above did not have enough time to break in holes of both the ES and the SHHSS.

However, values for t_b calculated for d_{32} were found to be significantly smaller than τ (up to 6x in the SHHSS) for Couette flows and up to 2x smaller in Extensional flows. Again, this would imply that drops in the order of and below d_{32} could break due to viscous forces in the flow through the stator holes.

It is possible that there is further break-up as the drops pass through the stator holes. In low viscosity systems this effect would be small and not influence the droplet size distribution significantly (as the performance of the two screens was similar).

The number of holes would also affect the turbulent energy dissipation as Sparks (1996) observed the fluid discharging from the rotor and turning abruptly by the upstream face of the stator teeth and emerging radially. A fast stream followed the leading edge of the stator and a region of recirculation accompanied this (Figure 2.8).

It was postulated that the tangential kinetic energy given to the fluid by the rotor was transformed into pumping power, skin friction losses and turbulent losses. It was suggested that the point where the abrupt turn in the flow takes place is where the losses are greatest.

Therefore, it is reasonable to believe that the on the leading edge of the rotor (where the pressure is positive) there is likely to be a maximum in the losses (as described by Sparks, 1996). This is also where the streamline flow through the stator will be greatest. As the rotor passes the holes, there will be a certain degree of back-mixing, as an area of low pressure will exist, which may draw liquid back into the slot/hole. This would cause the recirculating flow in the holes, until the positive pressure is applied again by the following rotor.

6.5.5. Volute

The flow in the volute will be determined by the velocity of the radial jets from the stator holes. Sparks (1996) described the flow in this region as being disordered. This region makes up the largest volume of the mixer and consequently will have the largest nominal residence times.

As D_{volute} and the open area are not significantly different between the two screens the values for Re_{volute} are similar (Table 6.9)

Table 6.9 shows that the Re_{volute} are high and the nominal shear rates in this region are very low. Therefore, it can be assumed that the drop break-up due to viscous stresses is unlikely in this region.

Table 6.9 Re_{volute} and corresponding values for τ and γ'

Stator	D_{volute} (m)	Q (m^3/s)	v_{jets} (m/s)	Re_{volute}	τ (s)	γ' (s^{-1})
ES & SHHSS	0.0267	0.0004	0.42	11136	0.16	16
		0.0008	0.83	22272	0.08	31

It is reasonable to assume that the turbulent energy dissipation rate is significantly smaller in the volute than in the rotor region of the mixer. However, due to the longer residence times in this part of the mixer it is possible that the any larger drops that may have by-passed the regions of high shear rates and high energy dissipation in the distribution may undergo further break-up due to inertial stresses.

6.5.6. Summary

The in-line rotor-stator mixer was divided into 5 sections based on flow patterns observed in the visualisation work of Sparks (1996). These sections were the inlet, rotor chamber, shear gap, stator and the volute. By defining the Re in each of these regions which made it possible to investigate which stress mechanism would be responsible for drop break-up.

The Re in the pipe were calculated to be 20,000 (at 0.4 l/s) and 40,000 (at 0.8 l/s), indicating that the flow was turbulent. It was established that the nominal residence time in the pipe was long enough to sustain drop break-up due to both viscous and inertial stresses. However, the high Re implied that inertial stresses would be more dominant.

In the rotor chamber it was considered more appropriate to define Re using the rotor tip speed and the blade length as the characteristic velocities and length. This was because the droplet size was seen to decrease with rotor speed. The resultant values for Re were calculated to be in the order of $4x10^5$, which points to turbulent conditions.

The effective shear rates (Grace, 1982) in this region were found to be considerably higher than the nominal shear rates. However, the critical burst times, t_B, were significantly smaller than τ suggesting that drop break-up due to viscous stresses was possible.

The values for d_{max} levelled off at 150μm after approximately 7000 rpm and as Re increased with N. It was assumed that the maximum eddy length scales would be in the order of d_{max}. It was concluded that inertial stresses in this region were responsible for drops with diameters close to d_{max}.

The values for Re in the shear gap ranged from 5000 to 20,000 with the ES and 1400 to 5000 with the SHHSS. These relatively low values of Re implied that the viscous stresses would be more dominant in the break-up of drops. The corresponding nominal shear rates were 23000 s^{-1} to 90,000 s^{-1} and 90,000 to 300,000s^{-1} for the ES and the SHHSS respectively.

However, despite these differences in Re and γ' there was no discernable difference in the droplet size distribution from the two screens. The nominal residence times in this region were not large enough to sustain the break-up of drops with sizes similar and above d_{max}. However, drops similar and below d_{32} would be broken in the short time in the shear gap. It could then be deducted that drops with diameters close to and below d_{32} most likely to be disrupted by viscous sub-range eddies.

In the stator the flow was considered to be laminar and break-up by viscous stresses would be more likely. However, the fact that the two screens showed no significant differences in performance would lead to inference that there is very little break-up in this region. It is also possible that some drops that have undergone deformation in the shear gap will break up in this region.

The flows in the volute would be responsible for break-up of larger drops that may have by-passed the regions of high energy and shear rates.

In summary, under turbulent conditions, it is reasonable to assume that drops are likely to break due to:

a) inertial stresses in the inlet to the mixer.

b) inertial and viscous stresses in the rotor region.

c) inertial sub-range eddies in the shear gap.

d) viscous stresses in the stator holes.

e) inertial stresses in the volute.

These regions can be put into the following order of residence times; Shear Gap < Stator < Inlet < Rotor < Volute. The very short residence times in the shear gap and the fact the regions of high localised energy dissipation are very small, would indicate that a large percentage of the drops are by-passing this region. The relatively long residence times and the magnitude of the stresses would point to the fact that droplet size distribution is predominantly determined by the viscous and inertial stresses in the rotor region.

CHAPTER 7. Conclusions

The main findings of this work are as follows:

1. The kerosene-water system was confirmed to be a non-coalescing system. Consequently, drop break-up at high dispersed phase concentrations could be investigated without having to deal with the complexities of coalescence phenomena. This also led to the fact that samples could be taken and droplet size measured without coalescence occurring, thus giving a true reflection of the droplet size distribution from the in-line rotor-stator mixer.

2. The comparison between the Video Probe (on-line droplets sizes measurement) and the Malvern Mastersizer (off-line measurement) showed that the Mastersizer could be used to measure the droplets generated from the rotor-stator mixer. The Mastersizer was found to be the better of the two techniques for measuring droplets below 20μm.

3. A continuous in-line sampling technique was developed that enabled the rapid measurement of large sample sizes.

4. The liquid-liquid contactor rig was designed and built specifically for this work. It allowed the measurement of droplet sizes generated from a single-pass through the in-line rotor-stator mixer. It was then possible to investigate the effects of varying; rotor speed, geometry, throughput and dispersed phase concentration on the droplet sizes.

5. A single-pass through the in-line rotor-stator mixer resulted in broad droplet size distributions with sizes ranging from below 10 μm to approximately 100 μm. This highlighted the inhomogeneous nature of the rotor-stator mixer.

6. The performance tests showed that the droplets sizes:
   - decreased with N, until a speed was reached, (approximately 7000 rpm) above which no significant size reduction was observed.

- increased linearly with dispersed phase concentration.
- were not influenced significantly by flowrate had little or no effect on the droplet size distribution.
- were similar from the Emulsor screen and the Square Hole High Shear Screen.
- increased with an increase in open area. The tests performed with the 50.8 mm rotor showed that the General Purpose Disintegrating Head resulted in the largest droplet size, then the Slotted Head, with the Emulsor Screen and the Square Hole High Shear Screen producing the smallest droplet.
- were not affected by the shear gap. The shear gap in the Emulsor Screen was twice that in the Square Hole High Shear Screen.

7. d_{32} was linearly proportional to d_{max} which indicated that the assumption that drop break-up was due to a single mechanism is valid. This then enabled d_{32} to be used in mechanistic correlations developed for d_{max}.

8. The Chen and Middleman correlation was found to be the most appropriate model for describing correlating d_{32}. This suggests that viscous sub-range eddies are the dominant break-up mechanism. The drop size data could be correlated for Φ up to 20%, by:

$$\frac{d_{32}}{D} = 2x10^{9}(1+20\Phi)(We\,\mathrm{Re}^{4})^{-1/7}$$

9. The dispersed phase concentration has a dampening effect on turbulent stresses.

10. The power supplied to the fluid by the in-line rotor-stator mixer was measured using a thermometric technique. The data collected from this rig enabled the estimation of the energy dissipation rate and the Kolmogorov length scale.

11. The Shaft power increases with rotational speed and flowrate. The shaft power can be related to N and Q by the following:

$$P_{SHAFT} = 0.01N^{2.8}Q^{0.25}$$

12. P_{shaft} was similar for both the Emulsor screen and the Square Hole High Shear Screen.

    -The effects of Shear gap were not significant on P_{shaft}.

    -Open area as an effect on P_{shaft}.

13. The power supplied to the fluid, P_{FLUID}, is proportional to N^3. The Power number for the Emulsor Screen and the Square Hole High Shear Screen is 0.21.

14. The mixer is operating in turbulent conditions.

15. Energy dissipation within the rotor-stator mixer is highly inhomogeneous and values of ε were estimated to range from 40 W/kg to 800 W/kg.

16. d_{32} was proportional to $\varepsilon^{-0.2}$, which best matched the Shinnar model for drop break-up caused by turbulent stresses in the viscous sub-range.

17. The Kolmogorov length scales, λ_k, ranged from 12μm down to 6μm.

18. Under turbulent conditions, drops are likely to break due to:

    a) inertial stresses in the inlet to the mixer.

    b) inertial and viscous stresses in the rotor region.

    c) inertial sub-range eddies in the shear gap.

    d) viscous stresses in the stator holes.

    e) inertial stresses in the volute.

19. The droplet size distribution from a single pass through an in-line rotor-stator mixer is predominantly determined by the viscous and inertial stresses in the rotor region.

CHAPTER 8. Future Work

8.1. Liquid-Liquid Dispersions

There is still a considerable amount of work required in the understanding of the mechanisms of droplet break-up in in-line rotor-stator mixers. This work concentrated on a turbulent system, at a single viscosity and interfacial tension. The majority of tests were performed at a single scale. However, it is apparent that the droplet size distribution is not determined solely by inertial stresses. Different regions of the mixer exhibit different flow tendencies.

It would be useful in the design of such units to be able to assess the influence of each of these regions on the final droplet size distributions at varying flow conditions. The definition of Re in the different regions of the mixer is a good indication of whether inertial or viscous stresses are responsible for drop break-up. The effects of varying the viscosity ratio (and μ_o) in addition to studying a wider range of throughputs (thus varying residence times in each region) will help to identify when viscous stresses are more dominant than inertial stresses and vice versa. This will help identify which parameters are useful in scale-up (rotor diameter, shear gap, open area, stator thickness etc) and under what conditions. In this work the shear gap was found to have no effect on the droplet size distribution, however, at higher viscosities it is possible that the shear stresses in the gap are mainly responsible for drop break up.

In considering turbulent flow regimes the determination of d_{max} in this work was made difficult due the amount of bypassing that occurred in the mixing-head. This could be overcome by inserting the mixer into a recycle loop and increasing the number of passes through the mixer. However, one draw back to this type of set-up is that temperature effects begin to come into play and will alter the physical properties of the system. One possible method of overcoming these temperature effects are to study a single pass multi-stage unit (one with a number of concentrically arranged rotor-stator teeth). Alternatively, the mixture could be passed completely through the mixer from one vessel to another and

then back through the mixer into feed tank. This second method would be dependant on the stability of the resultant dispersions and the both the vessels should be equipped with agitators to promote homogeneity.

The results at the higher dispersed phase concentrations suggested that feed strategy might improve the performance for a single-pass machine. This could be investigated by varying the location of the point where the dispersed phase is added to the continuous phase. This can be further investigated by introducing a known droplet size distribution to the inlet of the mixer. This could be done by way of adding a static mixer to the in-let and using the Video Probe to measure droplet size distributions generated by it. Smaller droplet sizes are more likely to break in the shear gap region (smaller values of t_b), which is where the highest shear rates are likely to be.

8.2. Power Measurement

The literature review highlighted that there is very little power draw data available for rotor-stator mixers. It has been discussed that very often rotor-stator mixers are operating in the laminar regime where viscous shear is more prominent. This would suggest that the identification of the operating regime in a rotor-stator mixer will help in the understanding of the break-up mechanisms involved.

A method of determining the flow regime is to determine the dependency of the power draw of the unit on rotational speed. If the power is found to be proportional to rotational speed raised to the power of 3, then turbulent conditions will apply. If the power is related to rotational speed raised to the power of 2, then the flow will be laminar.

Power measurements would also be necessary in order to determine the Kolmogorov length scale and energy dissipation rates for the interpretation of droplet size data. It would be useful to monitor power draw whilst mixing the immiscible liquids, as the effects of dispersed phase and viscosity and interfacial tension on power draw could be determined in these mixers. A method of doing this would be to measure the shaft

torque. A possible method of increasing the accuracy of measurement at high shaft speeds would be to use a gearing device. This requires an additional shaft with a torque transducer, connected to the mixer shaft using a toothed belt and pulley. A larger pulley on the secondary shaft would reduce the speed allowing accurate measurement of torque. Toothed belts typically have efficiencies of 95% and above.

References

Anderson, H.H., (1980), in *"Centrifugal Pumps"*. 3rd edition. Trade and Technical press. ISBN 85461 076 6

Avertukh, Yu. N., Nikoforov, N.M., Kostin, N.M. & Korshakov, A.V. (1988), "Computation of Dispersions for Emulsions Formed in a Rotor-Stator Unit". Journal of Applied Chemistry of the USSR, vol 61, (2). 396-397.

Becher, P (1966), in "Emulsions: Theory and Practice" 2nd edition, Reinhold Publishing Corporation (New York, USA).

Becher, P., (1964), "A particle-size analyzer for emulsion photomicrographs", Journal of Colloid Science, 19, 468-472.

Bohren, G. F. and Huffman, D. R. (1983), "Absorption and scattering of light by small particles" Wiley-Interscience.

Born, M. and Wolf, E. (1980), "Principle of optics, electromagnetic theory of propagation interference and diffraction of light" Pergamon Press.

Bourne, J. R. and Garcias-Rosas, J. (1985), "Rotor-stator mixers for rapid micromixing". Chem. Eng. Res. Des. Vol 64.

Brown, D. E. and Pitt, K., (1971), "Drop Break-up in a stirred liquid-liquid contactor", Proc. of Chemica '70, Melbourne and Sidney, August 1970, publ. Butterworths and IChemE., pp 83-96.

Brown, D. E. and Pitt, K., (1972), "Drop size distribution of stirred non-coalescing liquid-liquid system", Chemical Engineering Science, 27, 577-583.

Brown, D. E. and Pitt, K., (1974), "Effect of impeller geometry on drop break-up in a stirred liquid-liquid contactor", Chemical Engineering Science, 29, 345-348.

Brown, J., (1991), "Application of the thermometric method of pump efficiency measurement to bore hole pumps", BHR Group Report 47020, BHRG Ltd. Cranfield.

Calabrese, R. V. (1992), "Analysis of dilute liquid-liquid dispersions: Physical considerations, discriminating among mechanisms and modelling approaches". FMP Report 054, BHRG Limited, Cranfield.

Calabrese, R. V., Francis, M. K., Mishra, V. P. and Phongikaroon, S. (2000) "Measurement and analysis of drop size in batch rotor-stator mixer". Proceedings: 10th European conference on mixing, 149-156.

Chen, H. T. and Middleman, S. (1967), "Drop size distributions in agitated liquid-liquid systems", AIChE J., 13, 989-995.

Chen, S.J. and Libby, D.R. (1978), "Gas Liquid and Liquid-Liquid Dispersions in a Kenics Mixer", 71st Annual AIChE Meeting.

Cheung (1998), "Hiline Liquid-Liquid Literature Review". Hiline report HLL01 BHRG Limited Cranfield.

Clements, D. J., (1996), "Principles of ultrasonic droplet size determination in emulsions", Langmuir, 12, 3454-3461.

Cohen, D (1998), "How to Select Rotor-Stator Mixers" Chemical Engineering, August 1998, 76-79.

Davies, J. T., (1985), "Drop sizes of emulsions related to turbulent energy dissipation rates ", Chemical Engineering Science, Vol. 40, 5, 839-842

Dietsche, W (1998), "Mix or Match: Choose the Best Mixers Every time" Chemical Engineering, August 1998, 70-75.

Doulah, M. S. (1975), "An Effect of Hold-Up on Drop Sizes in Liquid-Liquid Dispersions" Industrial Engineering Chemistry Fundamentals, Vol. 14 (2), 137.

El-Hamouz, A.M., Stewart, A.C. and Davis, G.A. (1988), "Kerosene/Water Dispersions produced by a Lightnin In-Line Static Mixer", IChemE Symposium Series 136, 457-464.

Francis, M. K. (1999) "The development of a novel probe for the in-situ meaurement of particle size distributions, and application to the measurement of drop-size in rotor-stator mixers" Ph.D Thesis, University of Maryland.

Grace, H. P. (1982) "Dispersion phenomena in high viscosity immiscible fluid systems and application of static mixers as dispersion devices in such systems", Chem. Eng. Communications, Vol. 14, pp 225-277.

Greerco Mixers by Chemineer, Inc. (Company Brochure, bulletin 117, 1999).

Hearn, S. (1992), "Residence Time Distribution and Pressure Gain Measurements in a Weir Group Centrifugal Pump with an Open Impeller". HILINE report HLP 02. BHRG Ltd, Cranfield.

Hinze, J.O. (1955), "Fundamentals of the Hydrodynamic Mechanism of Splitting in Dispersion Process", AIChe Journal, Vol. 1 (3), 289-295.

ISO13320-1: 1999(E), "Particle Size Analysis – Laser diffraction methods – Part 1: General Principles"

Karam, H. J. & Bellinger, J. C. (1968), "Deformation and Break-up of liquid droplets in a simple shear field", Ind. Eng. Chem. Fundamentals, Vol. 7 (4), pp 576-581.

Karassik, I.J. Krutzsch, W.C. Fraser, W.H. & Messina, J.P. eds. (1986), in *"Pump Handbook"*, 2nd edition. McGraw-Hill, New York

Karbstein, H. & Schubert, H., (1995), "Developments in the Continuous Mechanical Production of Oil-in-Water Macro-Emulsions". Chem. Eng. & Processing, 34, (1995) 205-211.

Keey, R. B. (1967), "Interpreting mixing with isotropic turbulence theory". British Chemical Engineering, Vol. 12, No. 7, 341-344.

Kolmogorov, A.N. (1949), "The Break-up of Droplets in a Turbulent Stream", Dokl Akad Nauk, 66, 825-828.

Korshakov, A.V., Nikiforov, A.O., & Terentev, O.A. (1990), "Optimisation of the Process of Emulsification in a Rotor-Stator Apparatus". Izv Vyssh Uchebn zaved, Lesn ZH, N.5, 1990, 76-79.

Kroezen, A.B.J. & Wassink, J. Groot (1987), "Bubble Size Distribution and Energy Dissipation in Foam Mixers". Journal of Society of Dyers Colour, Vol 103, Nov. 1987, 386-394.

Levine, L. (1994) "High shear mixers", Cereal Foods World, 39 (11), 874-876.

Middleman, S. (1974), "Drop Size Distributions Produced by Turbulent Pipe Flow of Immiscible Fluids Through a Static Mixer", Ind. Eng. Chem. Process Des Dev, 3, 78-83.

Nikiforov, A.O., Korshakov, A.V., Averbukh, Yu.I. and Sergeev, E. Yu. (1990), "Dispersing Pumps for Producing Polyacrylamide Solution". Khimicheskoe I Neftyanoe Mashinostroenie, No. 11, pp. 14-15 November 1990.

Ottewill, R.H. (1984), in "Surfactants". ed Tadros, Th. F., Academic Press Inc. (London) Ltd, pp. 1-18.

Pacek, A. W. and Nienow, A. W., (1995), "Measurement of drop size distribution in concentrated liquid-liquid dispersions: Video and capillary technique", The 1995 IChemE Research Event, 1st European conference, University of Edinburgh, 5th-6th January, 725-727.

Pacek, A. W., Moore, I. P. T. and Nienow, A. W., Calabrese, R. V. (1994) "Video technique for measuring dynamics of liquid-liquid dispersion during phase inversion", AIChE Journal, December, Vol. 40, No. 12., 1940-1948.

Pedrocchi, L. & Widmer, F. (1988), "Formation of Emulsions in a Turbulent Shearfield". 6th European Conference on Mixing, Pavia, Italy, 24-26 May, 205-213.

Pedrocchi, L. & Widmer, F. (1989), "Emulsionsherstellung im Turbulenten Scherfeld." Ing. -T Chem. Ech. 61, Heft 1.

Rushton, J.H. Costich, E.W. & Everett, H.J., (1950), "Power Characteristics of Mixing Impellers". Chemical Engineering Progress. Vol 46, No 8.

Saadevandi, B. A. and Zakin, J., L. (1996), "A Study of Silicone Oil-in-Water Emulsions". Chem. Eng. Comm., 1996. Vol. 156, 227-246.

Schubert, H. (1997), "Advances in the mechanical production of food emulsions". Proceedings Seventh International Congress on Engineering and Food. Part 1, S. 82-87.

Shinnar, R. (1961), "On the behaviour of liquid dispersions in mixing vessels", J. Fluid Mech., Vol. 10, 259-275.

Silverson Applications Report April 1999 (Issue 4).

Silverson High Shear In-Line Mixers (Company Brochure), 1999.

Sparks, T.G. (1996) "Fluid Mixing in Rotor-Stator Mixers" Ph.D Thesis, Cranfield University.

Stepanoff, A.J. (1957). "Centrifugal and axial flow pumps, theory design and application". 2nd edition. John Wiley and Sons.

Streiff, F., (1977), "In-Line Dispersion and Mass Transfer using Static Mixing Equipment", Sulzer Technical Review 3, 108-113.

Streiff, F.A., Mathys, P. And Fischser, T.U., (1997), "New Fundmentals for Liquid-Liquid Dispersion using Static Mixers", Recents Progres en Génie des Procédés, Vol 1 (51), 307-314.

Rawle, A., "Basic principles of particle size analysis" Technical Paper, Malvern Instruments Ltd.

Tavlarides, L. L. and Stamatoudis, M. (1981),"The analysis of inter-phase reactions and mass transfer in liquid-liquid dispersions", Advances in Chemical Engineering, Vol. 11, Academic Press Inc. (ISBN 0-12-008511-9).

Taylor, G. I. (1934), "The formation of emulsions in definable fields of flow", Proceedings of the Royal Society of London, A146, pp501.

Wachtel, R. E. and La Mer, V. K., (1962), "The preperation and size distribution of some monodisperse emulsions", Journal of Colloid Science, 17, 531-564.

Walstra, Pieter (1983), "Formation of Emulsions" Encyclopaedia of Emulsion Technology, Vol. 1, (Basic Theory), ed. Becher, P., 57-127.

Walstra, Pietra (1993), "Principles of emulsion formation", Chemical Engineering Science, 48 (2), 333-349

Appendix 1 Experimental rig operating procedures

A schematic of the experimental rig is shown in Figure A.1. The liquids are pumped from the two feed tanks ($1m^3$) and the organic liquid was introduced to the aqueous line via a manifold located one pipe diameter up-stream of the rotor-stator mixer. The fluid was passed through the mixer to the settling tanks. The recycle loops were present on the feed lines for use when commissioning the flow transducers or testing the pumps.

Standard Operating Procedure

The operation can be divided into the following categories:

(a) Filling the feed tanks

(b) Start-up

(c) Shut-down

(d) Waste

(e) Cleaning procedures and checks

Protective clothing: Safety glasses, safety boots, nitrile gloves.

(a) Filling the feed tanks

1. Check that both the settling tanks are empty.
2. Move the kerosene drum into the bund. The kerosene is delivered in 200 litre drums (the stainless steel tanks can hold up to 1000 litres each).
3. Close V1 and V5.
4. Use the barrel pump (P4) to transport the organic phase from the drum to the feed tank. When filling the tanks, the sight glasses must be monitored to prevent overflowing. Note: Before using the barrel pump, flush through with warm water to ensure that it is clean.
5. The water is supplied from the mains line via a de-ionised cylinder. Ensure the flow through the cylinder is not too high (to cause damage to the ion exchange resin). The flow can be controlled by using a valve (V17), located on the mains water supply.

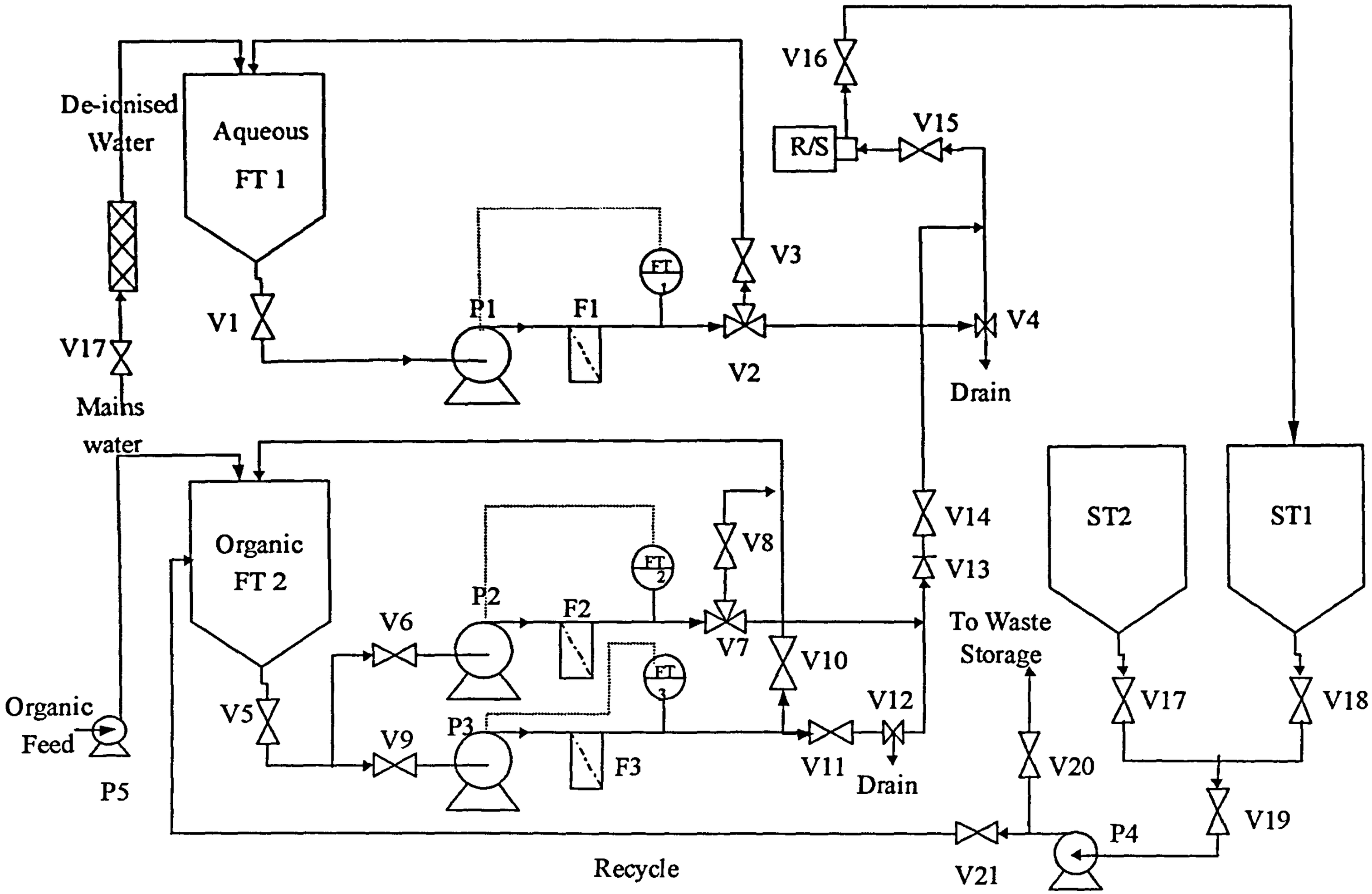

Figure A.1 Flow diagram of the rotor-stator liquid-liquid contactor rig

Once the feed tanks are full, the valves have to be positioned correctly to allow flow through the rig.

(b) Start-up

Aqueous line:

6. Close V3 and V4.
7. Position V2 (three-way valve) to allow flow to the mixer (as opposed to the recycle line).
8. Open V1.

Organic line:

<u>High flowrates</u>

9. Close V8, V9, V10 and V12
10. Open V6 and V14
11. Position V7 (three-way valve) to allow flow to the mixer (as opposed to the recycle line).

<u>Low flowrates</u>

12. Close V6, V10 and V12.
13. Open V9, V11 and V14
14. Position V7 to prevent flow back towards the pump (P2) and the recycle line.

15. Open V5.
16. Open V15 and V16.
17. Close V19
18. Open V17 and V18 (these valves should remain open when the rig is running, to prevent the settling tanks from overflowing).

Operation of the Flow controller and Pumps:

19. Ensure both feed tanks contain liquid.
20. Once all the valves are in the correct positions, check that the pump switches on the flow controller are all in the off position.

21. Turn the power on from the isolator switch. Check that the red button on the frequency controller is switched to Run and not Stop. Push the black button on the electrical box to turn on the inverter.
22. Select the correct organic pump depending on whether a high or low flowrate is required, (P2: 0.14-1.4 l/s and P3: 0.03-0.16 l/s). The switch is on the top of the control panel and is marked with the numbers 1 & 2. The number 1 refers to the large organic pump (P2) and 2 to the smaller one (P3). In addition, the switch on the power board has to be turned to the correct setting, this can be found to the right of the main electrical box and has three settings, 1, 2 and off.
23. Before starting the pumps, check that the correct scale factors have been inputted. Flick the program switch to on. Press the function button on the display panel, and continue to press until the scale factor option is displayed. If the value is incorrect, change by using the number buttons along the bottom of the display panel. Repeat this process for the aqueous flow controller (P1).
    The scale factors should be as following:
    Organic: (1) P2: 1.27380
    (2) P3: 0.16918
    Aqueous: P1: 1.29391
24. Flick the program switch to off.
25. Input the desired flowrate. Find the flowrate option by pressing the function button and use the number buttons on the bottom of the display panel to enter the correct flowrate. Note: The number on the display panel should be to three decimal places. This can be changed using the button labelled DP.
26. Press the RUN SET button to accept the flowrate.
27. Repeat steps 21-26 for the aqueous flow controller (P1)
28. Start P1 using the start switch on top of the flow controller.
29. When the flowrate has stabilised, the relevant organic pump (P2 or P3) can be started. The flowrate can be adjusted whilst the pumps are running by following the same procedure. Note: If the flow controller is showing 0 flowrate, switch off the pumps and check for closed valves that should be open.

Mixer Start-up

30. Read the Silverson installation, operating and maintenance manual for the rotor-stator mixer.
31. Open Valves V15 and V16.
32. Turn the isolator switch to on (at the bottom of the rotor-stator control panel).
33. Turn the power on (the green button at the top of the control panel).
34. Check the rotor speed, on the VACON display panel (the speed display can be found by pressing either the left or the right arrow).

    Note: Power, Torque and other information can be obtained from the display panel by pressing the arrow buttons until the required display is found.
35. Set the speed using the Speed Adjust knob.
36. Turn on the feed pumps (see 19-29)
37. Wait a 2 minutes before switching on the rotor-stator mixer using the green start button on the rotor-stator control panel.

(c) Shut Down

38. Stop the rotor-stator mixer.
39. Switch off the organic pump and then the aqueous pump (see 46-52 for pump shut down procedures).
40. Turn the rotor-stator power off.
41. Turn the isolator switch to off.
42. Close valves V15 and V16.
43. Drain the liquid from the volute (mixing head) from the drain valve located below it.
44. If the mixer is to be changed, turn all power off from the isolator switch on the pump control box.
45. When changing the mixer head, refer to the Silverson installation, operating and maintenance manual.

Pump Shut-down

46. Stop the organic pump (using the start switches on the flow controller)

47. Wait a few minutes before stopping the aqueous pump. This allows the water to flush most of the organic liquid out of the mixing sections.
48. Turn the switch on the power board to off.
49. Turn the isolator switch off.
50. Close V1 on the aqueous line.
51. Close valves V5, V6 and V9 on the organic line.
52. Close V17, V18 and V19.

Emergency shut-down

There are three emergency stop buttons (large red buttons) on the rig. The most important one is located on the back of the blue power board (facing towards the bund). When pressed, it will cut off all the power to the rig, switching off both the pumps and the rotor-stator mixer. The one that is located on the electrical box on the blue power board will only switch off the pumps. The one on the Rotor-stator control box will only switch off power to the rotor-stator mixer.

(d) Waste

To allow the dispersion in the settling tanks to fully separate it should be left for 24 hours. The organic (less dense) phase rises to the top of the tank creating an interface between the two phases. Pumping the aqueous phase to waste requires two people, one to monitor when the organic phase is reached and one to turn the pump off.

53. Close valve V18.
54. Close valve V21 (recycle line).
55. Open V19
56. Start P4 (which is a diaphragm pump and requires compressed air to operate)
57. Stop P4 when the interface is reached and there is only organic phase left in the tank.
58. Close V20.
59. Open V21.
60. Start P4.
61. Stop P4 when ST2 is empty.
62. Repeat for ST1.

(e) Cleaning procedures and checks

Before introducing new inventory, the whole rig should be flushed twice with de-ionised water and the tanks should be scrubbed if necessary. If the tanks require scrubbing an extra rinse using de-ionised water is required before filling.

The seals (o-rings) on the tank pipefittings and the gaskets on the pumps are made from nitrile rubber. The tri-clamp seals (green) on the organic line and the mixing lines are made from Viton and the seals on the aqueous line (blue) are EPDM. The seals should be checked for wear and tear whenever the tanks are empty and the mixer section seals should be checked when the mixing elements are changed.

Appendix 2 Names and Addresses of Equipment Suppliers

In-line Rotor-Stator Mixer

Silverson Machines Ltd.

Waterside, Chesham

Bucks, HP5 1PQ,

UK

Alcosol D70 (Kerosene)

Alcohols Ltd
Charringtons House
The Causeway
Bishop's Stortford
Herts, CM23 2EW

Pumps

Cougar Industries,

19 Empire Centre,

Imperial Way,

Watford,

Herts, WD2 4YH

UK

Latex Beads

Bangs Laboratories Inc.

9025 Technology Drive,

Fishers, IN 46038-2886,

USA

Pressure Transducer

Druck Limited

Fir Tree Lane

Groby

Leicester, LE6 0FH
UK

Pressure Gauge
WIKA Instruments Limited
Station Approach
Coulsdon,
Surrey CR5 2UD
UK

Flowmeters
Endress+Hauser Ltd
Floats Road,
Manchester, M23 9NF
UK

Temperature Measurement
RS Components
Lammas Road,
Weldon Industrial Estate,
Corby,
Northamptonshire, NN17 9RS,
UK

Appendix 3 Theoretical background to diffraction measurement

It is apparent that research into liquid-liquid systems from rotor-stator mixers has been limited to dilute systems by the constraints imposed by the drop size measurement technique.

The measurement technique for use in this research must incorporate the following important factors:

1. Measurement of drop sizes in the order of the Kolmogorov micro-scale and below.
2. The measurement of droplets in high dispersed phase concentrations.
3. The technique must show good repeatability.
4. Availability

The droplet sizes generated by an in-line rotor-stator mixer are expected to be too small for measurement using video techniques. Semi-in-line methods such as laser diffraction (Malvern Mastersizer) and electrical conductivity (Coulter Counter) are limited to low Φ.

However, despite it being an off-line technique and requires considerable dilution, the Malvern Mastersizer (laser diffraction) was the only available technique that can successfully measure the small droplet sizes that are expected from the rotor-stator mixer (<10μm). This was the most important criterion for work with high-energy dissipation rates and the validation of mechanistic models for $d < \lambda_k$. As this technique required considerable dilution at high Φ and was predominantly off-line, a sample had to be extracted and diluted for a measurement to be possible.

The sampling procedure was validated against an in-line video capturing technique that had been developed in-house at BHR group.

A degree of caution must be exercised when analysing particle size data, as different techniques measure different mean diameters and calculate or derive others from it. To

be able to correctly describe the drop size distribution (DSD) it is important to have an understanding of the principles of the measurement technique.

8.2.1. Principles of Laser Diffraction

The main principle behind laser diffraction is that particles passing through a laser beam scatter light at angles that are inversely proportional to their size. Instruments that use this principle measure the intensity of light scattered. The subsequent intensity pattern is then transformed by way of an appropriate optical model and mathematical procedure to a volume distribution.

Early laser diffraction devices only considered small scattering angles and were commonly described as Low Angle Laser Light Scattering (LALLS) or Fraunhofer diffraction devices. However, more recently the application of Lorenz-Mie theory has broadened the technique to include wider scattering angles.

(a) Fraunhofer Approximation

When a spherical particle is passed through a beam of light, the resultant forward scattering pattern consists of light resulting from diffraction and scattering between the particle and the light (reflection, refraction and absorption). If the particle is large compared to the wavelength of light then diffracted light will be mainly responsible for the resultant radial scatter pattern.

Fraunhofer diffraction, therefore, relies on the following assumptions:

i. The particles are spherical
ii. All particles are larger than the wavelength of light.
iii. Only scattering in the near-forward direction is considered (small angles of diffraction).

The scattering pattern of light by a single spherical particle using the Fraunhofer approximation can be described by:

$$I(\Theta) = \frac{I_0}{2k^2a^2}\alpha^4\left[\frac{J_1(\alpha\sin\Theta)}{\alpha\sin\Theta}\right]^2 \qquad \text{(A.0.1)}$$

Where, $I(\Theta)$ is the intensity of the scattered light (as a function of angle, Θ);

I_0 is the intensity of the incident light;

k is the wavenumber = $2\pi/\lambda$;

λ is the wavelength of the illuminating source in air;

a is the distance from scatterer to detector;

α is a dimensionless size parameter = $\pi x/\lambda$;

x is the diameter of the particle (μm);

J_1 is the Bessel function of the first kind of order unity.

The main advantage of Equation A.1 is that it is relatively simple and quick to calculate.

The Fraunhofer approximation does not incorporate the optical properties of the system and its use is limited to particles of diameters at least 40 times the wavelength of light. The Helium-Neon gas laser that the Mastersizer uses had a wavelength of 0.63μm. Therefore, this approximation is a good one for particle sizes larger than 25μm (ISO 13320-1:1999 (E)). However, the Mastersizer 2000 uses a blue laser (wavelength of 0.45μm) which enables it to measure sizes down to 18μm.

(b) Lorenz-Mie theory

When the particle size approaches that of the wavelength of light, the scattering becomes a complex function with maxima and minima present. The Lorenz-Mie theory provides equations to account for the complete light scattering pattern in a particulate system by considering the electromagnetic field, both inside and outside a single particle. Finite points within this field are used as sources and further the equations used for predicting how these sources radiate to elements in the far field (e.g. a detector).

Therefore, for any position in the far field, a summation for a given polarisation can be made for all the radiation's contributions from all points within the sphere. Many positions in the far field can be examined and thus a more concise description of the radiation pattern can be obtained.

The complex scattering pattern of a particle is a function of the scattering angle, the difference in the refractive indices of the particle and the continuous phase, the wavelength of the incident radiation and the diameter of the particle. Therefore, the equations derived using the Lorenz-Mie theory are a more complex version of Equation (A.1) and thus are more difficult to solve (Born & Wolf, 1980, Bohren & Huffman, 1983). The recent advent of powerful desktop computer technology enables the analytical solution of these complex equations in a reasonable time and allows many instruments to use full Lorenz-Mie theory.

The main difference between Lorenz-Mie Theory and Fraunhofer is the former assumes the volume of the particle as opposed to the latter, which predicts a projected area. It is claimed that the use of Lorenz-Mie theory allows accurate results over a wide size range, 0.02-2000 μm, (Rawle, 2002).

In addition to its ability to predict smaller particle sizes the other advantages of Lorenz-Mie theory is the assumptions, with the exception of spherical particles, which applied to the Fraunhofer Approximation, can be eliminated.

(c) Refractive Index

As mentioned earlier the scattering pattern of a particular particle is a function of its optical properties and size. In order to apply Lorenz-Mie Theory to particle size measurement then requires knowledge of the optical properties of the system. These include:

i. The complex refractive index of the particle, N_p, which consists of a real and imaginary part. The imaginary part refers to the amount of light that the particle absorbs (or the attenuation of light through the particle). N_p can be expressed as:

$$N_p = n_p - ik_p \qquad \text{(A.0.2)}$$

Where, n_p is the real part of the refractive index;

i is an indication for the imaginary part of the refractive index;

k_p imaginary (absorption) part of the of the particles refractive index.

ii. The complex refractive index of the particle relative to that of the medium, m, which can be expressed as:

$$m = N_p / n_m \qquad \text{(A.0.3)}$$

Where, n_m is the real part of the refractive index of the medium.

The real refractive indices of various compounds can be found readily in the literature or can be measured. However, the choice of the imaginary refractive index is a little more difficult, as there is very little information available in literature. Malvern Instruments recommend a rule of thumb for evaluating the correct imaginary refractive index a summary of which is given in Table 4.3.

Table A.1 A summary of estimated absorption values as recommended by Malvern Instruments Ltd.

Particle details	**Absorption**
Spherical; Transparent, e.g. Glass Beads	0
Spherical; not completely transparent, e.g. Oil drops	0.001
Not completely spherical; Transparent, e.g. Air pockets	0.01
Particles that appear grey under a microscope	0.1
Coloured and metal powders (appear black under a microscope)	1.0

Appendix 4 Droplet Size Distributions

Latex Bead Tests

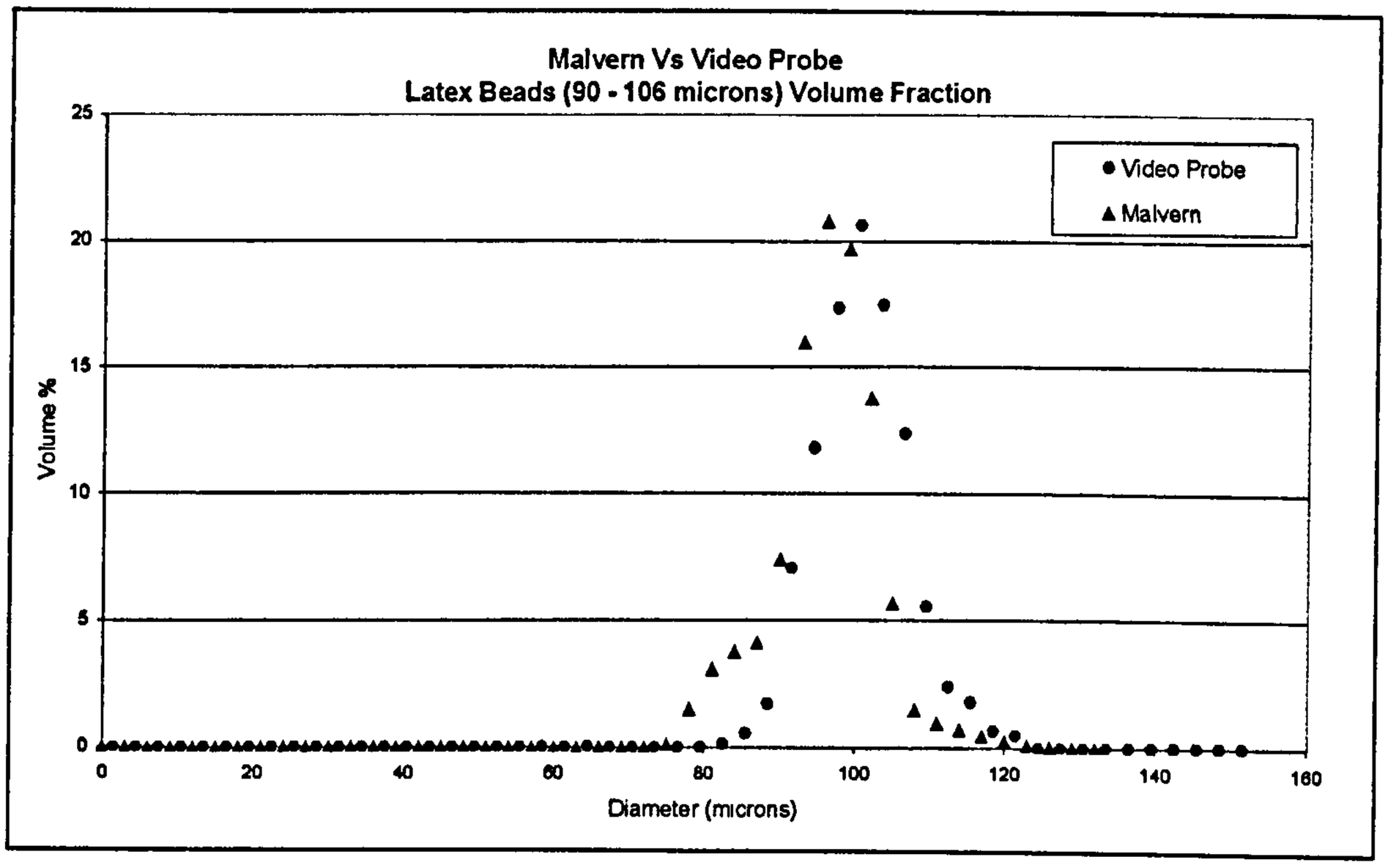

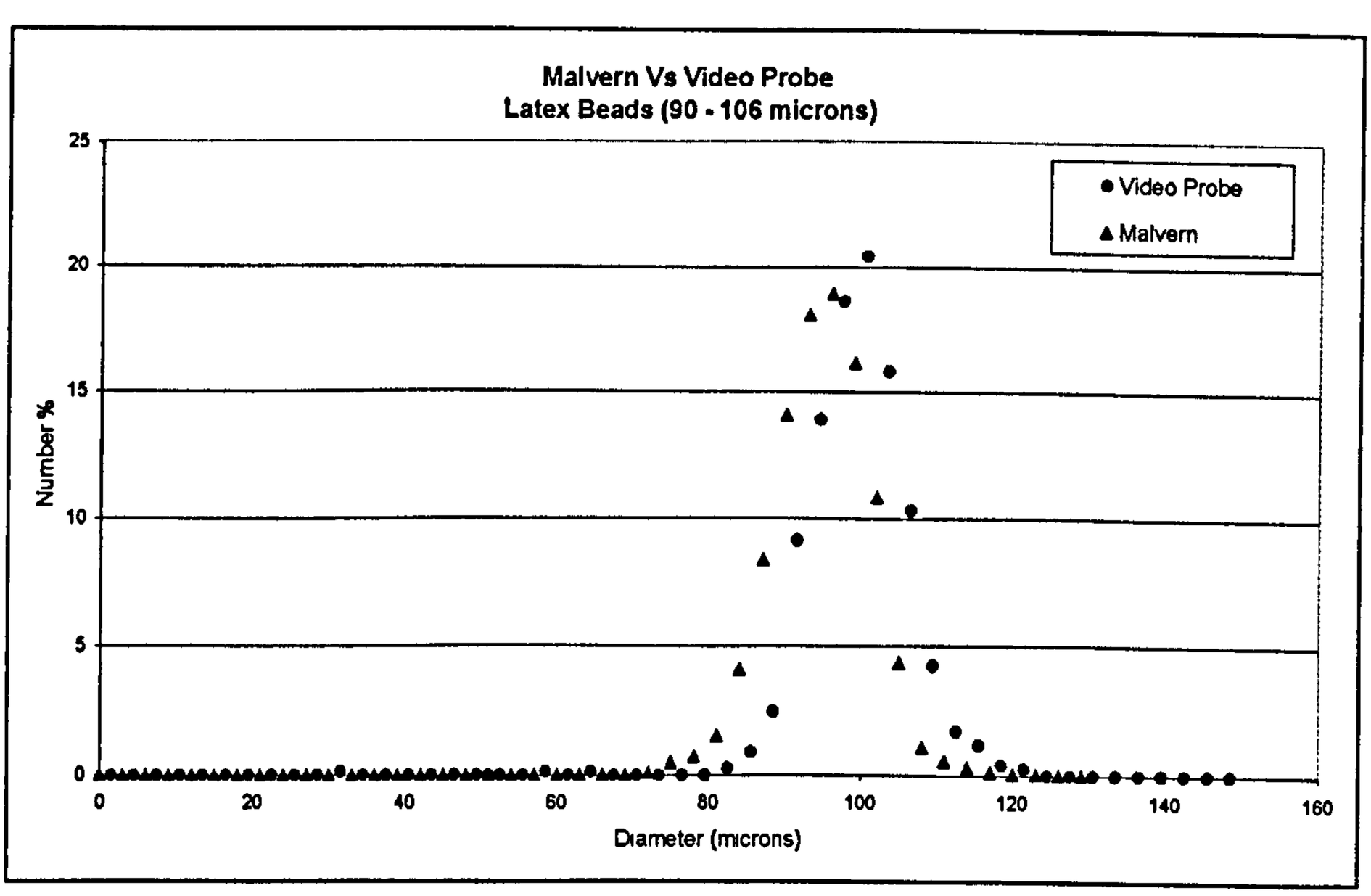

Figure A.2 A comparison of particle size distributions; Volume % (above) and Number % (below) generated by the Mastersizer and the Video Probe for Latex beads 98 μm.

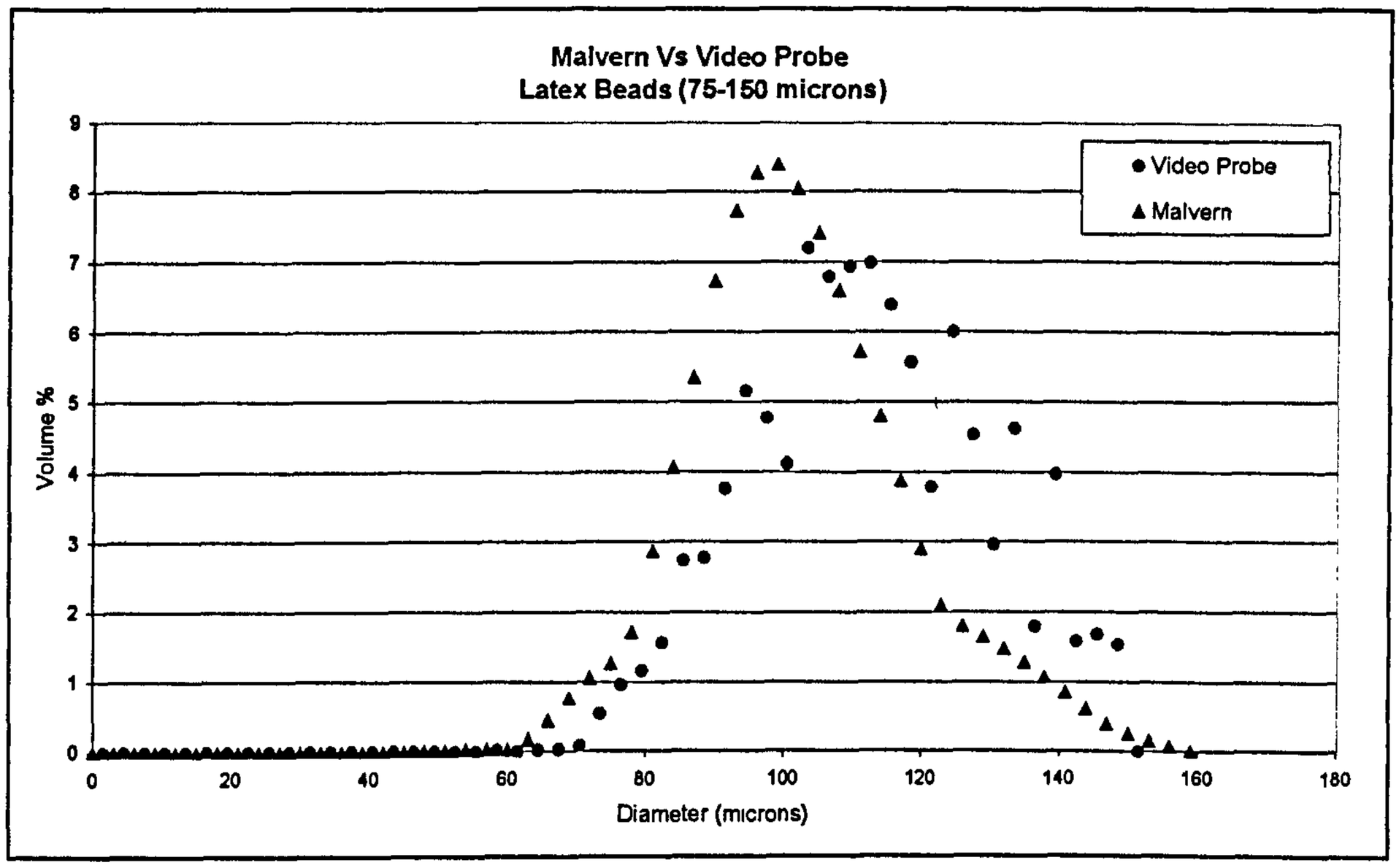

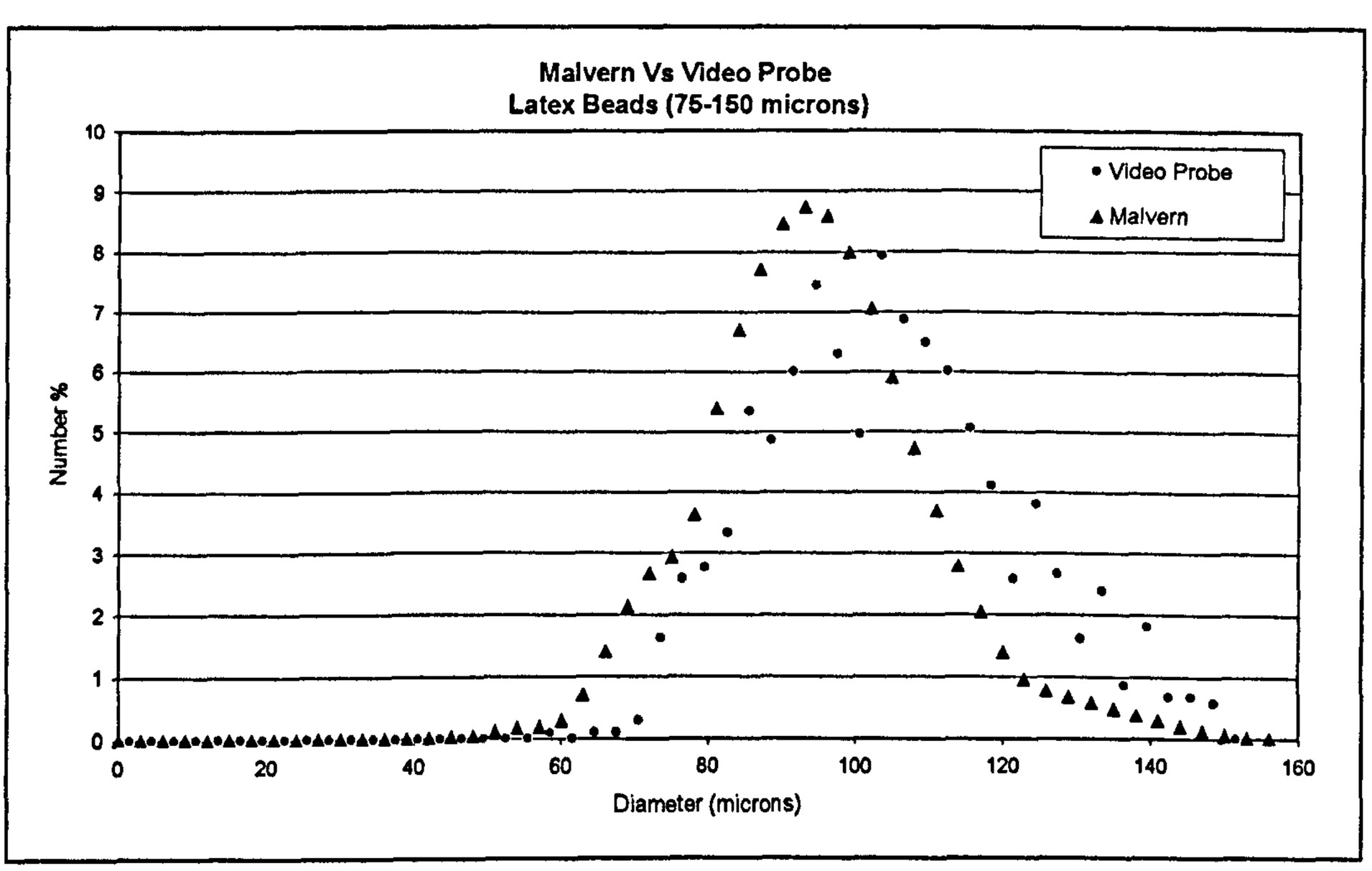

Figure A.3 Comparison of particle size distributions; Volume % (above) & Number % (below) generated by the Mastersizer and the Video Probe for Latex beads 113 μm.

Performance Tests: Droplet Size Distributions (Volume %)

69.85 mm Rotor: Emulsor Screen:

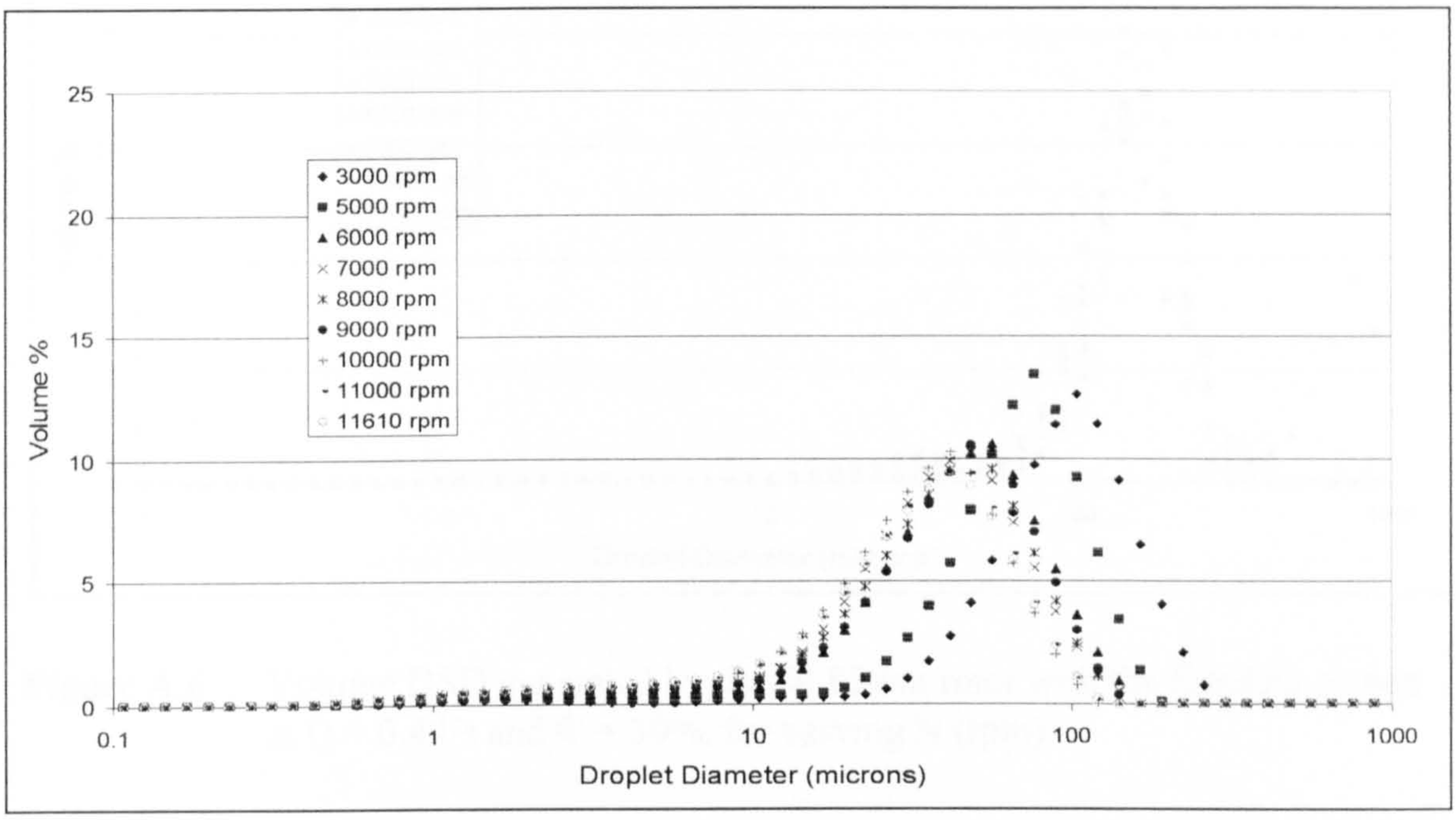

Figure A.4 Volume DSD generated by the 67.85mm rotor with the Emulsor Screen at Q = 0.4 l/s and Φ = 10%, for varying N (rpm).

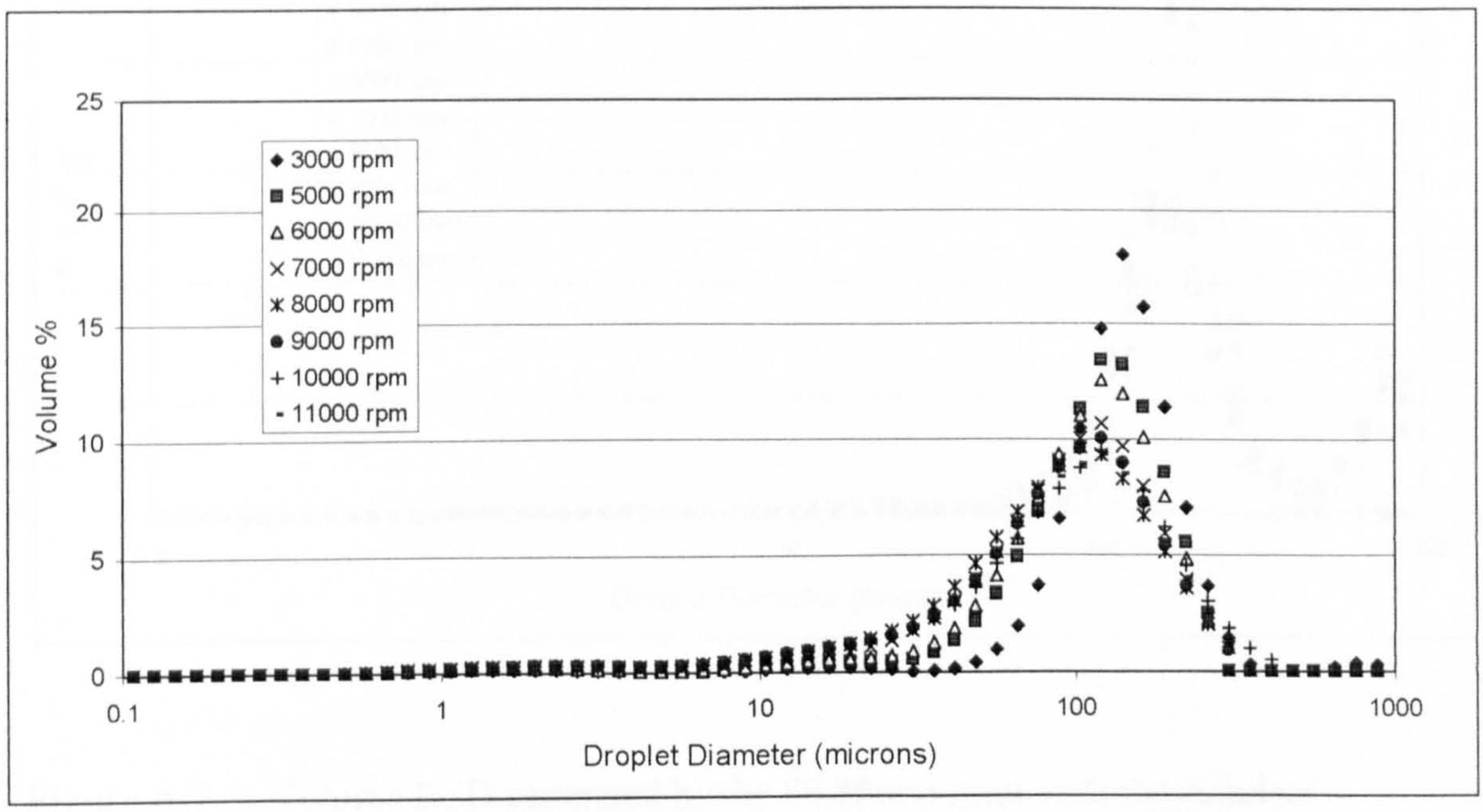

Figure A.5 Volume DSD generated by the 69.85mm rotor with the Emulsor Screen at Q = 0.4 l/s and Φ = 20%, for varying N (rpm).

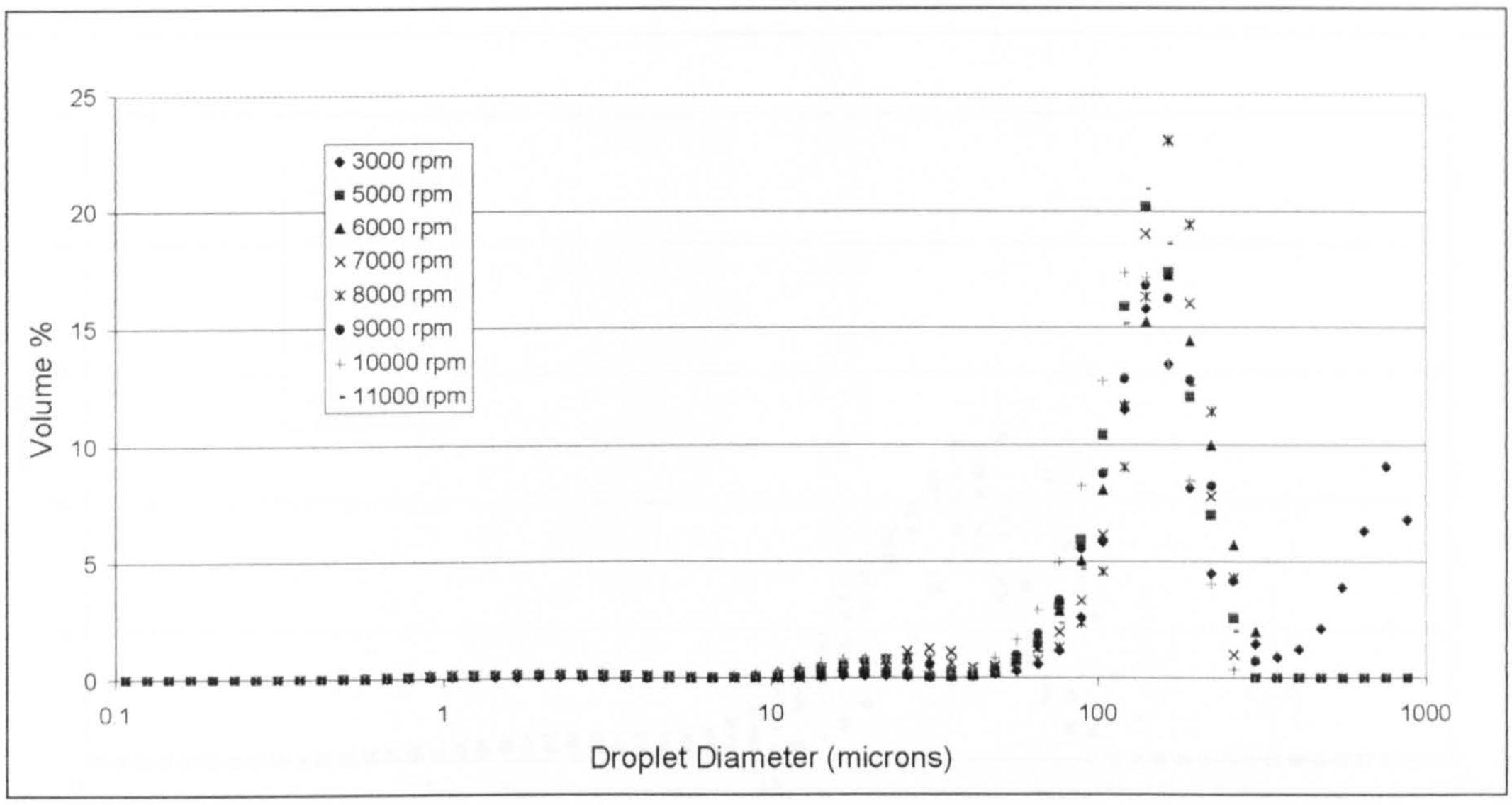

Figure A.6 Volume DSD generated by the 69.85mm rotor with the Emulsor screen at Q = 0.4 l/s and Φ = 30%, for varying N (rpm).

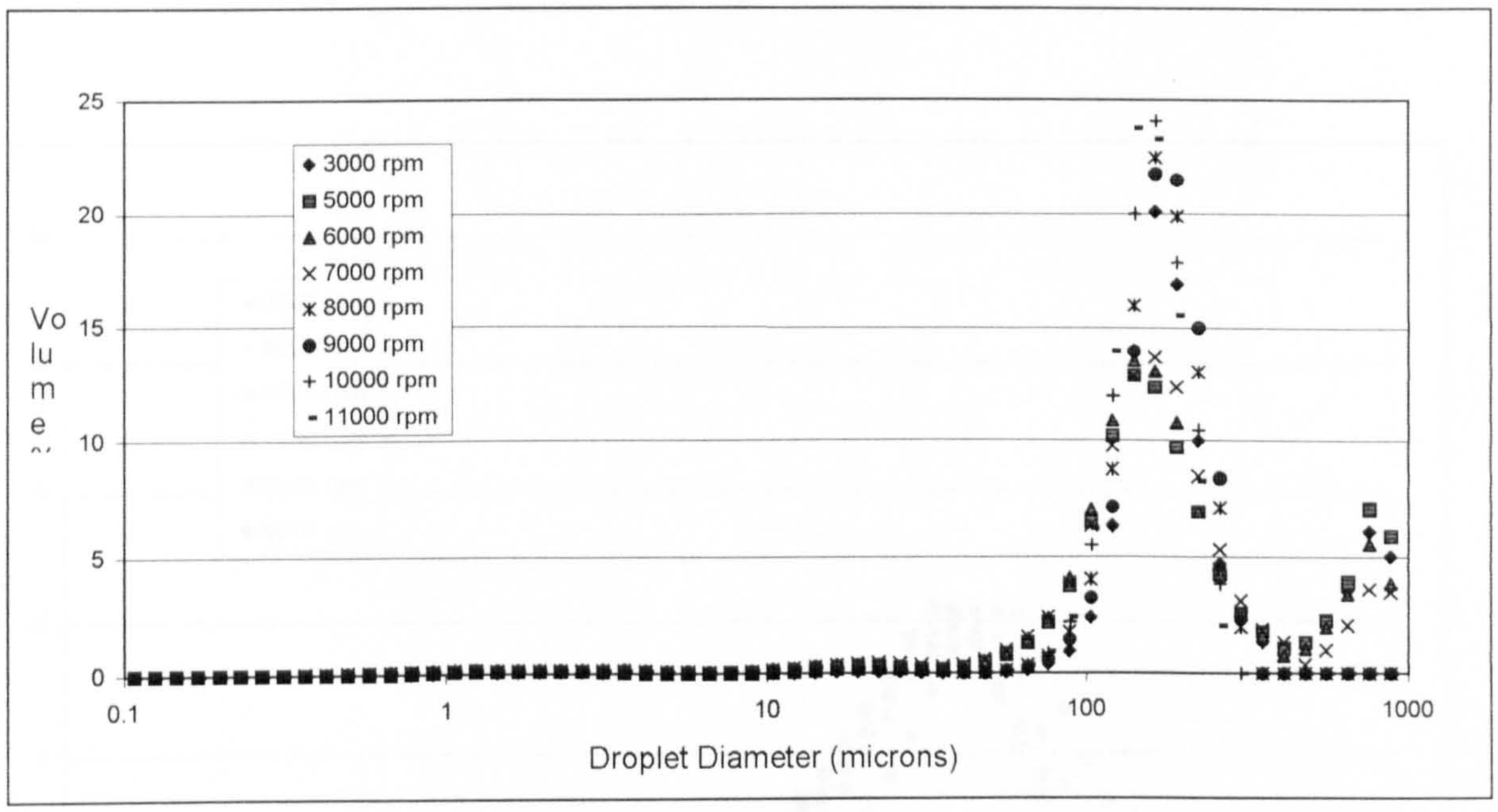

Figure A.7 Volume DSD generated by the 69.85mm rotor with the Emulsor Screen at Q = 0.4 l/s and Φ = 40%, for varying N (rpm).

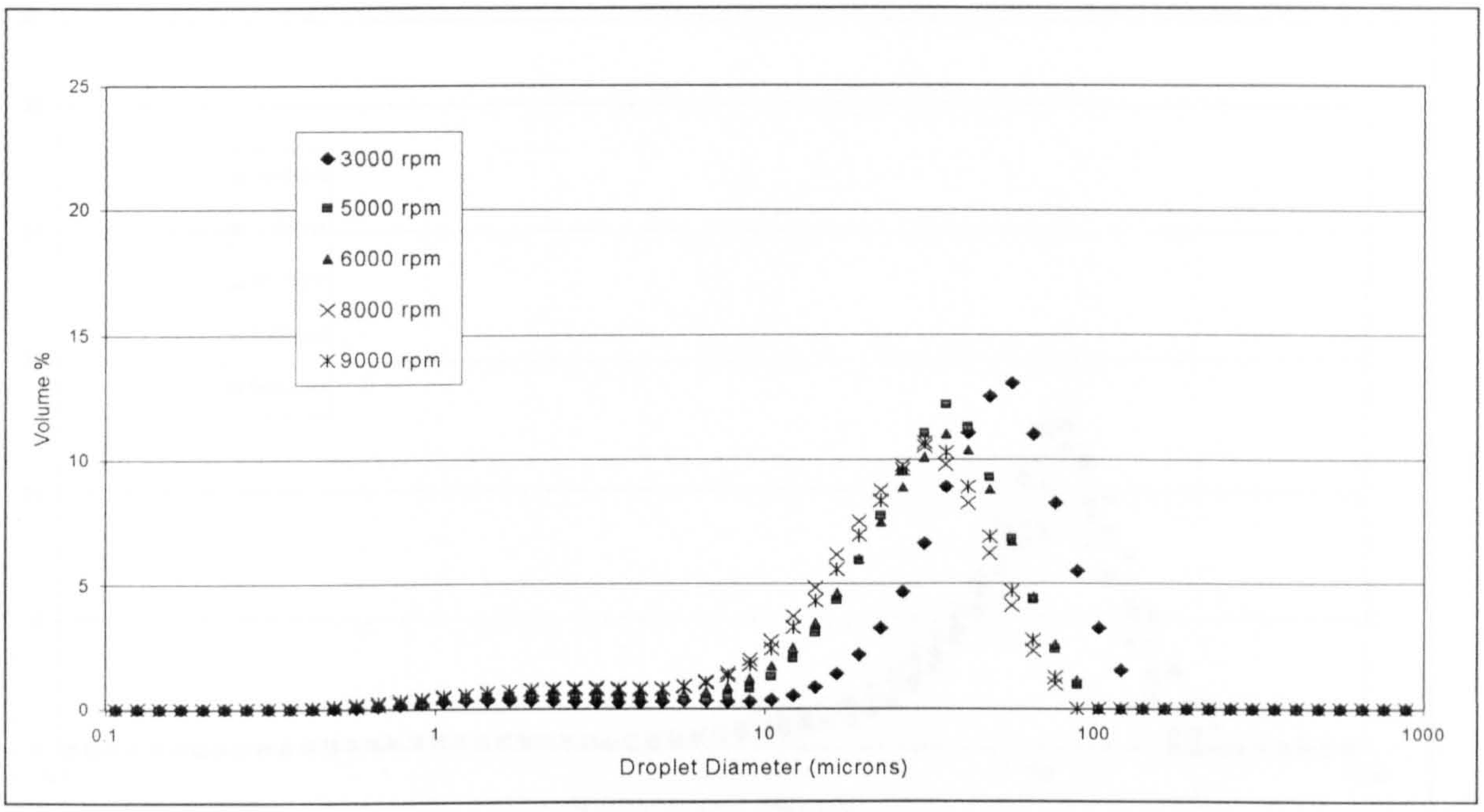

Figure A.8 Volume DSD generated by the 69.85mm rotor with the Emulsor Screen at Q = 0.8 l/s and Φ = 5%, for varying N (rpm).

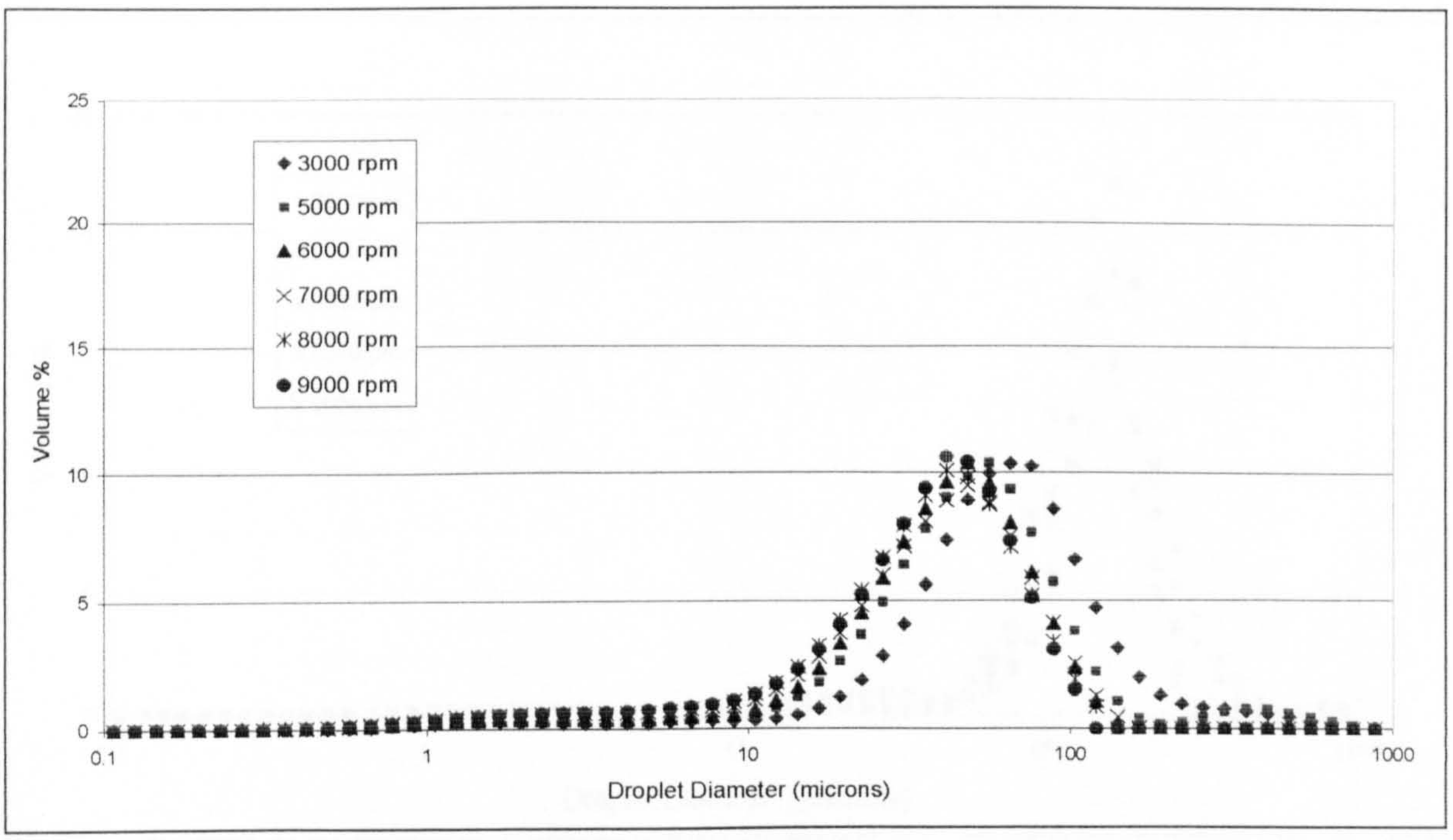

Figure A.9 Volume DSD generated by the 69.85mm rotor with the Emulsor Screen at Q = 0.8 l/s and Φ = 10%, for varying N (rpm).

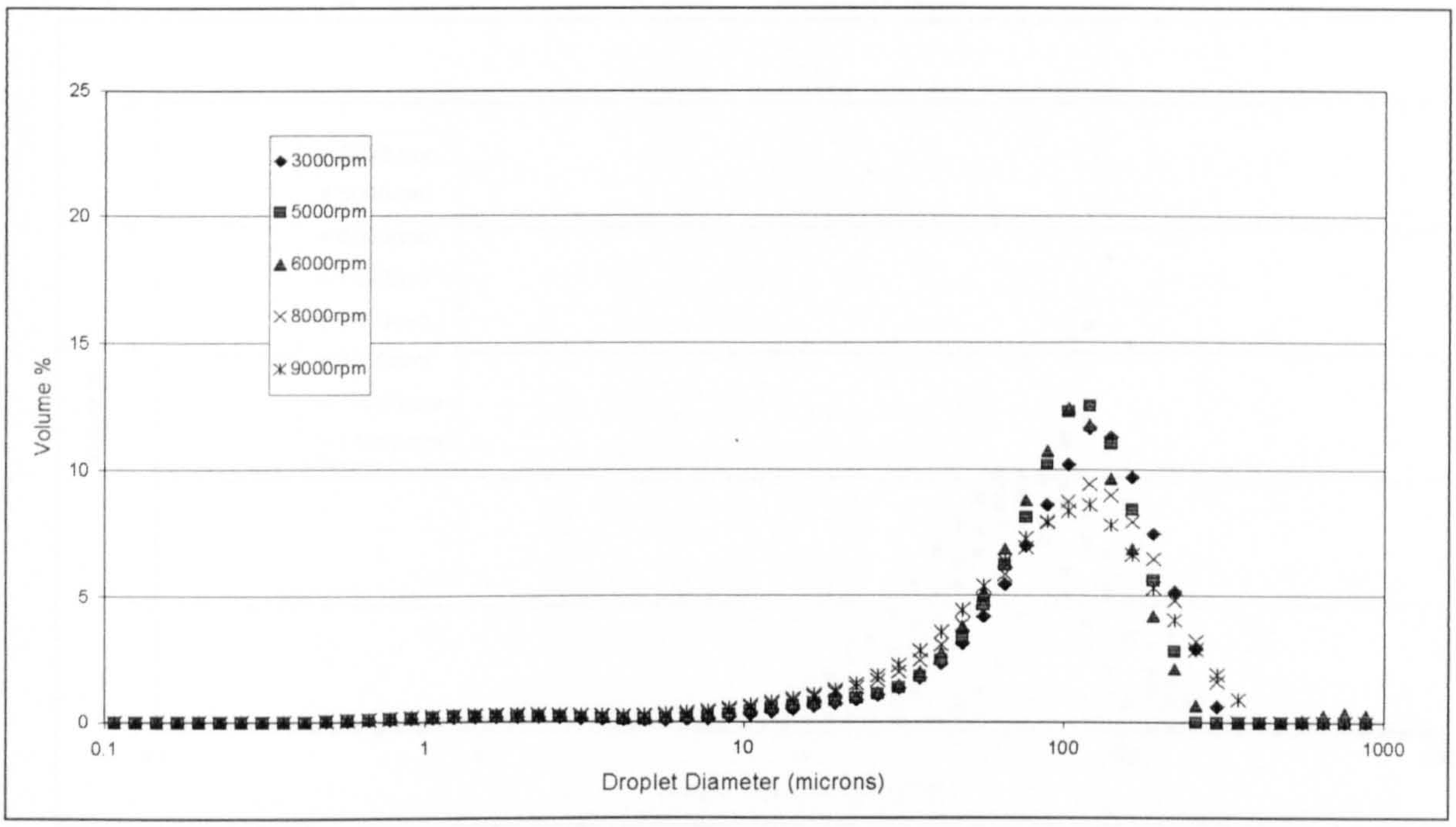

Figure A.10 Volume DSD generated by the 69.85mm rotor with the Emulsor Screen at Q = 0.8 l/s and Φ = 20%, for varying N (rpm).

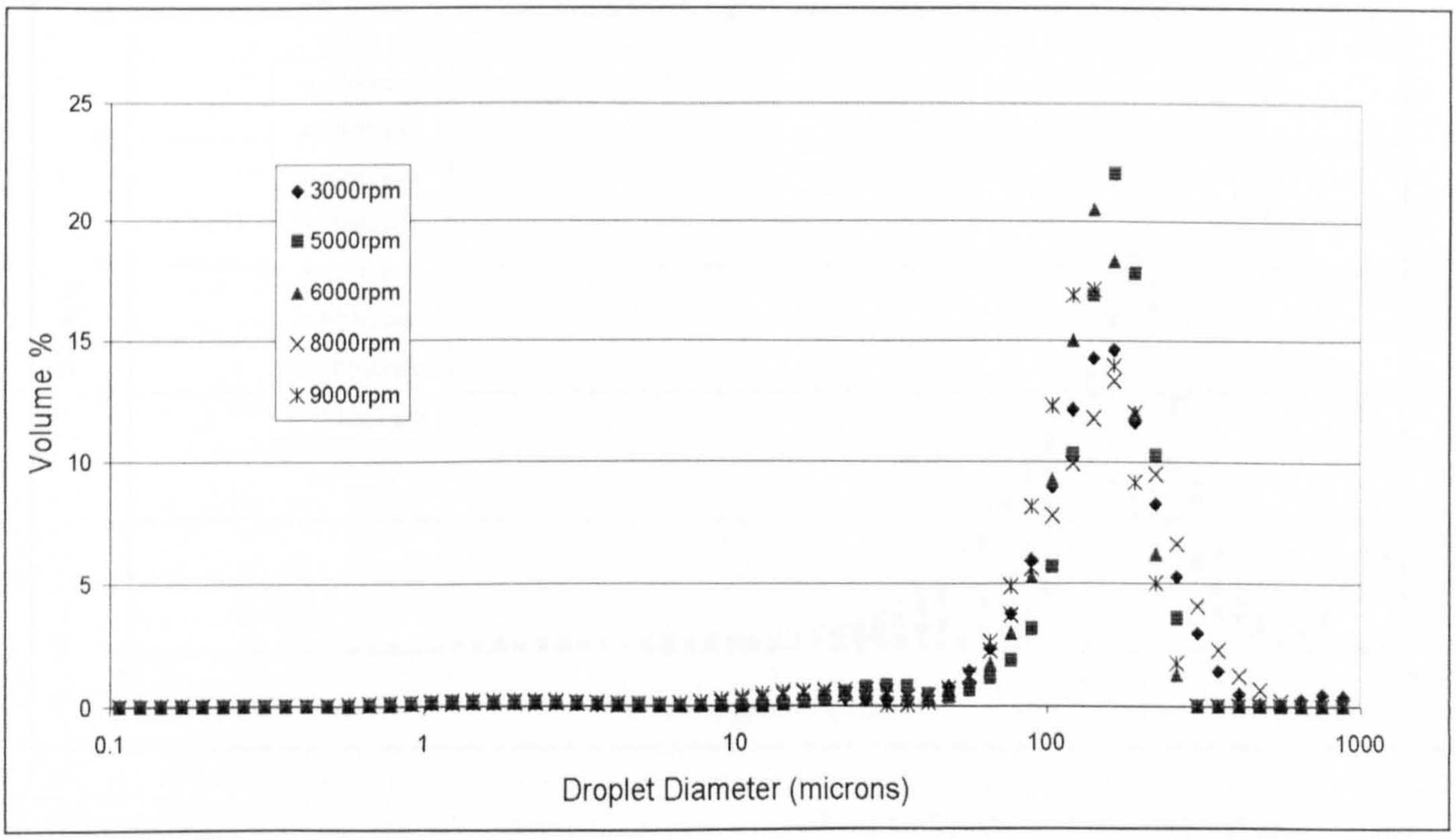

Figure A.11 Volume DSD generated by the 69.85mm rotor with the Emulsor Screen at Q = 0.8 l/s and Φ = 30%, for varying N (rpm).

Square Hole High Shear Screen (69.85 mm Rotor):

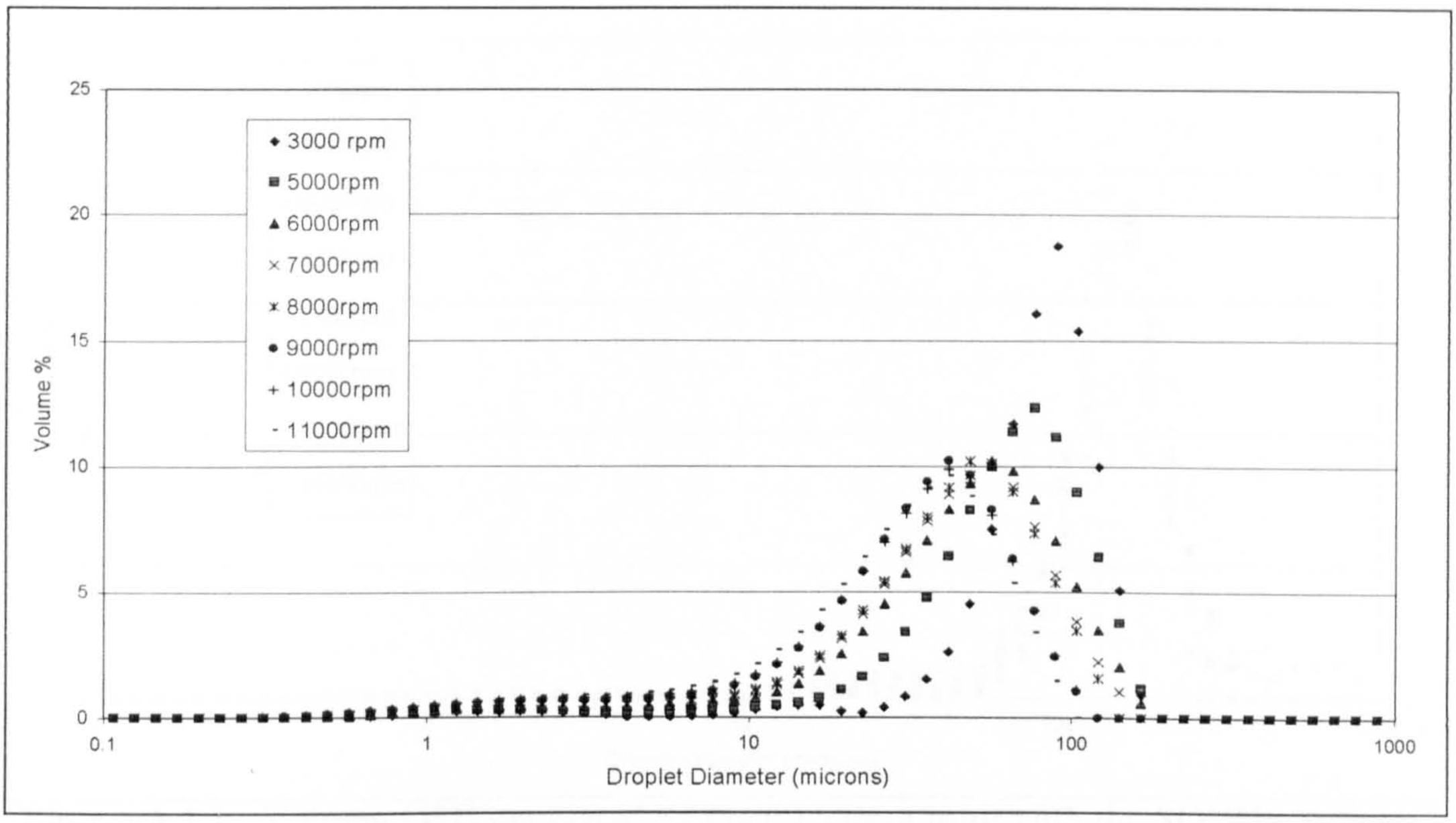

Figure A.12 Volume DSD generated by the 69.85mm rotor with the SQHHS Screen at Q = 0.4 l/s and Φ = 10%, for varying N (rpm).

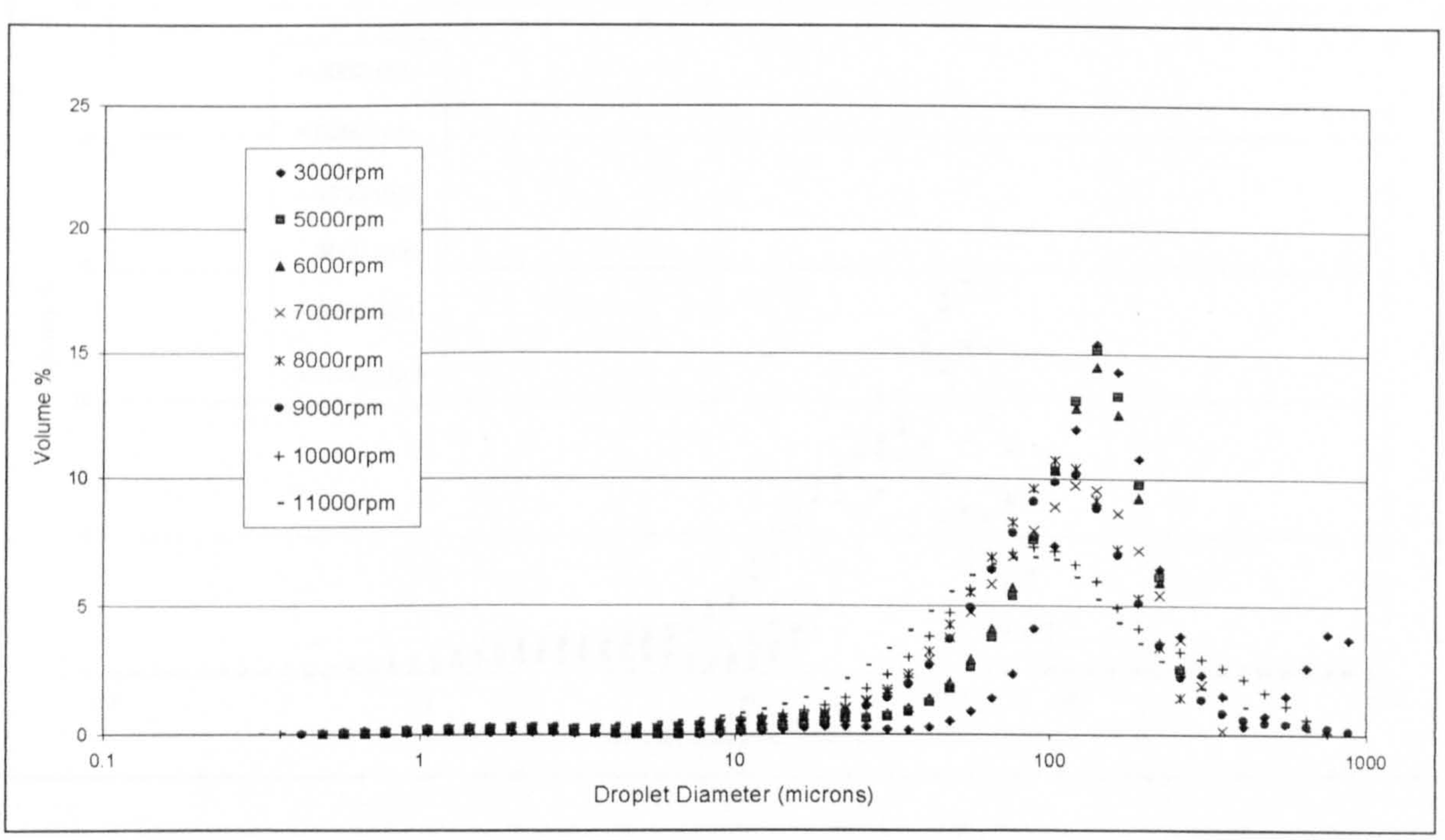

Figure A.13 Volume DSD generated by the 69.85mm rotor with the SQHHS Screen at Q = 0.4 l/s and Φ = 20%, for varying N (rpm).

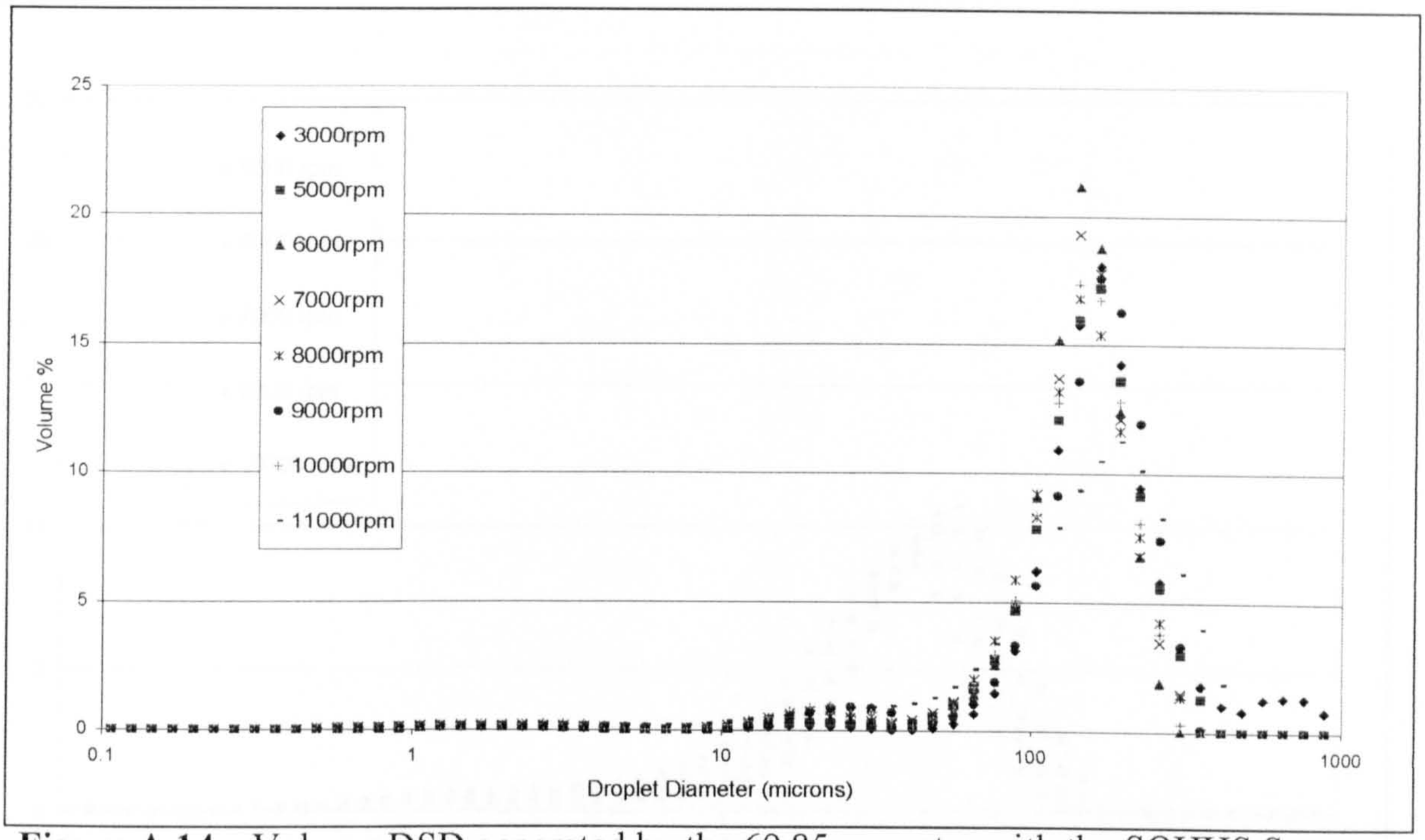

Figure A.14 Volume DSD generated by the 69.85mm rotor with the SQHHS Screen at Q = 0.4 l/s and Φ = 30%, for varying N (rpm).

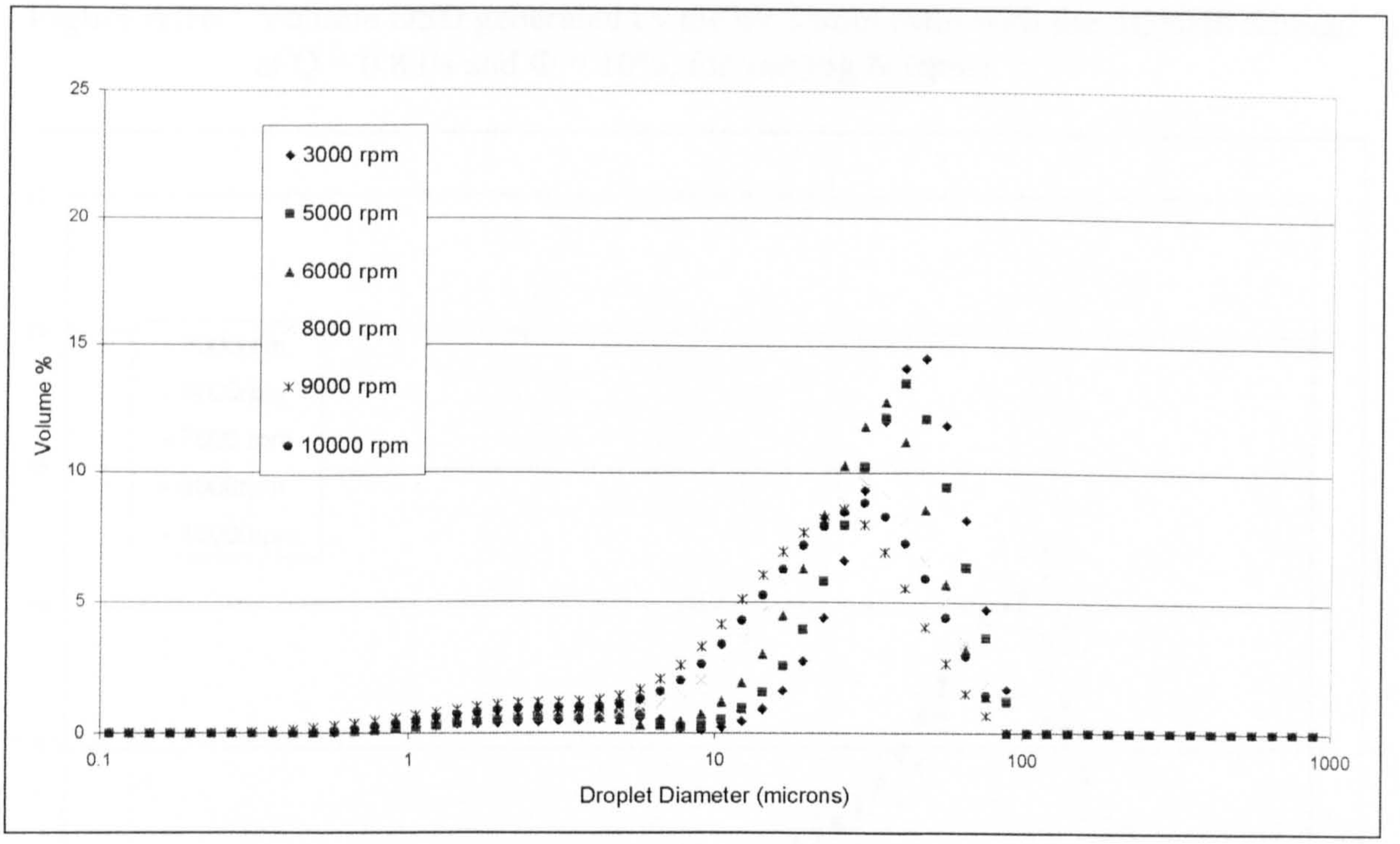

Figure A.15 Volume DSD generated by the 69.85mm rotor with the SQHHS Screen at Q = 0.8 l/s and Φ = 05%, for varying N (rpm).

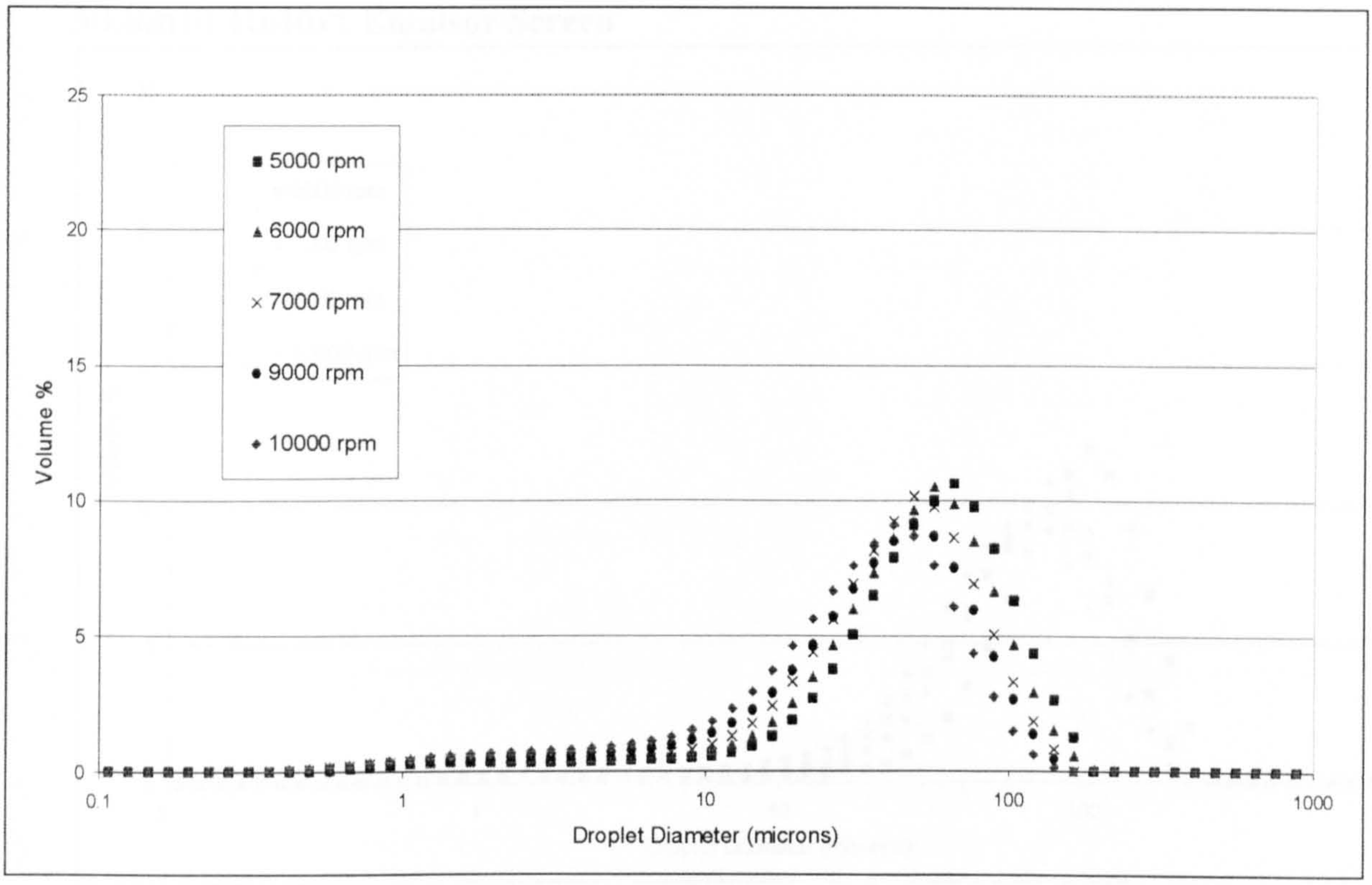

Figure A.16 Volume DSD generated by the 69.85mm rotor with the SQHHS Screen at Q = 0.8 l/s and Φ = 10%, for varying N (rpm).

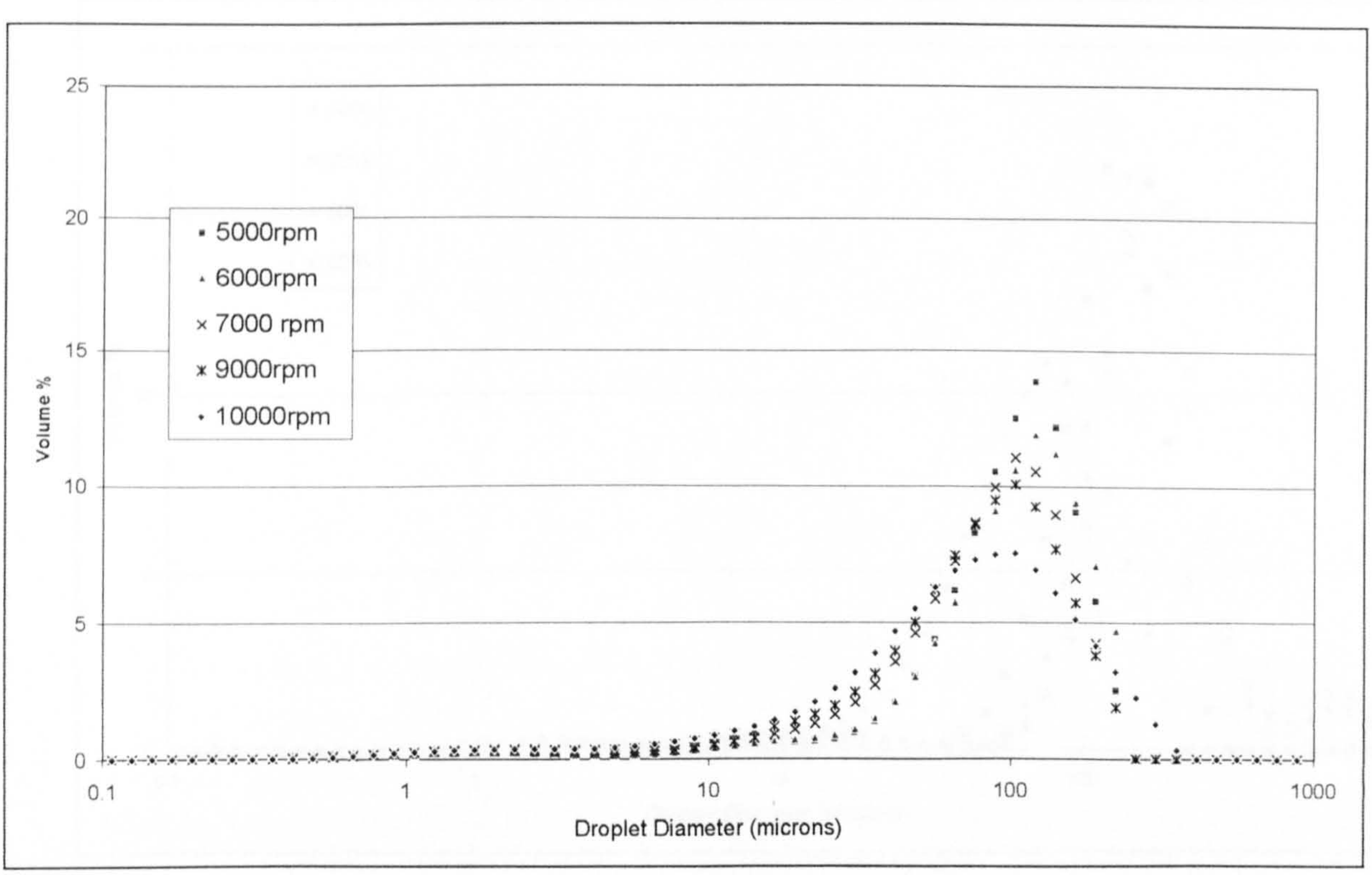

Figure A.17 Volume DSD generated by the 69.85mm rotor with the SQHHS Screen at Q = 0.8 l/s and Φ = 20%, for varying N (rpm).

50.8mm Rotor: Emulsor Screen

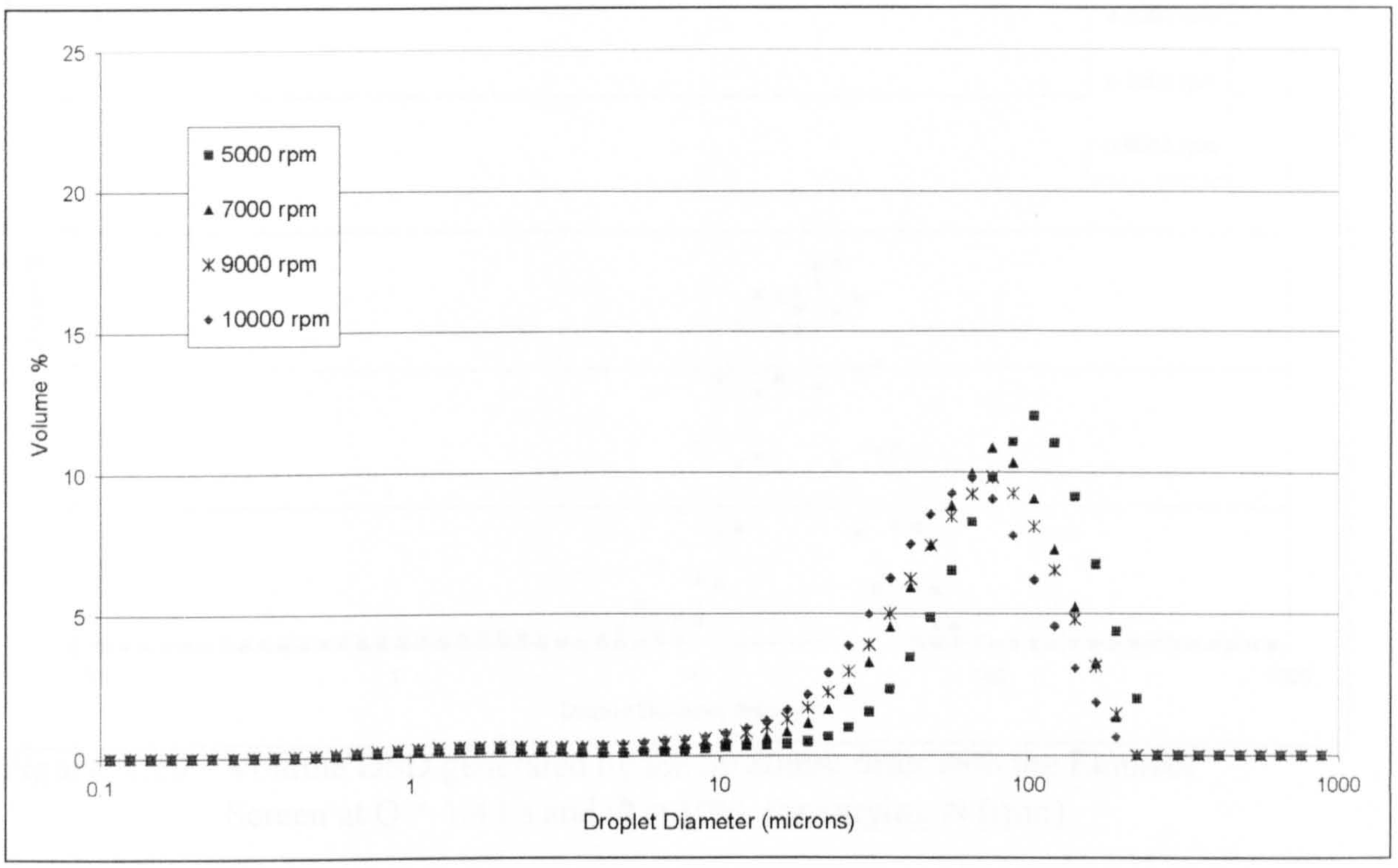

Figure A.18 Volume DSD generated by the 50.80mm rotor with the Emulsor Screen at Q = 0.4 l/s and Φ = 10%, for varying N (rpm).

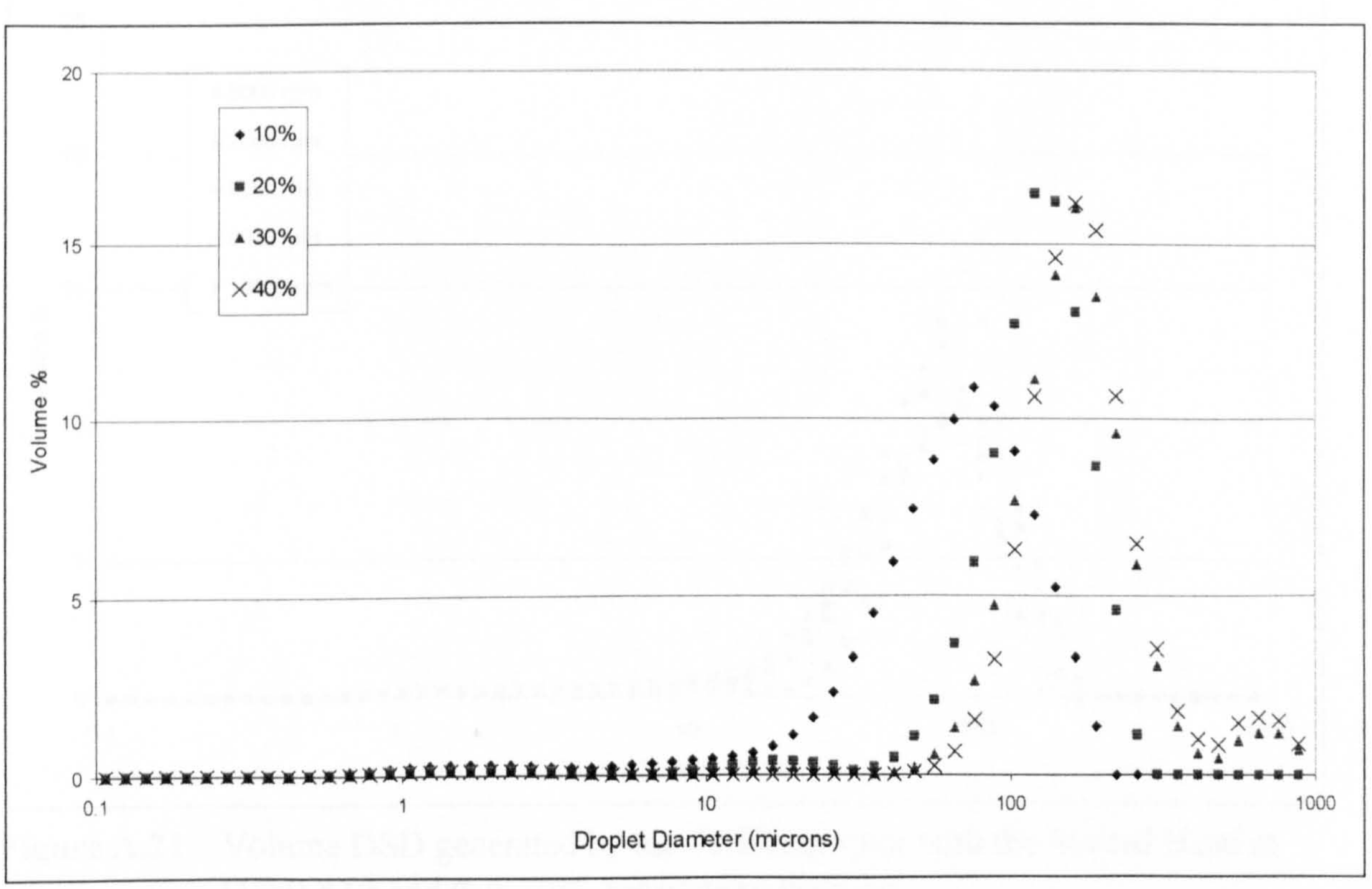

Figure A.19 Volume DSD generated by the 50.80mm rotor with the Emulsor Screen at Q = 0.4 l/s and N = 7000 rpm for varying Φ (%).

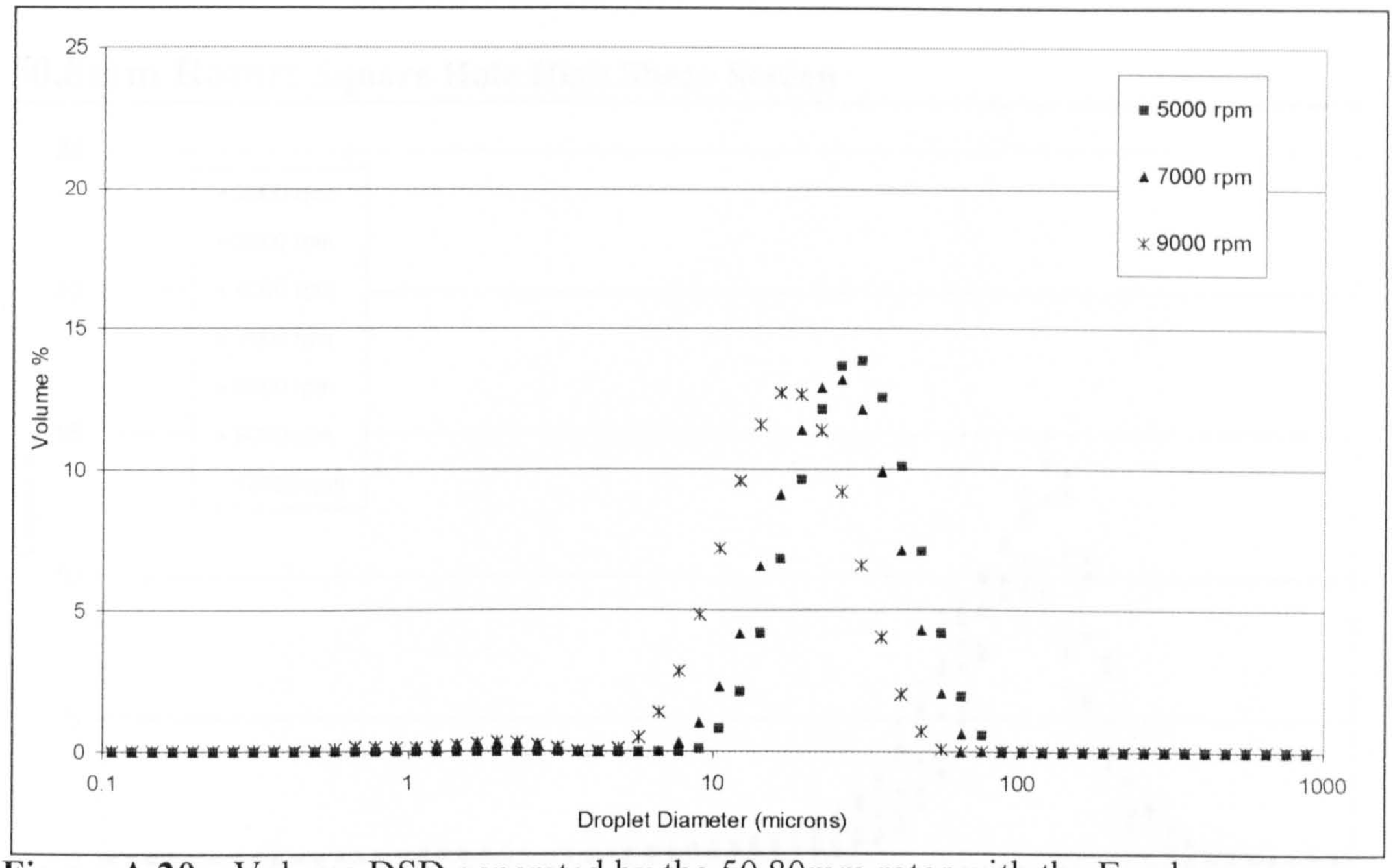

Figure A.20 Volume DSD generated by the 50.80mm rotor with the Emulsor Screen at Q = 1.4 l/s and Φ = 10%, for varying N (rpm).

50.8mm Rotor: Slotted Head

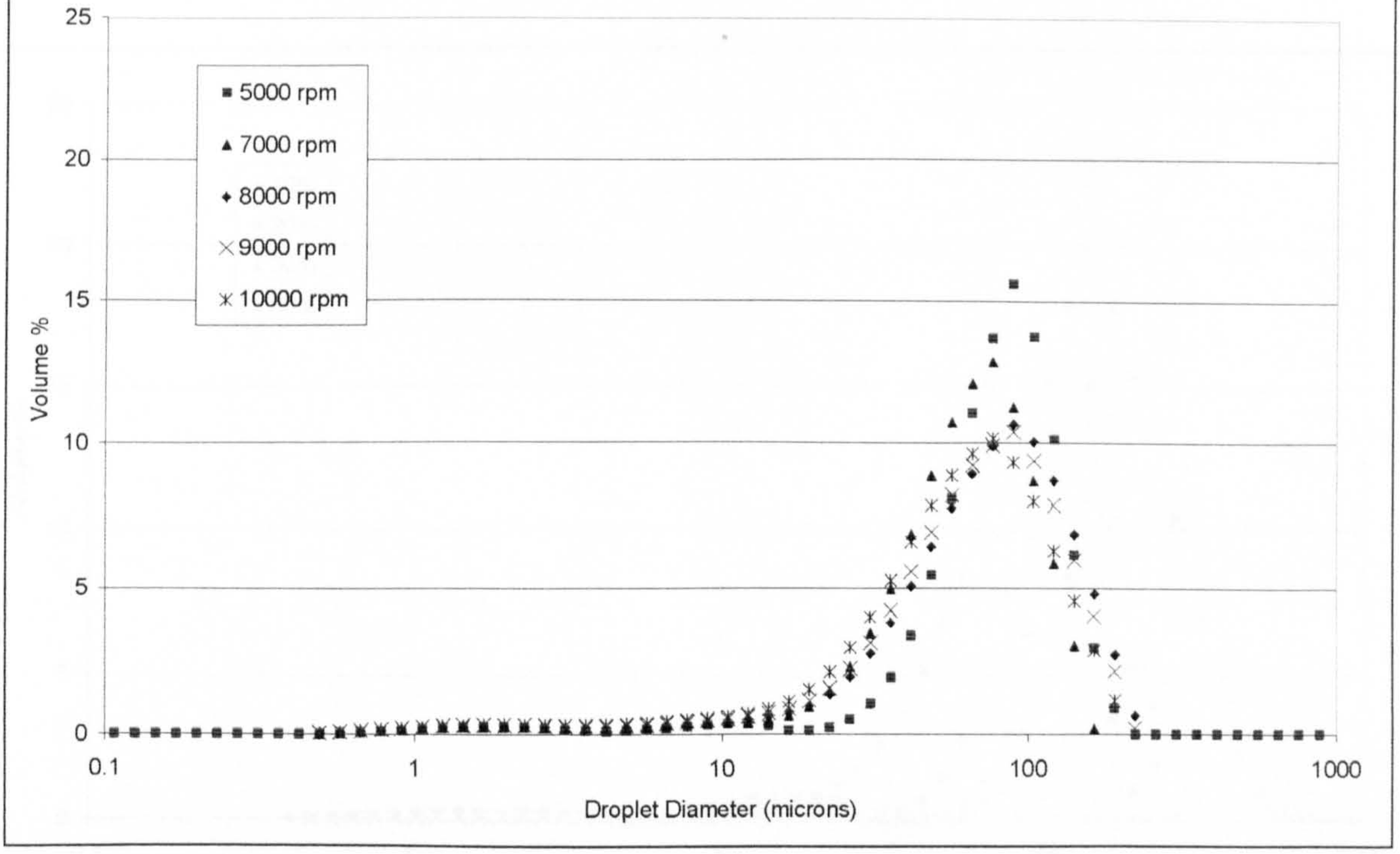

Figure A.21 Volume DSD generated by the 50.80mm rotor with the Slotted Head at Q = 0.4 l/s and Φ = 10%, for varying N (rpm).

50.8mm Rotor: Square Hole High Shear Screen

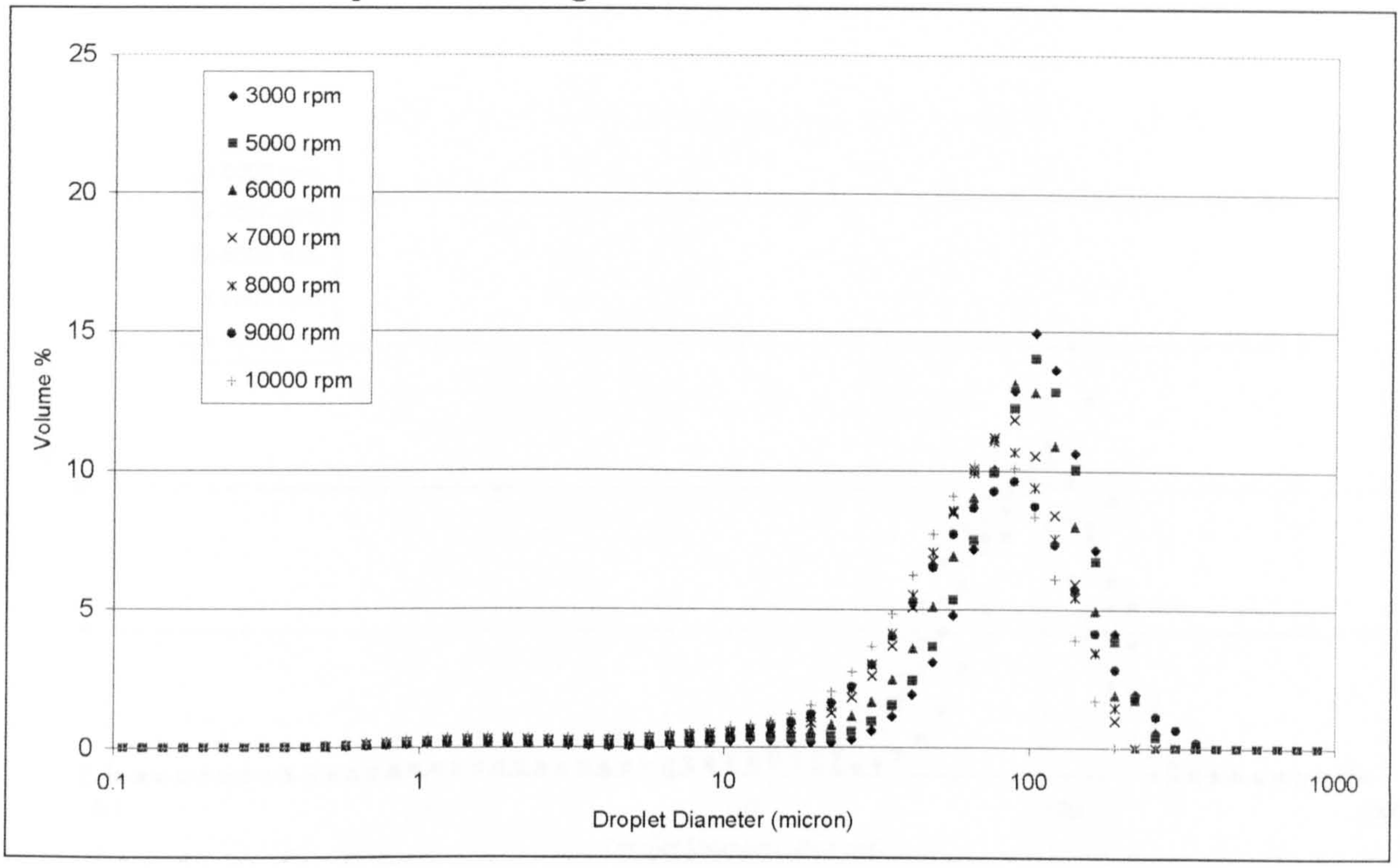

Figure A.22 Volume DSD generated by the 50.80mm rotor with the SHHS Screen at Q = 0.4 l/s and Φ = 10%, for varying N (rpm)

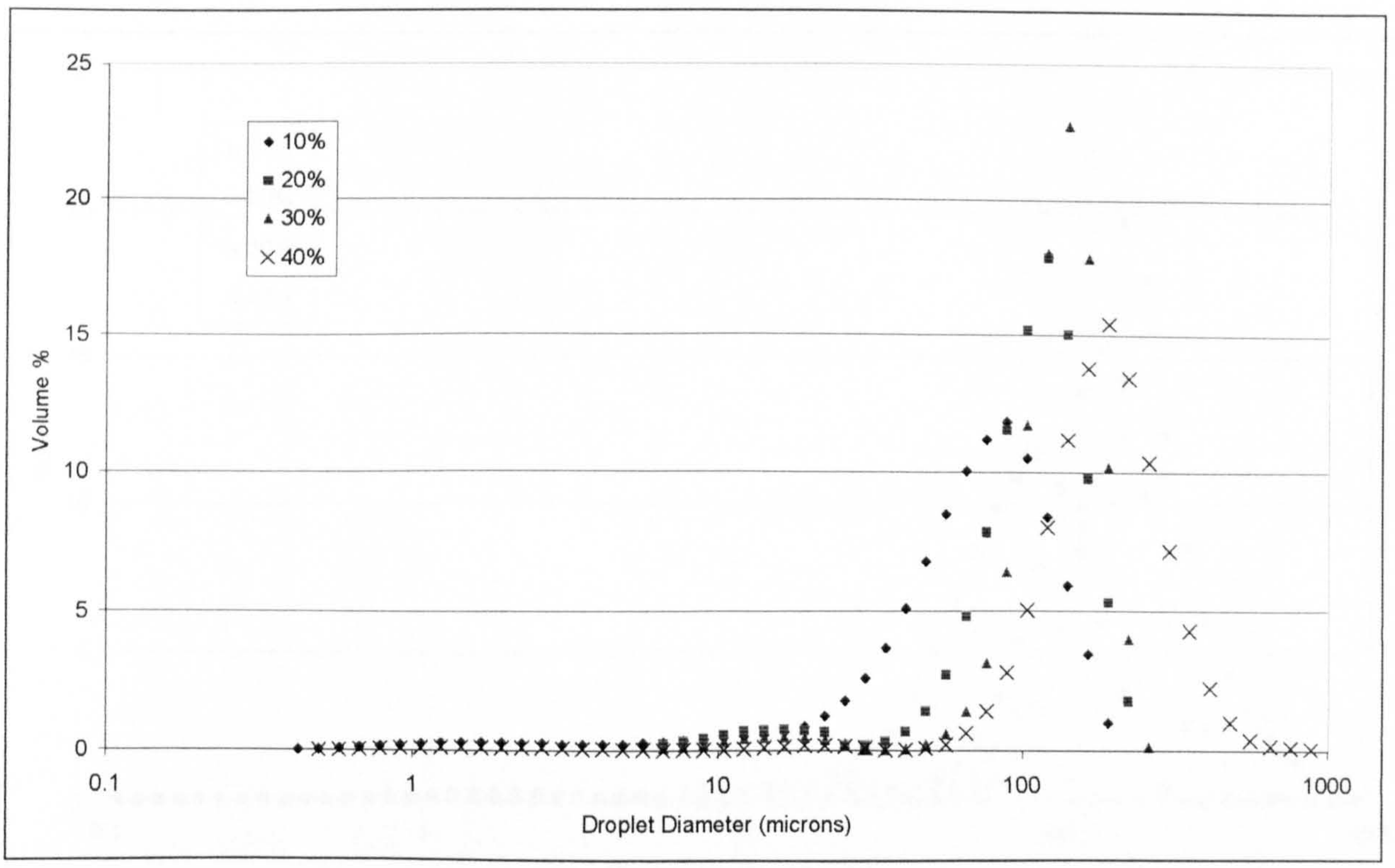

Figure A.23 Volume DSD generated by the 50.80mm rotor with the SHHS Screen at Q = 0.4 l/s and N = 7000 rpm for varying Φ (%).

50.8mm Rotor: General Disintegrating Head

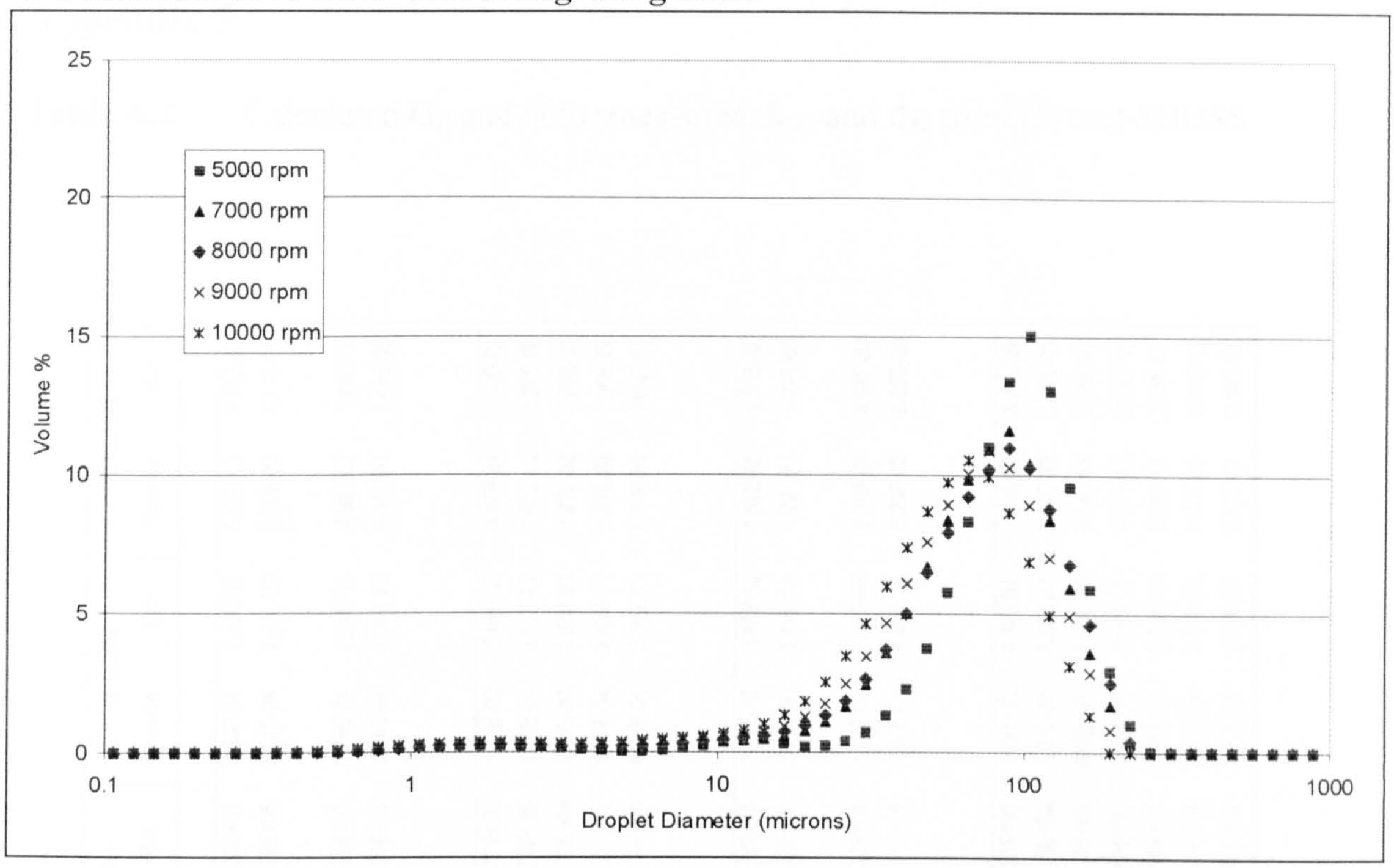

Figure A.24 Volume DSD generated by the 50.80mm rotor with the GDH at Q = 0.4 l/s and Φ = 10%, for varying N (rpm)

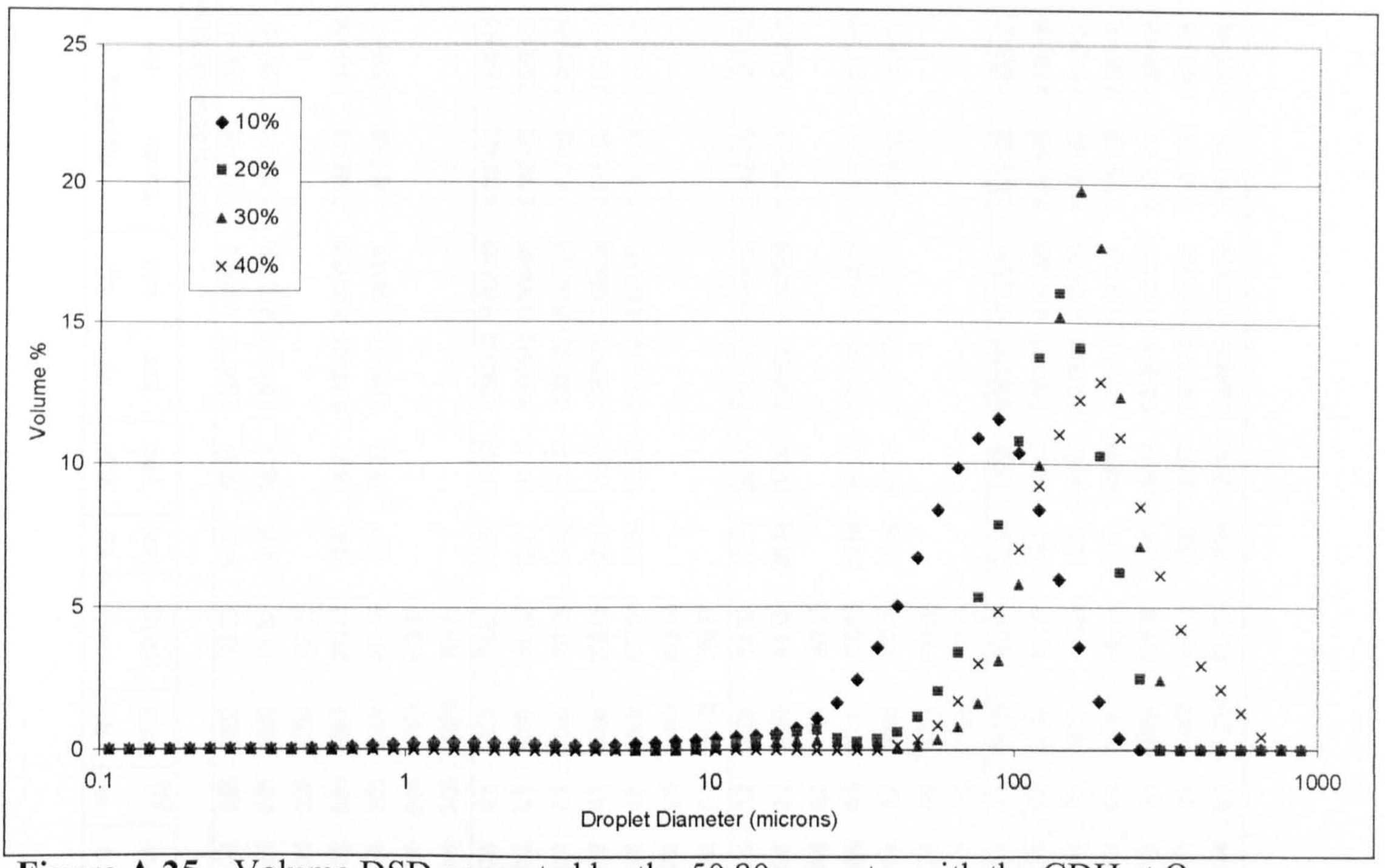

Figure A.25 Volume DSD generated by the 50.80mm rotor with the GDH at Q = 0.4 l/s and N = 7000 rpm for varying Φ (%)

Appendix 5

Table A.2 Calculated G_B and t_B for measured d_{max} and d_{32} from ES and SHHSS

Q (l/s)	Φ (%)	N RPM	ε (W/kg)	d_{32} (μm)	d_{max} (μm)	r_{32} (cm)	r_{max} (cm)	G_B, (s^{-1}), r_{32}		G_B, (s^{-1}), r_{max}		t_B, r_{32}, (s)		t_B, r_{max}, (s)	
								Couette	Ext	Couette	Ext	Couette	Ext	Couette	Ext
Emulsor Screen (69.85 mm)															
0.8	0.05	5000	73.60	14.31	88.91	0.000716	0.004446	5.71E+06	2.29E+06	9.20E+05	3.68E+05	9.33E-04	2.80E-03	5.80E-03	1.74E-02
0.8	0.05	6000	81.82	12.28	88.91	0.000614	0.004446	6.66E+06	2.66E+06	9.20E+05	3.68E+05	8.01E-04	2.40E-03	5.80E-03	1.74E-02
0.8	0.05	7000	167.25			-	-	-	-	-	-	-	-	-	-
0.8	0.05	8000	230.05	10.41	76.32	0.000521	0.003816	7.86E+06	3.14E+06	1.07E+06	4.29E+05	6.79E-04	2.04E-03	4.98E-03	1.49E-02
0.8	0.05	9000	477.93	9.74	76.32	0.000487	0.003816	8.40E+06	3.36E+06	1.07E+06	4.29E+05	6.35E-04	1.91E-03	4.98E-03	1.49E-02
0.8	0.05	10000	673.65			-	-	-	-	-	-	-	-	-	-
0.8	0.05	11000	786.77			-	-	-	-	-	-	-	-	-	-
0.8	0.1	5000	73.60	17.77	140.58	0.000889	0.007029	4.60E+06	1.84E+06	5.82E+05	2.33E+05	1.16E-03	3.48E-03	9.17E-03	2.75E-02
0.8	0.1	6000	81.82	12.85	163.77	0.000643	0.008189	6.36E+06	2.55E+06	4.99E+05	2.00E+05	8.38E-04	2.51E-03	1.07E-02	3.20E-02
0.8	0.1	7000	167.25	14.45	163.77	0.000723	0.008189	5.66E+06	2.26E+06	4.99E+05	2.00E+05	9.42E-04	2.83E-03	1.07E-02	3.20E-02
0.8	0.1	8000	230.05	12.37	120.67	0.000619	0.006034	6.61E+06	2.64E+06	6.78E+05	2.71E+05	8.07E-04	2.42E-03	7.87E-03	2.36E-02
0.8	0.1	9000	477.93	12.78	103.58	0.000639	0.005179	6.40E+06	2.56E+06	7.90E+05	3.16E+05	8.33E-04	2.50E-03	6.76E-03	2.03E-02
0.8	0.1	10000	673.65			-	-	-	-	-	-	-	-	-	-
0.8	0.1	11000	786.77			-	-	-	-	-	-	-	-	-	-
0.8	0.2	5000	73.60	27.75	258.95	0.001388	0.012948	2.95E+06	1.18E+06	3.16E+05	1.26E+05	1.81E-03	5.43E-03	1.69E-02	5.07E-02
0.8	0.2	6000	81.82	26.54	258.95	0.001327	0.012948	3.08E+06	1.23E+06	3.16E+05	1.26E+05	1.73E-03	5.19E-03	1.69E-02	5.07E-02
0.8	0.2	7000	167.25			-	-	-	-	-	-	-	-	-	-
0.8	0.2	8000	230.05	25.65	351.46	0.001283	0.017573	3.19E+06	1.28E+06	2.33E+05	9.31E+04	1.67E-03	5.02E-03	2.29E-02	6.88E-02
0.8	0.2	9000	477.93	23.46	351.46	0.001173	0.017573	3.49E+06	1.39E+06	2.33E+05	9.31E+04	1.53E-03	4.59E-03	2.29E-02	6.88E-02
0.8	0.2	10000	673.65			-	-	-	-	-	-	-	-	-	-
0.8	0.2	11000	786.77			-	-	-	-	-	-	-	-	-	-
0.4	0.1	5000	77.97	22.51	190.8	0.001126	0.00954	3.63E+06	1.45E+06	4.29E+05	1.71E+05	1.47E-03	4.40E-03	1.24E-02	3.73E-02
0.4	0.1	6000	122.37	15.5	140.57	0.000775	0.007029	5.28E+06	2.11E+06	5.82E+05	2.33E+05	1.01E-03	3.03E-03	9.17E-03	2.75E-02
0.4	0.1	7000	196.22	13.32	140.57	0.000666	0.007029	6.14E+06	2.46E+06	5.82E+05	2.33E+05	8.69E-04	2.61E-03	9.17E-03	2.75E-02
0.4	0.1	8000	284.61	13.7	140.57	0.000685	0.007029	5.97E+06	2.39E+06	5.82E+05	2.33E+05	8.93E-04	2.68E-03	9.17E-03	2.75E-02
0.4	0.1	9000	424.57	13.92	140.57	0.000696	0.007029	5.87E+06	2.35E+06	5.82E+05	2.33E+05	9.08E-04	2.72E-03	9.17E-03	2.75E-02
0.4	0.1	10000	613.13	10.92	120.67	0.000546	0.006034	7.49E+06	3.00E+06	6.78E+05	2.71E+05	7.12E-04	2.14E-03	7.87E-03	2.36E-02
0.4	0.1	11000	933.06	12.44	120.67	0.000622	0.006034	6.57E+06	2.63E+06	6.78E+05	2.71E+05	8.11E-04	2.43E-03	7.87E-03	2.36E-02

Q	Φ	N	ε	d_{32}	d_{max}	r_{32}	r_{max}	G_B, (s^{-1}), r_{32}		G_B, (s^{-1}), r_{max}		t_B, r_{32}, (s)		t_B, r_{max}, (s)	
(l/s)	(%)	RPM	(W/kg)	(μm)	(μm)	(cm)	(cm)	Couette	Ext	Couette	Ext	Couette	Ext	Couette	Ext
0.4	0.2	5000	77.97	41.27	258.95	0.002064	0.012948	1.98E+06	7.93E+05	3.16E+05	1.26E+05	2.69E-03	8.07E-03	1.69E-02	5.07E-02
0.4	0.2	6000	122.37	32.72	258.95	0.001636	0.012948	2.50E+06	1.00E+06	3.16E+05	1.26E+05	2.13E-03	6.40E-03	1.69E-02	5.07E-02
0.4	0.2	7000	196.22	30.28	301.68	0.001514	0.015084	2.70E+06	1.08E+06	2.71E+05	1.08E+05	1.97E-03	5.92E-03	1.97E-02	5.90E-02
0.4	0.2	8000	284.61	23.92	258.95	0.001196	0.012948	3.42E+06	1.37E+06	3.16E+05	1.26E+05	1.56E-03	4.68E-03	1.69E-02	5.07E-02
0.4	0.2	9000	424.57	24.58	301.68	0.001229	0.015084	3.33E+06	1.33E+06	2.71E+05	1.08E+05	1.60E-03	4.81E-03	1.97E-02	5.90E-02
0.4	0.2	10000	613.13	25.76	409.45	0.001288	0.020473	3.17E+06	1.27E+06	2.00E+05	7.99E+04	1.68E-03	5.04E-03	2.67E-02	8.01E-02
0.4	0.2	11000	933.06	22.97	301.68	0.001149	0.015084	3.56E+06	1.42E+06	2.71E+05	1.08E+05	1.50E-03	4.49E-03	1.97E-02	5.90E-02
0.4	0.3	5000	77.97	48.3	258.95	0.002415	0.012948	1.69E+06	6.77E+05	3.16E+05	1.26E+05	3.15E-03	9.45E-03	1.69E-02	5.07E-02
0.4	0.3	6000	122.37	43.91	351.46	0.002196	0.017573	1.86E+06	7.45E+05	2.33E+05	9.31E+04	2.86E-03	8.59E-03	2.29E-02	6.88E-02
0.4	0.3	7000	196.22	43.24	301.68	0.002162	0.015084	1.89E+06	7.57E+05	2.71E+05	1.08E+05	2.82E-03	8.46E-03	1.97E-02	5.90E-02
0.4	0.3	8000	284.61	43.27	301.68	0.002164	0.015084	1.89E+06	7.56E+05	2.71E+05	1.08E+05	2.82E-03	8.47E-03	1.97E-02	5.90E-02
0.4	0.3	9000	424.57	38.79	351.46	0.00194	0.017573	2.11E+06	8.43E+05	2.33E+05	9.31E+04	2.53E-03	7.59E-03	2.29E-02	6.88E-02
0.4	0.3	10000	613.13	37.99	301.68	0.0019	0.015084	2.15E+06	8.61E+05	2.71E+05	1.08E+05	2.48E-03	7.43E-03	1.97E-02	5.90E-02
0.4	0.3	11000	933.06	37.11	301.68	0.001856	0.015084	2.20E+06	8.81E+05	2.71E+05	1.08E+05	2.42E-03	7.26E-03	1.97E-02	5.90E-02
Square Hole High Shear Screen (69.85 mm)															
0.8	0.05	5000	112.02	15.3	88.91	0.000765	0.004446	5.34E+06	2.14E+06	9.20E+05	3.68E+05	9.98E-04	2.99E-03	5.80E-03	1.74E-02
0.8	0.05	6000		11.06	76.32	0.000553	0.003816	7.39E+06	2.96E+06	1.07E+06	4.29E+05	7.21E-04	2.16E-03	4.98E-03	1.49E-02
0.8	0.05	7000	167.03			-	-	-	-	-	-	-	-	-	-
0.8	0.05	8000	393.89	9.27	76.32	0.000464	0.003816	8.82E+06	3.53E+06	1.07E+06	4.29E+05	6.05E-04	1.81E-03	4.98E-03	1.49E-02
0.8	0.05	9000		6.66	76.32	0.000333	0.003816	1.23E+07	4.91E+06	1.07E+06	4.29E+05	4.34E-04	1.30E-03	4.98E-03	1.49E-02
0.8	0.05	10000	687.38	9.33	76.32	0.000467	0.003816	8.77E+06	3.51E+06	1.07E+06	4.29E+05	6.08E-04	1.83E-03	4.98E-03	1.49E-02
0.8	0.05	11000	1042.87			-	-	-	-	-	-	-	-	-	-
0.8	0.05	11500				-	-	-	-	-	-	-	-	-	-
0.8	0.1	5000	112.02	18.39	163.77	0.00092	0.008189	4.45E+06	1.78E+06	4.99E+05	2.00E+05	1.20E-03	3.60E-03	1.07E-02	3.20E-02
0.8	0.1	6000		12.82	163.77	0.000641	0.008189	6.38E+06	2.55E+06	4.99E+05	2.00E+05	8.36E-04	2.51E-03	1.07E-02	3.20E-02
0.8	0.1	7000	167.03	12.89	140.58	0.000645	0.007029	6.34E+06	2.54E+06	5.82E+05	2.33E+05	8.41E-04	2.52E-03	9.17E-03	2.75E-02
0.8	0.1	8000	393.89			-	-	-	-	-	-	-	-	-	-
0.8	0.1	9000		14.65	140.58	0.000733	0.007029	5.58E+06	2.23E+06	5.82E+05	2.33E+05	9.55E-04	2.87E-03	9.17E-03	2.75E-02
0.8	0.1	10000	687.38	10.13		-	-	-	-	-	-	-	-	-	-
0.8	0.1	11000	1042.87			-	-	-	-	-	-	-	-	-	-
0.8	0.1	11500				-	-	-	-	-	-	-	-	-	-

Q (l/s)	Φ (%)	N RPM	ε (W/kg)	d_{32} (μm)	d_{max} (μm)	r_{32} (cm)	r_{max} (cm)	G_B, (s^{-1}), r_{32}		G_B, (s^{-1}), r_{max}		t_B, r_{32}, (s)		t_B, r_{max}, (s)	
								Couette	Ext	Couette	Ext	Couette	Ext	Couette	Ext
0 8	0.2	5000	112 02	29.89	222.28	0.001495	0.011114	2.74E+06	1 09E+06	3 68E+05	1.47E+05	1.95E-03	5.85E-03	1.45E-02	4.35E-02
0.8	0.2	6000		29.04	258.95	0.001452	0.012948	2.82E+06	1 13E+06	3.16E+05	1.26E+05	1.89E-03	5.68E-03	1.69E-02	5.07E-02
0.8	0.2	7000	167.03	22.44	222.28	0.001122	0.011114	3.64E+06	1.46E+06	3 68E+05	1.47E+05	1.46E-03	4 39E-03	1.45E-02	4 35E-02
0.8	0.2	8000	393 89			-	-	-	-	-	-	-	-	-	-
0.8	0.2	9000		19.7	222 28	0.000985	0.011114	4.15E+06	1.66E+06	3.68E+05	1.47E+05	1.28E-03	3.85E-03	1.45E-02	4.35E-02
0.8	0.2	10000	687.38	19 96	301 68	0.000998	0.015084	4.10E+06	1.64E+06	2.71E+05	1.08E+05	1.30E-03	3.91E-03	1.97E-02	5.90E-02
0.8	0.2	11000	1042.87			-	-	-	-	-	-	-	-	-	-
0.8	0.2	11500				-	-	-	-	-	-	-	-	-	-
0.4	0.1	5000	52.44	23.03	163.77	0.001152	0.008189	3.55E+06	1 42E+06	4 99E+05	2.00E+05	1.50E-03	4.51E-03	1.07E-02	3.20E-02
0.4	0.1	6000		17.62	140.58	0 000881	0.007029	4.64E+06	1 86E+06	5.82E+05	2.33E+05	1.15E-03	3 45E-03	9.17E-03	2.75E-02
0.4	0.1	7000	212 08	14.86	140.58	0.000743	0.007029	5.50E+06	2.20E+06	5.82E+05	2.33E+05	9.69E-04	2.91E-03	9.17E-03	2.75E-02
0 4	0.1	8000	294 57	13.45	120 67	0 000673	0.006034	6.08E+06	2.43E+06	6.78E+05	2.71E+05	8.77E-04	2 63E-03	7.87E-03	2.36E-02
0.4	0,1	9000		10.53	103 58	0.000527	0.005179	7.77E+06	3.11E+06	7.90E+05	3.16E+05	6.87E-04	2.06E-03	6.76E-03	2.03E-02
0.4	0.1	10000	581.74	10.06	103.58	0.000503	0.005179	8.13E+06	3.25E+06	7.90E+05	3.16E+05	6.56E-04	1.97E-03	6.76E-03	2.03E-02
0.4	0.1	11000	859 70	10.52	88.91	0.000526	0.004446	7.77E+06	3.11E+06	9.20E+05	3.68E+05	6.86E-04	2.06E-03	5.80E-03	1.74E-02
0.4	0.2	5000	52.44	38.9	258.95	0.001945	0.012948	2.10E+06	8.41E+05	3.16E+05	1.26E+05	2.54E-03	7.61E-03	1.69E-02	5.07E-02
0.4	0.2	6000		36.61	258.95	0.001831	0.012948	2.23E+06	8 94E+05	3.16E+05	1.26E+05	2.39E-03	7.16E-03	1.69E-02	5.07E-02
0.4	0.2	7000	212 08	30.72	301.68	0 001536	0.015084	2.66E+06	1.06E+06	2.71E+05	1.08E+05	2.00E-03	6 01E-03	1.97E-02	5.90E-02
0 4	0.2	8000	294 57	26.75	258 95	0.001338	0.012948	3.06E+06	1.22E+06	3.16E+05	1.26E+05	1.74E-03	5.23E-03	1.69E-02	5.07E-02
0.4	0.2	9000		27.38		-	-	-	-	-	-	-	-	-	-
0.4	0 2	10000	581 74	23.74		-	-	-	-	-	-	-	-	-	-
0.4	0.2	11000	859 70	16.74		-	-	-	-	-	-	-	-	-	-
0.4	0.3	5000	52.44	49.85	351.46	0.002493	0.017573	1.64E+06	6.56E+05	2.33E+05	9.31E+04	3.25E-03	9.75E-03	2.29E-02	6.88E-02
0.4	0.3	6000		50.55	258.95	0.002528	0.012948	1.62E+06	6.47E+05	3.16E+05	1.26E+05	3.30E-03	9.89E-03	1.69E-02	5.07E-02
0 4	0.3	7000	212 08	41 93	301 68	0.002097	0.015084	1 95E+06	7 80E+05	2 71E+05	1.08E+05	2.73E-03	8 20E-03	1 97E-02	5.90E-02
0 4	0.3	8000	294.57	33.96	301 68	0 001698	0.015084	2.41E+06	9.63E+05	2.71E+05	1.08E+05	2.21E-03	6.64E-03	1.97E-02	5.90E-02
0 4	0.3	9000		39.97	351 46	0 001999	0.017573	2.05E+06	8 18E+05	2 33E+05	9.31E+04	2 61E-03	7 82E-03	2.29E-02	6.88E-02
0.4	0.3	10000	581 74	34,12	258 95	0.001706	0.012948	2.40E+06	9 59E+05	3.16E+05	1.26E+05	2.23E-03	6.68E-03	1.69E-02	5.07E-02
0 4	0.3	11000	859 70	34.06		-	-	-	-	-	-	-	-	-	-